

# THE INTERPLAY OF MAGNETISM AND STRUCTURE IN PATTERNED MULTILAYER THIN FILMS

By  
Christian John Kinane

SUBMITTED IN ACCORDANCE WITH THE  
REQUIREMENTS FOR THE DEGREE OF  
DOCTOR OF PHILOSOPHY

UNIVERSITY OF LEEDS  
DEPARTMENT OF PHYSICS AND ASTRONOMY  
LEEDS, WEST YORKSHIRE  
JULY 2008

The candidate confirms that the work submitted is his own and that appropriate credit has been given where reference has been made to the work of others. This copy has been supplied on the understanding that it is copyright material and that no quotation from the thesis may be published without proper acknowledgement.

*In Memory of*  
*Anne Swale and James Kinane*



# List of Tables

3.1	Transition metal elements' absorption edges. . . . .	64
4.1	Properties of a free neutron . . . . .	72

# List of Figures

1.1	Schematic of a d.c. magnetron sputtering gun. . . . .	7
1.2	The layout of the Mjolnir sputter system at Leeds University. . . . .	8
1.3	The internal layout of the Mjolnir sputter system at Leeds University. . . . .	9
1.4	Nanosphere self-assembly at a water/air interface. . . . .	10
1.5	Schematic of the Leeds x-ray diffractometer's geometry and components. . . . .	11
1.6	Example specular ( $\theta/2\theta$ ) scan for a single layer of Co $\approx 100\text{\AA}$ thick. . . . .	12
1.7	The Leeds Maglab <sup>VSM</sup> system and associated electronics. . . . .	13
1.8	Examples of VSM hysteresis loops for Co/Ru multilayers. . . . .	14
1.9	MOKE geometry showing 'S' and 'P' polarised light. . . . .	15
1.10	The three different modes of MOKE operation . . . . .	17
1.11	MOKE orientations, longitudinal and Polar. . . . .	18
1.12	Examples of longitudinal MOKE hysteresis loops for Co/Ru multilayers. . . . .	18
1.13	Schematic of an Atomic Force Microscope . . . . .	20
2.1	Bremsstrahlung background with fluorescence lines . . . . .	23
2.2	Absorption processes and fluorescence processes . . . . .	24
2.3	Circularly polarised light production. . . . .	27
2.4	Polarisation tuning curve for the U4B beamline. . . . .	27
2.5	Schematic of the layout of the U4B beamline at the NSLS. . . . .	30
2.6	Schematic of the fission process. . . . .	32
2.7	Schematic of the spallation process. . . . .	33
2.8	Schematic of layout of the ADAM beamline at the ILL. . . . .	35
2.9	Schematic of layout of the CRISP beamline at ISIS. . . . .	37
3.1	Absorption of photons by materials. . . . .	40
3.2	Plane wave incident on the boundary between two media. . . . .	41



3.3	Reflection and refraction from a multilayer structure. . . . .	43
3.4	2 circle scattering real space geometry. . . . .	48
3.5	Schematic of reciprocal space for the real space area shown in figure 3.4	48
3.6	Reciprocal space map for Cu $K_\alpha$ (1.54 Å) radiation. . . . .	49
3.7	Reflectivity simulation from an 100 Å Co layer. . . . .	52
3.8	Simulation of the reflectivity from a Co/Ru multilayer. . . . .	53
3.9	Schematics of structural and graded interfaces . . . . .	53
3.10	An example of specular and diffuse scatter . . . . .	55
3.11	Example DWBA specular curves with roughness and grading . . . . .	56
3.12	Example DWBA rocking curves with roughness and grading . . . . .	60
3.13	Schematic of flat, correlated and uncorrelated interfaces. . . . .	61
3.14	Schematic of charge and resonant scattering. . . . .	63
3.15	X-ray Magnetic Circular Dichroism (XMCD). . . . .	66
3.16	Definition of spin asymmetry. . . . .	69
4.1	The different scattering mechanisms for x-rays and neutrons . . . . .	70
4.2	Schematic of a polarised neutron experiment . . . . .	76
4.3	Relationship between $\mathbf{M}$ and $\mathbf{M}_\perp$ . . . . .	78
5.1	Example domain patterning structure. . . . .	80
5.2	Domain patterns and perfect interfaces with antiferromagnetic coupling.	81
5.3	Schematic of a structural and magnetic interface. . . . .	83
5.4	Domain width calibration for the Co/Pt multilayer. . . . .	85
5.5	Sample schematic and VSM data . . . . .	87
5.6	Cu $K_\alpha$ specular and rocking scans for the domain patterned sample. .	87
5.7	Energy scan over the Fe edges. . . . .	88
5.8	Specular scans on and off the Fe $L_3$ resonance. . . . .	89
5.9	$Q_x$ scans and spin asymmetry. . . . .	91
5.10	MFM stuff . . . . .	93
6.1	Nanosphere sample structures . . . . .	100
6.2	Sample A: Nanosphere microscopy . . . . .	101
6.3	Sample B: Nanosphere microscopy . . . . .	103

6.4	Samples A and B: Polar MOKE and Cu $K_\alpha$ x-rays of the patterned Co/Pt substrates. . . . .	104
6.5	SEM images of nanosphere residue. . . . .	106
6.6	Longitudinal MOKE and Cu $K_\alpha$ x-rays on sample A and an un-patterned sample. . . . .	107
6.7	Sample A: Spin down and up neutron reciprocal space maps at $H_c$ . .	110
6.8	Sample A: Spin down and up neutron reciprocal space maps at $H_{sat}$ .	111
6.9	Sample A: Neutron rocking curves at the antiferromagnetic and ferromagnetic peak positions . . . . .	112
6.10	Sample A: Neutron hysteresis loops at the antiferromagnetic and ferromagnetic positions . . . . .	113
6.11	Sample B: Energy scan with $\theta = 10^\circ$ of the Co edges. . . . .	115
6.12	Sample B: Specular scans on and off the Co $L_3$ resonance. . . . .	117
6.13	Sample B: Co $L_{III}$ edge rocking curves at coercivity and saturation .	118
6.14	Sample B: Rocking scan off resonance ( $E=750\text{eV}$ ) at saturation. . . .	119
6.15	Sample B: In-plane VSM comparison with SXRMS hysteresis loops. .	120
7.1	Co/Ru multilayer, with CoRu alloying at the interfaces. . . . .	126
7.2	Specular Cu $K_\alpha$ x-rays on the Co/Ru multilayer with 6 Å of CoRu alloy at the interfaces. . . . .	127
7.3	Composition and temperature dependence of the magnetic properties of CoRu alloy. . . . .	129
7.4	Co/Ru multilayer without alloy reciprocal space maps at RT and cooled to 10 K at $H_c$ . . . . .	131
7.5	Co/Ru multilayer without alloy reciprocal space maps at 10 K and $H_{sat}$ and back to $H_c$ . . . . .	132
7.6	CoRu alloyed sample reciprocal space map with a specular $Q_z$ cut and $Q_x$ cuts on the specular and AF and F positions. . . . .	135
7.7	CoRu alloyed sample reciprocal space maps a) 300K and $H_{sat}$ b) 300K back at $H_c$ . . . . .	136
7.8	CoRu alloyed sample reciprocal space maps a) Cooled to 10K at $H_c$ b) 10K back at $H_{sat}$ . . . . .	137

7.9	CoRu alloyed sample reciprocal space maps a) 10K back at $H_c$ with no AF scatter b) warmed to 300K at $H_c$ . . . . .	138
7.10	VSM moment vs temperature following the neutron experiment field history. . . . .	139
7.11	Co/Ru multilayer coupling curves with 6Å of CoRu alloy at the interfaces.	140
8.1	Depiction of a possible new sample structure. . . . .	144

# Acknowledgements

Firstly I would like to thank my supervisors, Dr Chris Marrows and Dr Sean Langridge for all their advice and support over the last three and a half years. Thanks must also go to Prof. Bryan Hickey for his support, especially at the beginning of things. This whole endeavour would not have been possible if it were not for the magnificent technical expertise of Dr Aidan Hindmarch. The assistance of Dr Mannan Ali and Dr Lisa Michez has also been invaluable over the last three and a half years.

My PhD has been completely reliant on x-ray and neutron scattering at various facilities, as such I must thank the local contacts for their patience and guidance. Firstly i must acknowledge Timothy Charlton and Rob Dalglish at the CRISP beamline at ISIS, who I will soon be joining. I also thank Dario Arena and Joseph Dvorak for always being either able to explain things or get them working again at U4B, no matter what time of the day or night, and finally Maximilian Wolff at the ADAM beamline at the ILL.

Special thanks must go to my collaborators on various projects, such as Dr Feodor Ogrin at Exeter University for patterning sample substrates, as well as Elizabeth Blackburn, Sujoy Roy and Prof. Sunil Sinha at UCSD in California.

Closer to home, I would like to acknowledge the staff of the mechanical and electronic workshops, who have repaired everything I have broken without fail and always been helpful. Special thanks go to John Turton for always fixing things at the drop of a hat, and for always being able to find spare tools and fittings from seemingly nowhere. Thanks also to Pete Harrison and Phil Cale for the continuous flow of cryogens.

I would like to thank the NSLS, ISIS and ILL facilities for provision of beamtime, as well as the CMPC/STFC Centre for Materials Physics and Chemistry and Leeds University for provision of funding for the studentship.

On a personal note, I must acknowledge Ania and Lara who have been with me from the very beginning though all the ups and downs, and without whose friendship this would not have been anywhere near as much fun. Old house mates Graham and Simon must also have a special mention for all the nights out and cups of tea, as well as for the crack Ghost Recon team Drug Penguin. My time in the condensed matter group would not have been the same if it were not for all the other members of the group and wider department who have livened up coffee time (which should really be called tea time) as well as day to day life in Leeds, it has been great fun!

Finally I would like to thank Clare and my family for all the faithful support they have given me, especially at the end of my PhD. You were all brilliant!

# Abstract

This thesis contains three studies on artificially roughened multilayers, with the aim of investigating how the structural disorder affects the magnetic structure.

The magnetically patterned system uses a Co/Pt multilayer, which exhibits strong perpendicular magnetic anisotropy, to magnetostatically imprint a domain pattern onto a 50 Å thick permalloy layer. Element specific SXRMS experiments were then performed. Off-specular magnetic satellite peaks, corresponding to a periodic domain stripe width of 270 nm, were observed, confirmed by magnetic force microscopy and micromagnetic modeling. Thus, we have exploited the element specificity of SXRMS to discern the purely magnetic correlations in a structurally flat permalloy film.

The next step was to structurally and magnetically roughen a magnetic system and use PNR to provide a reference to help separate the structural and magnetic contributions in the SXRMS. In this case, nanospheres were used to pattern a Co/ Pt multilayer into nanopillars. On top of this was deposited a Co/Ru multilayer, which was AF coupled. The SXRMS showed how the magnetic roughness correlates with the structural roughness. We saw that the magnetic disorder was similar over a range of length scales out as far as 15  $\mu\text{m}$ . In addition, the PNR data indicated that the domain reversal was facilitated by domain nucleation.

Finally, by introducing a solid solution at the interface of an AF coupled multilayer we have demonstrated a temperature controlled variation of the interlayer exchange interaction. The AF scattering is observed at room temperature and is maintained as the system is cooled down to 10K. However the AF correlations are destroyed upon magnetically saturating the system and are not recovered upon field cycling. The AF correlations reappear at about 150 K upon warming. A similar effect at low temperature was also seen in VSM measurements, however no mechanism for the observed effect could be determined.

# Table of Contents

List of Tables	ii
List of Figures	iii
Acknowledgements	vii
Abstract	ix
Table of Contents	xii
Publications	xiii
Abbreviations	xv
Introduction	1
<b>1 Sample Preparation and Characterisation</b>	<b>6</b>
1.1 Introduction . . . . .	6
1.2 d.c. Magnetron sputtering . . . . .	6
1.3 Patterning . . . . .	10
1.4 Laboratory X-rays . . . . .	11
1.5 Magnetometry . . . . .	13
1.5.1 Vibrating Sample Magnetometry . . . . .	13
1.5.2 Magneto Optical Kerr Effect . . . . .	15
1.6 Microscopy . . . . .	19
1.6.1 Atomic Force Microscopy . . . . .	19
1.6.2 Magnetic Force Microscopy . . . . .	21
1.7 Simulation . . . . .	22
1.8 Summary . . . . .	22
<b>2 X-ray and Neutron Sources</b>	<b>23</b>
2.1 Introduction . . . . .	23
2.2 Production of X-rays . . . . .	23
2.2.1 Laboratory X-ray sources . . . . .	23
2.2.2 Synchrotron X-ray sources . . . . .	24

2.2.3	Monochromation, polarisation and coherence of x-ray beams . . .	26
2.2.4	X-ray Detectors . . . . .	29
2.2.5	U4B Beamline at the National Synchrotron Light Source . . .	29
2.3	Production of neutrons . . . . .	31
2.3.1	Reactor based neutron sources . . . . .	32
2.3.2	Spallation based neutron sources . . . . .	32
2.3.3	Monochromation, polarisation and coherence of neutron beams	33
2.3.4	Neutron Detectors . . . . .	34
2.3.5	ADAM Beamline at the ILL . . . . .	34
2.3.6	CRISP Beamline at ISIS . . . . .	36
2.4	Summary . . . . .	38
<b>3</b>	<b>X-ray Scattering</b>	<b>39</b>
3.1	Introduction . . . . .	39
3.2	X-ray Interactions with Matter . . . . .	39
3.2.1	Absorption . . . . .	39
3.2.2	Refraction . . . . .	40
3.2.3	Scattering . . . . .	44
3.3	Reflectivity . . . . .	47
3.3.1	Types of X-ray Scan . . . . .	47
3.3.2	Specular Reflection . . . . .	51
3.3.3	The Effect of Roughness on Specular Scattering . . . . .	53
3.3.4	Diffuse Scatter . . . . .	56
3.3.5	The Effect of Roughness on Diffuse Scattering . . . . .	59
3.3.6	Correlations . . . . .	60
3.4	Magnetic X-ray Scattering . . . . .	61
3.4.1	Magnetic Enhancement . . . . .	62
3.4.2	X-ray Magnetic Circular Dichroism . . . . .	65
3.5	Summary . . . . .	69
<b>4</b>	<b>Neutron Scattering</b>	<b>70</b>
4.1	Introduction . . . . .	70
4.2	Properties of a Neutron . . . . .	72
4.3	Neutron Scattering . . . . .	72
4.4	Neutron Reflectometry . . . . .	74
4.5	Magnetic Neutron Reflectivity . . . . .	75
4.6	Polarisation Analysis . . . . .	76
4.7	Summary . . . . .	78
<b>5</b>	<b>Domain patterning</b>	<b>79</b>
5.1	Introduction . . . . .	79
5.2	Magnetic Roughness . . . . .	80
5.3	Experimental: Imprinted Magnetic Domain Pattern on a Flat Permalloy layer . . . . .	84



5.4	Results and Discussion . . . . .	88
5.5	Summary . . . . .	95
<b>6</b>	<b>Nanospheres Patterned Arrays</b>	<b>96</b>
6.1	Introduction . . . . .	96
6.2	Nanospheres Review . . . . .	97
6.3	Experimental . . . . .	99
6.3.1	Sample Preparation . . . . .	99
6.3.2	Characterisation . . . . .	101
6.3.3	Polarised Neutron Measurements . . . . .	107
6.3.4	Soft X-ray Measurements . . . . .	108
6.4	Results and Discussion . . . . .	108
6.4.1	Polarised Neutron Study . . . . .	108
6.4.2	Soft X-ray Magnetic Scattering Study . . . . .	115
6.5	Summary . . . . .	121
<b>7</b>	<b>CoRu Alloying at the interfaces of Co/Ru multilayers</b>	<b>123</b>
7.1	Introduction . . . . .	123
7.2	Co/Ru Multilayer Review . . . . .	124
7.3	Experimental . . . . .	126
7.4	Results and Discussion . . . . .	130
7.5	Summary . . . . .	141
<b>8</b>	<b>Conclusion</b>	<b>142</b>
8.1	Conclusion . . . . .	142
8.2	Future Work . . . . .	144
<b>9</b>	<b>Appendix A : Publications:</b>	<b>146</b>
	<b>References</b>	<b>153</b>

# Publications

‘Soft x-ray resonant magnetic scattering from an imprinted magnetic domain pattern’  
**C. J. Kinane** , A. K. Suszka, C. H. Marrows, B. J. Hickey, D. A. Arena, J. Dvorak,  
 T. R. Charlton and Sean Langridge

*Applied Physics Letters*, **89**, 092507, (2007).

‘Element specific separation of bulk and interfacial magnetic hysteresis loops’  
 A. K. Suszka, **C. J. Kinane**, C. H. Marrows, B. J. Hickey, D. A. Arena, J. Dvorak,  
 A. Lamperti, B. K. Tanner and Sean Langridge

*Applied Physics Letters*, **91**, 132510, (2007).

‘In-plane magnetic anisotropies of sputtered  $\text{Co}_{0.7}\text{Fe}_{0.3}$  films on AlGaAs(001) spin  
 light emitting diode heterostructures’

A. T. Hindmarch, **C. J. Kinane**, C. H. Marrows, B. J. Hickey, M. Henini, D. Taylor,  
 D. A. Arena and J. Dvorak

*Journal of Applied Physics*, **101**, 09D106, (2007).

‘Structural and magnetic roughness in a Co/Ru multilayer patterned into a large scale  
 hexagonal array’

**C. J. Kinane**, N. A. Porter, C. H. Marrows, B. J. Hickey, D. A. Arena, J. Dvorak,  
 E. Sirotkin, F. Y. Ogrin, T. Charlton and S. Langridge

*Journal of Applied Physics*, **103**, 07B513, (2008).

‘Bulk and Near-Surface Magnetic Properties of FeRh Thin Films’

Y. Ding, D. A. Arena, J. Dvorak, M. Ali, **C. J. Kinane**, C. H. Marrows, B. J. Hickey  
 and L. H. Lewis

*Journal of Applied Physics*, **103**, 07B515, (2008).

‘Interface induced uniaxial magnetic anisotropy in amorphous CoFeB films on Al-GaAs(001)’

A. T. Hindmarch, **C. J. Kinane**, M. MacKenzie, J. N. Chapman, M. Henini, D. Taylor, D. A. Arena, J. Dvorak, B. J. Hickey and C. H. Marrows

*Physical Review Letters*, **100**, 117201, (2008).

‘Effect of the stacking order on domain size and exchange bias of Co/Ru double superlattices’

J.A. González, M. Ali, **C.J. Kinane**, C.H. Marrows, B.J. Hickey T. Charlton and S. Langridge

*under preparation.*

# Abbreviations

AF:	Antiferromagnetic
AFM:	Atomic Force Microscopy
BA:	Born Approximation
DOS:	Density of States
DWBA:	Distorted Wave Born Approximation
GMR:	Giant Magnetoresistance
F:	Ferromagnetic
FFT:	Fast Fourier Transform
$H_c$ :	The coercive field
$H_{sat}$ :	The saturation field
LCP:	Left Circularly Polarised
MCD:	Magnetic Circular Dichroism
MFM:	Magnetic Force Microscopy
MOKE:	Magneto Optical Kerr Effect
MR:	Magnetoresistance
NSF:	Non Spin Flip
PNR:	Polarised Neutron Reflectometry
Py:	Permalloy – $\text{Ni}_{80}\text{Fe}_{20}$ at. %
RCP:	Right Circularly Polarised
rms:	Root Mean Square
RT:	Room Temperature
SA:	Spin Asymmetry
SEM:	Scanning Electron Microscopy
SF:	Spin Flip
SLD:	Scattering Length Density

SXRMS:	Soft X-ray Resonant Magnetic Scattering
TEY:	Total Electron Yield
TM:	Transition metal
TMR:	Tunneling Magnetoresistance
VSM:	Vibrating Sample Magnetometer
XMCD:	X-ray Magnetic Circular Dichroism

# Introduction

Magnetic thin films and multilayer structures have enjoyed a vast amount of interest in recent years due to the rapid expansion in their uses, both scientifically, as tailorable systems for testing fundamental physical interactions, and technologically for example in read heads and storage media[1]. This has led to the need for a proper understanding of the connection between structural interfacial disorder and the magnetic properties in these systems. Structural roughness at interfaces in magnetic multilayers affects properties like interlayer coupling[2] and giant magnetoresistance (GMR)[3], where roughness alters the amount of spin-dependent scattering events, causing a modification of the observed GMR[4, 5]. This has direct bearing on the transmission of spin polarised currents across interfaces, which is of importance in spintronic devices[6, 7]. There is some evidence that the disorder at the interface in the form of uncompensated spins has some part in the mechanism behind exchange bias[8, 9].

In recent years this has been followed by a large upsurge in the study of patterned media and nanostructures, requiring systems that are nano-scaled in all three dimensions. This has been with an aim of obtaining high storage densities in hard disk media[10] and magnetic random access memory (MRAM)[11] or high current densities for spin torque switching[12]. Studying single devices and nanostructures in this area has been of great use. However it is also important to understand how these devices behave in large scale arrays. This has attracted recent interest ranging from artificial frustrated magnetism[13] and digital computation[14]. Large arrays of nanostructures allow the study of interfacial effects or inter-feature coupling, resulting in localized deviations in the magnetization direction which can again affect electron transport. In all these cases, it is clear that the important factor is not just the chemical/structural disorder present at the interfaces and surfaces, but also the

magnetic disorder and the interactions between the two.

Large scale arrays lend themselves to neutron and x-ray scattering experiments, which are non destructive and able to give global statistical information about surfaces and internal interfaces over many length scales, unlike techniques like Atomic Force Microscopy (AFM), Scanning Tunneling Microscopy (STM) and other scanning probe microscopies[15] which give local information and are surface sensitive. Additionally, conventional magnetometry and imaging are not well suited to studying interfacial moments and buried spins, as they either lack the sensitivity or the ability to probe the internal chemical and magnetic structure.

X-ray and neutron scattering, have long been used to study the buried structural characteristics of thin film systems[16, 17], with well established techniques for studying structurally rough interfaces along with well developed theoretical tools for analyzing various interface morphologies[18]. In particular, off-specular scattering techniques have allowed lateral disorder to be investigated[19].

The study of magnetic disorder in multilayer films and nanostructures has up until relatively recently been carried out using neutron scattering, mainly Polarised Neutron Scattering (PNR)[20]. The interaction between the neutron and the sample magnetisation is simple to deal with. However, neutron sources suffer from low beam intensities, the result of which being that data collection times are very long and that samples for study by neutrons have to be much larger in order to make use of all available flux  $\approx 25 \text{ mm} \times 25 \text{ mm}$ . This is an issue when attempting to study nanostructures, as such large arrays are difficult to fabricate.

Within the last decade, recent advances in x-ray techniques, especially Soft X-ray Resonant Magnetic Scattering (SXRMS)[21], have allowed these structural formalisms to be used to study “magnetically rough” systems[22, 23]. In this case, synchrotron x-ray sources provide massive increase in source intensity over neutron sources as well as emitting a wide range of photon energies, allowing a high degree of energy selectivity. This allows the use of resonant magnetic scattering in the energy range 10 - 1000 eV (soft x-ray regime) allowing the transition metal resonances to be used. However, the problem of quantifying magnetic disorder by this method remains difficult, primarily due to the indirect and complicated nature of the spin-photon interaction[24].

## Aims of this thesis

The general aim of the work presented in this thesis is the investigation of how the physical structural disorder affects the magnetic structure and disorder. This is achieved by growing on patterned substrates with known structural or magnetic modulations, to obtain artificial systems with which the interplay between the two can be measured with some known and easily characterisable reference.

In order to achieve this aim, the techniques of SXRMS and PNR were used to investigate these systems. This has two purposes: the first is to show that by careful sample design and growth, that the SXRMS technique has the ability to measure the pure magnetic disorder only. The second is to test how well the two techniques complement each other, and to what extent they allow the full characterisation of the lateral magnetic structure.

The scattering experiments were performed at several large scale facilities. The SXRMS experiments were performed at the U4B beamline at the National Synchrotron Light Source (NSLS)[25] situated at Brookhaven National Laboratory (BNL) in New York state. The PNR measurements were made at the CRISP beamline[26] at the ISIS pulsed neutron facility in Oxford, and at the ADAM beamline at the Institute Laue-Langevin (ILL) research reactor in Grenoble, France[27].

We begin by outlining in chapter 1 the fabrication and patterning techniques used in making the structures that are studied. This is followed by a description of the techniques used to do the magnetic/structural characterisation of the samples, enabling the artificial structural/magnetic modulations to be well characterised before the growth was completed and the samples were taken to the scattering facilities. This includes a description of the capabilities of the laboratory X-ray apparatus used to structurally characterise the samples. This is followed by an in-depth description of the Magneto Optical Kerr Effect magnetometer due to the similarities with SXRMS. A brief description is also given of various microscopies that were used.

In chapter 2 the production of x-rays and neutrons is briefly explained, with x-ray production being explained in terms of production both by a tube source in the laboratory at the University of Leeds, and synchrotron light at the NSLS facility.



Descriptions of the beamlines used at the neutron and x-ray facilities are given along with properties of the x-ray and neutron beams, with regard to how they are produced and used on the various beamlines.

Chapter 3 covers the basic aspects of x-ray absorption, reflection and scattering that are necessary for the interpretation of the results in this work. The majority of the scattering theory and how information about the structural morphology is extracted from it is also applicable to neutron scattering. The last sections give the underlying physics behind magnetic resonant scattering as well as explaining the difficulties in separating the magnetic information from the structural.

Chapter 4 is a brief chapter covering the aspects of neutron scattering that are different from x-ray scattering, primarily neutron absorption and magnetic scattering. A brief introduction to the PNR technique follows, with a description of how it can be used to obtain information about the magnetisation of a system.

The results obtained on a sample designed to have a structurally flat magnetic layer, but which has a modulated magnetic pattern imprinted onto it, are described in chapter 5. We demonstrate how, with careful sample design, it is possible to circumvent the problem of losing the magnetic signal due to it being swamped by the structural signal when doing SXRMS scattering, in-line with the first aim of the work.

In chapter 6, self-assembled arrays of nanospheres have been used to pattern a Co/Pt multilayer into nanopillars. On top of this was deposited a Co/Ru multilayer which is antiferromagnetically (AF) coupled. The nanopillars introduce a known structural and magnetic lateral modulation into the multilayer. We show how SXRMS and PNR can be used to observe the interference from the patterned substrate and obtain selective magnetometry as a function of reciprocal space, hence probing the magnetic behaviour on different length scales. We also show how the two techniques complement each other for characterisation of these types of systems.

A different type of structural disorder is investigated in chapter 7. In this chapter we look at the effects of deliberately introducing interdiffusion on the interlayer coupling of a Co/Ru multilayer. This is studied using PNR, which allows the behaviour of the antiferromagnetic coupling to be followed as a function of temperature. This

is compared to a Co/Ru coupled multilayer which does not have grading at the interfaces.

Finally in chapter 8 we discuss the conclusions drawn from these results and consider the possible future directions that the work entails.

# Chapter 1

## Sample Preparation and Characterisation

### 1.1 Introduction

The main scattering results discussed in this work all required the use of large scale synchrotron x-ray and neutron facilities. The basic fabrication and magnetic and structural characterisation of the samples used to make these measurements was performed primarily at the University of Leeds using the techniques that are described below.

### 1.2 d.c. Magnetron sputtering

Sputtering was first discovered by W. R. Grove[28] in 1852 and has become widely used since the introduction of the planar magnetron[29] in the seventies to deposit films of metals and insulators.

The sputtering process involves the continual bombardment of a target by a suitable ion, in order to remove the individual target atoms and then impart enough momentum for the free atoms to diffuse to a substrate mounted directly in front of the target. This is achieved by introducing a noble gas, in this case argon (Ar), to the sputtering chamber at very low pressure typically  $\approx 3\text{mTorr}$  in the Leeds sputter systems. Argon is ideally suited to this purpose being heavy enough for efficient momentum transfer and chemically inert. A large potential difference is applied between the metal target (cathode) and the rest of the chamber (anode). The large potential difference results in the ionization of the Ar with the Ar ions then being accelerated

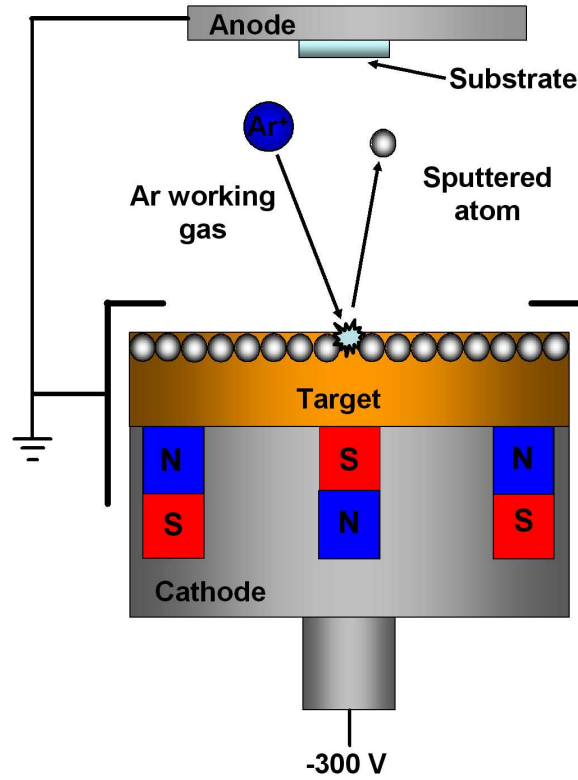


Figure 1.1: Schematic of a sputtering gun, showing the target (cathode) and substrate (anode) with the relative voltage biasing.

to the cathode (target). The momentum transfer from the Ar ions upon impact with the target atoms and the subsequent secondary transfers of momentum are what give rise to the sputtered atoms leaving the target surface[30]. Sputtering guns use d.c. current in the simplest configuration for sputtering metals and other conducting materials. For insulators radio frequency (RF) voltage supplies must be used. However RF sputtering is outside the scope of this work. The general layout of a magnetron sputtering gun is shown in figure 1.1.

The energy of the sputtered atoms depends on many factors: the relative potential of the target, the masses of the sputtering gas and the target atoms, the sputter gas pressure and the target to substrate distance [30].

In magnetron sputtering, a set of permanent magnets are positioned behind the target to create a magnetic field parallel to the target surface. Electrons close to the target surface are then trapped by the Lorentz force along the field lines. This increases the amount of Ar ionization near the target surface, thus improving the

deposition rate and reducing the necessary working gas pressure[31]. The magnet arrangement is shown in figure 1.1.

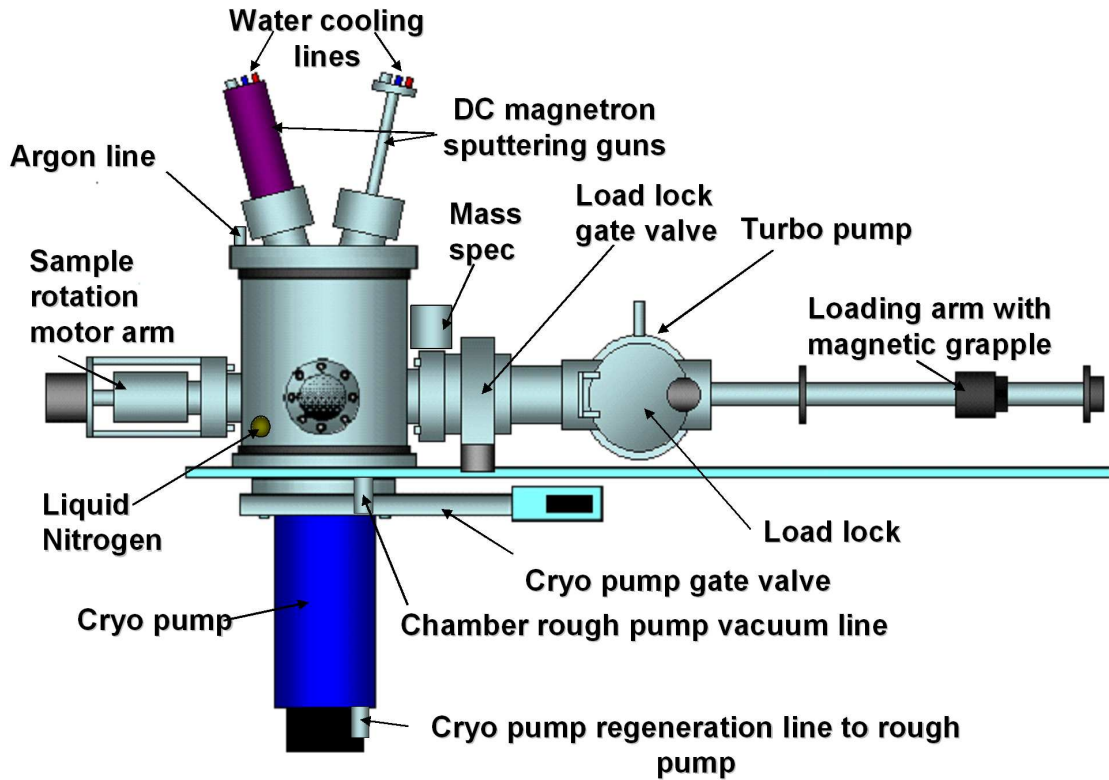


Figure 1.2: The layout of the Mjolnir sputter system at Leeds University.

Leeds has three sputtering systems, of which the smallest, shown schematically in Figure 1.2, was used primarily throughout the duration of this work. This is a magnetron sputtering system with a vacuum system capable of a base pressure of lower than  $10^{-8}$  Torr monitored by a mass spectrometer. The vacuum is achieved by roughing the deposition chamber with a rotary vane pump to reduce the pressure to the order of 10 mTorr, and then switching to a He cryopump for a pump down period of  $\approx 8$  hours to reach base pressure. A Meissner cold trap employing liquid nitrogen is also used to improve the vacuum by removing, through further condensation, any reagents such as water that are remaining in the chamber after this. The nitrogen is usually allowed to flow in the trap for an hour before a growth takes place.

The sputtering system has four water cooled d.c. magnetrons angled at  $16^\circ$  from the vertical, allowing co-sputtering of alloys. Cross contamination of the other guns is prevented by a separator blade between the four guns as is shown in figures 1.3 (a) and

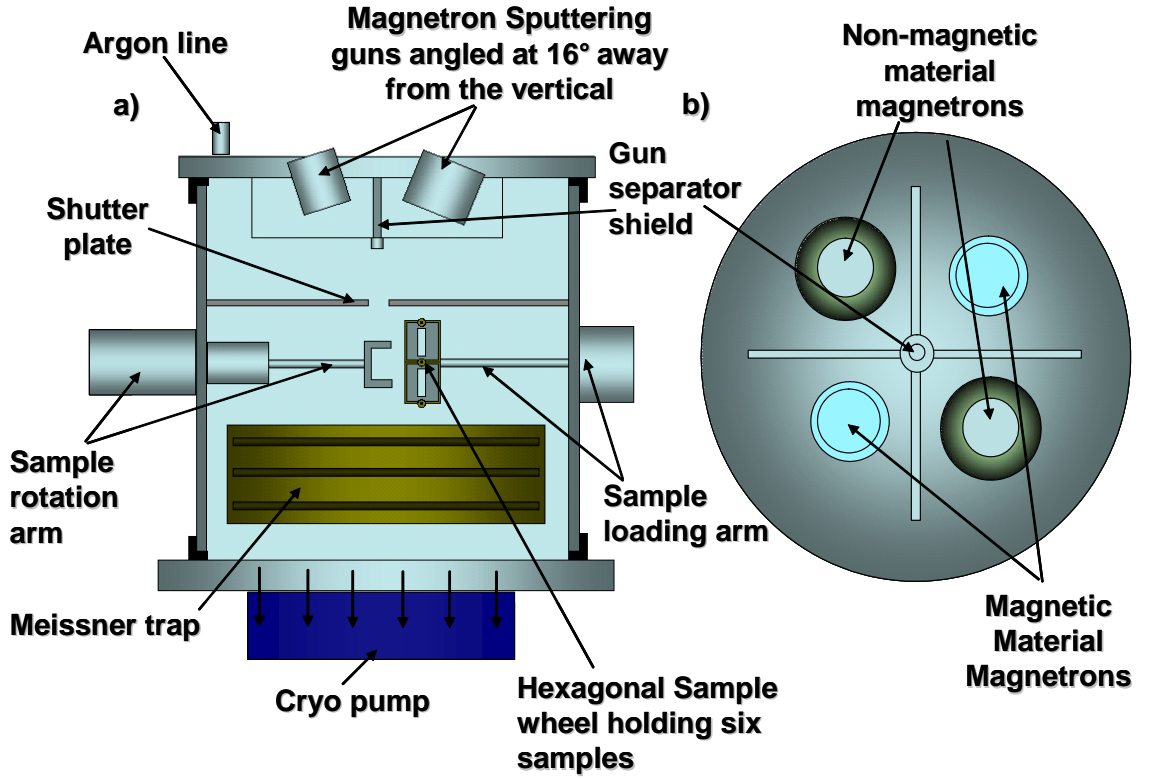


Figure 1.3: The internal layout of the Mjolnir sputter system at Leeds University.

(b). The magnetrons are computer controlled via four Advanced Energy MDX500 magnetron controllers. These provide constant power outputs and hence reproducible deposition rates by supplying a constant current in the 10's of mA range for a voltage drop of  $\approx 300$  V across the target. Growth rates are typically  $1 \text{ \AA/s}$  for a current of 150mA.

The magnetrons are separated from the substrate holder by a shutter plate with a hole positioned just above the sample holder to avoid any cross contamination of the other samples. This system allows up to six samples to be grown at a time. An additional load lock and turbo pump allow for multiple growths per single vacuum cycle of the main chamber.

The samples are deposited onto Si(100) wafers. Si provides an ideal initial flatness of the order of  $\approx 5 \text{ \AA}$  along with an  $\approx 10 \text{ \AA}$  thick natural oxide layer[32]. Initially samples are cleaned by rinsing in acetone to remove grease and dust. Isopropanol is then used to remove any traces of the acetone. The samples are mounted on a hexagonal copper sample block, which allows for samples with sizes up to  $20 \text{ mm} \times$

20 mm to be grown.

### 1.3 Patterning

In order to investigate the interplay between magnetism and structure it was necessary to fabricate structures with a known structural modulation. In the case of this work, hexagonal dot arrays were used as a mask to produce Co/Pt multilayer pillars or dots, details of which are given later.

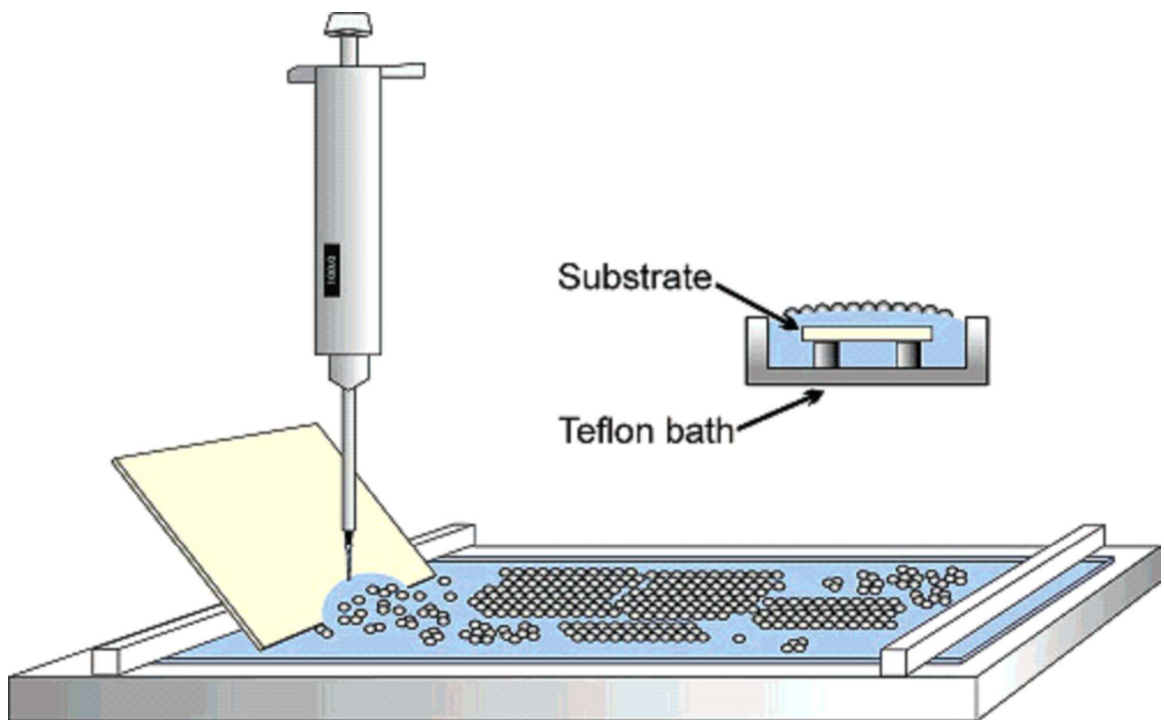


Figure 1.4: Self-assembly at a water/air interface. Self-assembly was accomplished on the surface of ultra-pure water, within a Teflon bath of dimensions  $190 \times 45 \text{ mm}^2$ . Diagram courtesy of Weekes *et al.* [33].

The patterning was performed at Exeter University by the group of Dr Feodor Ogrin. Hexagonal dot arrays were fabricated using commercially available suspensions of monodisperse polystyrene nanospheres with diameters of approximately 780 nm.

Self-assembly was accomplished on the surface of ultra-pure water within a Teflon bath of dimensions  $190 \times 45 \text{ mm}$  as shown in figure 1.4. Teflon sliders were used to compress and position the monolayer, the water being retained in the bath by surface tension. The spheres were introduced to the water surface via a glass microscope slide

placed at one end of the bath at an angle of  $\sim 45^\circ$  with respect to the water surface. On contact with the water, the spheres immediately form a monolayer and start to assemble.

This technique allows arrays with ordering over the range of  $\sim 1 \text{ cm}^2$  to be made. A combination of reactive ion etching (RIE) and Ar ion milling was employed to produce nanosphere capped Co/Pt pillars, and the spheres were then removed via abrasion.

Further details on this process can be found in the following references by Weekes *et al.*[33, 34].

## 1.4 Laboratory X-rays

X-ray production and x-ray scattering for both laboratory-based and facility-based x-ray sources are discussed in detail in chapters 2 and 3. The laboratory x-ray kit at Leeds is a Siemens diffractometer[35]. All x-ray optics discussed are fully described in the reference “Elements of x-ray diffraction” by B. D. Cullity[36].

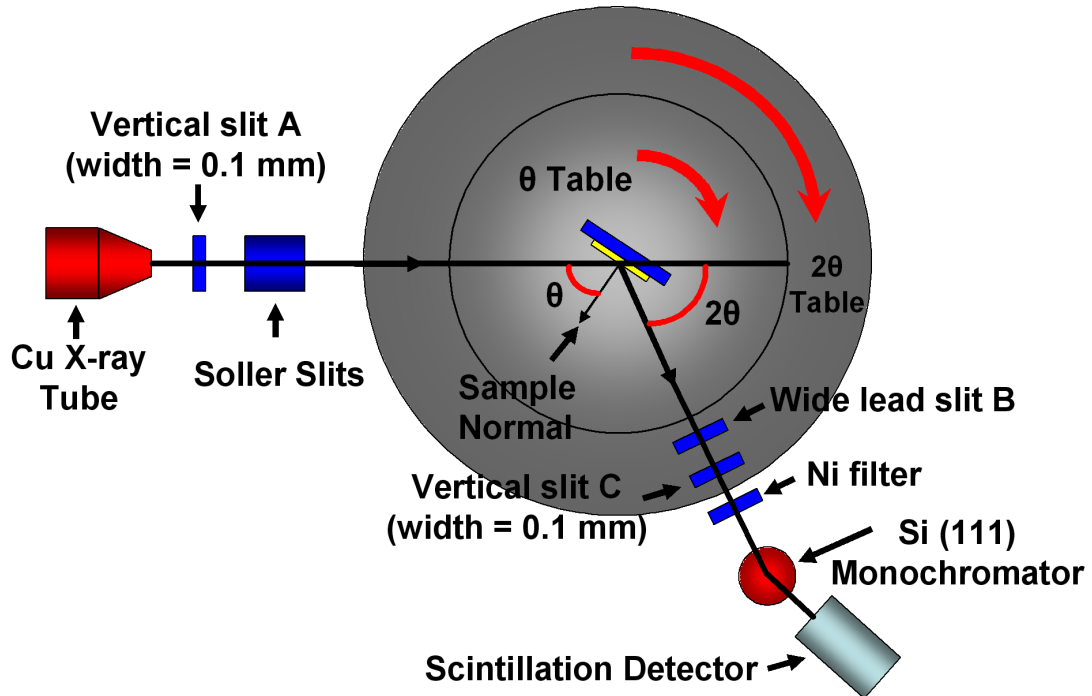


Figure 1.5: Schematic of the Leeds x-ray diffractometer’s geometry and components.

The beam is produced by a Cu tube run at a potential of 40 kV and 30 mA. The



x-ray tube is water-cooled. The geometry of the Leeds x-ray diffractometer is shown in figure 1.5.

This beam is initially passed through a single vertical slit of width 0.1 mm and then into a set of Soller slits before being allowed to be diffracted/reflected from the sample. Soller slits are a collection of closely spaced very long thin metal plates parallel to the plane of the reflectometer circle. The Soller slits provide a high degree of collimation[36]. After striking the sample the beam then goes through another set of 2 vertical slits: a wide lead slit to cut down on any stray reflections and background and another 0.1 mm vertical slit. The x-ray beam then passes through a Ni filter which cuts back on the Bremsstrahlung background and any  $\text{Cu } K_{\beta}$  that is coming through from the Cu x-ray tube. This leads on to a Si(111) single bounce monochromator that is set to reflect x-rays at the Si(111) Bragg peak ( $28.2^{\circ}$ ) if the incident x-ray wavelength is  $1.54 \text{ \AA}$  further reducing any background and providing more precise monochromation. The detector used is a NaI scintillator coupled to a high sensitivity photomultiplier tube, and is described in detail in reference[37].

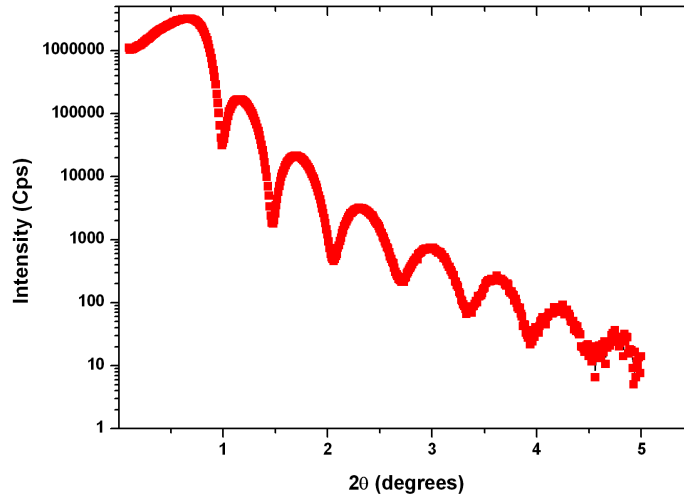


Figure 1.6: Specular ( $\theta/2\theta$ ) scan for a single layer of Co  $\approx 100 \text{ \AA}$  thick. Kiessig fringes are clearly visible.

The computer control and gearing of the  $\theta$  and  $2\theta$  arms is such that specular, off specular  $\theta/2\theta$  scans, transverse diffuse scans or rocking scans can be easily performed.

For a definition of the different scan types and their properties see chapter 3. The angular resolution of the  $\theta$  and  $2\theta$  arm motors is  $0.005^\circ$  and  $0.01^\circ$  respectively. An example of the data produced for a simple thickness calibration of a Co layer is show in figure 1.6

## 1.5 Magnetometry

### 1.5.1 Vibrating Sample Magnetometry

The Vibrating Sample Magnetometer (VSM) at Leeds is a Maglab<sup>VSM</sup> manufactured by Oxford Instruments[38]. It is capable of applying magnetic fields up to  $\pm 9$  T via a superconducting magnet which is immersed in a He<sup>4</sup> cryostat. The temperature range available is from 1.2 K to 330 K for the variable temperature insert.

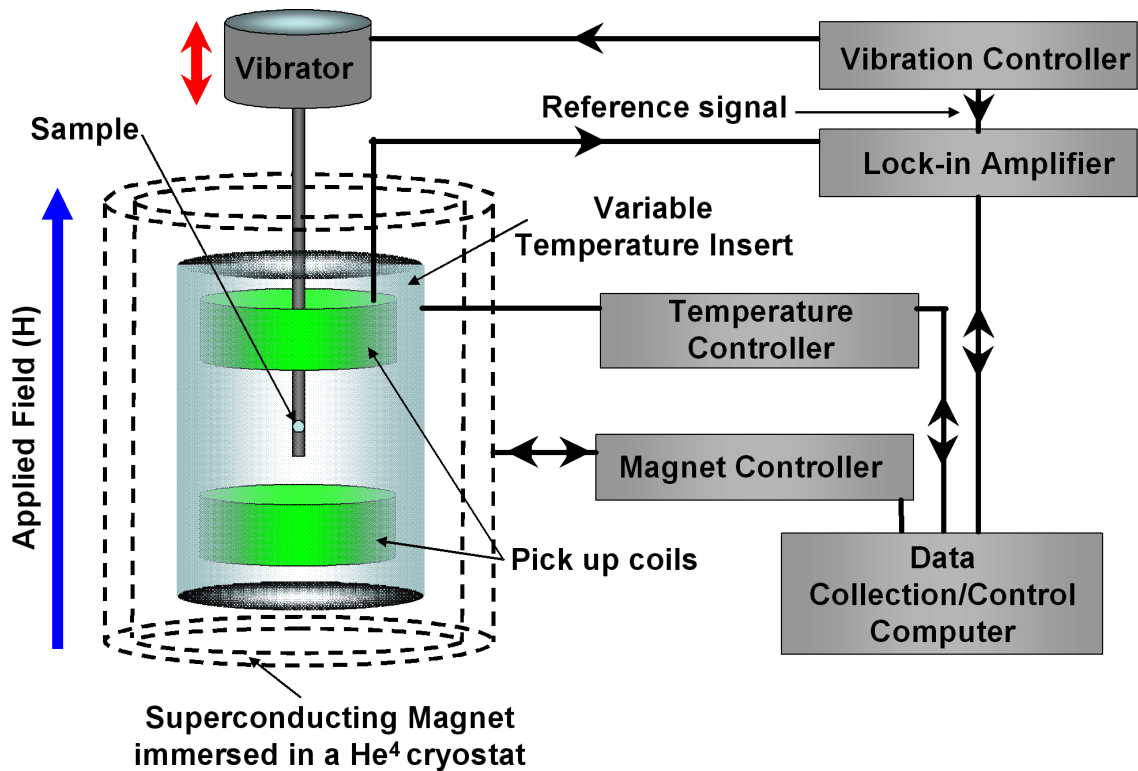


Figure 1.7: The Leeds Maglab<sup>VSM</sup> system and associated electronics.

Vibrating sample magnetometry is based on Faraday's law of induction. This at its simplest involves measuring the current induced in a pair of pickup coils from a sinusoidally oscillating sample, mounted on a rigid rod, which oscillates parallel to

an applied magnetic field, as shown in figure 1.7. The induced AC signal is proportional to the magnetic moment of the sample. For a more detailed description of the theoretical background and construction of a VSM instrument see S. Foner [39].

The sample is vibrated at a reference frequency of 55Hz. The signal response from the sample may be very small and, as such, any noise in the system is a problem. This is alleviated by using a lock-in amplifier [40] set to detect the reference frequency, thus reducing the noise associated with other frequencies, while producing a dc output signal.

The main advantages of using VSM is that it performs a bulk magnetization measurement over the whole sample volume. It is robust and allows for fast sample changes. By sweeping the applied magnetic field it is possible to measure hysteresis loops, given that the sample has been centered correctly between the two pickup coils. It must be noted that VSM measurements measure the substrate and sample stick as well as the sample (unlike Magneto Optical Kerr Effect measurements), and that the diamagnetic signal from both of these must be accounted for and removed from any measurement[41]. Some example data is shown in figure 1.8 of Co/Ru multilayers with ferromagnetic and antiferromagnetic coupling.

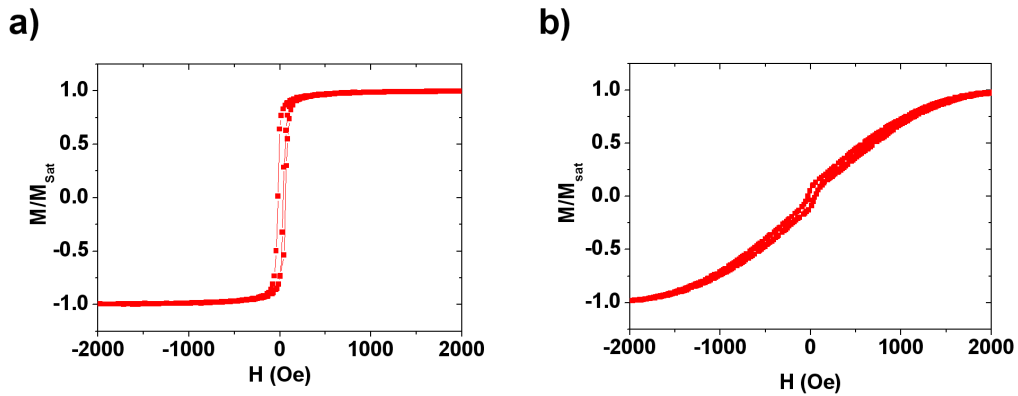


Figure 1.8: Examples of VSM hysteresis loops of Co/Ru multilayers with thicknesses of Ru giving a) ferromagnetic coupling (8Å of Ru), b) antiferromagnetic coupling (4Å of Ru). The data had been normalised to the saturation magnetisation and corrected for the diamagnetic signal.

### 1.5.2 Magneto Optical Kerr Effect

The field of Magneto-optics was invented in the 19th century by Michael Faraday when he discovered what would later become known as the Faraday effect. He observed a rotation of the plane of polarisation of light that was passed through longitudinally magnetised glass in 1845[42]. The complementary Magneto-Optic Kerr effect (MOKE), was discovered by Rev John Kerr for reflected polarised light in 1876[43].

The present theoretical description follows that outlined by Bader [44] and that outlined in the thesis of Ali [45]. The MOKE effect is described in some detail as the technique ties in well with the scattering theory in chapter 3. However this account is not intended to be rigorous, and the reader is referred to the previous references for a more in-depth explanation.

The Magneto-Optical Kerr effect changes the state of linearly polarised light by introducing a linear or elliptical component to the polarisation after reflection from a magnetic material.

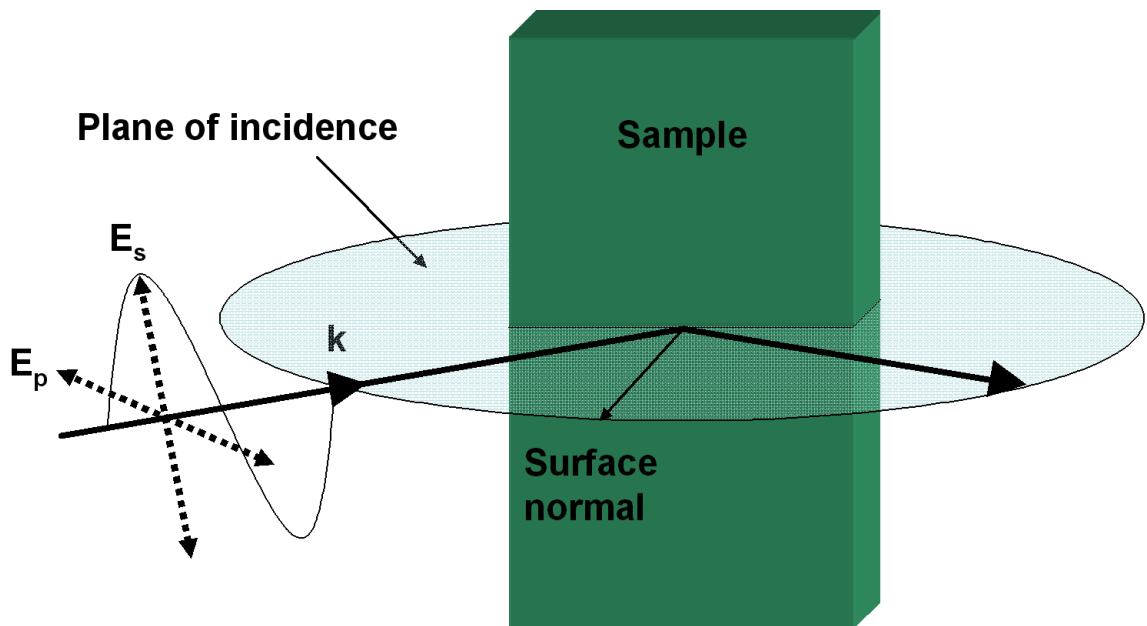


Figure 1.9: Plane of incidence and the difference between ‘S’ and ‘P’ polarised light with an ‘S’ polarised beam shown.

In order to describe the macroscopic effects of MOKE some basic terminology must be described. The plane of polarisation is usually defined as the plane containing the electric field vector of the incident light as shown in figure 1.9. The incident light can

be described as either ‘s’ or ‘p’ linearly polarised light. In ‘p’ polarised the electric field vector is parallel to the plane of incidence, and in ‘s’ polarised it is perpendicular. The plane of incidence is defined as the plane containing the incident and reflected beams, and hence the normal to the sample surface[46].

The MOKE effect is macroscopically described by the dielectric law[47]. The microscopic mechanism behind the magneto-optic coupling is based on the spin-orbit interaction[48] and its explanation is beyond the scope of this work.

When a beam of light is incident from a non-magnetic to a magnetic medium with an arbitrary magnetisation direction, the dielectric tensor can be generalized as,

$$\epsilon = \epsilon_0 \begin{pmatrix} 1 & -iQ_z & iQ_y \\ -iQ_z & 1 & -iQ_x \\ -iQ_y & iQ_x & 1 \end{pmatrix}, \quad (1.1)$$

where  $Q_{x,y,z}$  is the magneto-optic Voigt constant describing the magneto-optical effect. This term is proportional to the magnetisation of the material to first order[45]. These complex off-diagonal Voigt terms give rise to the MOKE effect. Upon entering the magnetic material the incident linearly polarised light can be considered to be made up of the superposition of left and right, circularly polarised beams. These two circular polarisation states have different refractive indices  $n$ , where for a general magnetisation direction  $\mathbf{M}$ ,  $n$  is given by,

$$n = N(1 \pm gQ), \quad (1.2)$$

where  $g$  is the direction cosine between the propagation vector of the light  $k$  and  $\mathbf{M}$  and  $N$  is the refractive index[44]. The two circular polarisation states travel with different velocities, and attenuate differently due to the differences in the real and imaginary parts of the potential inside the magnetic medium.

When the two beams emerge from the magnetic medium they recombine. The part of the response that is in phase with the incident light gives rise to the rotation and the part that is out of phase gives rise to an ellipticity. For an in-depth description of this the reader is directed to the work of Zak *et al*[49] and You *et al*[50].

There are three MOKE orientations: polar, longitudinal and transverse, which are defined in terms of the direction of the magnetization vector  $\mathbf{M}$  with respect to the surface of the material and the plane of incidence of an incident optical beam as shown in figure 1.10.

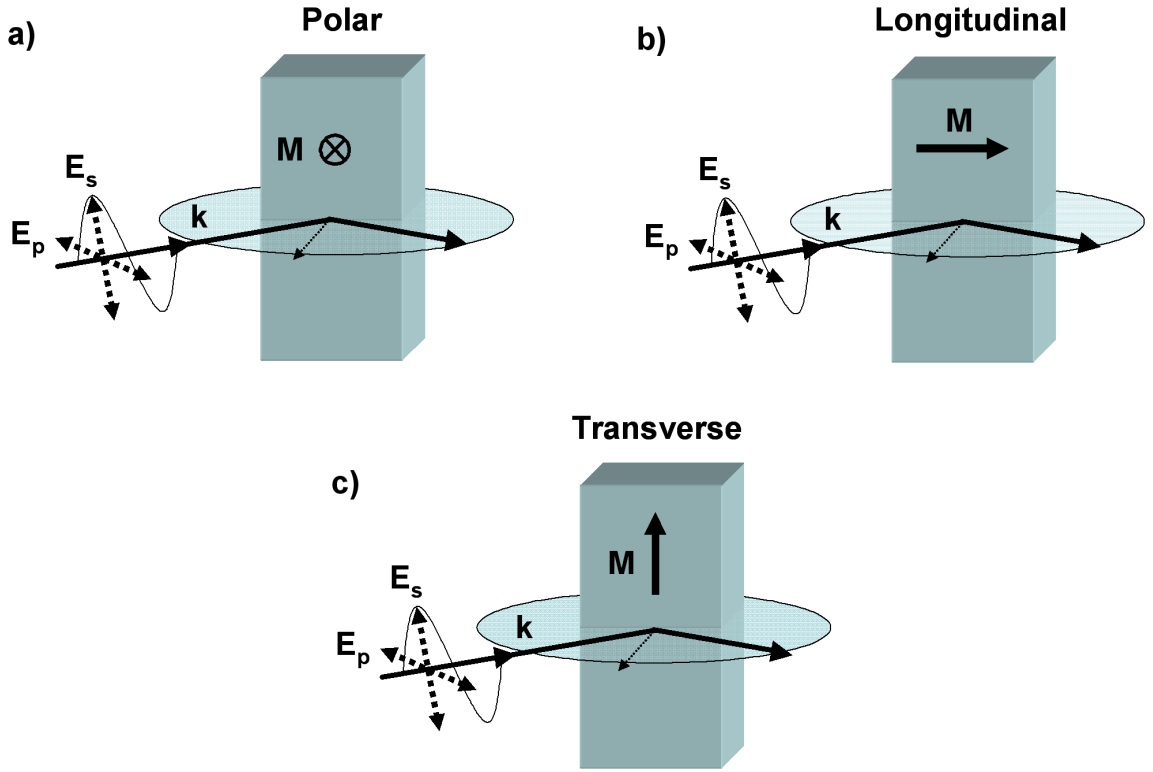


Figure 1.10: MOKE modes a) Polar b) Longitudinal c) Transverse.

In the polar geometry the magnetisation is perpendicular to the plane of the sample. In longitudinal and transverse, the magnetisation is parallel and perpendicular to the plane of incidence respectively, but lies parallel to the plane of the sample.

The MOKE magnetometer at Leeds is capable of performing longitudinal and polar measurements as shown in figure 1.11, and due to this the transverse case is not considered here. The MOKE system also has a heating stage capable of reaching  $\approx 700\text{K}$ . A detailed description of the experimental setup can be found in reference [51].

The experimental setup at the time of writing consists of a 15 mW HeNe laser ( $\lambda = 632.8\text{ nm}$ ), two Glan-Thompson polarizers for use as a polarizer and analyzer, a 1 T electromagnet, photodiode and amplifier. The photodiode is connected to a

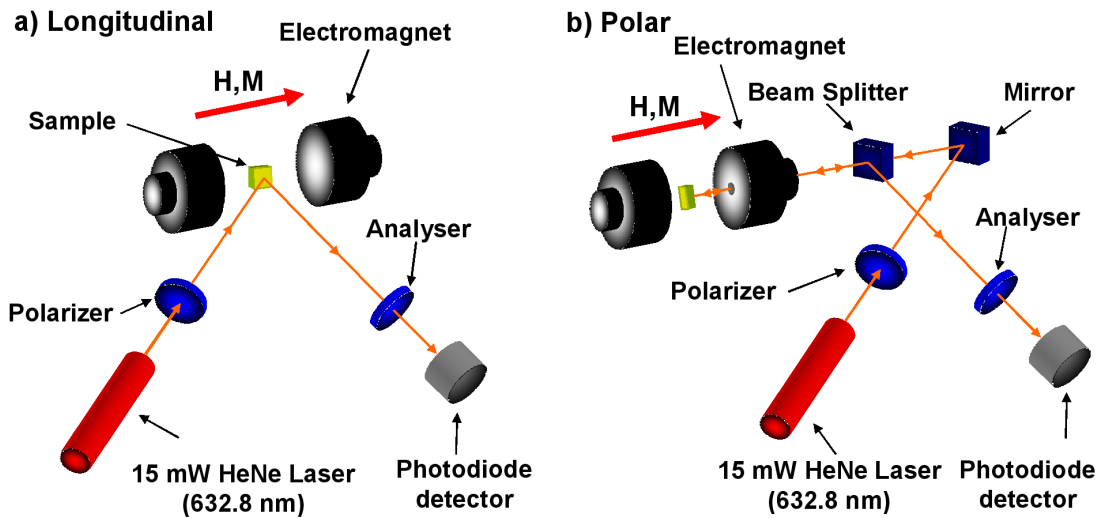


Figure 1.11: MOKE Orientations a) Longitudinal orientation magnetization is in the plane of the sample. b) Polar orientation magnetization is perpendicular to the plane of the sample.

computer using an analogue-to-digital converter card. The applied magnetic field is measured by a Hall probe at the sample position. The analog-to-digital card allows for several thousand readings to be taken at each point of the hysteresis loop and then averaged. The data collection time for a typical hysteresis loop is 1 to 2 minutes. Example MOKE hysteresis loops are shown in figure 1.12 for Co/Ru multilayers with ferromagnetic and antiferromagnetic coupling.

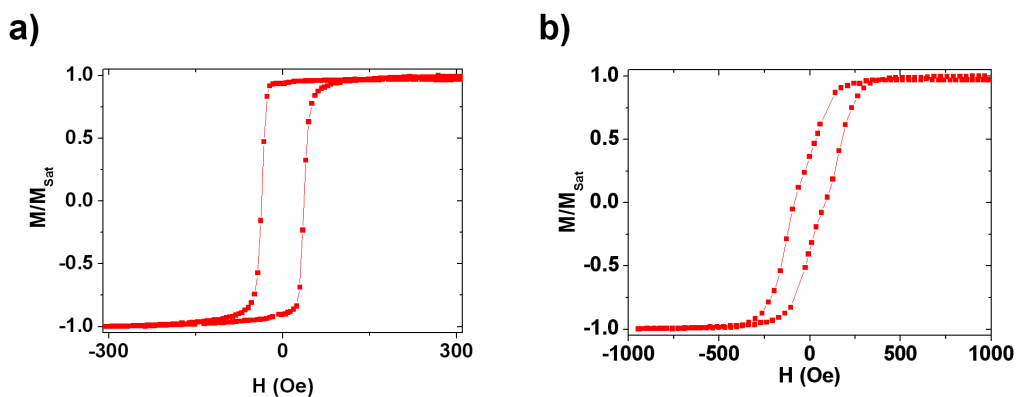


Figure 1.12: Examples of longitudinal MOKE hysteresis loops of Co/Ru multilayers with thicknesses of Ru giving a) ferromagnetic coupling (20 Å of Ru), b) antiferromagnetic coupling (12 Å of Ru). The data had been normalised to the saturation magnetisation only.

In the longitudinal case shown in figure 1.11 (a), the incident beam is ‘p’, polarized by the first polarizer and is then reflected off the sample, which is located between the poles of an electromagnet. The beam is then passed through an analyzer, which has its axis nearly crossed with the polarisation of the incident beam. The output voltage of the photodiode is then recorded as a function of magnetic field. The sign and magnitude of the voltage are proportional to  $\mathbf{M}$  and its direction to first order. In this way, any variation in the plane of polarization, due to the Kerr rotation from the magnetization of the sample, is seen as a change of intensity by the photodiode.

In the polar orientation the magnetization is perpendicular to the plane of the sample, requiring the use of a beam splitter and mirror to reflect the beam through the center of the electromagnet, as shown in figure 1.11 (b).

It must be noted that the analyzer setting is important. It should be set as close to extinction as possible to obtain a large fractional change in the measured intensity. However this is the least linear part of the  $\cos^2$  response curve given by Malus’ Law,

$$\mathbf{I} = (\mathbf{I}_0 \cos^2 \theta_i), \quad (1.3)$$

where  $\mathbf{I}_0$  is the initial intensity, and  $\theta_i$  is the angle between the light’s initial plane of polarization and the axis of the polarizer[46]. Being too close to full extinction can produce a non linear response, hence a balance between the two is needed.

It must further be noted that in contrast to VSM measurements where the whole sample is probed, MOKE is a surface probe. The probing depth of MOKE is governed by the penetration depth (skin depth) of visible light. This is typically a few tens of nm for visible light[52, 53]. This is in stark contrast to the bulk measurement performed by the VSM. However the MOKE data does not have to be corrected for diamagnetic signals from the substrate and sample stick.

## 1.6 Microscopy

### 1.6.1 Atomic Force Microscopy

In this section a brief summary of basic Atomic Force Microscopy (AFM) and Magnetic Force Microscopy (MFM) is given. This is due to the size of the field in question



and the fact that only limited use was made of the technique. The reader is directed to the references for further information.

The AFM is one of about two dozen types of scanning probe microscopies. All of these microscopes work by measuring a local property, such as height, optical absorption, or magnetism, with a probe or tip placed very close to the sample. In this case AFM works by measuring the vertical deflection of the tip due to the atomic force between the tip and the sample. The tip is connected to a cantilever and a laser beam is then reflected off the cantilever such that any flexing causes a change of intensity at a split photodiode. This allows a resolution comparable to an interferometer, as shown in figure 1.13.

To acquire an image the microscope raster-scans the probe tip over the sample while measuring the local property in question. Unlike some traditional microscopes, scanned-probe systems do not use lenses, so the size of the probe rather than diffraction effects limits their resolution.

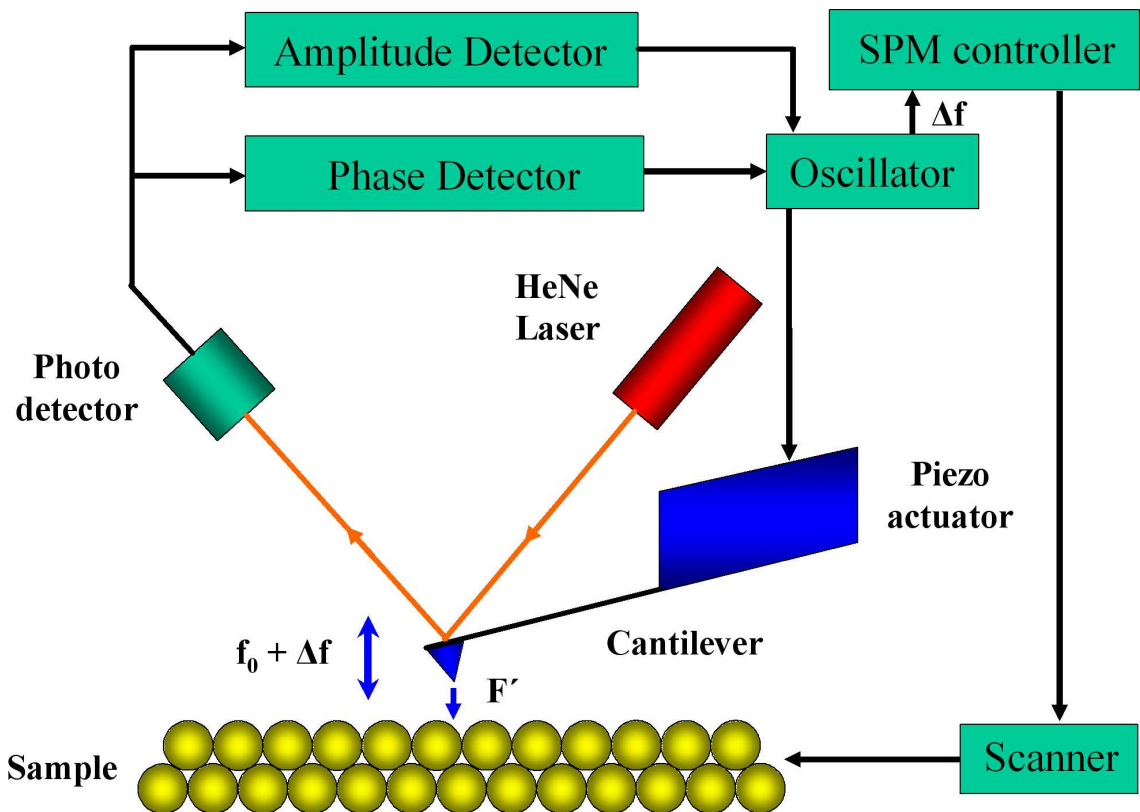


Figure 1.13: Schematic of the general setup of an Atomic Force Microscope using frequency modulated force gradient detection[15].

One method of detecting the deviation of the cantilever is frequency-modulation. The cantilever is represented as a simple harmonic oscillator with spring constant  $k$  and mass  $m$ . This has a resonant frequency of  $f_0$  when no external forces are acting on it, given by,

$$f_0 = \frac{1}{2\pi} \sqrt{\frac{k}{m}}. \quad (1.4)$$

When the tip is in close proximity to a sample surface, a force gradient  $F'$  has to be added to the spring constant. The resultant change to the resonant frequency is,

$$f = \frac{1}{2\pi} \sqrt{\frac{k + F'}{m}} \approx f_0 + \frac{f_0}{2k} F' \equiv f_0 + \Delta f. \quad (1.5)$$

The frequency shift  $\Delta f$  can be measured with high accuracy and using this technique atomic resolution is possible[54].

All measurements were made in ‘tapping’ mode in which cantilever is driven to oscillate up and down at near its resonance frequency as described above. Any deviation caused by forces from the sample surface acting on the tip. An electronic servo uses the piezoelectric actuator to control the height of the cantilever above the sample. The servo adjusts the height to maintain a set cantilever oscillation amplitude as the cantilever is scanned over the sample. A Tapping AFM image is therefore produced by imaging the force of the oscillating contacts of the tip with the sample surface. This is an improvement on conventional contact AFM, in which the cantilever just drags across the surface at constant force and can result in surface damage.

For further details on the principles of AFM the reader is referred to the work of Chen, Binnig *et al.*, Alexander *et al.* and Meyer *et al.* [15, 55, 56, 57]. The AFM used in this work was a Digital Dimension 5000 Atomic Force Microscope [58] located at the Rutherford Appleton Laboratory.

## 1.6.2 Magnetic Force Microscopy

Magnetic force microscopy is a special mode of operation of the AFM. It was recognized that detection of magnetostatic interactions at a local scale was possible by equipping an atomic force microscope with a ferromagnetic probe, that is then raster-scanned across any ferromagnetic sample in the same way as the AFM[59, 60].

The ferromagnetic tip is first scanned over the surface of the sample in a standard AFM mode to obtain topographic information. Then the tip is lifted up just off the surface in what is called ‘lift mode’. The surface topography from the initial scan is then added to the lift height to maintain a constant separation during the lifted scan. The influence of the magnetic force on the magnetic tip is then measured using the force gradient detection method as described for AFM above.

## 1.7 Simulation

In order to verify certain results in this work it was necessary to simulate magnetic domain structures that formed in some of the samples. This was achieved by using the Object Oriented Micro-Magnetic Framework (OOMMF) a public domain micromagnetics program developed at the National Institute of Standards and Technology[61].

OOMMF works by solving the Landau-Lifshitz Gilbert (LLG) equation for arbitrary two and three dimensional systems that are defined by the user. A finite difference solver is used to iteratively solve the system as it is moved forward in time. The ordinary differential equation (ODE) solver in OOMMF integrates the Landau-Lifshitz equation[62],

$$\frac{d\mathbf{M}}{dt} = -|\bar{\gamma}|\mathbf{M} \times \mathbf{H}_{\text{eff}} - \frac{|\bar{\gamma}|\alpha}{M_S}\mathbf{M} \times (\mathbf{M} \times \mathbf{H}_{\text{eff}}), \quad (1.6)$$

where  $\bar{\gamma}$  is the Landau-Lifshitz gyromagnetic ratio (m/(As)) and  $\alpha$  is the damping coefficient (dimensionless),  $\mathbf{M}$  is the magnetisation,  $M_S$  is the saturation magnetisation (A/m) and  $\mathbf{H}_{\text{eff}}$  the effective applied field (A/m).

A full overview of micromagnetic simulation is vastly beyond the scope of this work as only limited use of the technique was made. The reader is referred to the detailed overview given in reference [63] and to the OOMMF user-guide [64].

## 1.8 Summary

In this Chapter, we have described the fabrication and magnetic/structural characterisation techniques used to create and characterise the samples used in this work.

## Chapter 2

# X-ray and Neutron Sources

### 2.1 Introduction

In this section the production of x-rays and neutrons are briefly outlined. The beam-lines at the various facilities that were used in this study are also outlined and some relevant practical considerations are discussed.

### 2.2 Production of X-rays

Both laboratory and facility based x-ray sources have been used in this work, both of which are outlined here. The reader is referred to the references for a more thorough description of the technology involved [65, 66, 67].

#### 2.2.1 Laboratory X-ray sources

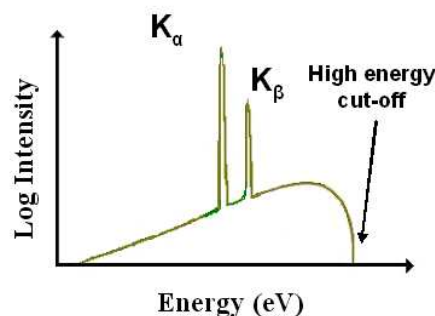


Figure 2.1: Bremsstrahlung background with fluorescence lines

Initially simple x-ray tubes (Coolidge 1912) with powers of about 2 kW [66][68], and later rotating anode sources with powers of about 18 kW were used as the main

sources of laboratory x-rays. Both are limited in intensity by heat dissipation within the target material.

Both use metal targets which are bombarded by electrons producing a bremsstrahlung (braking radiation) spectrum with a sharper, more intense line spectrum superimposed on top, as depicted in figure 2.1. The line spectrum is characteristic of the target metal.

The characteristic lines are labeled K,L,M, etc with principle quantum numbers  $n=1,2,3,\dots$  and are related to the shell at the end of the transition. Hence the  $K_\alpha$  line corresponds to L to K transitions, and  $K_\beta$  M to K as shown in figure 2.2.

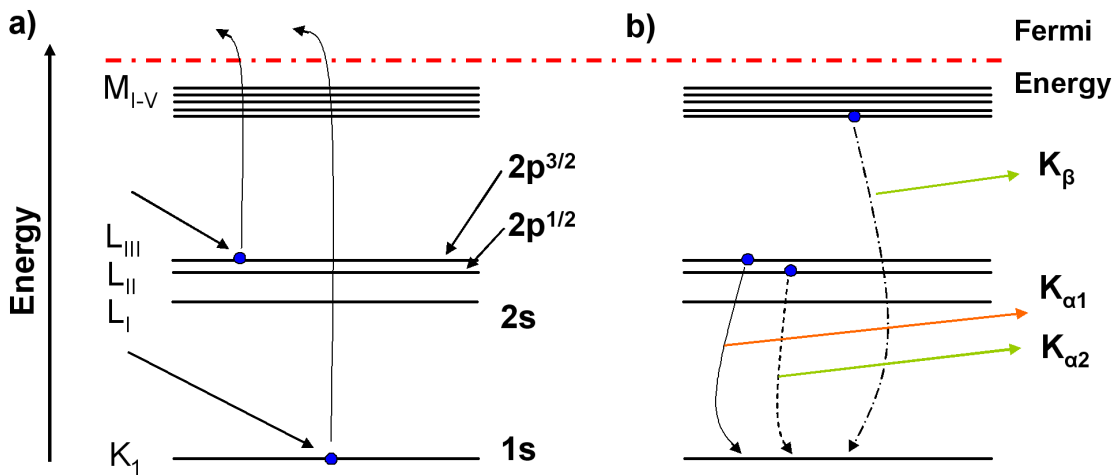


Figure 2.2: a) Absorption process b) Fluorescence Processes

Lab-based tube sources have several drawbacks from the point of view of this study. The three main ones are lack of intensity, energy tunability and adequate polarisation. To overcome these and gain access to phenomena such as magnetic scattering, large scale synchrotron sources are required.

### 2.2.2 Synchrotron X-ray sources

In the 1970s it was realized that synchrotron radiation emitted from charged particles orbiting in high energy particle physics accelerators was a much more intense and useful source of x-rays.

A synchrotron ring can be thought of as a many sided polygon, in which the charged particles, primarily electrons, are orbited in bunches at a constant energy

(3 GeV at the DIAMOND ring in Oxfordshire), at this energy they are moving at relativistic speeds.

Most purpose-built synchrotron light sources have the same basic layout. The electrons are produced and accelerated in a linear accelerator into a smaller booster synchrotron. Upon being further accelerated they are then injected into the main storage ring. This is all achieved using the Lorentz force,

$$\mathbf{F} = e\mathbf{v} \times \mathbf{B}. \quad (2.1)$$

Synchrotron light is produced either at the bending magnets, or by insertion devices such as undulators or wigglers situated in the straight sections. Synchrotron light is produced when the electrons pass through a magnetic field perpendicular to their direction of motion, bending magnets being the classic example. As the electrons undergo this acceleration they start to radiate. The emitted light leaves the bending magnet tangentially in the form of a cone shape due to the Lorentz transformation. Out of the plane of the orbit the angular divergence is excellent being given by equations 2.2 and 2.3.

$$\Delta\theta \approx \gamma^{-1}, \quad (2.2) \quad \gamma = \sqrt{1 - \left(\frac{v}{c}\right)^2}, \quad (2.3)$$

where  $\gamma$  is the relativistic factor for a particle with velocity  $v$  and  $c$  is the speed of light. However in the plane of the orbit the angular divergence is proportional to the time the electron experiences the Lorentz force, and therefore is much wider than for the out of the plane. The final beam is therefore emitted in a fan shape, the angle of which depends on the length of the bending magnet.

The energy that is lost as synchrotron light is replaced by a radio frequency (RF) cavity. Any losses of the electrons stored in the ring due to degradation of the orbit or collisions with stray gas molecules, are replaced by fresh injections of electrons at regular intervals from the injector accelerator.

Insertion devices can be added to the straight sections of synchrotrons in order to produce x-rays, giving increases in intensity, especially of circularly polarised light. The main types of insertion devices are wigglers and undulators. At their simplest

these consist of a succession of alternating magnets. The alternating magnetic field cause the electrons to wiggle or undulate, and therefore emit x-rays. Only x-rays produced at a bending magnet source were used in this study and the reader is referred to the references for information about undulator and wiggler sources[65, 66].

The main advantages of synchrotrons over laboratory based sources are the massive increase in source intensity, that a continuum of photon energies is emitted, allowing energy selectivity, as well as allowing the photon polarisation to be tuned to be circularly or linearly polarised to a very high degree. There is also a much smaller degree of angular divergence.

### 2.2.3 Monochromation, polarisation and coherence of x-ray beams

It is important when making scattering measurements to have a monochromatic beam, as both synchrotron and lab-based sources produce white beams of x-rays with additional emission lines. The simplest method of monochromation for lab based sources is to pass the incident x-rays through a filter such as Ni foil for a Cu  $K_\alpha$ . Ni has an absorption edge between the Cu K  $\alpha$  and  $\beta$  peaks and is very effective at reducing the Cu  $K_\beta$  peak however it is at the cost of intensity and has very poor wavelength dispersion.

Monochromation is usually carried out via Bragg reflection from a grating or crystal. Better wavelength resolution is obtained by collimating the incident beam before the monochromator by using a set of slits or by using several monochromating crystals, this is at the expense of intensity. The properties of monochromators are discussed in more detail by J. W. M. DuMond[69] and in the book by Holý *et al.*[70].

A major feature of synchrotron light is that the radiation emitted in the plane of the electron orbit is linearly polarised, but if the orbit is viewed from above or below, the degree of circular polarisation increases dramatically at the expense of intensity[71]. Figure 2.3 shows how whether the light is right or left circularly polarised is selected by being above or below the orbit of the synchrotron[72].

In this way the degree of circular polarisation can be selected by changing the height of a vertical focusing mirror, above or below the orbital plane, to select right

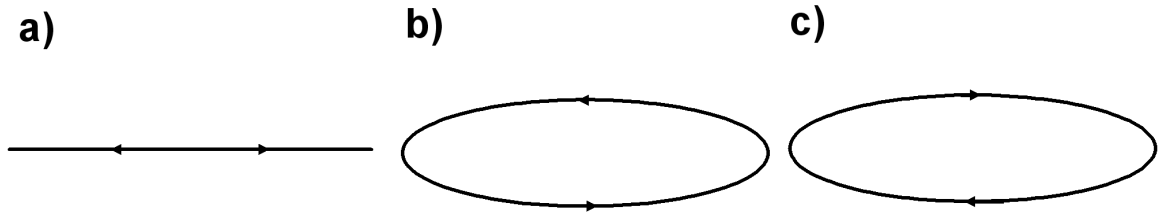


Figure 2.3: a) Looking in the plane of the electron orbit the emitted x-rays are linearly polarized. b) Looking from above the plane of the electron orbit the x-rays appear elliptically polarized. c) Again from below the electron orbit the x-rays appear elliptically polarized but in the opposite direction.

or left-handed elliptical polarised light as described in figure 2.3. In order to set the polarisation, a polarisation tuning curve measurement must be carried out. This involves moving the vertical focusing mirror through the beam and plotting out the intensity as shown in figure 2.4. 90 % circularly polarised light is obtainable for a loss of two thirds of the intensity[72]. The mirror height can then be set accordingly.

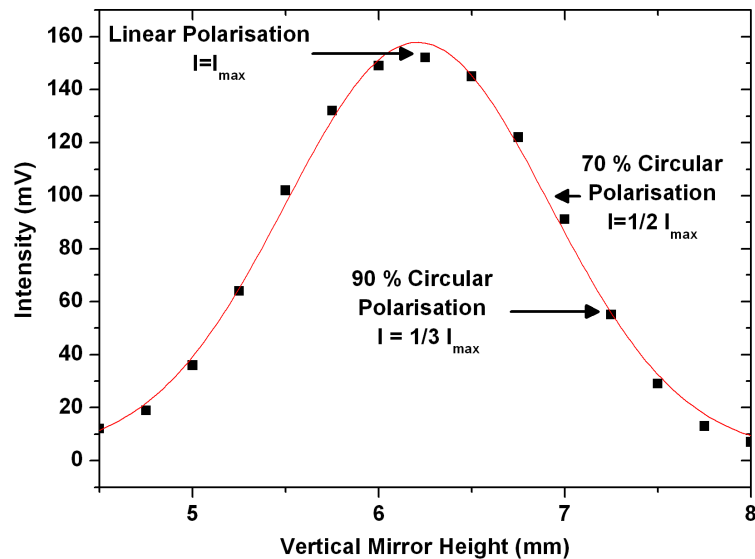


Figure 2.4: Polarisation tuning curve for the U4B beamline. The red line is a Gaussian fit to the data.

A real beam deviates from an ideal plane wave in two ways. Firstly it is not perfectly monochromatic and secondly it does not propagate in a perfectly defined



direction. For example if there are two waves of slightly different wavelengths starting at some position  $P$ , how far would the beams have to move before they were perfectly out of phase with each other. This is the definition of the longitudinal coherence length for a real beam. This is important as the longitudinal and transverse coherence lengths can limit the maximum size of the separation of the features that can be studied.

The coherence length of a real beam can be constrained by two things, the coherence of the scattering sample, for instance the periodicity of the bilayers in a multilayer, or inhomogeneity of the coherence of the incident light, for instance how monochromatic the light is and the source size etc. In general a scattering experiment probes the smaller coherence length of the two. A reduction in the coherence of either is seen as a broadening of the features in the scattering curve. It is important therefore to make some effort to calculate the coherence of the incident light in order to know whether the experiment is instrument resolution limited or sample resolution limited.

To do this, a lateral and vertical coherence length can be defined in the scattering plane, assuming initially no optical elements between source sample and detector. The longitudinal/temporal coherence length  $L_L$  is dependent on the wavelength resolution  $\Delta\lambda/\lambda$ ,

$$L_L = \frac{1}{2} \frac{\lambda^2}{\Delta\lambda}. \quad (2.4)$$

The spatial or lateral coherence length  $L_T$  is determined by the geometry of the beamline,

$$L_T = \lambda \frac{R}{2r_T} \approx \frac{\lambda}{2\phi_T} \approx \frac{\lambda}{\Delta\alpha_i}, \quad (2.5)$$

where  $R$  is the distance between the source and the sample, and  $r_T$  is the source size, which in turn gives the divergence angle  $\phi_T$ . Introduction of any optical elements that change the spectral width or angular divergence of the incident beam have to be taken into account. For instance placing a monochromator into the beamline can change the transverse coherence length  $L_T$ . This can be expressed in terms of the divergence angle of the monochromator  $\Delta\alpha_i$  as is done in the last section of equation 2.5. This then becomes the angular divergence of the beam at the sample position.

Similar relations exist for the detector, and the reader is referred to the books by Jens Als-Nielsen and Des McMorrow or V. Holý *et al.* [66, 70] for a more complete description.

The following example is for the U4B beamline setup which is described fully in section 2.2.5. The approximate calculation is for a wavelength set to  $\lambda=17 \text{ \AA}$  (near the Co L absorption edges) and a  $\Delta\lambda/\lambda$  of  $10^{-4}$ [25], giving a value of  $L_L = 8500 \text{ \AA}$ , or just under a  $\mu\text{m}$ . A similar order of magnitude value for  $L_T$  is also obtained. Hence the setup is instrument resolution limited when looking at features bigger than  $1 \mu\text{m}$ .

### 2.2.4 X-ray Detectors

X-ray detectors come in many forms. The reader is referred to the book by Michette *et al.*[65] for further information on the many types of x-ray detectors and their relative advantages and disadvantages, a full discussion of which is beyond the scope of this work.

In this work two types of detector are used. The first is a simple scintillation detector on the laboratory-based kit at the University of Leeds, details of which are given in chapter 1. These detectors are based on a material that produces a pulse of light upon absorbing an x-ray photon. These photons are then absorbed by a photocathode of a photomultiplier tube causing electrons to be ejected. It is these electrons that are measured. Scintillation detectors are robust and efficient but have poor energy resolution.

The soft x-ray photons at the U4B beamline are measured using a photodiode detector. When an x-ray photon is absorbed an electron hole pair is excited. The collected charge is then proportional to the incident number of photons.

### 2.2.5 U4B Beamline at the National Synchrotron Light Source

The U4B beamline is situated at the VUV ring of the National Synchrotron Light Source (NSLS) at the Brookhaven National Laboratories in the United States of America[73]. A general schematic of the beamline layout is shown in figure 2.5. An overview of the U4B beamline can be found at this URL [25].

Following the schematic in figure 2.5, the beamline consists of a bending magnet,

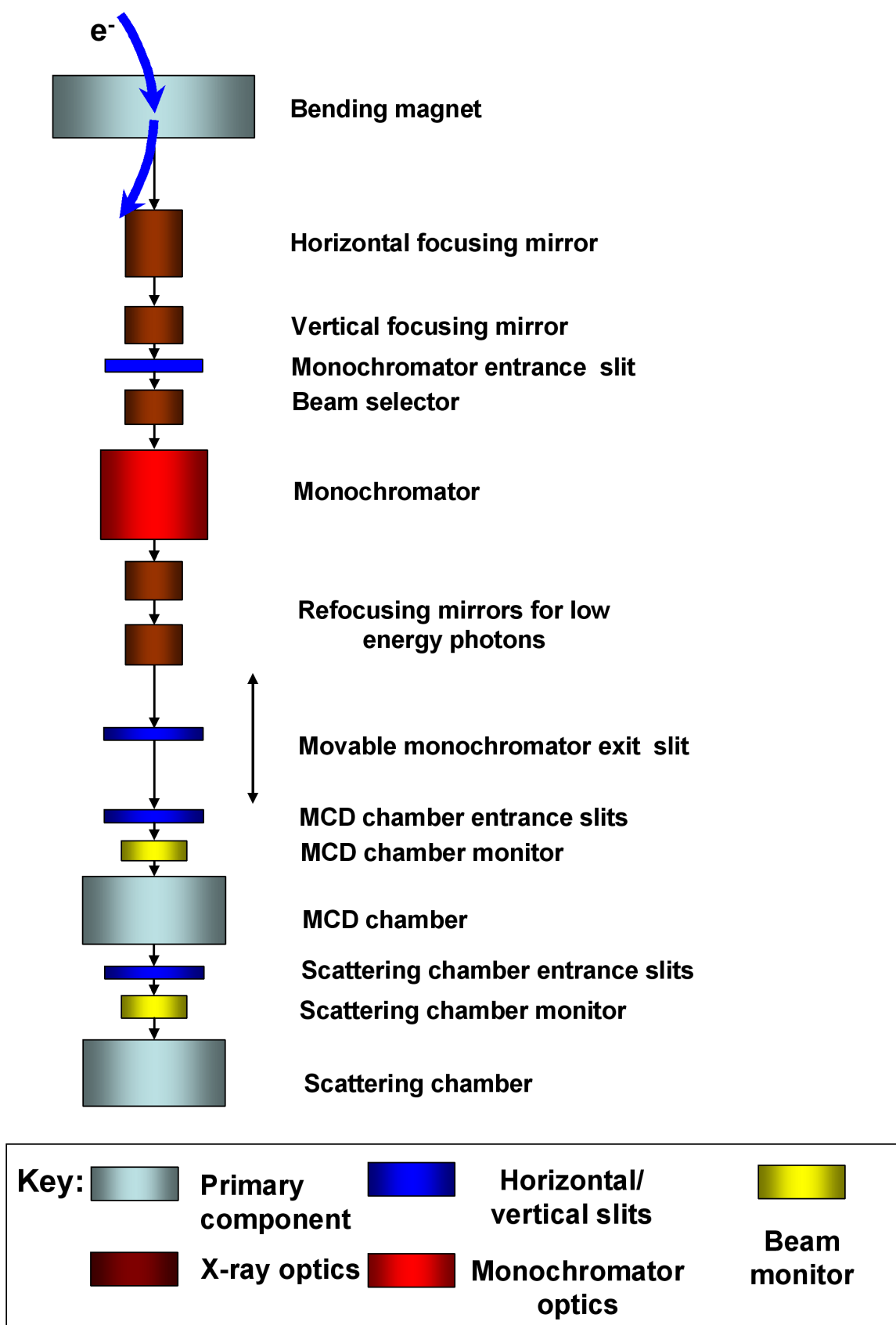


Figure 2.5: Schematic of the layout of the U4B beamline at the NSLS.

that provides white x-rays in the energy range 20-1200 eV. The white x-ray beam is then focused by horizontal and vertical focusing mirrors. The vertical focusing mirror focuses the source onto the entrance slit of the monochromator located further downstream.

The monochromator consists of 3 soft x-ray spherical gratings with ruling densities 300, 600, and 1200 lines/mm and 2 VUV gratings for low energy work. These gratings focus vertically onto the moveable exit slit of the soft x-ray monochromator. The monochromator works using Braggs law as described in section 3. Adjustment of the monochromator entrance and exit slits allow the fine tuning of the energy resolution with smaller entrance slits giving better energy resolution but at the expense of intensity. Details of the monochromator can be found at the following URL [25] and in the following work by Chen *et al.* [74][75] and Idzerda *et al.*[76].

Following this are the magnetic circular dichroism (MCD) chamber entrance slits. These define the beam size at the sample position in the MCD chamber. They can also be used to cut down the horizontal size of the beam at the sample position in the scattering chamber. An Au grid monitor is mounted immediately after the entrance slits to record the incident intensity.

For the purposes of scattering, the MCD sample arm is simply moved out of the beam. This allows the beam to pass through the scattering chamber entrance slits with a second Au grid monitor mounted immediately after.

The main scattering chamber contains a soft x-ray reflectometer with liquid nitrogen cryostat with a base temperature of  $\approx 150$  K, and a small heating stage capable of obtaining temperatures of  $\approx 700$  K. The magnet assembly can apply a maximum magnetic field of approximately 300 Oe in the plane of the sample, co-planar with the incident beam. The beamline and experimental chambers are all kept under high vacuum ( $\approx 10^{-9}$  torr) via ion pumps positioned at intervals along the beamline in order to reduce air absorption of the soft x-rays.

## 2.3 Production of neutrons

Neutrons are produced in one of two ways at large scale facilities, nuclear fission or spallation also see the book by Weinstein [77].

### 2.3.1 Reactor based neutron sources

In the case of a reactor source such as the Institute Laue-Langevin (ILL) research reactor in Grenoble, France, Uranium 235 undergoes fission upon the absorption of a thermal neutron ( $\sim 0.025$  eV). This produces on average 2.5 fast neutrons ( $\sim 1$  MeV) and 180 MeV of energy per fission. Of the 2.5 neutrons produced on average only 1 will be of use for scattering, the others being used to continue the nuclear fission reaction or being absorbed into other material present in the reactor. The reaction is shown in equation 2.6 and schematically in figure 2.6.

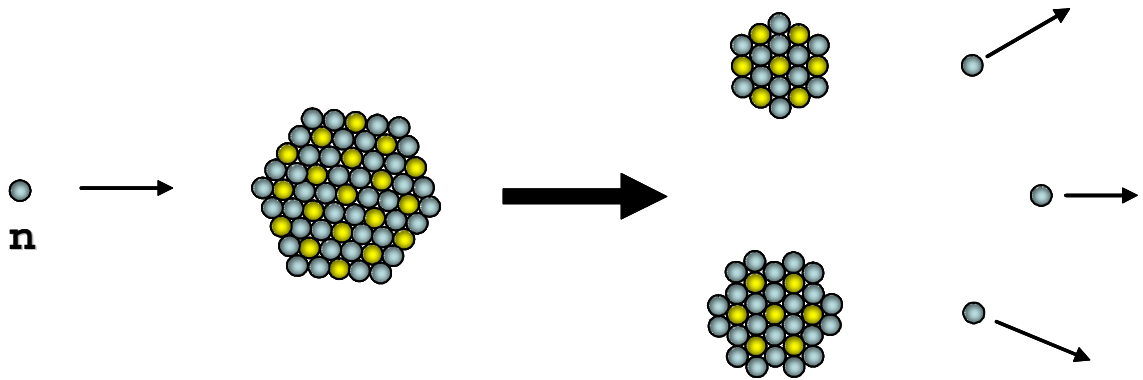


Figure 2.6: Schematic of the fission process.

### 2.3.2 Spallation based neutron sources

In the case of spallation sources, such as the ISIS neutron spallation source at the Rutherford Appleton Laboratory near Oxford, a particle accelerator is used to accelerate protons directly into a heavy element target. The reaction occurs above a certain energy threshold, usually 5 - 15 MeV. The reaction is a sequential one as illustrated in figure 2.7. In the case of the ISIS spallation source, protons are accelerated towards a Ta target at 800 MeV. These are absorbed by the target nucleus, then an internal nucleon cascade follows an internuclear cascade, where high energy neutrons are ejected and an evaporation process where the target nuclei de-excite by the emission of slow neutrons and a variety of other particles.

For each proton about 25 neutrons are produced. However the output is pulsed so that the time averaged intensity is less than that at a reactor source even though the flux is higher.

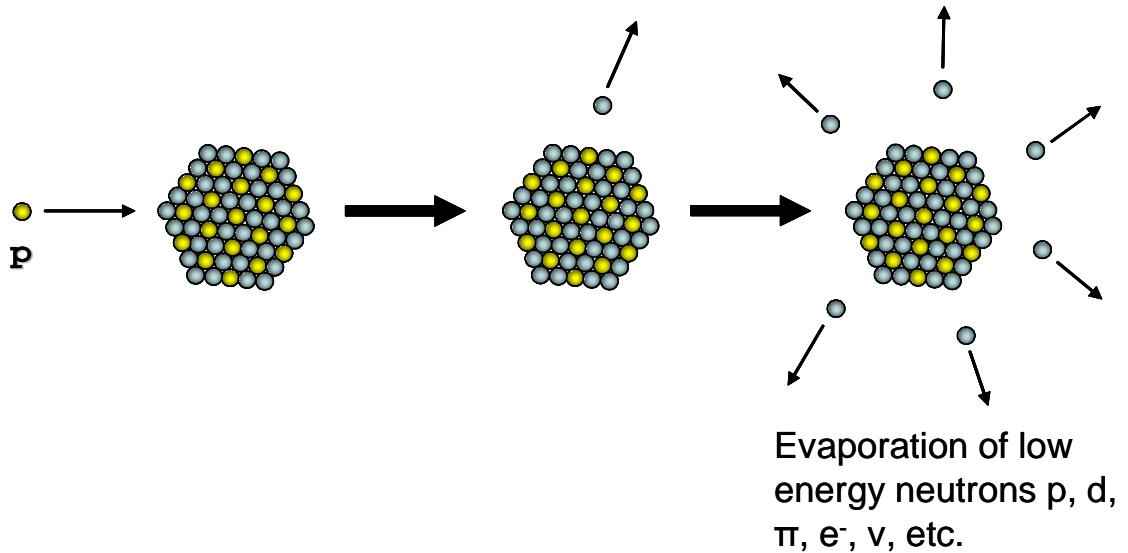


Figure 2.7: Schematic of the spallation process.

In both reactor and spallation sources the neutrons produced have very high energies (epithermal neutrons) therefore a moderator has to be used in order to bring the energy of the neutrons down to an energy which is of use for scattering experiments  $\sim 25$  meV giving a neutron wavelength of  $\sim 1$  Å. The moderator slows the neutron down via inelastic collisions. In this way, the neutrons eventually come into thermal equilibrium with the moderator. Light elements are often used such as  $H_2O$  or methane. The resultant energy spectrum is reasonably described by a Maxwell - Boltzmann distribution. See reference [78] for an overview of neutron production.

### 2.3.3 Monochromation, polarisation and coherence of neutron beams

Monochromation for neutrons is dependent on the experiment and the source and has to take into account the low flux of neutron sources. For instance at the ILL the majority of monochromation is performed in the same way as for x-rays, by using Bragg reflections from perfect crystals or via a grating as well as by using filters such as Be filters to remove higher harmonics from Bragg reflecting monochromators.

At spallation sources monochromation can make use of the pulsed nature of the beam. The energy of the neutron is proportional to its velocity, therefore the time it takes the neutron to reach the sample determines the wavelength as the neutron pulse from the source will spread out over the traversed distance. Instruments built on this principle are referred to as time of flight instruments. They employ a mechanical chopper, consisting of a disk of material of high neutron absorbance (Gd or Cd) with a hole cut through it. This is rotated at a fixed frequency such that it passes a well defined pulse of a certain wavelength range. The wavelength of the detected neutrons can then be calculated from the time taken to reach the detector[77]. The reader is also referred to the references listed in the paper by Penfold *et al.* [79] for further information on the design of time of flight instruments.

Polarisation for neutrons is also possible. A neutron beam contains a 50:50 mix of the two possible spin states  $\pm 1/2$  or spin up (***u***) and spin down (***d***). A polarised beam can be produced by the use of a polariser. There are several ways of doing this using magnetic fields such as neutron supermirrors and He<sup>3</sup> cells. The majority of these methods produce beams of polarised spin up or spin down neutrons by rejecting the other 50 % and therefore halving the intensity.

### 2.3.4 Neutron Detectors

Neutrons have no overall electric charge as well as a very low energy compared to soft X-rays, hence neutron detectors are often based on nuclear reactions such as;



This aim of such reactions is to produce charged particles that can then be detected by more conventional methods, hence the use of scintillation and gas detectors in neutron instruments, see references [77, 80].

### 2.3.5 ADAM Beamline at the ILL

The Advanced Diffractometer for the Analysis of Materials (ADAM) is located at the Institute Laue Langevin research reactor in Grenoble, France. A detailed description of the beamline, as well as the work that has been carried out on it, can be found in

the following work by A. Schreyer *et al.*[81]. A schematic of the beamline setup for full polarisation analysis is shown in figure 2.8 as well as at the following URL[82].

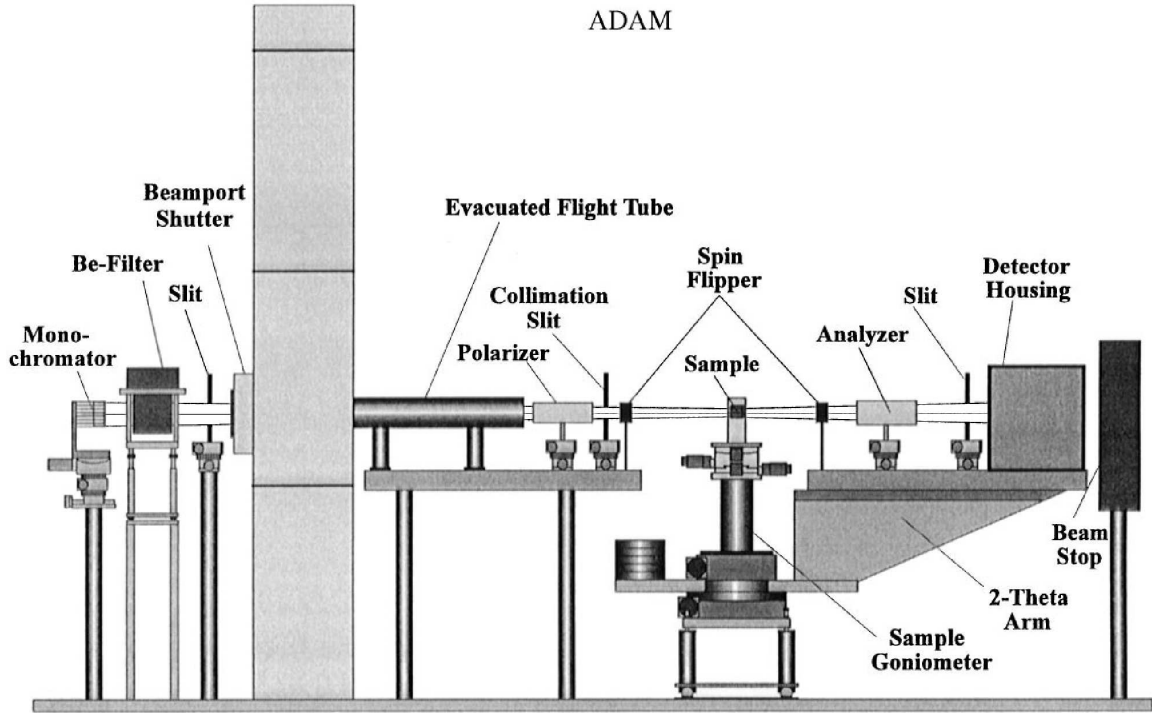


Figure 2.8: Schematic of layout of the ADAM beamline at the ILL reactor source in Grenoble. The picture was taken from the work of A. Schreyer *et al.*[81]

ADAM is situated on ILL's neutron guide H 53 which is fed by a liquid deuterium cold source. Monochromatic neutrons with a wavelength  $\lambda$  of 4.4 Å are reflected by the monochromator through a Be filter which removes any higher harmonics  $\lambda/n$ ,  $n=2, 3$ , etc, which are also reflected by the monochromator.

ADAM is a fixed wavelength instrument, with a standard 2 circle diffractometer allowing high resolution off specular measurements like rocking scans to be performed, the reader is referred to section 3 for details of reciprocal space scans and their implications. The reflectometer has a horizontal scattering plane, defined as the  $x$ - $z$  plane, with the samples being mounted vertically on a motorised heavy load goniometer head, with the  $z$ -direction lying along the sample normal.

For the purpose of polarised neutron reflectometry, optional supermirror polarisers and flippers positioned in front of and behind the sample are available. Detection is performed using  $\text{He}^3$  pencil detectors mounted in a shielded detector housing. A



two-dimensional position-sensitive detector is also available, significantly reducing counting times for off-specular measurements. The detected intensity is normalized to the beam by means of a monitor mounted immediately downstream of the first supermirror.

The sample environment includes a customised electromagnet, allowing fields to be applied in the  $y$  direction, with a maximum field of 4 kOe. There is also a cryofurnace available. For measurements on large samples a sample holder with an integrated heater can provide temperatures of up to 150 °C.

### 2.3.6 CRISP Beamline at ISIS

The CRISP beamline belongs to the large scale structures group at the ISIS neutron spallation source Rutherford Appleton Laboratory near Oxford. Details of the present day setup can be found at the following URLs [26, 83]. While the original descriptions of the beamline in its unpolarised setup can be found in the paper by Penfold *et al.* [79] and for its polarised setup in the paper by Felici *et al.* [84], a schematic of the beamline setup for full polarisation analysis is shown in figure 2.9.

The instrument views the 20K hydrogen moderator giving an incident wavelength range approximately between 0.5 to 6.5 Å. A variable aperture disc chopper defines the wavelength band, and prompt pulse suppression is achieved by a nimonic chopper. Additional frame overlap suppression is provided by the nickel coated silicon wafer frame overlap mirror, which reflect out of the main beam wavelengths greater than 13 Å. The incident beam is well collimated allowing a variable beam size and angular divergence, with typical dimensions of 40 mm wide (horizontal direction) and anything up to 10 mm in height (vertical direction).

A polarising mirror followed immediately by a Drabkin spin flipper and a static guide field provide variable polarisation at the sample position. The detected beam is normalised to a monitor positioned just before the sample space. Full polarisation analysis is achieved by the inclusion of a supermirror after the sample position.

The reflected neutrons are detected either by a single detector or a one dimensional

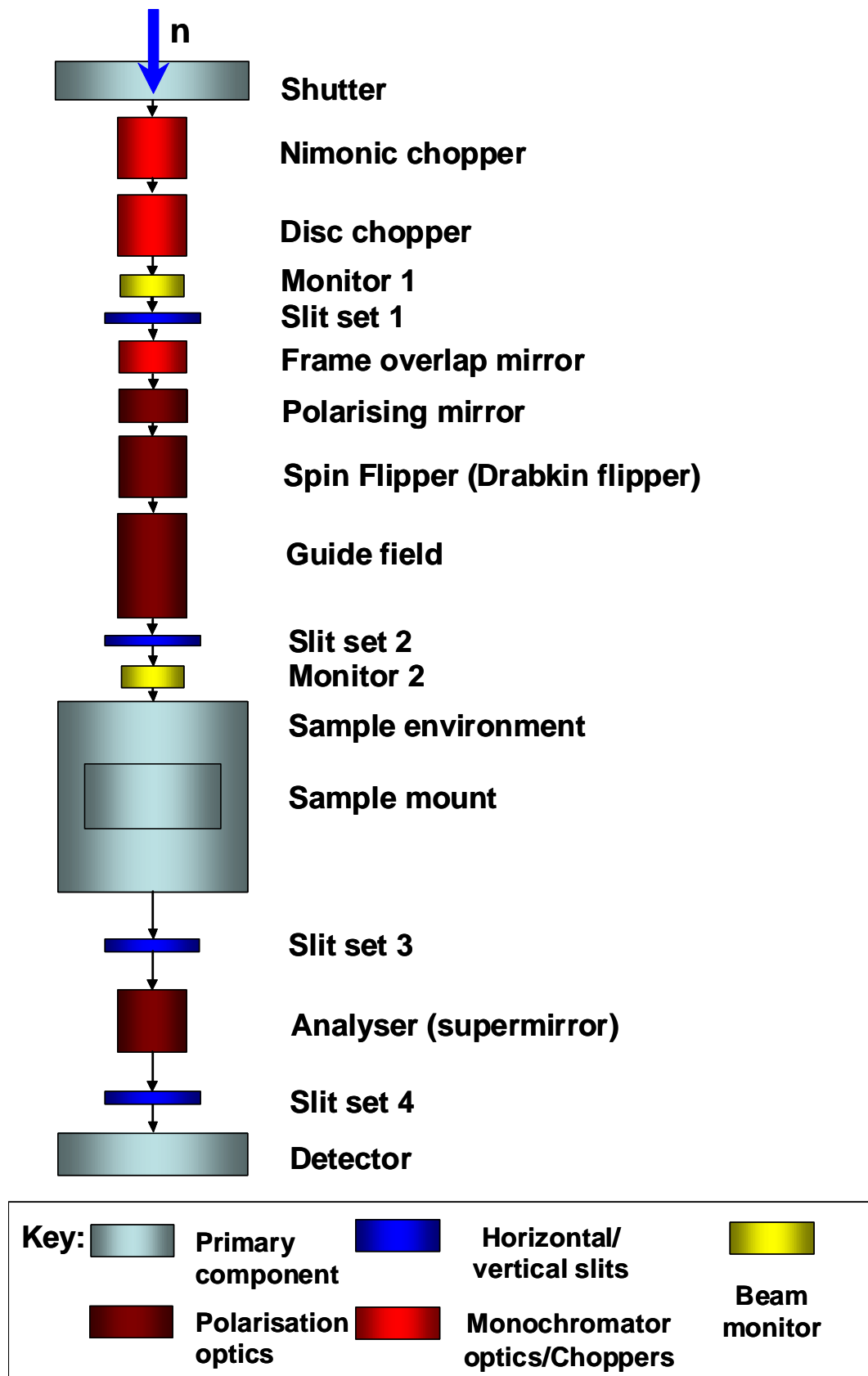


Figure 2.9: Schematic of layout of the CRISP beamline at the ISIS spallation source in Oxford.

$^3\text{He}$  detector. The combination of the time-of-flight technique and multi-detector ensures that both the parallel  $Q_z$  and perpendicular  $Q_x$  (to the surface normal) components of the neutron wave vector are obtained in a single measurement. Typical acquisition times are of the order of 4 hours for an entire reciprocal space map.

The beamline allows for multiple sample environments details of which can be found at the following reference[26]. In the case of this work an electromagnet was placed at the sample position providing an in-plane reversible field of  $\pm 4.7$  kOe. Temperatures of 4K can be achieved rapidly (1-2 hours) by the use of an Oxford Instruments continuous flow cryostat.

## 2.4 Summary

In this Chapter, we have described the x-ray and neutron facilities used and discussed some of the more salient points of their function and operation necessary for the measurements undertaken in this work. It should be noted that the larger part of this work was performed using the U4B soft x-ray beamline hence the greater detail used in its description.

## Chapter 3

# X-ray Scattering

### 3.1 Introduction

X-rays are classified as the part of the EM spectrum in the range  $\lambda \approx 0.1 - 20 \text{ \AA}$  with photon energies  $\approx 100\text{eV}$  to  $120 \text{ keV}$ , inline with equation 3.1. In particular the wavelengths below the  $2 \text{ keV}$  energy range are defined as the soft x-ray energy regime due to the high rate of absorbtion by air. The photon energy is related to wavelength through,

$$E(\text{eV}) = \frac{12431.25}{\lambda(\text{\AA})}. \quad (3.1)$$

First discovered by W.C. Röntgen in 1895 [85], they have become one of the major tools in the study of condensed matter physics. This is primarily due to their highly penetrating nature and their absorption being highly dependent on the atomic number of the material under investigation. A more complete overview of the development of x-ray science is covered by Michette *et al.* [65].

### 3.2 X-ray Interactions with Matter

There are three basic processes that can occur when x-rays interact with matter; they are absorption, diffraction (also called scattering), and refraction.

#### 3.2.1 Absorption

Absorption of x-rays by materials occurs via the photoelectric effect. An atom absorbs a photon and the energy is transferred to an electron, which may then be expelled

from the atom, leaving the atom ionized (see figure 3.1 (a)). The subsequent hole left over from the expelled electron is then filled by an electron from a higher energy level resulting in the emission of a photon; this process is known as fluorescence (see figure 3.1 (b)). Alternatively, the energy used to emit the photon in fluorescence can be used to expel another electron from the atom, known as Auger electron emission (see figure 3.1 (c)).

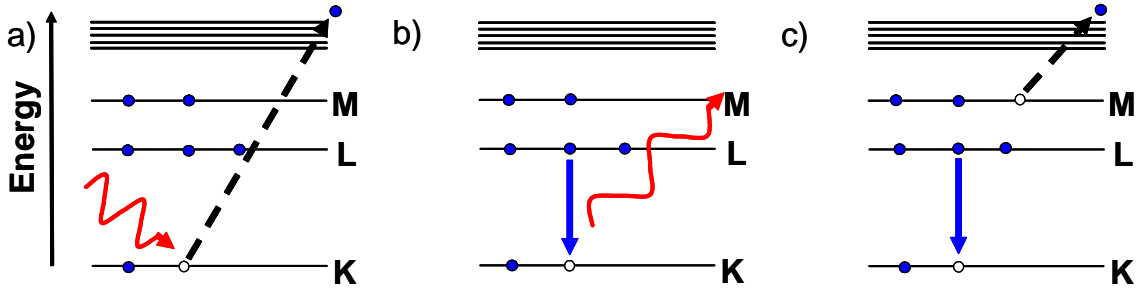


Figure 3.1: a) Absorption process b) Fluorescence Processes c) Auger electron emission

The linear absorption coefficient,  $\mu$  ( $\text{cm}^{-1}$ ) is defined such that  $\mu dz$  is the attenuation of the beam through an infinitesimally thin sheet of thickness  $dz$  at a depth  $z$  from the surface. This leads to the absorption equation,

$$I = I_0 \exp(-\mu t), \quad (3.2)$$

where  $t$  is the thickness and  $I_0$  the initial intensity. This allows  $\mu$  to be determined experimentally by measuring the intensity through a sample of known thickness and comparing it to the full intensity. The proportionality factor between the two is by definition the absorption cross section,  $\sigma_a$ .

### 3.2.2 Refraction

When an electromagnetic wave enters one transparent medium from another, it will change direction due to the difference in refractive indices. The refractive index  $n$  for x-rays passing through a transparent medium of some kind is described as a complex number,

$$n = 1 - \delta - i\beta, \quad (3.3)$$

where  $\delta$  is related to the dispersion in the system and  $\beta$  is related to the absorption. For x-rays,  $\delta$  and  $\beta$  are both small positive numbers resulting in  $n'$  being less than unity. Snell's law relates the incident angle  $\theta_i$  to the refracted angle  $\theta'$ ,

$$n \cos \theta_i = n' \cos \theta'. \quad (3.4)$$

Taking into account that for x-rays the refractive index is just less than one. Then upon entering a medium x-rays are refracted away from the normal rather than towards it as is the case for visible light. This does not violate special relativity due to the fact that when the phase velocity becomes superluminal, no information can be transmitted faster than light as this travels at the group velocity which is always less than  $c$  in a normal dispersive media[46].

It is also implied that below a certain angle, total external reflection takes place. By expanding the cosine in equation 3.10 and substituting in equation 3.3 with  $\theta_i = \theta_c$  and  $\theta' = 0$  then the critical angle can be related to  $\delta$ ,

$$\theta_c = \sqrt{2\delta}, \quad (3.5)$$

where  $\beta$  has been set to zero by assuming no absorption in the system. For angles greater than the critical angle the x-rays penetrate into the medium. For a perfect interface, the amplitudes of the reflected and transmitted waves are governed by Fresnel's laws.

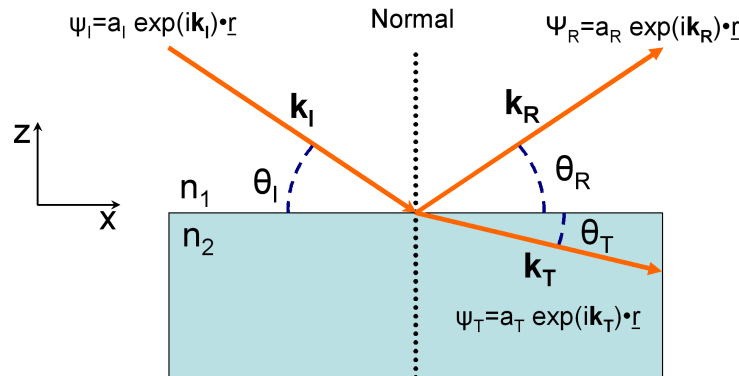


Figure 3.2: A plane wave incident on the boundary between two homogenous, isotropic, flat, lossless media.

Consider an incident plane wave on an interface as shown in figure 3.2. Snell's

Law and Fresnel's equations can both be derived by imposing the boundary conditions that the in-plane components of the wave and its derivative must be continuous at an interface. This requires that the amplitudes of the waves are related by,

$$a_I + a_R = a_T, \quad (3.6)$$

and

$$a_I \mathbf{k}_I + a_R \mathbf{k}_R = a_T \mathbf{k}_T, \quad (3.7)$$

where the wavenumber in a vacuum is denoted as  $k = |\mathbf{k}_I| = |\mathbf{k}_R|$  with  $n_1 = 1$  and in the material  $n_2 k = |\mathbf{k}_T|$ . Then by taking the components of  $\mathbf{k}$  parallel and perpendicular to the surface with specular reflection ( $\theta_I = \theta_R = \theta$ ) one obtains,

$$a_I k \cos \theta + a_R k \cos \theta = a_T (nk) \cos \theta_T, \quad (3.8)$$

and,

$$-(a_I - a_R)k \sin \theta = -a_T (nk) \sin \theta_T. \quad (3.9)$$

Snell's Law comes about from taking equation 3.8 and combining it with equation 3.6.

$$\cos \theta_i = n \cos \theta'. \quad (3.10)$$

Then using equation 3.9 for the projection perpendicular to the surface combined with equation 3.6, one can obtain,

$$\frac{a_I - a_R}{a_I + a_R} = n \frac{\sin \theta'}{\sin \theta} \equiv \frac{\theta'}{\theta}, \quad (3.11)$$

From this it is possible to derive the Fresnel equations via further use of equation 3.6,

$$r = \frac{a_R}{a_I} = \frac{\theta - \theta'}{\theta + \theta'}, \quad (3.12) \quad t = \frac{a_T}{a_I} = \frac{2\theta}{\theta + \theta'}, \quad (3.13)$$

where  $r$  is the amplitude reflectivity and  $t$  is the amplitude transmissivity. The

intensity of the reflected and transmitted waves is given by the square of the amplitude reflectivity and transmissivity.

For an in-depth derivation of Fresnel's equations, both perpendicular and parallel to the plane of incidence, the reader is directed to the optics book by Eugene Hecht [46] and the x-ray scattering book by Jes Als-Nielsen [66].

A recursive relation was developed by Parratt[86] that describes the reflectivity of multilayered structures starting with a simple 2 layer structure as depicted in figure 3.3 by matching the tangential electric vectors  $\mathbf{E}$  across the interface, therefore following the derivation outlined by Parratt[86],

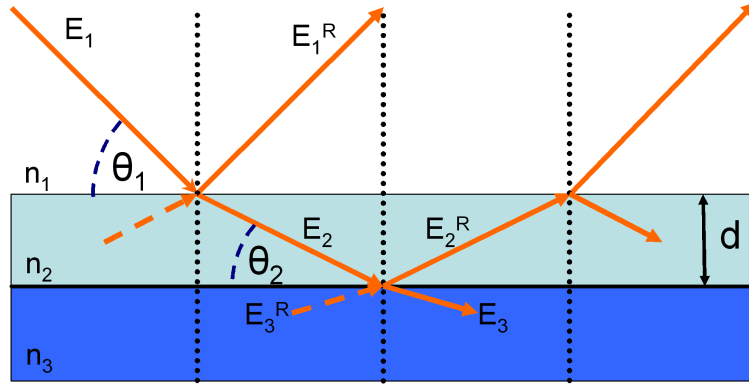


Figure 3.3: Reflection and refraction from a multilayer structure[86].

Parratt then goes on to describe his recursion relation for a system containing in  $N$  layers with the result of,

$$R_{n-1,n} = a_{n-1}^4 \left[ \frac{R_{n,n+1} + F_{n-1,n}}{R_{n,n+1}F_{n-1,n} + 1} \right], \quad (3.14)$$

where  $R$  and  $F$  are respectively,

$$R_{n,n+1} = a_n^2 \left( \frac{E_n^R}{E_n} \right), \quad (3.15) \quad F_{n-1,n} = \frac{f_{n-1} - f_n}{f_{n-1} + f_n}, \quad (3.16)$$

and  $a_n$  and  $f_n$  are respectively,

$$a_n = \exp \left( -\frac{i\pi f_n d_n}{\lambda} \right) \text{ and } a_1 = 1 \text{ (top surface)}, \quad (3.17)$$

$$f_n = \sqrt{(\theta^2 - 2\delta_n - 2i\beta_n)} \text{ and } f_1 = \theta, \quad (3.18)$$



where  $\theta$  is the angle of incidence at the top surface and  $d_n$  is the thickness of any particular layer. Equation 3.14 is solved by starting at the bottom layer medium  $N$  and working up. It must be noted that the bottom layer is assumed to be an infinitely thick substrate and that the top layer is assumed to be air or vacuum. The ratio of reflected to incident intensity,  $I_R/I_0$ , is obtained by separating equation 3.14 for  $R_{1,2}$  into its real and imaginary terms and multiplying by the complex conjugate. This is symbolized by,

$$\frac{I_R}{I_0} = \left| \frac{E_1^R}{E_1} \right|^2, \quad (3.19)$$

A matrix version of Parratt recursion relation is formulated by Manciu *et al.* [87] and the reader is also directed to the theses of T.P. Hase and A. A. Cole for further descriptions of the whole process[88, 89].

### 3.2.3 Scattering

X-ray scattering or diffraction arises due to the electromagnetic interaction between the electric field of the incident x-ray and the electrons within the material. Classically the wavelengths of the incident and scattered waves are the same; hence the scattering is elastic, which is the main process exploited in x-ray diffraction. The scattering vector  $\mathbf{Q}$  is subsequently defined as,

$$\mathbf{Q} = (\mathbf{k}_f - \mathbf{k}_i), \quad (3.20)$$

and has units of ( $\text{\AA}^{-1}$ ) where  $\mathbf{k}_f$  and  $\mathbf{k}_i$  are the out going and incoming wavevectors respectively, where  $|\mathbf{k}|$  is given by  $2\pi/\lambda$ . A free electron's ability to scatter x-rays is defined as the Thomson scattering length,

$$r_0 = \left( \frac{e^2}{4\pi\epsilon_0 mc^2} \right) = 2.82 \times 10^5 \text{\AA}. \quad (3.21)$$

At this point it becomes necessary to introduce some basic concepts in scattering. The first is the concept of a differential cross section denoted as  $(d\sigma/d\Omega)$ . This gives the probability of observing a scattered particle per solid angle unit, if the target area is irradiated by a flux of one particle per unit area and is expressed as,

$$\frac{d\sigma}{d\Omega} = \frac{(\text{Number of x-rays scattered per second into } \Delta\Omega)}{(\text{Incident Flux})(\Delta\Omega)} = |f|^2, \quad (3.22)$$

where  $\Delta\Omega$  is the solid angle of the detector and  $f$  is the scattering factor. The number of scattered particles per unit area per unit time is then defined by,

$$I_S = I_0 \Delta\Omega \frac{d\sigma}{d\Omega}, \quad (3.23)$$

where  $I_0$  is the incident flux,  $\Delta\Omega$  is the solid angle of the detector and  $d\sigma/d\Omega$  is the differential cross section as stated above.

Fermi's Golden rule allows the calculation of the transition rate from one state of a quantum system to a continuum of states due to an interaction. Hence for scattering, the intensity of the scattering is proportional to the matrix element,

$$|\langle Final | \text{INTERACTION} | Initial \rangle|^2, \quad (3.24)$$

where the final state is assumed to be a plane wave defined by a wavevector  $\mathbf{k}$ [90]. In an atom there are  $Z$  electrons which are smeared out over its volume. The scattering ability of these smeared out electrons is summed up in the scattering factor  $f$ , which can be written using Fermi's golden rule as the Fourier transform of the electron density,

$$f = \int_V \rho(r) \exp[2\pi\mathbf{Q} \cdot \mathbf{r}] dV, \quad (3.25)$$

where  $\rho$  is the electron density per unit volume and  $r$  the radius. The condition for constructive interference is Bragg's law [91],

$$\lambda = 2d \sin \theta, \quad (3.26)$$

where  $\lambda$  is the wavelength,  $d$  the lattice spacing, and the incident angle  $\theta$ . The scattering amplitude must be obtained by expanding equation 3.25 as a Fourier series which sums over the unit cell  $j$  and then over all unit cells  $\mathbf{R}_n$ ,

$$F^{crystal}(\mathbf{Q}) = \sum_j f_j(\mathbf{Q}) \exp(2\pi i \mathbf{Q} \cdot \mathbf{r}_j) \sum_{\mathbf{R}_n} \exp(2\pi i \mathbf{Q} \cdot \mathbf{R}_n), \quad (3.27)$$

where  $\mathbf{R}_n$  is a vector to any lattice point in the real lattice and is defined as,

$$\mathbf{R}_n = \mathbf{h}n_1 + \mathbf{k}n_2 + \mathbf{l}n_3, \quad (3.28)$$

where  $n_1$ ,  $n_2$  and  $n_3$  are integers and  $f_j(\mathbf{Q})$  is the atomic structure factor given by equation 3.25 and  $\mathbf{r}_j$  is the fractional co-ordinate of the atom  $j$  within the unit cell,  $\mathbf{R}_n$ . For an introduction to crystallography the reader is directed to the book “Introduction to Solid State Physics” by Charles Kittel[92].

The first term of equation 3.27 is called the structure factor and is dependent on the basis of atoms in the unit cell, and gives the intensity of an allowed reflection. The second term is the form factor and is solely dependent on the real crystal lattice and gives information on the position of the peaks and how they are distributed in reciprocal space. The intensity can then simply be found from the square of the amplitude:  $F^{crystal}$ . The form factor will always be of the order of unity unless the scattering vector  $\mathbf{Q}$  meets the following condition,

$$\mathbf{Q} \cdot \mathbf{R}_n = 2\pi \times \text{integer}. \quad (3.29)$$

A unique solution to equation 3.29 can be found by using the idea of a reciprocal lattice. This lattice is spanned by the reciprocal lattice basis vectors  $\mathbf{a}^*$ ,  $\mathbf{b}^*$ ,  $\mathbf{c}^*$  which are defined as,

$$\mathbf{a}^* = 2\pi \frac{\mathbf{b} \times \mathbf{c}}{\mathbf{a} \cdot \mathbf{b} \times \mathbf{c}}, \quad (3.30) \quad \mathbf{b}^* = 2\pi \frac{\mathbf{c} \times \mathbf{a}}{\mathbf{a} \cdot \mathbf{b} \times \mathbf{c}}, \quad (3.31) \quad \mathbf{c}^* = 2\pi \frac{\mathbf{a} \times \mathbf{b}}{\mathbf{a} \cdot \mathbf{b} \times \mathbf{c}}, \quad (3.32)$$

where  $\mathbf{a}$ ,  $\mathbf{b}$  and  $\mathbf{c}$  are the basis vectors of the real lattice. Then any reciprocal lattice point can be represented by,

$$\mathbf{G} = h\mathbf{a}^* + k\mathbf{b}^* + l\mathbf{c}^*, \quad (3.33)$$

where  $h$ ,  $k$  and  $l$  are the Miller indices. The product of  $\mathbf{G}$  with  $\mathbf{R}_n$  is then,

$$\mathbf{G} \cdot \mathbf{R}_n = 2\pi(\mathbf{h}n_1 + \mathbf{k}n_2 + \mathbf{l}n_3) = 2\pi \times \text{integer}. \quad (3.34)$$

This is exactly the same result as obtained in equation 3.29. It then follows that for diffraction to take place the condition that must be satisfied must be,

$$\mathbf{Q} = \mathbf{G}. \quad (3.35)$$

This is the Laue condition for diffraction from a crystal lattice, and shows that  $F_{crystal}(\mathbf{Q})$  vanishes unless  $\mathbf{Q}$  coincides with a reciprocal lattice vector. It can be shown to be equivalent to Bragg's law. The structure factor shows how the intensity of the diffracted peak is proportional to the position of the atoms in the unit cell. This can easily be seen from the exponential of the structure factor, which is the sum over the fractional coordinates of all the basis atoms in the unit cell,

$$\sum_j \exp[2\pi i(\mathbf{q} \cdot \mathbf{r}_j)] = \sum_j \exp[2\pi i(\mathbf{h}u + \mathbf{k}v + \mathbf{l}w)] \quad (3.36)$$

This explanation of diffraction does not allow for the possibility of multiple scattering events. This assumption lends considerable simplicity to the theory and is known as the kinematical approximation.

For further information on diffraction, the reader is referred to the books by B. E. Warren[93], J. Als-Nielsen and D. McMorrow [66] and B. D. Cullity[36].

## 3.3 Reflectivity

### 3.3.1 Types of X-ray Scan

At this point it becomes useful to introduce the notions of the different types of x-ray scan that can be performed in the scattering geometry used in this work as described in section 1.4. Restating equation 3.20 for the scattering vector  $\mathbf{Q}$ ,

$$\mathbf{Q} = (\mathbf{k}_f - \mathbf{k}_i),$$

it becomes possible to derive expressions for the orthogonal reciprocal space vectors  $\mathbf{Q}_z$  and  $\mathbf{Q}_x$  by taking the respective components of  $\mathbf{k}_f$  and  $\mathbf{k}_i$  in the  $\mathbf{Q}_z$  and  $\mathbf{Q}_x$  directions and putting them back into equation 3.20. The geometry of the 2 circle diffractometer is shown schematically in figure 3.4 and its reciprocal space equivalent in figure 3.5. It must be noted that  $\theta$  and  $\phi$  are the sample and detector angles

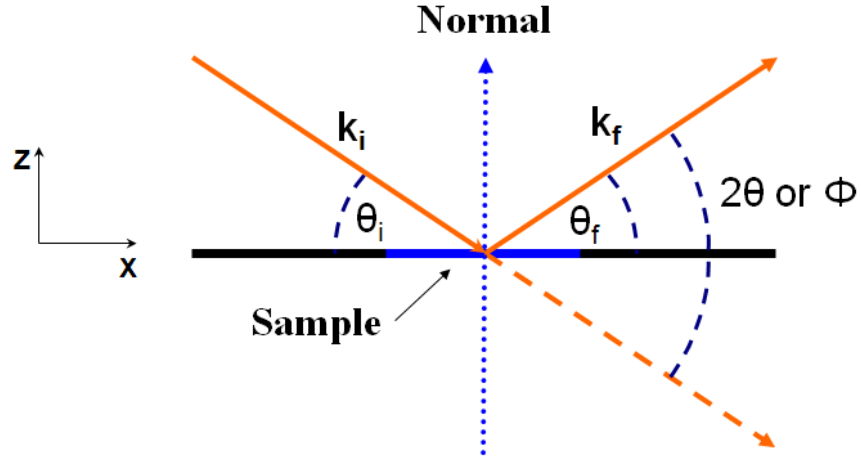


Figure 3.4: 2 circle scattering real space geometry.

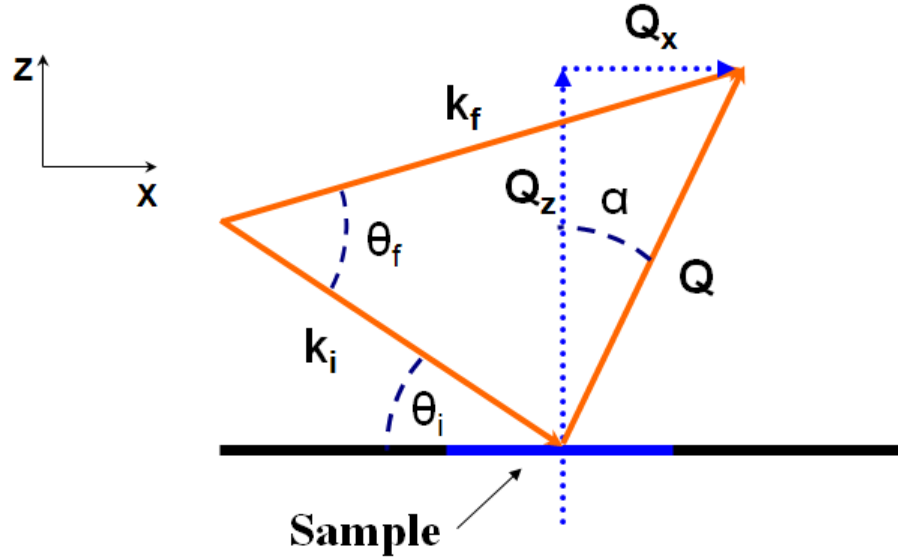


Figure 3.5: Schematic of reciprocal space for the real space area shown in figure 3.4 respectively as was shown in figure 1.5 in section 1.4 ( $\phi = \theta_f + \theta_i$  where  $\theta_i = \theta$ ). This gives the following for  $Q_z$  and  $Q_x$ ,

$$Q_z = \frac{2\pi}{\lambda}(\sin(\phi - \theta) + \sin(\theta)), \quad (3.37)$$

$$Q_x = \frac{2\pi}{\lambda}(\cos(\phi - \theta) - \cos(\theta)), \quad (3.38)$$

where  $\theta$  and  $\phi$  are the sample and detector angles respectively.

These two equations can also be expressed in terms of  $\phi$  and  $\alpha$  giving,

$$Q_z = \frac{4\pi}{\lambda}(\sin(\phi/2) \cos(\alpha)), \quad (3.39)$$

$$Q_x = \frac{4\pi}{\lambda}(\sin(\phi/2) \sin(\alpha)), \quad (3.40)$$

where  $\alpha = \theta - \frac{\phi}{2}$ .

From these equations the different types of x-ray scan that can be performed on a 2 circle diffractometer can be described, as shown in figure 3.6. A third component of  $\mathbf{Q}$  in reciprocal space  $\mathbf{Q}_y$  is also present but requires a  $\chi/\phi$  stage and different slit geometry to sample it.

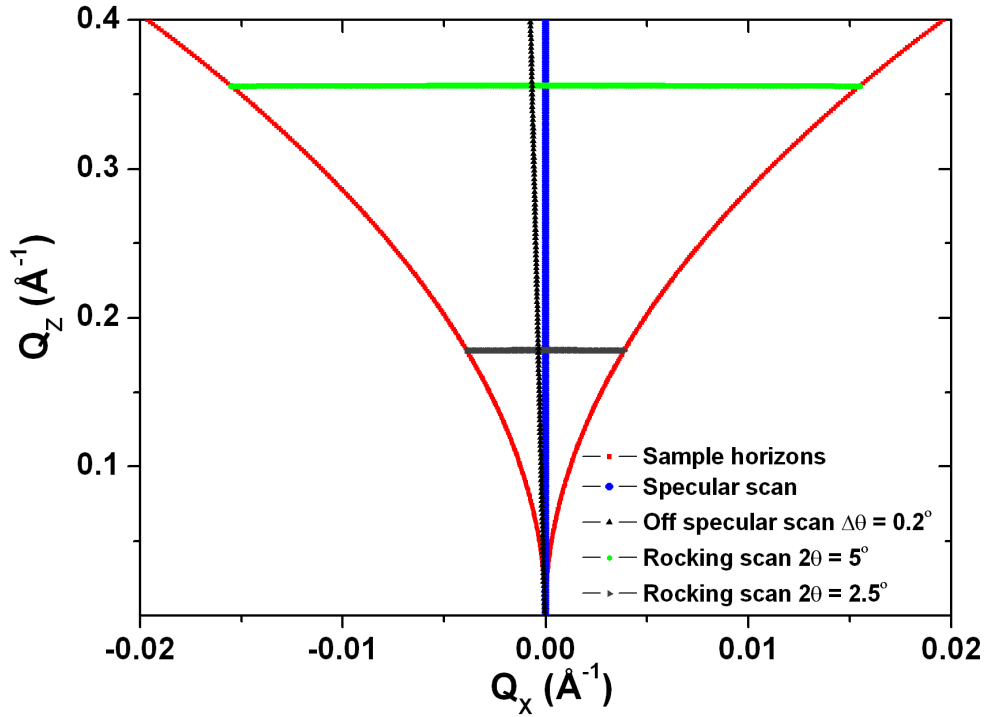


Figure 3.6: Reciprocal space map for Cu  $K_\alpha$  (1.54 Å) x-rays showing the line scans cut through reciprocal space for the various scans that can be performed on a 2 circle diffractometer[88, 89]. The two rocking scans shown are in fact very shallow arcs the curve of which is not visible on this plot. Hence at Cu  $K_\alpha$  wavelengths it is possible to not have to use  $Q_x$  rod scans.

### Specular scan

A specular scan or  $\theta/2\theta$  scan consists of the coupled motion of the sample and detector arms such that the detector arm moves at twice the rate of the sample arm. This 2:1 ratio is maintained throughout the scan and is known as the specular condition ( $\mathbf{Q}_x = \mathbf{0}$ ), and collapses equation 3.39 down to,

$$\mathbf{Q}_z = \frac{4\pi}{\lambda} \sin(\theta). \quad (3.41)$$

This probes the  $\mathbf{Q}_z$  component of the scattering plane giving information perpendicular to the plane of the sample. A specular scan is often referred to as mapping out the specular ridge. The specular scan will also contain diffuse scattering. In order to remove this and obtain the true specular, it is necessary to perform an offspecular scan (as described next) and subtract this intensity from the specular scan.

### Offspecular scan

An off-specular scan, or longitudinal diffuse scan, is essentially the same as a specular scan, except that  $\theta$  is off set by a small angle. In the case of figure 3.6 this is 0.2 degrees. The arms are then moved with the same 2:1 ratio as for a normal specular scan. This is important as a normal specular scan contains some diffuse scatter that needs to be subtracted to obtain the true specular information. A standard offspecular scan has a slightly varying  $\mathbf{Q}_x$  dependence as can be seen in figure 3.6. It is sometimes necessary to perform a direct  $\mathbf{Q}_z$  scan to get around this, for instance at soft x-ray wavelengths when the  $\mathbf{Q}_x$  variation becomes significant.

### Rocking scan

In order to sample the diffuse scattering away from the specular ridge in the  $\mathbf{Q}_x$  direction and probe the structure in the plane of the sample, rocking scans or transverse diffuse scans are used. A rocking scan consists of setting the detector angle at a constant value and then sweeping the sample angle from zero out to the detector angle. Again there is a slight varying dependence on  $\mathbf{Q}_z$  resulting in a slight arc which is negligible for longer wavelengths, as can be seen for the two rocking scans shown in

figure 3.6. Again, it is sometime necessary to perform  $\mathbf{Q}_x$  rod scans to get around this.

The two red arcs to either side of the specular ridge are known as sample horizons. They are mapped out by introducing the condition that  $\theta$  is equal to zero or  $2\theta$  into equation 3.40. The limit of the observed scatter is due to the incident and scattered x-rays being below the surface of the sample.

Just as correcting the specular by subtracting an offspecular scan to obtain the true specular, rocking curves sometimes require a footprint correction[94]. At low angles, the footprint of the incident x-ray beam on the sample is bigger than at high angles. The volume of the sample that is probed is proportional to surface area  $A_0$  multiplied by  $\sin \theta$ . This results in low angles being reflected more intensely than higher angles, resulting in an asymmetry of the rocking curve. To correct for this the measured intensity can be multiplied by the following factor,

$$\frac{\sin \theta}{\sin 2\theta}. \quad (3.42)$$

where  $\theta$  and  $2\theta$  are the sample and detector angles respectively.

### 3.3.2 Specular Reflection

As has been described earlier, total external reflection is observed for x-ray wavelengths when the angle of incidence is below the critical angle. This is shown for a Si substrate, which is taken as having an infinite thickness, in figure 3.7 (red curve). However if the angle of incidence is increased above the critical angle then a large reflectivity signal is still observed for many degrees. This is known as the low angle reflectivity regime and for Cu  $K_\alpha$  x-rays is located in the approximate region of  $\approx 1^\circ$  to  $15^\circ$ . This is because at these angles the scattering vector is of approximately the same size as the layer thicknesses for the types of sample studied in this thesis. Above  $\approx 10^\circ$  the high angle regime is probed where the scattering vector is of the same size as the reciprocal lattice vector. Away from the critical edge ( $\theta > 2\theta_c$ ) the reflected intensity dies off approximately as  $\theta^{-4}$  in accordance with Fresnel's equations or faster if there is roughness present.



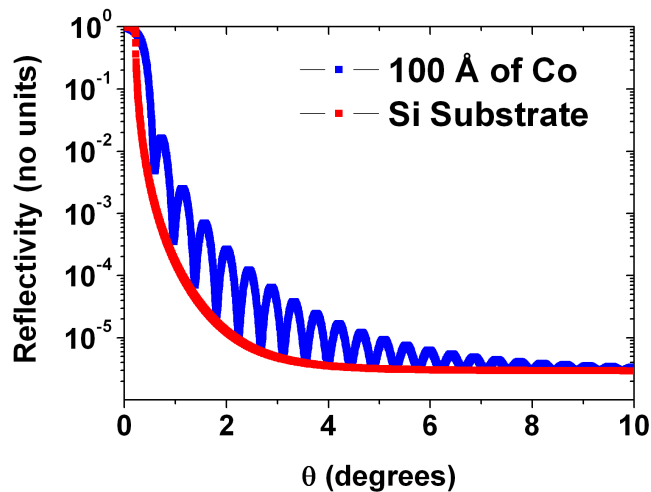


Figure 3.7: Simulation of the reflectivity from 100 Å thick layer of Co on a Si substrate (blue curve). For comparison a simulation of the Si substrate which is considered to be infinite in extent is also shown (red curve) the critical edge is clearly viable. Both systems contain no roughness. Simulation performed using the Bede REFS software package[95].

In the simplest case of a finite layer of material deposited on a substrate, interference fringes are observed. These fringes were first observed by Kiessig in 1931[96] and now bear his name. They originate from the interference of the x-rays reflected from the surface and from the interface between the material and the substrate as shown in figure 3.7 (blue curve). The periodicity of these fringes can be used to determine the thickness of the layer on the substrate.

Multilayer structures introduce another periodicity due to the repeated bilayer of the system. This gives rise to constructive/destructive interference for certain incident angles resulting in a series of Bragg peaks[91, 66] in the low angle specular reflectivity data as is shown in figure 3.8. This is for a simple Co/Ru multilayer with 20 repeats. The position of the Bragg peaks can be used to calculate the thickness of the bilayer repeat unit using Bragg's law stated earlier in equation 3.26.

Figures 3.7 and 3.8 were produced using the Bede REFS software package as described in references by Wormington *et al.*[95, 97] for Cu  $K_\alpha$  radiation (1.54 Å), where both systems contain no roughness.

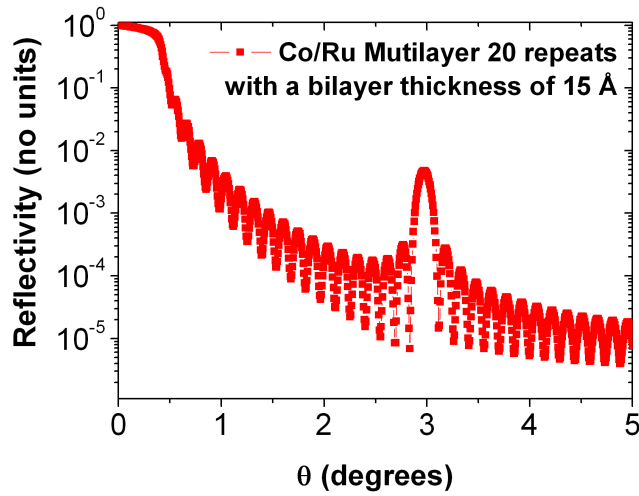


Figure 3.8: Simulation of the reflectivity from a Co/Ru multilayer with 20 repeats and a bilayer repeat thickness of 15 Å (red curve). The system contains no roughness. Simulation performed using the Bede REFS software package[95].

### 3.3.3 The Effect of Roughness on Specular Scattering

It becomes necessary at this point to differentiate between the different types of roughness. For a single interface there are two main deviations from a perfectly flat layer. The first can be ideally described as a distinct boundary between two atomic species, as shown in figure 3.9 a). The second form is grading, where the boundary is blurred by the intermixing of the two atomic species and is depicted in figure 3.9 b). In reality, a mixture of the two is what would be expected.

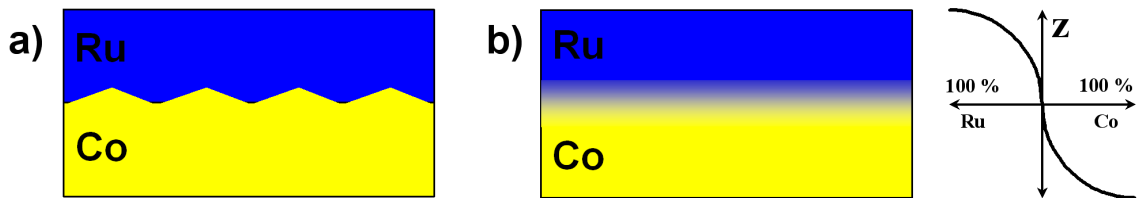


Figure 3.9: a) Distinct structural boundary. b) Gradual graded boundary.

In the first case of a distinct boundary between the two atomic species as shown in figure 3.9 panel (a) the rough interfaces are characterized by a root mean square roughness (RMS). This is achieved by replacing the surface by a collection of flat

surfaces with a distribution about an average surface position. If this distribution is gaussian in nature it will have a standard deviation  $\sigma$ , which can also be thought of as the interface width. The Fresnel coefficient  $F_{n-1,n}$  as described by equation 3.16 can then be modified by an exponential damping term,

$$\mathbf{R} = F_{n-1,n} \exp(-\mathbf{Q}_z^2 \sigma^2). \quad (3.43)$$

A more generalized form for the reflection between two media was derived by Névot and Croce[98]. This allows the RMS roughness to be extracted from reflectivity data [99], by modeling the decay of reflectivity curves.

The effect of this form of roughness on the specular scatter is that the intensity decreases at a rate faster than the usual  $\theta^{-4}$  decrease obtained for a perfectly flat interface, as some intensity is reflected off as diffuse scatter rather than being reflected as specular scatter as shown in figure 3.10.

In the second case of a graded interface, as depicted in figure 3.9 (b), the idea of modeling the roughness profile using a gaussian distribution of flat surfaces is replaced by modeling the grading profile with an error function, with the width of the error function defining the roughness at the interface.

$$f(z) = \text{erf} \left( \frac{z}{\sigma_g \sqrt{2}} \right). \quad (3.44)$$

where  $\sigma$  is the width of the graded region. By following the derivation in the book by Als-Nielsen and Des McMorrow[66], it is possible to then show that the reflected intensity for a graded interface is the absolute square of the Fourier transform of the normalised gradient of the density across the interface. The derivative of an error function is a gaussian, and the fourier transform of a gaussian is another gaussian. This allows the intensity for the reflectivity to be written,

$$R(\mathbf{Q}) = F_{n-1,n}(\mathbf{Q}) \exp -\mathbf{Q}^2 \sigma_g^2. \quad (3.45)$$

This increases the rate of die off for the specular reflectivity in the same way as for distinct structural boundaries. It should be noted that this has the identical form to equation 3.43. However, there is one important difference. Unlike before the reduced intensity is not reflected off as diffuse scatter. Instead, destructive interference builds

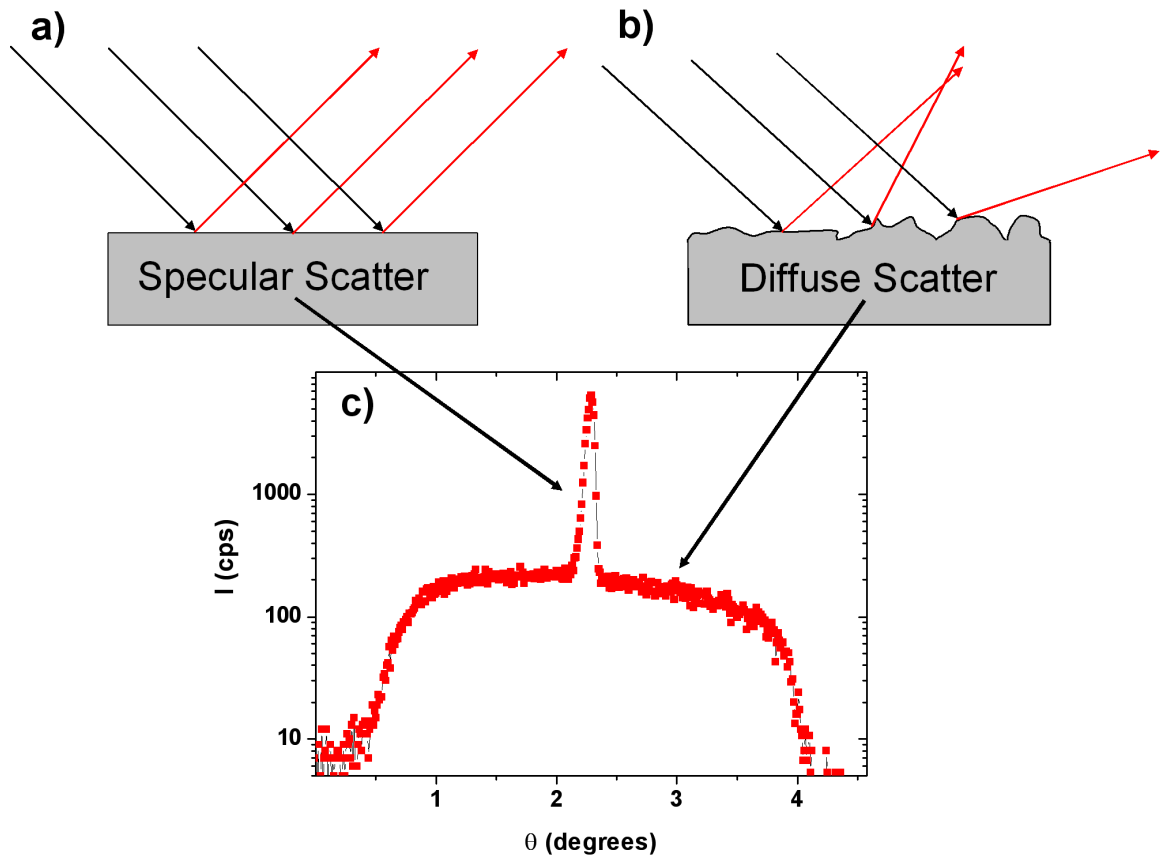


Figure 3.10: a) Pure specular scattering from a perfectly flat surface. b) Diffuse scatter from a rough surface. c) A rocking curve showing some basic specular and diffuse scattering features.

up over the graded region leading to a reduction in specular scatter. As such, specular scatter cannot tell the difference between a distinct boundary between two atomic species and grading[97, 100]. This is shown in figure 3.11 for 150 Å of Co. These curves were simulated using the Bede REFS software package working within the Born Approximation. It can clearly be seen that there is no difference in the rates of the die off for the same amounts of grading and structural roughness. As a result of this, specular scattering allows the determination for the interface width, this being the sum of the structural roughness  $\sigma$  and grading  $\sigma_g$  in quadrature [97].

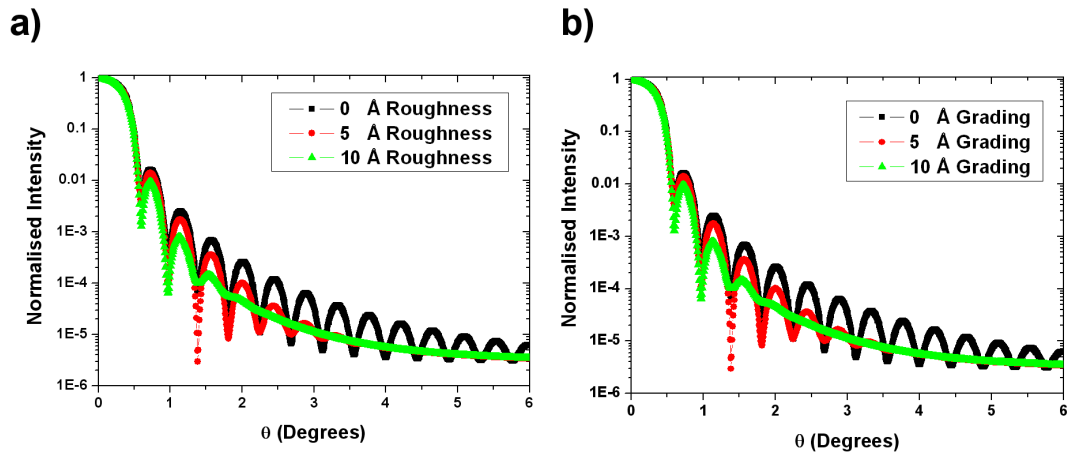


Figure 3.11: BA simulations for a 150 Å Co layer a) Varying roughness with no grading. b) Varying grading but with 5 Å of structural roughness to produce some diffuse scatter to aid otherwise only delta functions would be visible.

### 3.3.4 Diffuse Scatter

It has been shown earlier that the RMS roughness of the interfaces can be determined. However any grading present cannot be distinguished from the RMS roughness, although in order to estimate the grading, diffuse scattering (offspecular scattering) needs to be performed. Diffuse scatter comes from any structural deviations in the structure leading to a reduction in specular scatter and an increase in diffuse scatter which is show in figure 3.10 b). Grading does not contribute to the diffuse scatter as any diffuse scatter due to grading is removed due to destructive interference. Diffuse scatter also allows lateral correlation function of the rough surface or interface to be probed.

In 1988 Sinha *et al.* [19] produced a theory for scattering from smooth and rough interfaces. He initially makes the assumption that the scattering can be thought of as weakly interacting and therefore the Born approximation can be used.

### Born Wave Approximation

Following Sinha *et al.*, the Born Approximation (BA)[90] assumes that there is an incident and out going plane wave with all interactions being weak. This is within the kinematical scattering model so any dispersion or multiple scattering events in the system are ignored. For small angle scattering this approximation is valid if

$\mathbf{Q}a \ll 1$ , where  $\mathbf{Q}$  is the reciprocal space vector and  $a$  is the typical length scale for any roughness in the solid. Allowing the differential cross section to be written,

$$\frac{d\sigma}{d\Omega} = N^2 b^2 \int_V d\mathbf{r} \int_V d\mathbf{r}' e^{-i\mathbf{Q} \cdot (\mathbf{r} - \mathbf{r}')}, \quad (3.46)$$

where  $b$  is the characteristic scattering length, (Thompson scattering length for electrons) and  $N$  is the number density of scattering particles. The integrals are over the volume of the solid and  $\mathbf{Q}$  is given by equation 3.20.

He then goes on to describe a rough surface using the type of self affine fractal surfaces described by Mandelbrot[101] that show great similarities to real surfaces. He starts by defining a surface  $S_0$  in the  $(x,y)$  plane with  $z(x,y)$  being a single valued height above the surface at the coordinates  $(x,y)$ . He then makes the assumption that the distribution of heights above the plane  $S_0$ ,  $[z(x',y') - z(x,y)]$  is a gaussian random variable whose distribution depends on the relative coordinates  $(X,Y) \equiv (x' - x, y' - y)$ . Then by taking an average over all the pairs of points on the surface whose  $(x,y)$  coordinates are separated by  $(X,Y)$  it can be stated that,

$$\langle [z(x', y') - z(x, y)]^2 \rangle = g(X, Y). \quad (3.47)$$

This is the difference in height between two points a distance  $R$  apart. For many isotropic solid surfaces we may represent  $g(X,Y)$  as,

$$g(X, Y) = g(R) = AR^{2h} \quad (0 < h < 1), \quad (3.48)$$

where  $R \equiv \sqrt{(X^2 + Y^2)}$  and  $h$  is a constant between 0 and 1 describing the texture of the roughness. A large value of  $h$  would look like smooth hills, while small  $h$  is equivalent to very jagged ground[19]. The  $h$  parameter is also known as the fractal exponent or Hurst parameter and is related to the fractal component. The problem with this method is that it uses an ideal case of a fractal surface and the function  $g(R)$  will diverge at infinity. To get around this, a roughness cutoff has to be introduced known as the correlation length  $\xi$ . The correlation length corresponds to a length scale on the surface where the correlation function between the two points is reduced to a value of  $1/e$  [102], giving an estimate of the probability of finding another point of height  $z$  within a distance  $x$  at any position on the sample surface, leading to,

$$g(R) = 2\sigma[1 - e^{-(R/\xi)^{2h}}], \quad (3.49)$$

where  $\sigma$  is the RMS roughness. Now as  $R(X,Y)$  goes to infinity, the relative height difference between two points goes to a maximum of  $2\sigma$ . This has for  $R \ll \xi$  the same form as equation 3.48. This allows equation 3.46 to be rewritten using Stokes theorem for an area of a surface  $(L_x, L_y)$  as,

$$\frac{d\sigma}{d\Omega} = \frac{N^2 b^2}{\mathbf{Q}_z^2} L_x L_y \int \int_{S_0} dX dY e^{-\mathbf{Q}_z^2 g(X,Y)/2} e^{-i(\mathbf{Q}_x X + \mathbf{Q}_y Y)}. \quad (3.50)$$

Sinha then defines the more useable height to height correlation function  $C(X,Y)$  rather than the height difference function  $g(X,Y)$ ,

$$C(X,Y) = \sigma^2 e^{-(R/\xi)^{2h}}, \quad (3.51)$$

using this equation 3.50 becomes,

$$S(\mathbf{Q}) = \frac{1}{\mathbf{Q}_z^2} e^{-\mathbf{Q}_z^2 \sigma^2} \int \int_{S_0} dX dY e^{\mathbf{Q}_z^2 C(X,Y)} e^{-i(\mathbf{Q}_x X + \mathbf{Q}_y Y)}, \quad (3.52)$$

where  $S(\mathbf{Q})$  is the reflectivity defined by the (cross section per unit surface area)/( $N^2 b^2$ ), and  $N$  is the number density of the electron and  $b$  the Thompson scattering length. Equation 3.52 can then be split into a specular  $S_{Spec}$  and a diffuse  $S_{Diff}$  part: The specular part is written as

$$S_{Spec}(\mathbf{Q}) = \frac{4\pi^2}{Q_z^2} e^{-\mathbf{Q}_z^2 \sigma^2} \delta(\mathbf{Q}_x) \delta(\mathbf{Q}_y), \quad (3.53)$$

where  $\delta(\mathbf{Q}_x)$  and  $\delta(\mathbf{Q}_y)$  are delta functions containing the conditions for specular reflection also see reference [66] for more on this. The diffuse part is given by

$$S_{Diff}(\mathbf{Q}) = \frac{2\pi^2}{\mathbf{Q}_z^2} e^{-\mathbf{Q}_z^2 \sigma^2} \int_0^\infty R \left[ \exp(\mathbf{Q}_z^2 \sigma^2 e^{-(R/\xi)^{2h}}) - 1 \right] J_0(\mathbf{Q}_{x,y} R) dR, \quad (3.54)$$

where  $J_0$  is a Bessel function of the first kind. The diffuse component must generally be evaluated numerically. The BA breaks down for small values of  $\mathbf{Q}$  near the critical angle. The total scattering is given by the sum of the specular and diffuse components in equations 3.53 and 3.54.

### Distorted Wave Born Approximation

In order to get around the shortcomings of the Born approximation at low  $\mathbf{Q}$ , Sinha *et al.* make use of the Distorted Wave Born Approximation (DWBA). This basically takes the Fresnel solutions for transmitted and reflected waves from a perfectly smooth surface and applies a perturbation representative of the rough surface to them. The full derivation can be found in reference [19] as well as a summary in reference [88]. A brief summary of the results for the DWBA is given here, and the reader is directed to the references for the main results for the specular and diffuse scatter and derivations due to their length. Upon simplification of the main expression for the specular scatter using the DWBA, this gives an expression for the reflectivity as,

$$|\tilde{\mathbf{R}}(\mathbf{k}_1)|^2 = |\mathbf{R}(\mathbf{k}_1)|^2 e^{-\mathbf{Q}_z \mathbf{Q}_z^t \sigma^2}, \quad (3.55)$$

where  $\mathbf{Q}_z^t$  is the wavevector transfer for the transmitted wave. This matches the BA equation in its regime of validity but overestimates the reflectivity at high angles where the BA comes into play. Another consequence of using the DWBA is that it correctly reproduces critical angle phenomena such as the critical edge and Yoneda wings, which are seen at large values of  $\mathbf{Q}_x$ .

#### 3.3.5 The Effect of Roughness on Diffuse Scattering

The results of increasing roughness on diffuse scatter are briefly outlined here. Due to conservation of energy, any decrease in specular scattering must lead to an equal increase in diffuse scattering.

This is shown in figure 3.12 panel (a) where the structural roughness  $\sigma$  is increased from 0 Å to 10 Å and as a result the amount of diffuse scatter increases. The two features on either side are Yoneda wings and the asymmetry in the intensity is due to the lack of a footprint correction.

When this is done for grading the reverse is true as grading does not deflect any scatter into the diffuse, the effect is to reduce the overall intensity so that a large grading reduces the diffuse scatter rather than increasing it. However the overall line shape of the features is not effected. These simulations were run using the BEDE REFS software as mentioned earlier.



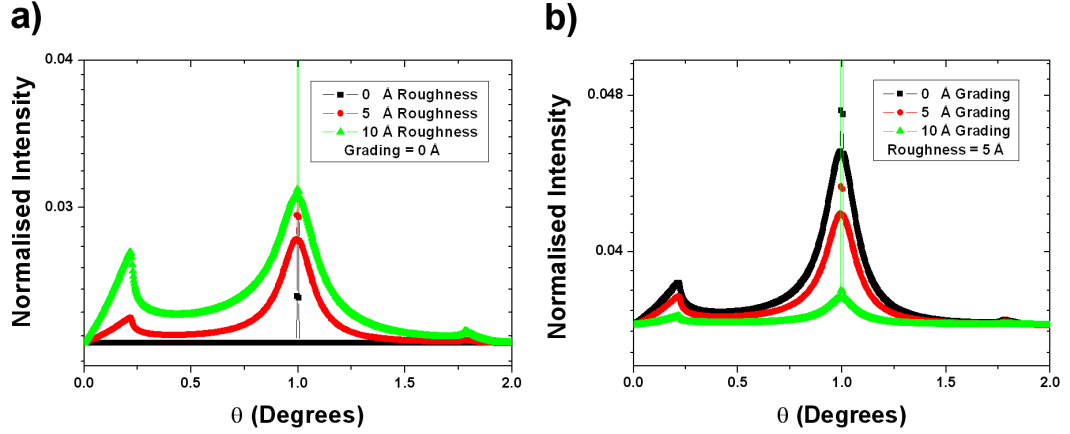


Figure 3.12: DWBA simulations for a Si substrate: a) Varying roughness. b) Varying grading.

Savage *et al.* [94] developed a method of obtaining estimates for the RMS roughness from diffuse scattering without resorting to fitting. He derives the following equation relating the integrated diffuse intensity to the integrated specular intensity.

$$\frac{I_{Diff}}{I_{Spec} + I_{Diffuse}} = \exp(\mathbf{Q}_z^2 \sigma_c^2) - 1. \quad (3.56)$$

However, Savage *et al.* shows this method gives an underestimation of the actual total roughness.

### 3.3.6 Correlations

Multilayered structures have a further complication in that the various interfaces may or may not have the same roughness profile through the multilayer stack in the  $z$  direction, as shown in figure 3.13. Panel (a) of figure 3.13 shows perfectly correlated interfaces which would only produce specular scatter, while panels b) and c) show perfectly correlated and uncorrelated interfaces respectively. What is expected in a real system is some mixture of the two cases shown in panels (b) and (c).

The model by Sinha *et al.* has been extended to multilayer structures by Holý *et al.* and Pape *et al.* [100, 103]. Following the paper by Pape *et al.* an out-of-plane correlation length  $\xi_v$  is characterized in a similar way to the in-plane correlation length. In this case the out-of-plane correlation is modeled by a covariance function between two interfaces and the out-of-plane correlation length is defined as when this

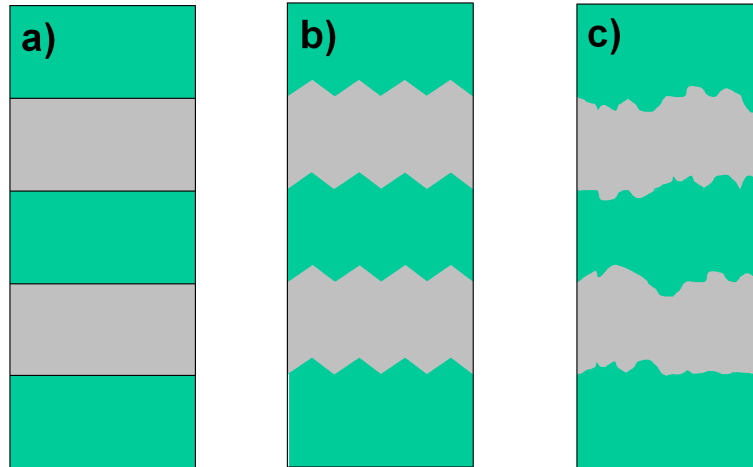


Figure 3.13: a) Perfectly correlated perfectly flat interfaces. b) Perfectly correlated rough interfaces. c) Totally uncorrelated rough interfaces.

function has reduced by a factor of  $1/e$ . In this model no correlations are present in the case  $\xi_v = 0$  and nearly perfect correlation exists when  $\xi_v$  is much larger than the thickness of the multilayer.

The degree of correlation between interfaces results in a change in the width of features like Bragg peaks, where for long vertical correlation lengths Bragg sheets are produced in the diffuse scatter[103]. This is also seen experimentally by Holý and Pape[100, 103]. For no vertical correlations this diffuse scatter is spread out uniformly about the specular ridge, with it gradually falling off in intensity as a function of  $\mathbf{Q}_x$ .

The vertical correlation length can be estimated from the full width at half maximum (FWHM) of the Bragg peak using  $\xi_v = 2\pi/\text{FWHM}$  in the  $\mathbf{Q}_z$  direction. Examples of the use of this can be found in the following references [102, 104].

Estimates for the correlated and uncorrelated roughness can then be obtained using the method outlined in section 3.3.5 of Savage *et al.* by taking rocking scans on a Bragg peak and one off a Bragg peak respectively providing there is a reasonable amount of vertical correlation.

### 3.4 Magnetic X-ray Scattering

Magnetic scattering is a magneto optical effect and has many parallels with the MOKE effect described in chapter 1. Magnetic x-ray scattering is much smaller than Thomson

x-ray scattering by  $\approx 10^{-6}$  orders of magnitude[105]. The first observation of non-resonant magnetic scattering was from antiferromagnetic NiO in 1972 by de Bergevin and Brunel [106] using x-rays from a Cu x-ray tube. They observed a Bragg peak at a position in reciprocal space forbidden for a ferromagnetically ordered structure.

The first resonant scattering from a ferromagnet was observed in 1985 from Nickel by Namikawa *et al.*[107]. The first resonant scattering with a 50 fold increase in the magnetic scattering was observed in 1988 at the  $L_{III}$  edge in Holmium by Gibbs *et al.*[24] following predications of magnetic enhancement at M and L edges by Hannon *et al.*[108] for linearly polarised light. The reader is directed to the review article by Lander [21] and Vettier[109] for an overview of the science that can be conducted using resonant magnetic scattering.

### 3.4.1 Magnetic Enhancement

In order to improve the weak scattering of x-rays by magnetism it is necessary to use resonant scattering near an absorption edge thus allowing magnetic phenomena to be probed. When this is used in conjunction with polarisation analysis it becomes a powerful tool for investigating magnetism. In the case of this thesis only circularly polarised light was used so the reader is referred elsewhere for a discussion of linear polarisation analysis[110] with only the magnetic enhancement being discussed here. The scattering amplitude of an atom can be written as,

$$f(\mathbf{Q}, \hbar\omega) = f(\mathbf{Q}) + f'(\hbar\omega, \mathbf{Q}) + f''(\hbar\omega, \mathbf{Q}) \quad (3.57)$$

where  $f'$  and  $f''$  are the resonant scattering terms (also called the anomalous scattering terms)[66]. Quantum mechanically electrons occupy discrete energy levels. Electrons in the K shell are tightly bound. Hence if an incident x-ray photon has energy much less than the binding energy of the K shell, the response of the bound electrons to the externally driving field of the x-ray is small, therefore the scattering intensity can be said to be reduced by an amount denoted  $f'$ . For energies much greater than the binding energy, the electrons behave as if they are free electrons and consequentially  $f'$  is zero. But for energies in the range around the binding energy,

resonant behavior is observed where an enhancement to the scattered intensity is obtained at the absorption edge. The absorption edge energy is specific to the element involved and this effect is the basis of resonant x-ray scattering. As well as altering the real part of the scattering length, we expect by analogy with a damped harmonic oscillator, the response of the electron to have a phase lag with respect to the driving field. This dissipation in the system is represented by another modifier denoted  $f''$ , which is imaginary and related to the absorption cross section. The Thomson term  $f(\mathbf{Q})$  does not depend on the photon energy, only  $\mathbf{Q}$ .

Resonant scattering is elastic, and quantum mechanically this can be seen as an electron being excited to a higher energy level and then decaying back to its initial state via the emission of a photon as shown in figure 3.14 (b).

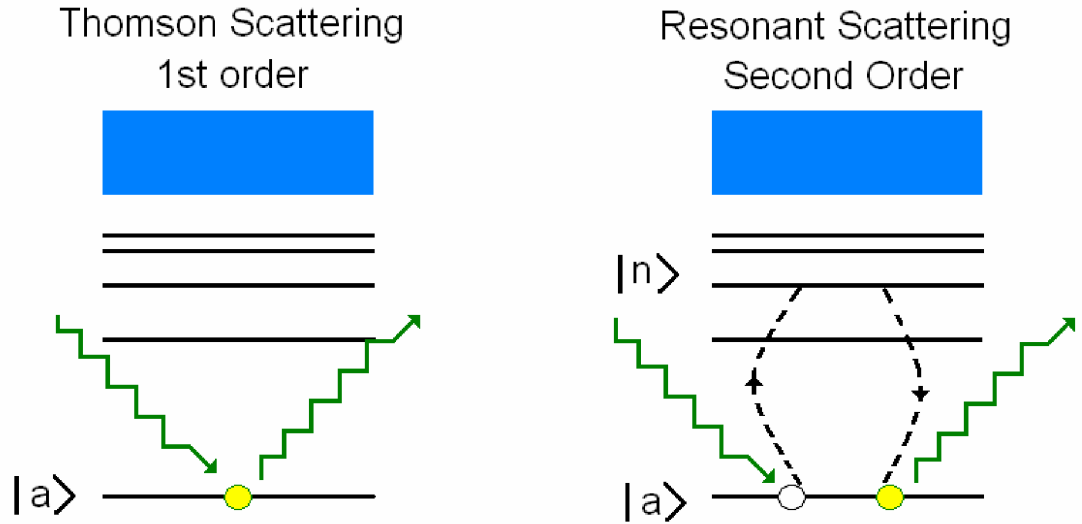


Figure 3.14: a)Thompson Scattering b) Resonant Scattering. Figure from book by J Als-Nielsen and Des McMorow [66].

Second order perturbation theory is required to explain this, The transition probability  $W$  of the scattering event occurring is

$$W = \frac{2\pi}{\hbar} \left| \langle f | H_I | i \rangle + \sum_{n=1}^{\infty} \frac{\langle f | H_I | n \rangle \langle n | H_I | i \rangle}{E_i - E_n} \right|^2 \rho(\varepsilon_f) \quad (3.58)$$

where  $|i\rangle$  and  $|f\rangle$  are the initial and final states,  $E_i$  and  $E_n$  are the incident photon and intermediate state energies respectively.  $E_i = \hbar\omega + E_a$  where  $E_a$  is the ground state energy.  $H_I$  is the Hamiltonian describing the interaction of the photon and the

electron. The interaction Hamiltonian allows scattering by the use of an intermediate state. A photon is absorbed exciting an electron to an intermediate state and then decays back down emitting a photon of the same energy in the process. The resonant behavior arises when the incident energy is close to that of the intermediate state as the second term in equation 3.58 then takes on a large value compared to the first term producing the resonant scattering. This method was put forward in a paper by Hannon *et al.* [108] in 1988 and has widely been accepted as an explanation for resonant scattering in terms of electric dipole (E1) and quadrupole (E2) transitions to intermediate states in the  $d$  and  $f$  shells. The transitions to the intermediate states have two controlling factors. The Pauli exclusion principle specifies that only unoccupied states are accessible and the usual quantum mechanical selection rules apply. The second factor results in an “exchange interaction” sensitive to the magnetisation of the  $f$  and  $d$  bands, as it is the spin-orbit interactions that split these intermediate states.

The energy regime below 2 keV corresponds to the soft x-ray regime where the E1 dipole transitions are from the  $p_{3/2(1/2)} \rightarrow d_{5/2(3/2)}$  states. This involves a transition of  $\Delta l = \pm 1$  where  $l$  is the orbital quantum number. Some of the early experiments on transition metal L edges were done using reflectivity by MacKay *et al.* [111] and Kao *et al.* [112] on the Co and Fe edges respectively. One of the first experiments on a magnetically coupled multilayers was by Tonnerre *et al.* [113]. It should be noted that resonant magnetic scattering comes from dipole transitions, not any interaction between the electrons in a sample and the magnetic part of the wave in question.

This work concentrates on the L absorption edges of Ni, Fe and Co. The energy values for these edges are listed in table 3.1.

Element	L <sub>II</sub>	L <sub>III</sub>
Ni	870.0 eV	852.7 eV
Fe	719.9 eV	706.8 eV
Co	793.2 eV	778.1 eV

Table 3.1: Transition metal elements’ absorption edges.

For clarification on this the reader is referred to the appendixes of the book by Jens

Als-Nielsen and Des McMorrow [66]. For more information on resonant scattering and possible uses see the book by Lovesey and Collins [114] as well as the paper by G. Y. Guo for an itinerant electron version of magnetic x-ray scattering effects[115].

### 3.4.2 X-ray Magnetic Circular Dichroism

Resonant magnetic scattering is essentially an absorption process and as such magnetic dichroism occurs due to any magnetism in the system in question. X-ray Magnetic Circular Dichroism (XMCD) is a preferential absorption of one circular polarisation state over the other and is very closely linked to magnetic scattering via the optical theorem[66]. This states that the absorption cross-section is related to the imaginary part of the atomic scattering length  $f''$  in the forward direction. The flip side of this is that for absorption there must be an imaginary part to the scattering length, hence scattering and absorption are one and the same, and rely on the same physics. The Kramers-Kronig relations can be used to show that there is also a real part to the scattering length as a result of this, implying the existence of resonant scattering about absorption edges. This section closely follows the explanation given in the books by Jens Als-Nielsen and Des McMorrow [66] and Lovesey and Collins[114].

XMCD was predicted in 1975 by Erskine *et al.* [116] for circularly polarised light at the  $M_{2,3}$  absorption edges of ferromagnetic Ni. In 1987 the first experimental proof was observed at the Iron K edge by Schütz *et al.* [117]. This technique is also element specific as the dichroism is strongest around absorption edges. XMCD has the ability to determine the element-specific spin and orbital magnetic moments via the sum rules[118]. Most x-ray absorption experiments are performed by measuring the Total Electron Yield (TEY), in which all the photoelectrons are collected and the photocurrent is proportional to the amount of x-ray absorption.

XMCD arises due to the selection rules for the change in the quantum numbers describing the initial and final states of an electronic transition. In the case of the transition metals, this is an electric dipole (E1) transition as mentioned earlier. Figure 3.15 depicts an ideal XMCD system containing eight electrons, in the form of a simple energy level diagram. An E1 transition requires the principle quantum number  $l$  to

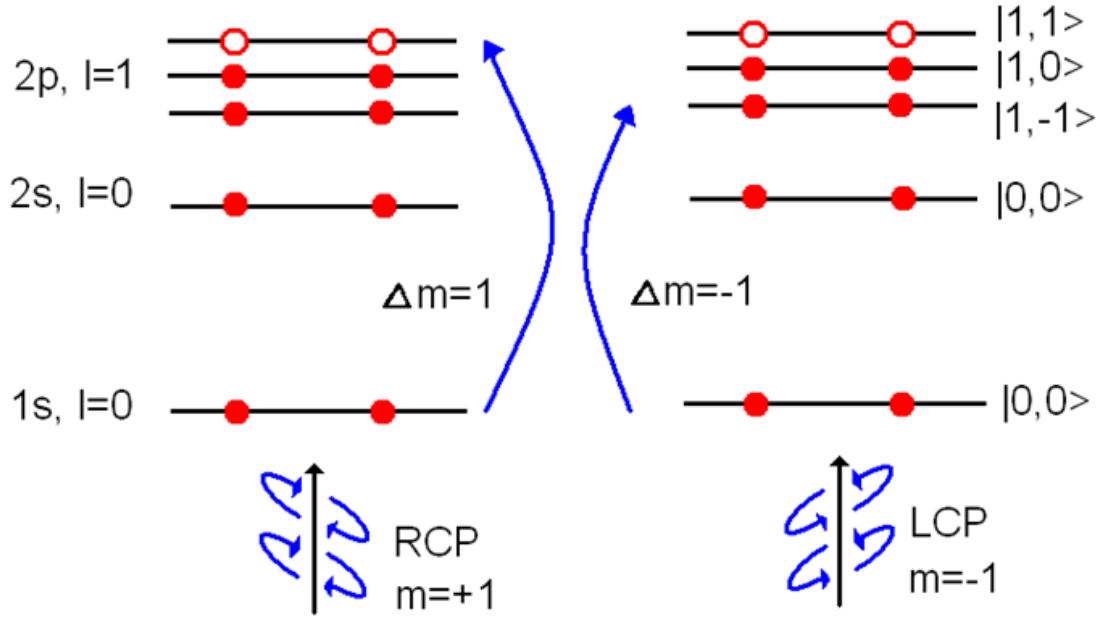


Figure 3.15: X-ray Magnetic Circular Dichroism (XMCD)[66].

change by one, in order to allow a transition ( $\Delta l = \pm 1$ ). This is known as the dipole transition selection rule[66]. The next selection rule is given by the fact that for a transition to happen the incident photon must be absorbed. The incident photon is circularly polarised and upon absorption its angular momentum ( $J_z$ ) must be conserved. For circularly polarised light  $\Delta m = +1$  for right circularly polarised light (RCP), and  $\Delta m = -1$  for left circularly polarised light (LCP). The  $2p$  level contains 4 electrons and two empty states, the degeneracy of this level having been lifted by the Zeeman effect. Assuming no spin-orbit interaction, the only allowed transition is for RCP light to the  $|1,1\rangle$  level since the  $|1,-1\rangle$  level is occupied where  $|l,m\rangle$ . Only RCP photons will be absorbed as this is a perfect dichroism effect. The internal magnetic field serves to split the final level with any applied field defining the overall magnetisation direction[108]. This approach is applicable to soft x-rays due to the energies involved.

It becomes necessary at this point to look in greater detail at the polarisation dependence of the absorption. Following the work by Hannon and Tramell[108] the

scattering amplitude for resonant magnetic scattering, considering only dipole transitions is,

$$f_{E1}^{res} = [(\varepsilon_f \cdot \varepsilon_i)F^{(0)} - i(\varepsilon_f \times \varepsilon_i) \cdot \mathbf{M}F^{(1)} + (\varepsilon_f \cdot \mathbf{M})(\varepsilon_i \cdot \mathbf{M})F^{(2)}], \quad (3.59)$$

where  $\varepsilon_i$  and  $\varepsilon_f$  are the incident and final polarisation vectors,  $M$  is a unit vector in the direction of the magnetic moment and the  $F^{(n)}$  terms are the resonance responses given by,

$$F^{(0)} = \left(\frac{3}{4k}\right) [F_{1,1} + F_{1,-1}], \quad (3.60)$$

$$F^{(1)} = \left(\frac{3}{4k}\right) [F_{1,1} - F_{1,-1}], \quad (3.61)$$

$$F^{(2)} = \left(\frac{3}{4k}\right) [2F_{1,0} - F_{1,1} - F_{1,-1}]. \quad (3.62)$$

$F_{L,M}$  is the resonance response, where  $L$  is the order of the transition ( $L=1$  for Dipole transitions) and  $M$  is the change in angular momentum ( $\Delta M = 0, \pm 1$ ). The reader is again directed to the book of Lovesey and Collins[114] for a theoretical description of the  $F_{L,M}$  terms.

The first term of equation 3.59 contributes to the charge scattering. The second term gives rise to first order magnetic satellites (linear in  $\mathbf{M}$ ) and responsible for circular dichroism, while the third term gives second order satellites as seen in Ho. A description of linear dichroism is not necessary for this report, and it is neglected from now on. It is possible to see from the second term that the absorption is dependent not only on the handedness of the circularly polarised light but also on the direction of the magnetisation  $\mathbf{M}$ .

XMCD reflectivity experiments are usually performed in a geometry similar to that described for longitudinal MOKE in section 1, with the magnetisation in the plane of the sample and parallel or anti-parallel to the scattering plane. In this geometry, switching the direction of the magnetisation via an external applied magnetic field is equivalent to switching the handedness of the circularly polarised light and changing the sign of the second term in equation 3.59. The first case is the mode of operation at the U4B beamline as described in section 2.

However, when trying to study purely magnetic scattering it is often the case that it is located at the same position in reciprocal space as structural scattering. XMCD,



when used in the reflection geometry above, can be used to get around this problem. The scattering factor can be taken to be made up of a charge  $f_c$  and magnetic  $f_m$  term. The advantage of circularly polarised light is it allows the charge and magnetic terms to interfere constructively or destructively.

$$\frac{d\sigma}{d\Omega} = |f|^2 = |f_m + f_c|^2 = f_c^2 + f_m^2 + 2f_cf_m. \quad (3.63)$$

The first term in the last part of equation 3.63 is due to charge scattering and the second is due to the magnetic scattering and is usually dwarfed by the charge scattering. The interference term  $2f_cf_m$  represents charge magnetic interference and is much stronger than the magnetic scattering term. The interference term is sensitive to the magnetisation and can be made to change sign by reversing the applied magnetic field during the measurement such that,

$$I^+ \approx f_c^2 + f_m^2 + 2f_cf_m, \quad (3.64) \quad I^- \approx f_c^2 + f_m^2 - 2f_cf_m, \quad (3.65)$$

$$\text{Sum} = I^+ + I^- \approx 2f_m^2 + 2f_c^2, \quad (3.66) \quad \text{Difference} = I^+ - I^- \approx 4f_m^2 f_c^2. \quad (3.67)$$

By measuring  $I^+$  and  $I^-$  as shown in figure 3.16 and taking the sum and the difference defined in equations 3.66 and 3.67, it is then possible to separate the charge and magnetic scattering from the charge-magnetic interference terms.

More commonly it is the spin asymmetry (SA) ratio that is looked at in order to study the magnetism,

$$SA = \frac{I^+ - I^-}{I^+ + I^-}. \quad (3.68)$$

This has the advantage of removing various factors such as attenuation and detector efficiencies. The reader is referred to the work by Lovesey and Collins for a more rigorous derivation of the above terms[114], as well as the next chapter for a discussion on the interpretation of the above with regard to measuring magnetic roughness.

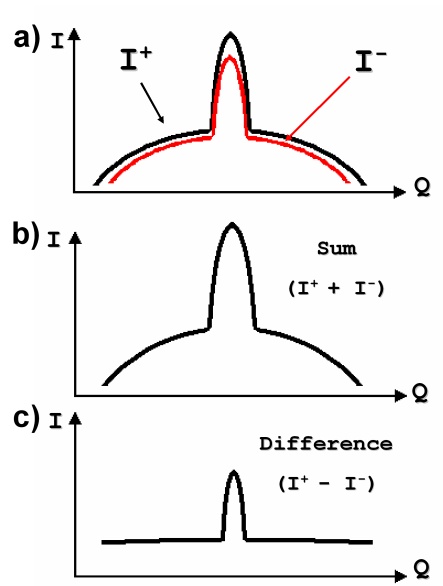


Figure 3.16:  $I^+$  and  $I^-$  are the individual intensities for the positive and negative applied field directions

### 3.5 Summary

This Chapter has covered the basic aspects of the absorption, reflection and scattering that are necessary for the interpretation of the results in this work. The reader is directed to the review article on structural roughness by Sinha [17].

# Chapter 4

## Neutron Scattering

### 4.1 Introduction

Neutrons were discovered by James Chadwick in 1932, and he later went on to win the nobel prize for the discovery in 1935[119]. The use of neutrons as a probe of condensed matter was realised soon after with the 1994 Nobel Prize going to Bertram Brockhouse and Clifford Shull for the development of Neutron spectroscopy and neutron diffraction respectively[120]. Neutron scattering is analogous to x-ray scattering, hence the majority of the scattering theory in Chapter 3 is also applicable to neutron scattering.

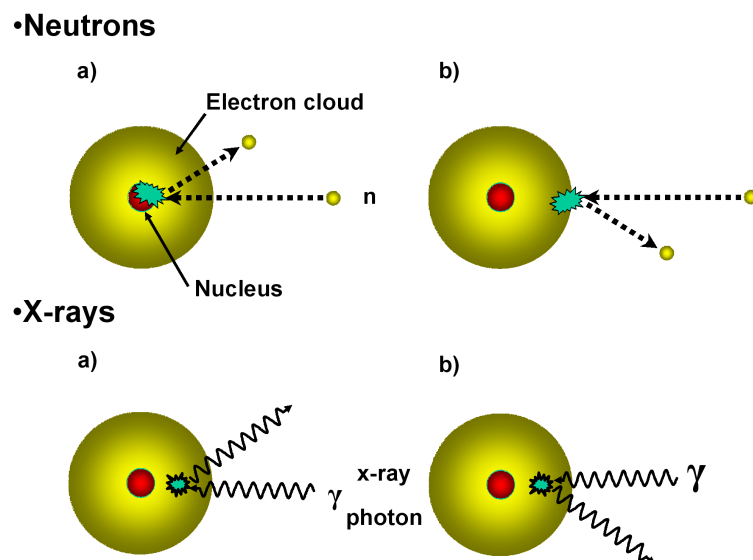


Figure 4.1: The different scattering mechanisms for x-rays and neutrons a) For structural scattering. b) For magnetic scattering.

Absorption happens by a fundamentally different method to x-rays. For a neutron to be absorbed, a nucleus must absorb it leading to a further nuclear reaction within that nucleus. Regarding refraction, the difference between x-rays and neutrons lies in how the terms within the complex refractive index are derived, with the overall results being analogous to x-rays. This is touched upon in the appendices of the book by Jens-Nielsen and McMorrow [66]. As with absorption, scattering of neutrons occurs in a different manner, as shown schematically in figure 4.1.

Neutron reflectometry has several advantages over soft x-ray reflectometry. Firstly, neutrons are more penetrating than soft x-rays, allowing the whole of a multilayer structure to be sampled. Secondly, neutron scattering occurs via the nuclear strong force as the uncharged nature of the neutron means that it can penetrate deeply into matter getting very close to the nuclei, as there is no coulomb barrier to overcome. Thirdly, the fundamental property describing the strength of the interaction between the neutron and the nucleus is the scattering length of the particular neutron-nucleus system in question. The scattering lengths vary irregularly from element to element across the periodic table, hence making low energy neutrons, with their large dependence on the scattering length, ideal tools to distinguish between different elements.

More importantly the magnetic scattering interaction is via the magnetic moment of the neutrons, rather than the indirect spin-photon interaction. It should be noted that lateral coherence length as defined in section 2.2.3 of neutron beams is greater than that of soft x-rays,  $\sim 30\mu\text{m}$  compared to  $\sim 1\mu\text{m}$  obtained from synchrotron x-ray sources. This makes studying magnetic domain structures far more efficient, as several magnetic domains can be sampled at the same time. This, when coupled with polarised neutron scattering, allows detailed study of magnetic materials.

However neutron sources lack the flux produced by synchrotron sources, the result of which being that data collection times are much longer being of the order of several hours per scan and that samples for study by neutrons have to be much larger in order to make use of all available flux  $\approx 25\text{ mm} \times 25\text{ mm}$ . This is an issue when attempting to study nanostructures, as large arrays are difficult to fabricate.

Neutron scattering has been used in this work to complement the x-ray scattering results. For further details the reader is directed to the books “Introduction

to the Theory of Thermal Neutron Scattering” by G. L. Squires[121] and “Neutron Scattering from Magnetic Materials” by Tapan Chatterji [122].

## 4.2 Properties of a Neutron

Neutrons with a de Broglie wavelength of about 1 Å are referred to as thermal neutrons and have an energy in the range  $\sim 5$ -100 meV. The basic properties are summarized in Table 4.1.

Mass	$1.675 \times 10^{-27} \text{ kg}$
Magnetic Dipole moment	$-1.913 \mu_N$
Spin	$1/2$
Gyromagnetic ratio	$8.5161 \times 10^8 \text{ rad s}^{-1} \text{ T}^{-1}$
Charge	0
Nuclear magneton ( $\mu_N$ )	$5.051 \times 10^{-27} \text{ JT}^{-1}$

Table 4.1: Properties of a free neutron

The wavelength of a neutron is related to its kinetic energy and hence its velocity by the de Broglie relation,

$$\lambda = \frac{h}{mv}, \quad (4.1)$$

where  $m$  is the mass of the neutron and  $v$  its velocity. The energy of thermal neutrons is simply the non-relativistic kinetic energy,

$$E = \frac{mv^2}{2}. \quad (4.2)$$

Upon combination the relation between energy and wavelength and the temperature of the neutron is obtainable,

$$E = k_B T = \frac{1}{2}mv^2 = \frac{h^2}{2m\lambda^2} = \frac{\hbar^2 k^2}{2m} = \hbar v. \quad (4.3)$$

## 4.3 Neutron Scattering

The interaction between an incident neutron and an atom is mediated by the strong force. The scattering potential of the nucleus can be approximated by using a Fermi

pseudo-potential,  $V(r)$ :

$$V(\mathbf{r}) = \frac{2\pi\hbar}{m} b_j \delta(\mathbf{r} - \mathbf{r}_j), \quad (4.4)$$

where  $m$  is the mass of the neutron,  $b_j$  is the scattering length of a nucleus labeled  $j$  located at position  $\mathbf{r}_j$ . Then in an analogous way to x-rays, the atomic scattering factor can be defined as:

$$f_n(\mathbf{q}) = \frac{m}{2\pi\hbar^2} \left[ \int_V V(\mathbf{r}) \exp[2\pi i(\mathbf{q} \cdot \mathbf{r})] dV \right]. \quad (4.5)$$

Then, by assuming that the fermi pseudo potential is zero outside a radius,  $r_0$ , and a constant,  $a$ , within it then:  $0 < a < r_0$  the integral in equation 4.5 can be carried out. The wavelength of a thermal neutron is about  $\approx 1 \text{ \AA}$  while the average nucleus has a radius of about 1 fm to 7 fm. The large size of the wavelength of the neutron with respect to the size of the nuclei allows the scattering to be considered to be point like in nature. Then, with  $r_0 \mathbf{q} \ll 1$ , the atomic scattering factor for neutrons can be written:

$$f_n = \frac{m}{2\pi\hbar^2} a \left( \frac{4}{3} \pi r_0^3 \right), \quad (4.6)$$

where  $f_n$  is a constant, usually denoted as,  $b$ , the nuclear scattering length. From this the scattering cross section for neutrons can be written as,

$$\frac{d\sigma}{d\Omega} = b^2, \quad (4.7)$$

this is very similar to that derived for x-ray scattering, only there is now no energy dependence. At this point Fermi's golden rule for scattering has to be modified by introducing a scattering amplitude operator,  $a(\mathbf{q})$ :

$$\langle \mathbf{k}_1, \sigma_1 | a | \mathbf{k}_0, \sigma_0 \rangle = \langle \sigma_1 | a_{\mathbf{q}} | \sigma_0 \rangle = \frac{m}{2\pi\hbar^2} \langle \mathbf{k}_1, \sigma_1 | V(\mathbf{r}) | \mathbf{k}_0, \sigma_0 \rangle, \quad (4.8)$$

Now the final and initial states are defined in terms of their wavevector and spin. The main point to note is that as the scattering depends on the form of the nucleus in question, as all the different elements have different scattering factors. This accounts

for why there is a large difference between the scattering powers for x-rays and neutrons. For x-rays, the scattering is proportional to the atomic number of the element  $Z$ , while the scattering amplitude  $b$ , shows no systematic variation with  $Z$ .

The scattering in Bragg reflections then arises from the average scattering length also called the coherent scattering length. There is also an incoherent scattering length due to disorder in the scattering length densities, resulting from, different isotopes of the atom in question. However this is somewhat beyond the scope of this work and is ignored for simplicity from now on.

An expression similar to equation 3.27 can then be written down for neutrons,

$$F^{crystal}(\mathbf{Q}) = \sum_j b_j(\mathbf{Q}) \exp(2\pi i \mathbf{Q} \cdot \mathbf{r}_j) \sum_{R_n} \exp(2\pi i \mathbf{Q} \cdot \mathbf{R}_n), \quad (4.9)$$

where  $\mathbf{R}_n$  is a vector to any lattice point in the real lattice as defined in section 3.

## 4.4 Neutron Reflectometry

Following the general explanation given in reference [78] for both nuclear and magnetic neutron scattering, in the case of neutron reflectometry the incident neutron interacts with a potential  $V_0$  given as,

$$V_0 = \frac{2\pi\hbar^2}{m}Nb, \quad (4.10)$$

where  $N$  is the density of atoms in the material and  $b$  the scattering length as defined above. The quantity  $Nb$  is referred to as the Scattering Length Density (SLD). In the case of a perfectly flat semi infinite slab, then it is only the component of the incoming wavevector  $k$  and the kinetic energy  $E_{i\perp}$  normal to the surface that see the potential barrier of the surface,

$$E_{i\perp} = \left( \frac{(\hbar k_i \sin \theta_i)^2}{2m} \right). \quad (4.11)$$

If the  $E_{i\perp} < V_0$  then the neutron is totally externally reflected so the critical angle  $Q_c$  is given when  $E_{i\perp} = V_0$ ,

$$Q_c = \sqrt{16\pi Nb} \quad \text{with} \quad Q_c = \frac{4\pi}{\lambda} \sin \theta_c. \quad (4.12)$$

For  $E_{i\perp} > V_0$  then the neutrons can be either reflected or transmitted. This is governed by the Fresnel equations as derived in section 3.

$$R \approx \frac{16\pi^2}{Q^4}(Nb)^2. \quad (4.13)$$

At this point there has been little difference in the results between neutrons and x-rays upon reflection, with Kiessig fringes coming from the substrate and surface reflections interference, and Bragg reflections arising from any periodicities in the sample. The main difference between neutron and x-ray scattering so far is the non uniform variation of the scattering length  $b$  as described above. Another significant difference is when magnetic scattering is taken into account.

## 4.5 Magnetic Neutron Reflectivity

The neutron magnetic moment interacts with the internal magnetic field of the magnetic atom. For a full derivation of magnetic scattering for a single magnetic atom the reader is directed to the book by Squires[121]. The main points for magnetic scattering from a crystal are summarised here.

The total scattering from a magnetic sample is proportional to the sum of the nuclear and magnetic scattering lengths,

$$b_{total} = b_{nuclear} + b_{mag}. \quad (4.14)$$

If an incident neutron enters a material it experiences a potential  $V_0$ , and if the material is magnetic then there is an extra potential  $V_{mag}$

$$V_{mag} = -\mu \cdot \mathbf{B}. \quad (4.15)$$

where  $\mu$  is the magnetic moment of the neutron and  $\mathbf{B}$  is given by,

$$\mathbf{B} = \mathbf{B}_0 + \mu_0 \mathbf{M}, \quad (4.16)$$

where  $\mu_0$  is the permeability of free space and  $\mathbf{M}$  is the magnetisation vector.  $\mathbf{B}_0 = \mu_0 H_0$  is identical inside and outside the sample and does not contribute to the scattering, serving only to define the magnetisation direction. If the incoming neutron is polarised up or down with respect to the magnetisation then the magnetic potential



changes sign and subsequently the total scattering length is different for spin up and spin down neutrons, this forms the basis for polarised neutron reflectometry.

$$V_{\pm} = V_{nuclear} \pm V_{mag} = \frac{2\pi\hbar^2}{m}N(b_{nuclear} \pm b_{mag}), \quad (4.17)$$

The total scattering length now has a neutron polarisation dependence. It should be noted that the polarisation of the neutron beam is defined so that the plus sign (spin up neutron state) corresponds to a beam of neutrons polarised by a polariser with its magnetisation in the same direction as the sample magnetisation.

## 4.6 Polarisation Analysis

In order to get the most sensitivity to magnetism in the sample the incident neutron beam can be polarised. Moon *et al.* [123] produced four equations that can be used in a simplified version of polarisation analysis. Taking a setup like that described for the CRISP or ADAM beamlines in chapter 3, shown schematically in figure 4.2, there is an incident polarised neutron beam, spin flippers before and after the sample position and an analyser. The neutron polarisation state is maintained between system elements by a weak guide field ( $\approx 20Oe$ ).

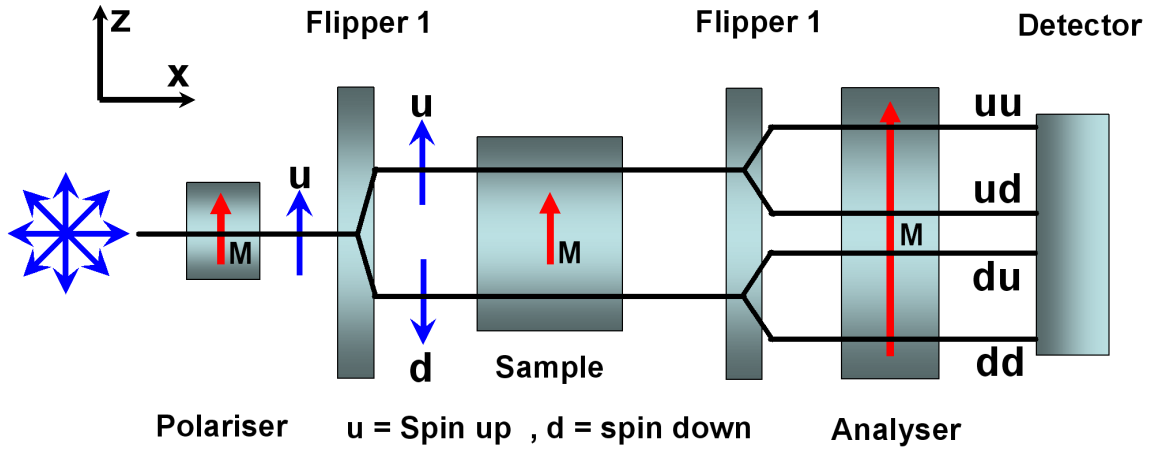


Figure 4.2: Schematic of a polarised neutron experiment. Allows the measurement of the spin up (**u**) and spin down (**d**) states. The magnetisation of the sample lies in the plane of the sample in the  $z$  direction and defines the spin up neutron polarisation. Diagram taken from reference [78].

The polariser and analyser can be considered to only reflect spin up state (**u**) neutrons. There are two spin flippers before and after the sample, and with first flipper

inactive the **u** state is incident on the sample. Only neutrons that are scattered by the sample without undergoing a spin flip will be reflected by the analyser. It should be noted that none of these flipping and polarising processes are perfect. However the efficiencies are well known and can be corrected. So with both flippers inactive the detector measures the **uu** state. Turning the first flipper on changes the state of the incident beam at the sample to the spin down state (**d**), but the analyser only reflects the **u** state so the **du** is measured. Vice versa is true when the first flipper is turned off and the second flipper is turned on allowing the **ud** to be measured. Then subsequently with both flippers on the **dd** is obtained. The nomenclature then becomes to refer to Non Spin Flip (NSF) for the **uu** and **dd** states and Spin Flip (SF) for the **ud** and **du** states.

Moon *et al.* then make the simplifying assumption that it is only the component of the final polarisation still in the direction of the initial polarisation direction that is measured. They then define four scattering amplitudes **uu**, **dd**, **ud**, **du** corresponding to the initial and final states defined by the neutron polarisation, given below in a simplified form taken from reference [78],

$$\mathbf{U}^{uu} = N + M_{\perp,z}, \quad (4.18)$$

$$\mathbf{U}^{dd} = N - M_{\perp,z}, \quad (4.19)$$

$$\mathbf{U}^{ud} = M_{\perp,x} + iM_{\perp,y}, \quad (4.20)$$

$$\mathbf{U}^{du} = M_{\perp,x} - iM_{\perp,y}, \quad (4.21)$$

where  $N$  is the nuclear structure factor,  $z$  refers to the direction of the polarisation and  $M_{\perp}$  is related to the magnetisation and is defined,

$$\mathbf{M}_{\perp} = \mathbf{M} - (\mathbf{M} \cdot \mathbf{k})\mathbf{k} \quad \text{with} \quad \mathbf{M}_{\perp} = \mathbf{M}_{\perp,x} + \mathbf{M}_{\perp,y} + \mathbf{M}_{\perp,z} \quad (4.22)$$

and  $k$  is a unit vector as is clarified in figure 4.3. The reader is directed to the book by Squires [121] and the paper by Moon *et al.* [123] for a full derivation of these

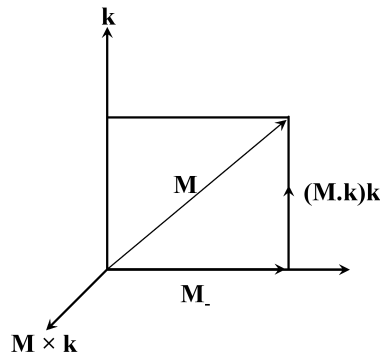


Figure 4.3: Relationship between  $\mathbf{M}$  and  $\mathbf{M}_{\parallel}$

factors and explanation of the terms. It should be noted that only magnetic scattering can cause SF scattering, provided the polarisation vector is along the scattering vector, while coherent nuclear scattering is always NSF scattering, as can be seen from equations 4.18 and 4.19. Hence in the first approximation the NSF scattering is sensitive to any component of the magnetisation which are parallel to the applied field, while the SF scattering is sensitive to the components of the magnetisation which are perpendicular to the applied field.

This provides a clear way of separating magnetic and structural scattering. For further information the basic principles of PNR are outlined in the review articles by Majkrzak [124] and Fitzsimmons [125].

## 4.7 Summary

This section briefly summarised neutron scattering and some of the differences between it and x-ray scattering. Polarisation analysis has been explained with regards to the clear distinction between nuclear and magnetic scattering, as this was the extent to which the technique was used in this work. However it should be noted that it is a huge field.

For an overview of science conducted using neutron reflectometry on magnetic thin films and nano structures, the review articles by Zabel *et al.* [126, 127], Ankner *et al.* [128] and Ott [129] and the book entitled “Handbook of Magnetism and Advanced Magnetic Material: Volume 3” [71] are recommended.

# Chapter 5

## Domain patterning

### 5.1 Introduction

As has been mentioned earlier, x-rays have the advantages of large intensities and energy selectivity, although difficulties in the interpretation of data arise due to the indirect nature of the spin-photon interaction, as compared to neutrons, as has been discussed in chapters 3 and 4. This makes it hard to separate the structural and magnetic contributions; for circularly polarized photons, the difference in scattering for the two opposite helicities of photons has been shown to be related to cross-correlations between structure and magnetism[130, 131], whilst intensity related to purely magnetic correlations is found in the sum signal, where it is usually dwarfed by scattered intensity from the structural correlations.

In this section, the results obtained on a sample designed to have a structurally flat magnetic layer, but which has a modulated magnetic pattern imprinted onto it are described. This demonstrates how with careful sample design it is possible to circumvent the problem of losing the magnetic signal due to it being swamped by the structural signal. In order to do this a magnetic domain pattern was imprinted on a structurally smooth permalloy ( $\text{Py} = \text{Ni}_{80}\text{Fe}_{20}$ ) layer by a Co/Pt multilayer, which exhibits strong perpendicular magnetic anisotropy[132], and hence forms a stripe domain state that generates a strong stray field just above its surface. The Py is separated from the Co/Pt multilayer by a thick Ta layer, ensuring that the only coupling between the layers is magnetostatic as shown in figure 5.1. As shall be seen, the structural roughness in this structure is very low, and thus we have exploited the element specific features of the SXRMS to discern the purely magnetic correlations

in the sum signal.

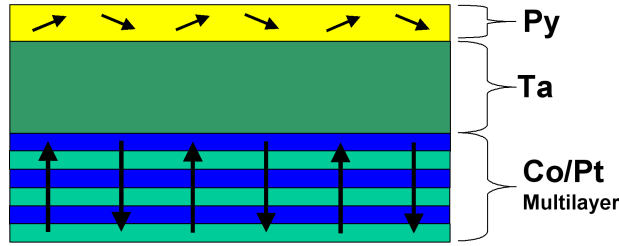


Figure 5.1: Example domain patterning structure using stray fields to imprint a domain pattern onto a structurally flat Permalloy layer.

## 5.2 Magnetic Roughness

At this point a brief introduction to magnetic roughness is appropriate. Unlike structural roughness that is describable by a scalar quantity, magnetization is a vector quantity, and as such can display many different types of magnetic disorder. This disorder can take the form of variations in the height of the magnetic surface, or variations of the orientation and magnitude of the local magnetisation vectors near the interface/surface. This is further complicated by the formation of magnetic domains in the plane of the film giving another form of magnetic disorder. Magnetic disorder can be very broadly separated into two categories by the mechanisms that allow them to take place;

- Magnetic domains
- Magnetic dead layers/Spin mis-tracking at interfaces

A domain structure is a non-uniform distribution of magnetization direction in the sample shown in figure 5.2 a), and will give rise to off-specular scatter even for a structurally flat system. Ferromagnetic and anti-ferromagnetic domains form in the magnetic layers as a way of reducing the energy of the system associated with dipolar fields, and the reader is directed to the references for an in-depth explanation of domain formation[92]. This is further complicated by antiferromagnetic coupling between layers aligning their magnetisations antiparallel to each other as in figure 5.2 b). This leads to magnetic Bragg peaks in the specular scatter at half the  $\mathbf{Q}_z$  of the

structural Bragg peaks. Also, each layer can have its own domain structure which will be correlated with the domain structures above and below it to some degree [133, 134], in a way analogous to how the structural correlations are described in section 3.3.6.

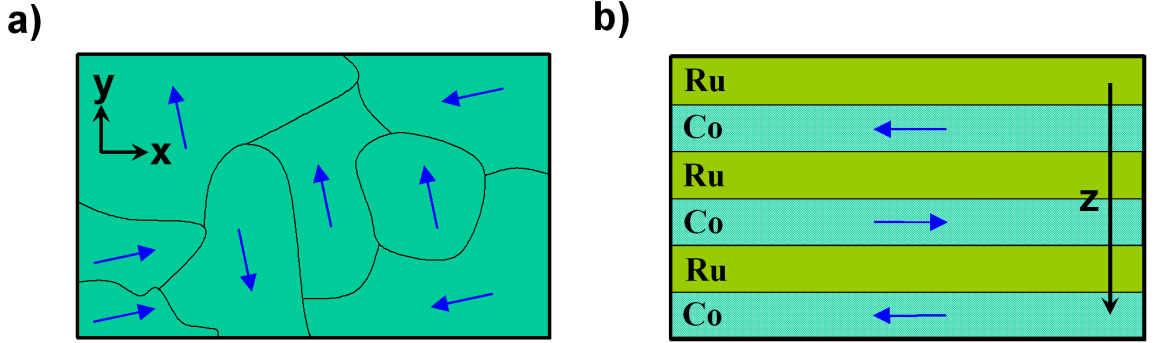


Figure 5.2: a) A nonuniform domain pattern with in-plane magnetisation. b) Structurally perfect interfaces with antiferromagnetic coupling.

In order to interpret measurements of this, some kind of formalism is needed. Langridge *et al.* [135] used the following: the magnetization direction is taken to be constrained within the sample plane to describe the directional differences of magnetic domain structure. Then a correlation function similar to that for structural roughness can be written,

$$M(\mathbf{R}) = \sigma_m^2 \exp(-[R/\xi_m]^{2h_m}) \quad (5.1)$$

where  $\sigma_m$  is the width of the angular distribution and characterizes the magnetic domain disorder.  $\xi_m$  is the lateral correlation length, which gives a measure of the typical domain size and  $h_m$  is the fractal exponent for the magnetic surface. They follow the formalism of Sinha [19] and hence it is possible to obtain two functions for the specular and diffuse scattering,

$$S_{spec}(\mathbf{Q}) = 4\pi^2 D \delta(\mathbf{Q}_{\parallel}) \quad (5.2)$$

$$S_{diff}(\mathbf{Q}) = D \int d^2\mathbf{r} \exp(\mathbf{Q}_{\parallel} \cdot \mathbf{r}) [s + m + sm] \quad (5.3)$$

where  $D$  is a joint Debye-Waller factor and  $\mathbf{Q}_{\parallel}$  is the in-plane component of  $\mathbf{Q}$ . The three terms in the square brackets in equation 5.3 correspond to three diffuse scattering contributions. The first is equivalent to the structural term derived by Sinha [19]. The second corresponds to domain distributions, while the final cross term

deals with the magnetic roughness. This formalism has the advantage of being able to quantify diffuse scatter due to domain distribution in the case of neutron scattering, as the neutron spin-magnetization interaction is explicitly included. However, because x-ray resonant scattering factors are energy dependent, this makes developing a similar formalism for x-ray magnetic scattering difficult. The lack of any clear separation of magnetic and structural scattering, results in any magnetic scattering getting dwarfed out by the structural scattering, making it very hard to observe.

It should be noted at this point that the lateral coherence length of the x-ray beam, as described in section 2.2.3, is important when scattering from magnetic domains. In the case that the coherence length is smaller than the lateral size of the magnetic domains, then the scattering is the incoherent sum of the scattering from the magnetised regions. If there is no net magnetisation then domain scattering can cancel itself out or be reduced to the point that it is not visible in the diffuse scattering. When the average size of the domains is smaller than the lateral coherence length of the beam, then scattering due to magnetic domains can be seen in the diffuse scattering.

The second category of magnetic roughness is harder to envisage, as this deals with magnetic dead layers or spin mis-tracking at interfaces. This is based on the idea that the structural and magnetic boundaries between layers are not commensurate as depicted in figure 5.3.

Work by Lee *et al.* has covered magnetic scattering in the DWBA from a magnetic interface as described above for both specular and diffuse scattering[22, 23] respectively. However, due to the length and complexity of these papers, and as only limited use of the ideas presented in them was made in this work, only a brief description is given here.

The structural roughness at the interface results in the moments near the interface experiencing anisotropy and exchange fields that fluctuate spatially. Hence, the magnetic and structural roughnesses are almost certainly correlated as they are governed by the magnetic energies in the system. Material parameters such as the exchange constant  $A$ , anisotropy  $K$  and saturation moment  $M_S$  will all play a role in determining the magnetic roughness. As a result of this, magnetic roughness will also be

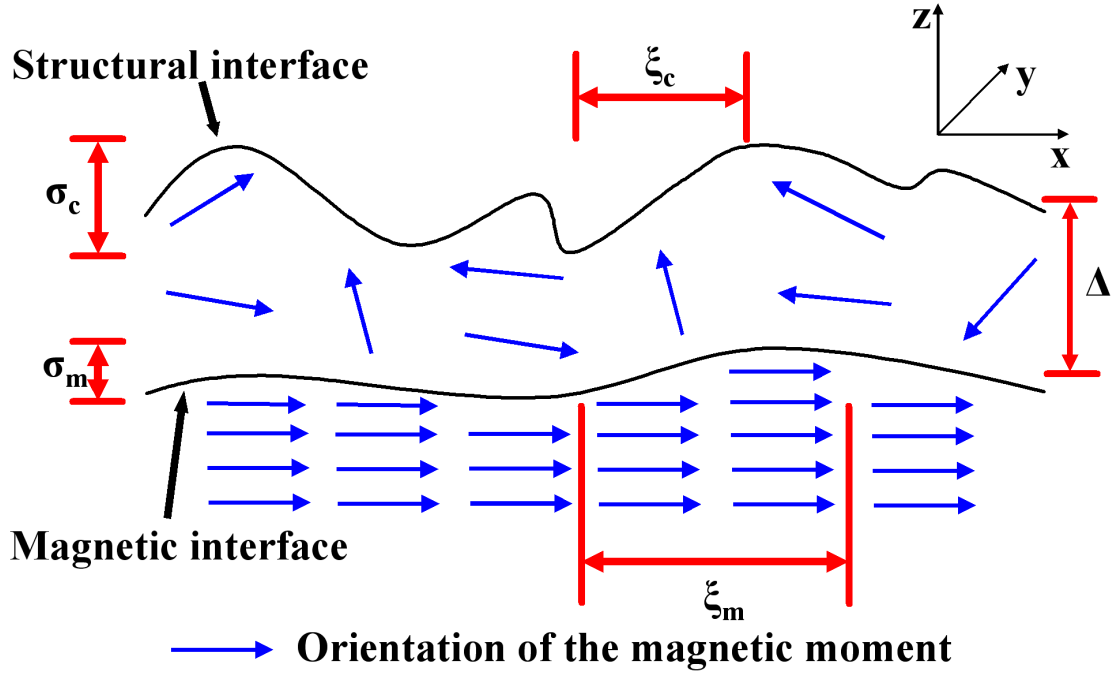


Figure 5.3: Schematic of a structural and magnetic interface that gives rise to diffuse scatter. The symbols  $\sigma_c$  and  $\sigma_m$  are the structural and magnetic RMS roughness respectively and  $\xi_c$  and  $\xi_m$  the structural and magnetic correlation lengths.  $\Delta$  is the thickness between the structural and magnetic boundaries.[136, 22]

dependent to some degree not only on the structure and materials of the system, but also on variables like the temperature, etc.

Upon taking this into consideration it is possible to see how the moments near the interface can then become misaligned with respect to the magnetisation of the bulk magnetic material below them, as shown in figure 5.3. Magnetic disorder is then represented by the height fluctuations of this interface under the assumption that it never coincides with the structural interface via its height fluctuations or its average position.

The basis for this assumption is that the short length-scale fluctuations (atomic) of the moments away from the direction of the average magnetization give rise to diffuse scattering at fairly large scattering wave vectors, whereas we are dealing here with scattering at a small wave vector  $q$ , which represent the relatively slow variations of the average magnetization density. The actual interface can be then considered as really composed of two interfaces, a chemical interface and a magnetic interface, each



with their own average height, roughness, and correlation length[22].

Magnetic dead layers are often seen as yet another layer[130, 137]. These layers do not necessarily contribute to the overall magnetisation of the magnetic layer in question. This region can have both non magnetic and magnetic atoms present, as well as surface anisotropy effects, which leads to the idea of spin mis-tracking at the interfaces or reduced magnetisation. Kelly *et al.*[136] put forward three suggestions for what happens to the moments in this region.

The first was that moments could be pinned at the magnetic-interface region, preventing them rotating with a magnetic field. This could be a result of an anisotropy at the interface that makes out of plane alignment energetically favorable. Secondly, the moments could be chemically quenched. This would result in a reduced magnetisation  $M$  for the interface moments. Thirdly, a reduced exchange coupling of the moments in the interface region may exist. Moments at a disordered interface have lower coordination. These moments have fewer nearest neighbours and have a reduced coupling to moments in the bulk.

Only the first model predicts moments at the interface that do not follow the applied field. The second theory was eliminated by measuring a clean Co sample and observing that it behaves in the same way as a buried interface. They were unable to eliminate either of the other two models. Qualitative evidence for different structural and magnetic interfaces have been seen with neutrons [138, 139] and with diffuse x-ray resonant magnetic scattering[76]. In both cases the magnetic interface was seen to be smoother than the structural one. Early attempts to quantitatively measure magnetic roughness with diffuse soft x-ray magnetic scattering[111, 131, 140] both show a smoother magnetic than structural interface. The papers mentioned earlier by D.R. Lee *et al.*[22, 23] give a good overview of magnetic roughness from the x-ray perspective.

### 5.3 Experimental: Imprinted Magnetic Domain Pattern on a Flat Permalloy layer

The structures studied were prepared using a DC magnetron sputtering system with a base pressure of  $\approx 10^{-8}$  Torr as described in the sputtering section of chapter 1.

The working gas was Ar at a pressure of 2.8 mTorr. The samples were deposited onto a (001)Si substrates. It should be noted that the samples were not grown in a magnetic field.

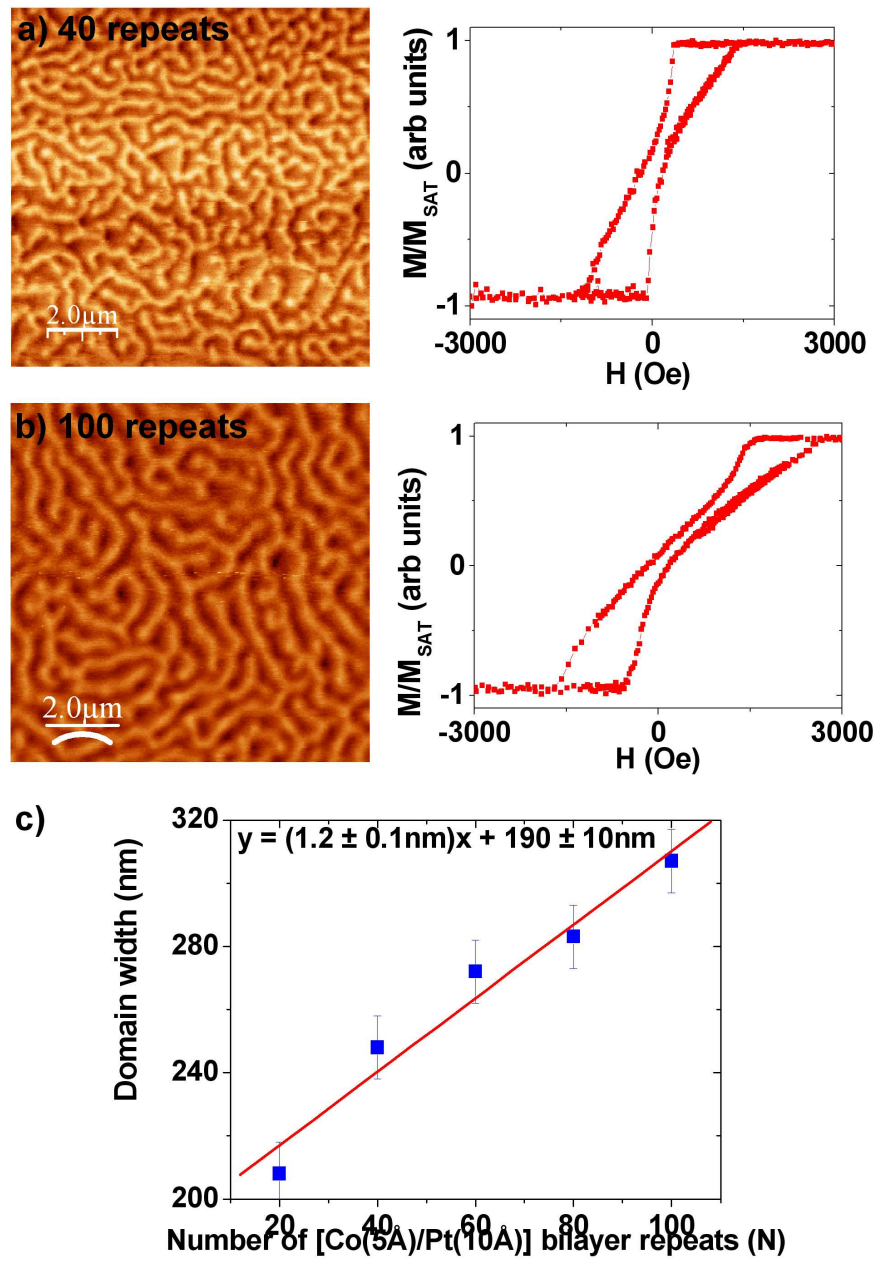


Figure 5.4: a) 40 Co/Pt bilayer repeats giving a domain width of  $250 \pm 10$  nm b) 100 Co/Pt bilayer repeats giving a domain width of  $310 \pm 10$  nm c) Domain width calibration for the Co/Pt multilayer.

The magnetic domain pattern was imprinted on the Py layer by a perpendicularly magnetised Co/Pt multilayer with 60 bilayer repeats and hence forms a stripe domain state that generates a strong stray field above the multilayer with domains of width  $\approx 250$  nm. The domain width was achieved by growing several Co/Pt multilayers and varying the number of bilayer repeats. MFM images were taken of the samples, as MFM is sensitive to the stray fields above the films. Two of the MFM images and associated polar MOKE loops are shown in panels (a) and (b) of figure 5.4 in which it is clear to see how the domains increase in width as the number of bilayer repeats is increased. There is a slight increase in the amount of canting of the wasp waisted polar MOKE loops as N increases because of stronger demagnetising fields stabilising the domain structure. The plot in panel (c) of figure 5.4 shows the linear relationship between domain width and the number of Co/Pt bilayer repeats.

The Py is separated from the Co/Pt multilayer by a thick Ta layer, ensuring that the only coupling between the layers is magnetostatic as any coupling due to exchange coupling should be sufficiently damped down at this distance so as to be negligible. This is followed by a thin Ta cap to prevent oxidation. The nominal structure of the samples is shown in figure 5.5 panel (a).

$$\text{Pt}(20\text{\AA})[\text{Co}(5\text{\AA})/\text{Pt}(10\text{\AA})] \times 60 / \text{Ta}(80\text{\AA})/\text{Py}(50\text{\AA})/\text{Ta}(40\text{\AA})$$

Out-of-plane and in-plane vibrating sample magnetometer (VSM) hysteresis loops are shown in figure 5.5 panels (b) and (c). Separate switching of the Py layer is difficult to discern, indicating that it is strongly coupled to the Co/Pt through the stray field. The loop shapes are typical of a perpendicularly magnetized system.

The structure was initially characterized by x-ray reflectometry using Cu  $K_\alpha$  radiation as described in section 3. The first order Bragg peak for the Co/Pt multilayer is the strongest feature in the specular scan at  $0.34 \text{ \AA}^{-1}$  in  $Q_z$  as shown in figure 5.6 panel (a), giving a bilayer repeat thickness of  $\sim 18 \text{ \AA}$ . A rocking scan taken on the Co/Pt Bragg peak is shown in figure 5.6 panel (b). The interfacial roughness was determined by the method employed by Savage *et al.*[94], giving a interfacial roughness of  $\sim 2.5 \text{ \AA}$ .

Figure 5.6 panel (a) also contains Kiessig fringes, the separation of which give a thickness of  $\sim 170 \text{ \AA}$  corresponding to the total thickness of the Ta(80  $\text{\AA}$ )/Py(50

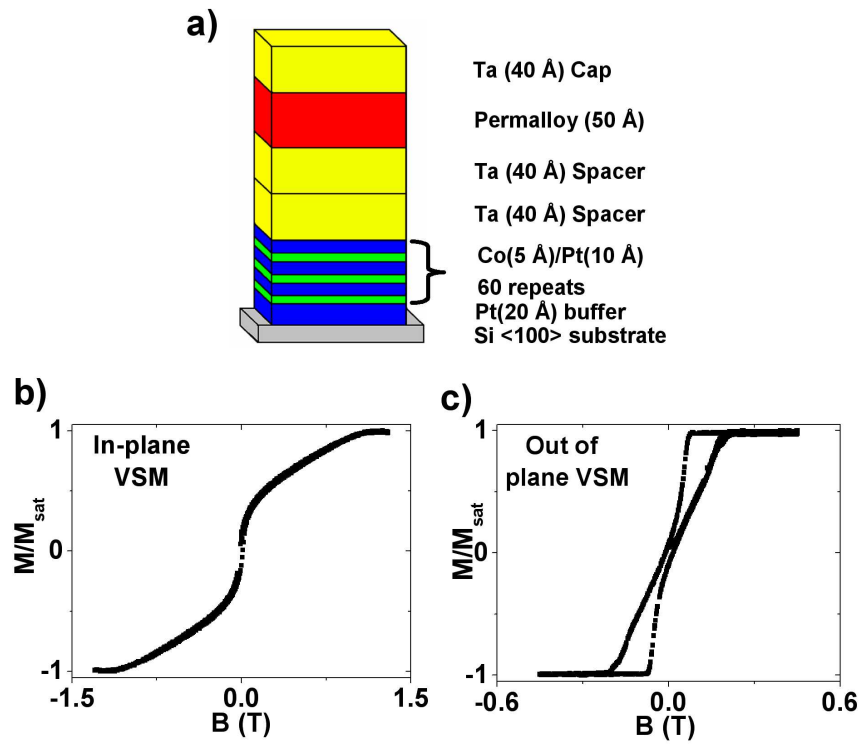


Figure 5.5: a) Nominal sample structure. The important parts are a structurally smooth Py film separated from a perpendicularly magnetised Co/Pt multilayer by a thin Ta spacer b) In-plane VSM hysteresis loop c) Out-of-plane VSM hysteresis loop.

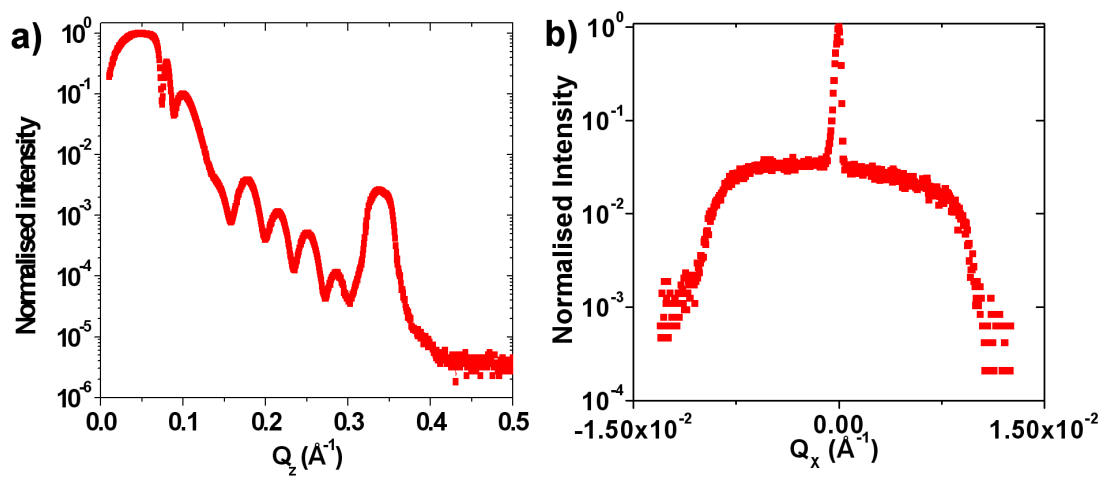


Figure 5.6: Cu  $K_\alpha$  x-rays: a) Specular scan. b) Diffuse rocking scan measured at the detector angle corresponding to the Co/Pt multilayer Bragg peak.

$\text{\AA}$ )/Ta(40  $\text{\AA}$ ) layers atop the Co/Pt multilayer. Rocking curves were also taken at these positions giving a roughness of  $\sim 5.4$   $\text{\AA}$ . AFM images allowed the RMS roughness of the sample surface to be determined to be  $\sim 7.5$   $\text{\AA}$ . Hence, although roughness is accumulated through the stack, the Py layer is structurally rather smooth, with sub-nm roughness.

These samples were then taken to the U4B beamline at the NSLS, as discussed in chapter 2, for the SXRMS measurements, making use of the energy selectivity of the technique to probe the Fe edges in the permalloy layer, hence having no sensitivity to the Co layers. Measurements were made using 90 % circularly polarized x-rays.

## 5.4 Results and Discussion

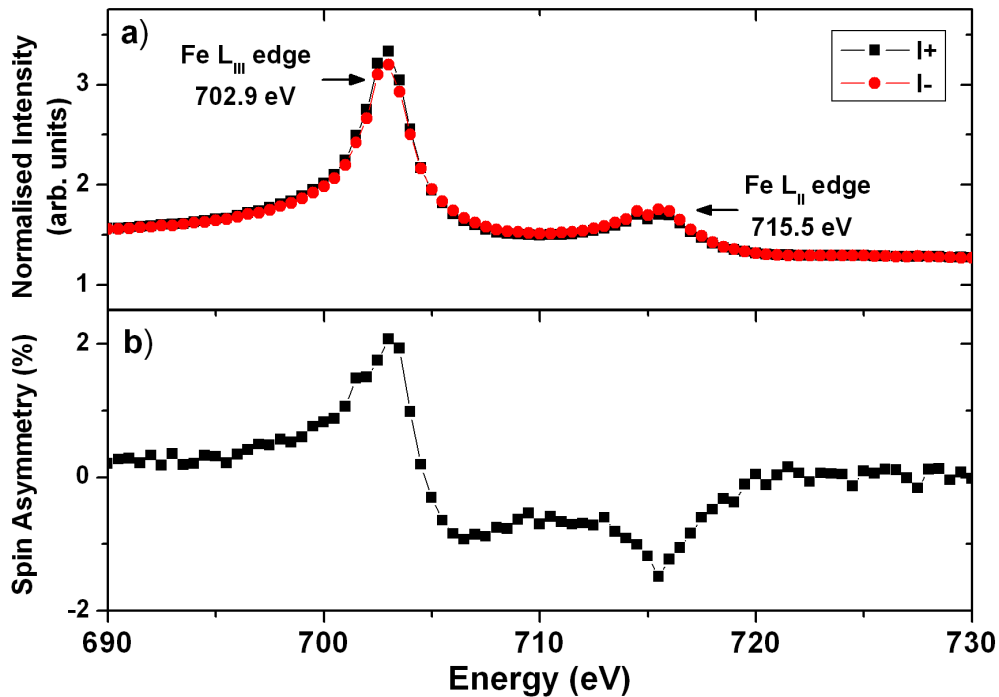


Figure 5.7: Spin Asymmetry and corresponding energy scan for the Fe  $L_{II}$  and  $L_{III}$  resonances. Measured at a  $2\theta = 5^\circ$ .

In order to study the effect of the perpendicular magnetization of the Co/Pt stack

on the permalloy layer, the resonant energy for Fe was selected. Energy scans were performed to find the Fe edges. The results for the scan with  $\theta$  set to  $5^\circ$  are shown in figure 5.7, with the Fe  $L_{III}$  edge being at 702.9 eV and the Fe  $L_{II}$  being found at 715.5 eV. These are shifted from literature values of 706.8 eV ( $\sim 17.6$  Å) and 719.9 eV ( $\sim 17.2$  Å) respectively. This could be put down to the chemical environment of the Fe in the permalloy layer or miscalibration of the beamline.

It should be noted that energy scans around the Ni  $L_{II}$  and  $L_{III}$  (870.0 eV 852.7 eV respectively) edges were also carried out but even with the 80% Ni in the permalloy there was a much reduced dichroism signal and hence the Ni energies were not used to obtain the final results. For the purposes of the experiment all measurements were made with energy set to give the biggest spin asymmetry on the Fe  $L_{III}$  resonance. However even this dichroism is small due to the applied field only disturbing the magnetisation slightly as shall be shown later.

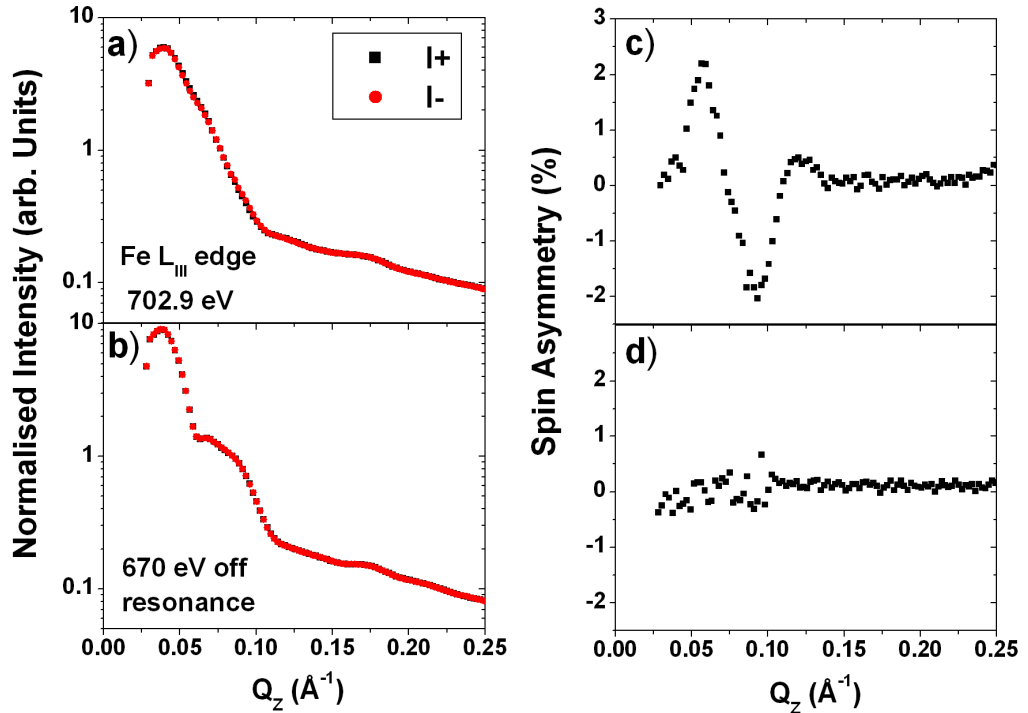


Figure 5.8: Specular scans on and off the Fe  $L_3$  resonance and corresponding spin asymmetry plots.

Initial specular  $\theta/2\theta$  scans were taken on and off the Fe  $L_{III}$  resonance and are shown in figure 5.8 panels (a) and (b). These show very few features. In the on resonance case this is most likely due to absorption of the beam in the sample. Off resonance (670 eV) there is a fringe like bump visible which is most likely due to more of the sample being penetrated by the non-resonant x-rays, and by comparison with figure 5.6 is probably due to interference from the top and bottom of the top Ta and Py layer. The width of the fringes supports this giving a spacing of  $\approx 100$  Å slightly bigger than the nominal structure.

The effects of tuning to the Fe  $L_{III}$  resonance can be more easily seen in the spin asymmetry panels (c) and (d) of figure 5.8. There is some magnetic structure visible in the spin asymmetry panel (c) which must be from the Fe in the permalloy layer, with two peaks at  $\approx 0.05$  Å<sup>-1</sup> and  $0.1$  Å<sup>-1</sup> in  $Q_z$  probably due to the interference between the reflections off the top and bottom interface of the magnetic layer. The peaks correspond to roughly the same positions as the beginning and end of the fringe visible in panel (b) making it probable that this is due to the permalloy layer. Off resonance the spin asymmetry peaks disappear, giving strong evidence for the peaks being magnetic in origin.

The initial survey in  $Q_z$  was then used to select the best position for studying any lateral magnetic structure via transverse ( $Q_x$ ) scans as described in chapter 3. These are shown in figure 5.9, again with the photon energies set to be on (702.9 eV) and off (670 eV) the Fe  $L_3$  resonance, for  $Q_z = 0.059$  Å<sup>-1</sup>. This position in  $Q_z$  corresponds to the largest spin asymmetry on the  $Q_z$  scan figure 5.8 (Fe  $L_3$  resonance). The off resonance scattering data shown in panel (b), has an extremely weak diffuse background, confirming the smoothness of the Py layer. A Gaussian fit to the diffuse scatter shown in this panel gives an in-plane correlation length of  $\approx 900$  Å for any disordered structural roughness. The spin asymmetry shown in panel (d) is zero confirming that the energy is away from Fe resonance.

On resonance, magnetic satellite peaks are observed panel (a), offset at  $Q_x \approx \pm 0.001$  Å<sup>-1</sup>. This corresponds to a real space period of  $2\pi/Q_x \approx 565$  nm. A Gaussian fit to the magnetic satellites gives an in-plane magnetic correlation length of  $\approx 8000$  Å. A Gaussian fit to the low intensity broad diffuse scattering below the well defined

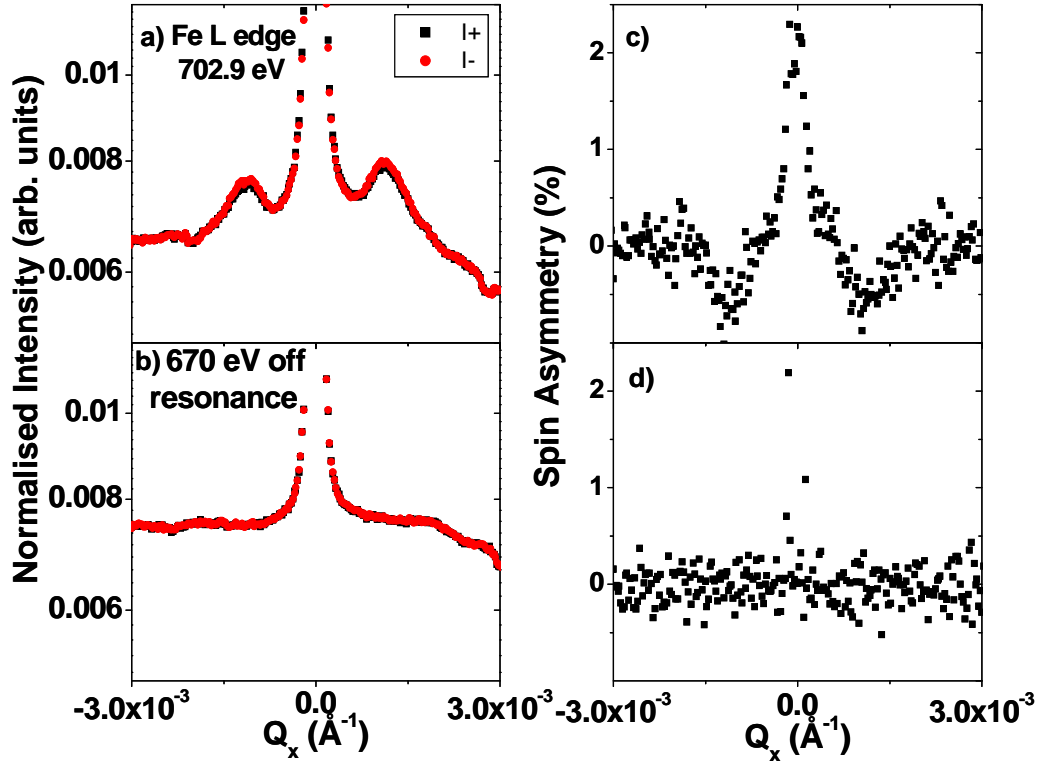


Figure 5.9:  $Q_x$  scans at  $Q_z$  equal to  $0.059 \text{ \AA}^{-1}$  at a) the Fe  $L_3$  resonance at 702.9 eV, and b) off resonance at 670 eV. Spin asymmetry at c) the Fe  $L_3$  resonance at 702.9 eV, and d) off resonance at 670 eV.

magnetic structural peaks scatter gives a disordered correlation length of  $\approx 1000 \text{ \AA}$ . The magnetic origin of the satellite peaks is confirmed, as a small spin asymmetry, of opposite sign to that on the specular ridge are visible in panel (c), the position of which is at the same off-specular values of  $Q_x$ . For truly pure magnetic correlations this asymmetry would be expected to be absent. The fact that it is so weak shows that the experiment has largely succeeded in minimizing the structure-magnetism cross-correlations. They are clearly due to a periodic magnetic structure in the Py, the only layer in the structure containing Fe.

Satellite peaks have also been observed in other systems. For instance Dürr *et al.*[141] and Dudzik *et al.*[142] also observed them in FePd films which exhibit perpendicular magnetic anisotropy. However they did not apply a magnetic field during



there measurements. What is more, their spin asymmetry plots show a distinct sign change from one side of the specular ridge to the other, unlike the spin asymmetry shown in figure 5.9 (c) which is symmetric about the specular ridge. They also observed second order peaks which we did not observe.

In order to verify the above findings and gain more of an understanding of the processes involved, real space images of the micromagnetic structure have been obtained by magnetic force microscopy (MFM). The image shown in figure 5.10 (a) is a rendering of an image obtained over a  $5\ \mu\text{m} \times 5\ \mu\text{m}$  scan, which shows stripes with a period of 540 nm, consistent with our SXRMS results. Panel (e) of figure 5.10 shows a Fast Fourier Transform (FFT) of a  $50\ \mu\text{m} \times 50\ \mu\text{m}$  MFM image. The FFT appears as an annulus with the two bright spots of intensity reflecting the preferential alignment of the periodic stripes. The preferential alignment was most likely introduced during the SXRMS measurements upon application of the external magnetic field needed for the XMCD measurements. There is no way to relate the in-plane  $Q$  vectors to that of the  $Q$  vectors from the SXRMS exactly, so they are set arbitrarily. A cut through the 2D FFT, convoluted with the instrument function of the SXRMS apparatus, including a  $\delta$ -function at  $Q_x = 0$  to simulate the specular ridge, is shown in figure 5.10 (f). The resemblance to the SXRMS data of figure 5.9 (a) is self-evident.

The satellite peaks are in the correct positions and of a comparable width. However, there is no intensity asymmetry in the satellite peaks, as expected for an FFT, which is seen in the SXRMS scan. Asymmetry in scattering data can arise from beam footprint corrections, but this would lead to the satellite peak at negative  $Q_x$  being the more intense. Dürr *et al.* observed magnetic satellite peaks from a stripe domain state in an epitaxial FePd film[141, 143], with an asymmetry related to the coupling between the helicity of the photon and the chirality of the domain structure. Since we used a bending magnet source in this experiment our helicity is fixed, and we cannot perform the exact experiment that this group carried out. However this is a plausible explanation for the observed asymmetry in our data being of similar magnetic origin.

MFM detects forces due to gradients in the stray field above the sample surface. Whilst it is possible to infer the internal micromagnetic structure qualitatively from this, a quantitative knowledge is desirable, particularly since it is this to which our

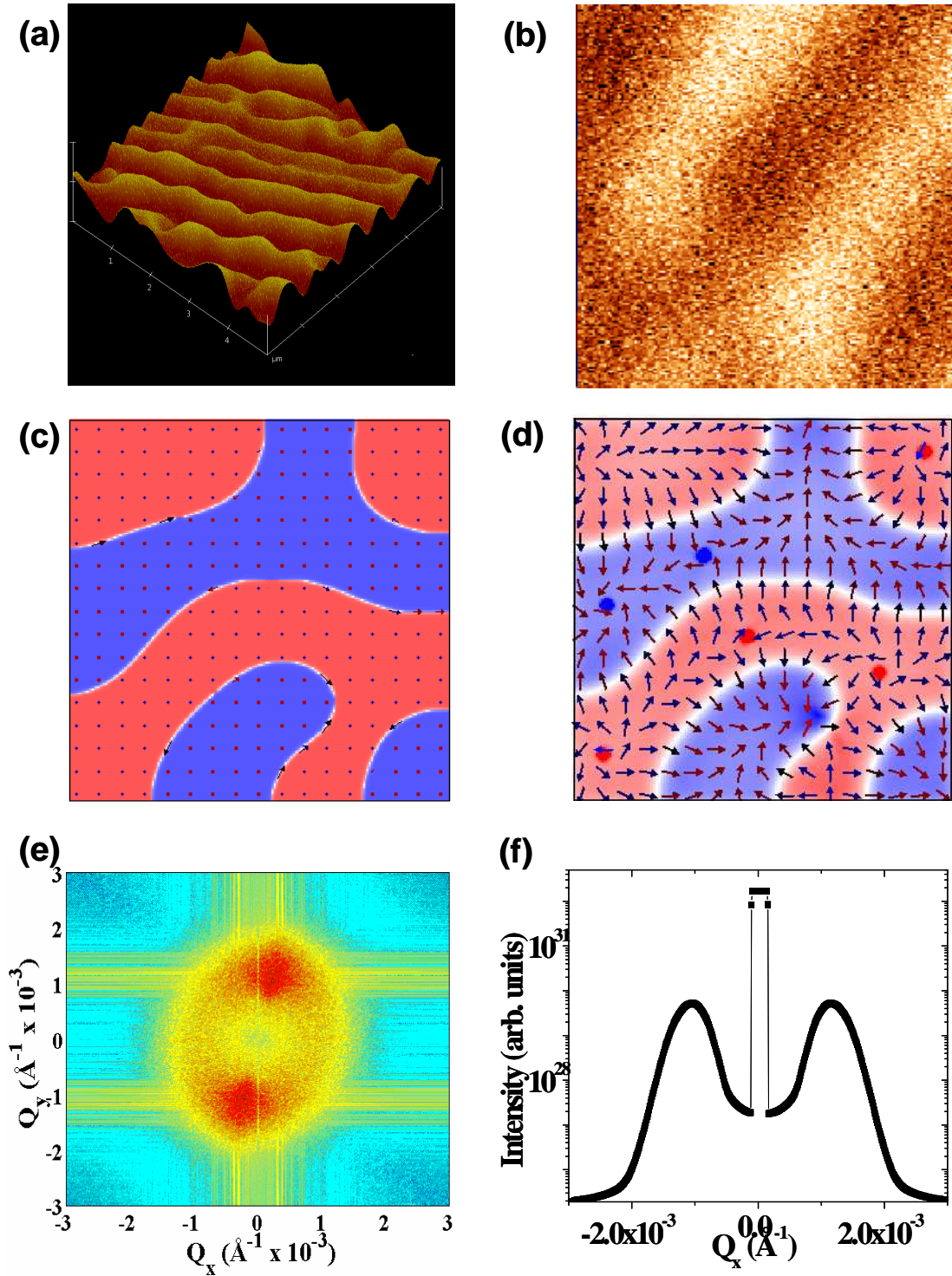


Figure 5.10: a) 3D rendering of a  $5 \times 5 \mu\text{m}^2$  MFM image of the completed sample. b) 2D  $1 \mu\text{m}^2$  zoom of the MFM image. c)  $1 \mu\text{m}^2$  OOMMF simulation of the Co/Pt in zero field. d)  $1 \mu\text{m}^2$  OOMMF simulation of the Py separated from the Co/Pt stack by a Ta layer in zero field. Several vortices are visible. e) FFT of a  $50 \times 50 \mu\text{m}^2$  MFM image. f) Cut through the FFT convoluted with the experimental SXRMS resolution.

SXRMS is sensitive. To simulate the domain pattern obtained in the Py layer from the Co/Pt stack, micromagnetic simulations were performed using the OOMMF code[61]. A cell size of  $5 \text{ nm} \times 5 \text{ nm} \times 5 \text{ nm}$  in a  $1 \mu\text{m} \times 1 \mu\text{m}$  sample area was used. The Co/Pt multilayer was modeled as a continuous slab with the perpendicular anisotropy constant  $K_u = 0.21 \text{ MJ/m}^3$  and magnetisation  $M_{\text{sat}} = 0.26 \text{ MA/m}$ ; these values are derived from our VSM data and are in good agreement with those found in the literature[132].

The Kaplan-Gehring[144] formula was used to calculate the stripe domain width, which then allowed us to calculate a value for the domain wall energy, leading to an exchange stiffness constant  $A = 4.6 \text{ pJ/m}$  for Co/Pt. A magnetically dead spacer layer was used to separate the Co/Pt layer and the Py layer taking the standard OOMMF values of  $K_u = 0$ ,  $M_{\text{sat}} = 0.86 \text{ MA/m}$  and  $A = 13 \text{ pJ/m}$ . Calculated domain patterns for the zero applied field case, in the Co/Pt stack and the Py layer are shown in panels c) and d) of figure 5.10 respectively. There is a  $1 \mu\text{m}^2$  MFM image displayed in panel b) for comparison. From this it can clearly be seen that the magnetic texture in the Py layer closely matches the domain pattern in the Co/Pt. Examination of the results shows that the highest stray field in the Ta spacer just below the Py is roughly  $0.23 \text{ MA/m}$ , about  $0.8 \times M_{\text{sat}}$  for the Co/Pt.

A closer inspection shows that the magnetization in the Py always lies across the top of the Co/Pt domain walls, where the stray field will be horizontal. The magnetization lies in alternating directions on subsequent walls, giving the same spatial period as the underlying domain pattern, and it is this periodic structure that the SXRMS has detected in the Py layer. Where the stray field is vertical, above the Co/Pt domains, the Py moments are canted out of the plane by a few degrees, but otherwise only follow the Co/Pt in as much as the moments try to form flux-closed structures between those that are locked to the top of the walls. We have also performed calculations seeded with this structure for in-plane applied fields of  $\pm 300 \text{ Oe}$ , as in the experiment. We found that the Py moments locked to the walls are rigid, and barely change direction in these fields. Large regions of the permalloy above the domains are easily reversed in these fields, but as their lateral structure is aperiodic, they will only give rise to an incoherent off-specular background in the

SXRMS. The simulations also showed a slow preferential alignment with the applied field, as is observed from the MFM data taken after the NSLS experiment.

## 5.5 Summary

In summary, we have investigated a domain pattern imprinted on a structurally smooth permalloy layer and detected off-specular satellite peaks in the soft x-ray resonant magnetic scattering corresponding to a periodic magnetic modulation. These appeared in the sum signal ( $I^+ + I^-$ ) but were extremely weak in the difference ( $I^+ - I^-$ ), indicating that the magnetism self-correlation function contains a strong periodic part which is almost absent from the structure-magnetism cross-correlation function. Thus we have exploited the element specific features of SXRMS to discern the purely magnetic correlations with little or no overlap from the charge and charge-magnetic cross correlations. This is in good agreement with Osgood *et al.* [137].

These results have since been published by Kinane *et al.* [145] and presented in poster form at the 19th International Colloquium on Magnetic Films and Surfaces (ICMFS).

## Chapter 6

# Nanospheres Patterned Arrays

### 6.1 Introduction

So far in this work SXRMS has been used to investigate a structurally flat system with a magnetic modulation imposed upon it, with the aim of testing whether SXRMS can be used to study the magnetic disorder, as well as gaining insight into the interplay between the structure disorder and the magnetic disorder. Having found that SXRMS can be used to study the magnetic disorder with little overlap from the structure, the next step in the study is to add a structural and magnetic modulation, and see how it affects a magnetic structure using SXRMS and PNR, where the PNR allows clear separation of the magnetic information to aid in the interpretation of the SXRMS.

In this chapter, self-assembled arrays of nanospheres have been used to pattern a Co/Pt multilayer into nanopillars. On top of this has been deposited a Co/Ru multilayer which is antiferromagnetically (AF) coupled. The nanopillars introduce a known structural and magnetic lateral modulation into the multilayer. SXRMS and PNR have been used to observe the interference from the patterned substrate. This has allowed us to show how the magnetic roughness correlates with the structural roughness, and obtain selective magnetometry of the various magnetic elements in the case of the soft x-ray scattering as well as selective magnetometry in reciprocal space in both cases. A quick review of work done in a similar vein on structurally rough and patterned systems follows, in an effort to gain some insight into the presented work.

## 6.2 Nanospheres Review

The reader is directed to the reference article by Martin *et al*[146] for an overview of laterally patterned nanostructures patterned from magnetic multilayers. A review of some recent relevant articles is given below.

MacKay *et al*[111] measured a flat Co/Cu multilayer using SXRMS, finding that the roughness of the magnetic interface was smoother than the structural interface. They put this down to Co atoms at the interface that produce the short-wavelength roughness being pinned and unable to follow the magnetic reversal of the bulk of the magnetic layer hence not contributing to the magnetic scattering.

An attempt to see how the magnetic disorder is affected by random structural disorder has been made by Freeland *et al*[140], who grew several CoFe samples with varying structural (rms) roughness  $\sigma_c$ . The surface roughness was tailored via the growth process and by using diffuse SXRMS the magnetic roughness was determined. Their results show that the magnetic roughnesses  $\sigma_m$  and in-plane magnetic correlation length  $\xi_{\parallel,m}$  scale with increasing structural roughness with the magnetic parameters being  $\approx 30\%$  smaller than the structural values and with a longer correlation length.

In 2000 Hase *et al.* [147] also measured a flat Co/Cu multilayer using linearly polarised SXRMS. The main findings was that the length scales of the structural and magnetic in-plane correlation lengths,  $\xi_{\parallel,s}$  and  $\xi_{\parallel,m}$ , differed by two orders of magnitude, with the  $\xi_{\parallel,m}$  always being the larger. This was also found to be magnetisation direction dependent, with the longer  $\xi_{\parallel,m}$  and smaller (rms) roughness  $\sigma_m$  in the easy axis direction. The magnetic roughness was also seen to be strongly correlated through the multilayer stack.

A further study in 2003 by Hase *et al.*[102] on flat AF coupled Co/Cu and Co/Ru multilayers used both linearly polarised SXRMS and PNR in an effort to contrast the two techniques. In the case of the Co/Cu the PNR found that for the structural and magnetic out-of-plane correlation lengths,  $\xi_{\perp,s}$  and  $\xi_{\perp,m}$ , were of approximately the same size  $\approx, 600$  Å. In the case of the Co/Ru the  $\xi_{\perp,s}$  was comparable, while  $\xi_{\perp,m}$  was an order of magnitude bigger  $\approx 2000$  Å. For the SXRMS  $\xi_{\perp,s}$  was found to be similar for both systems. Again, in the Co/Ru system the  $\xi_{\perp,m}$  was always greater than the

structural. This was not found to be magnetisation direction dependent. What was more, the SXRMS data for the Co/Cu displayed AF specular Bragg peaks, while Co/Ru did not. However AF Bragg peaks were present in the diffuse scattering in the case of the Co/Ru. The AF peaks are clearly visible on specular for the neutron data in both cases.

Temst *et al.*[148, 149] used off-specular PNR to study the magnetisation reversal of large arrays of Co disks. The magnetisation reversal process is shown to be via domain wall motion rather than coherent rotation. Temst *et al.* also performed a complete structural characterisation of the periodic arrays of dots using Cu  $K_\alpha$  x-rays and scanning probe microscopies[150].

Theis-Bröhl *et al.*[151, 152] also used off-specular PNR to study CoFe stripes, seeing how the magnetisation reversal differed for different orientations of the stripes to an applied magnetic field. They found that for a strip orientation perpendicular to an applied field, the reversal is via a coherent rotation, whilst if the strips are parallel to the applied field, domain wall motion and nucleation dominate. Both Theis-Bröhl *et al.* and Temst *et al.* proved the validity of using PNR to study lateral nanostructures and contrast it to other techniques.

Michez *et al.*[153] have studied the effect on AF coupled Co/Ru multilayers patterned into stripes, via circularly polarised SXRMS. In this case the magnetic and structural information is cross correlated as described in chapter 3. The result of a Fourier analysis on this work was that the magnetic wave form across the magnetic grating differed markedly from the actual grating shape, and only reproduces the large scale features of the structure, not the fine detail.

A precursor to the work presented in this chapter was carried out by Langridge *et al.*[154]. Nanospheres were used to make templates, which were then used as a mask to deposit Cr/Au into a hexagonal pattern nano-array. This formed the substrate that added a structural modulation to an AF coupled Co/Ru multilayer, which was then studied via PNR at the CRISP beamline at ISIS. The magnetic roughness in this case was found to be on a length scale similar to the sphere size used. The overall domain structure was found to be undisturbed.

The effects of CoRu alloying as described earlier on a Co/Ru multilayer grown on

a similar Cr/Au roughed nano-array have also been studied by Michez *et al.* [155] using SXRMS at the NSLS. The main result was that the alloying smoothed out the magnetic roughness compared to the un-alloyed samples, while having little effect on the un-patterned samples.

In a further attempt to study the interplay between magnetism and structure, we have extended the ideas used in the chapter on magnetic patterning by patterning the Co/Pt stack into a large area array of dots or pillars. This could be used to provide a periodic roughness with a known structural and magnetic roughness, combining the studies carried out by Kinane *et al.* on a structurally flat but magnetic modulated system and Langridge *et al.* on a structurally modulated system, and what effect this has on a magnetic multilayer grown on top of it. The effect of these pillars, which are magnetised perpendicularly out of the plane, on an anti-ferromagnetically coupled Co/Ru multilayer (in-plane magnetization) were then studied using the various techniques discussed below.

## 6.3 Experimental

### 6.3.1 Sample Preparation

The samples studied were grown by a d.c. magnetron sputtering system with a base pressure of  $\approx 10^{-8}$  Torr as described in the sputtering section of chapter 1. The working gas was Ar at a pressure of 2.8 mTorr. The samples were deposited onto (001)Si substrates. It should be noted that the samples were not grown in a magnetic field. Two samples were prepared with the nominal structures:

Sample A  $[\text{Co}(5\text{\AA})/\text{Pt}(10\text{\AA})] \times 20(\text{patterned})/\text{Ru}(400\text{\AA})/[\text{Co}(40\text{\AA})/\text{Ru}(18\text{\AA})] \times 20$ ,

Sample B  $[\text{Co}(5\text{\AA})/\text{Pt}(10\text{\AA})] \times 20(\text{patterned})/\text{Ru}(400\text{\AA})/[\text{Co}(31\text{\AA})/\text{Ru}(32\text{\AA})] \times 20$ .

These are referred to as samples A and B. Both samples were grown with the Ru thickness tailored to be on an antiferromagnetic (AF) coupling peak[2]. In the case of sample A this was the 2<sup>nd</sup> AF coupling peak, and in the case of sample B the 3<sup>rd</sup> AF coupling peak. This is due to the maximum field available from the magnets at the ADAM and U4B beamlines, as described earlier 2, so as to allow each sample to be saturated during the measurements.



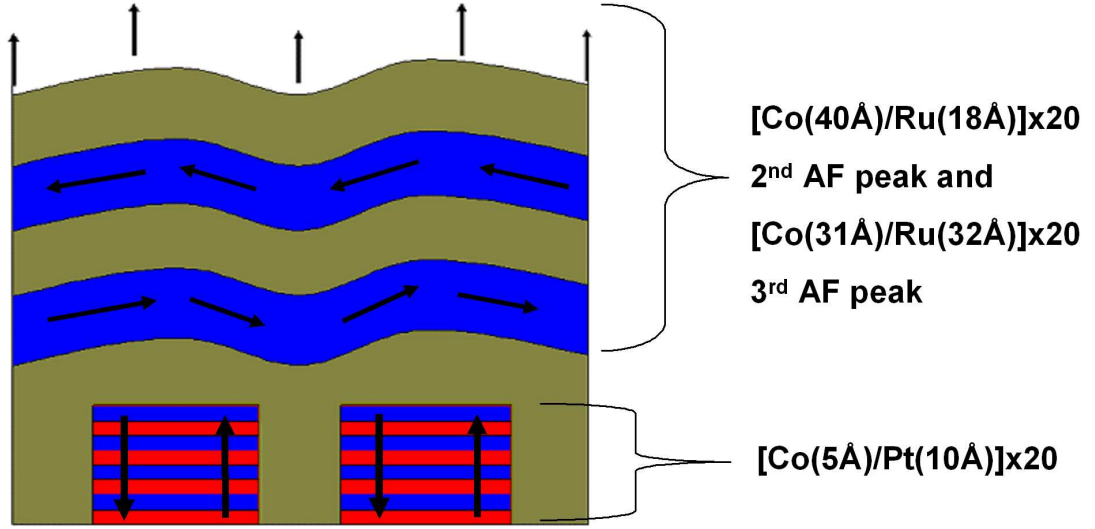


Figure 6.1: Nominal sample structure grown on the patterned perpendicularly magnetised Co/Pt pillars. Two different Co/Ru multilayers were grown. One on the 2<sup>nd</sup> antiferromagnetic peak and the other on the 3<sup>rd</sup> antiferromagnetic coupling peak[2] to allow for the different magnet strengths at the U4B and ADAM beamlines.

In order to obtain both a structurally and magnetically modulated pattern a Co/Pt multilayer was grown to obtain a perpendicularly magnetised film[156, 132]. This Co/Pt multilayer was then patterned into a hexagonal dot array by coating the surface with a monolayer of polymer spheres by the method described in chapter 1 in section 1.4 on patterning. This allows arrays with lateral ordering over a length scale of  $\sim 1 \text{ cm}^2$ . The hexagonal arrays of nanospheres with a diameter of 780nm act like a mask during a combination of reactive ion etching (RIE) and Ar ion milling. This produced nanosphere capped Co/Pt pillars, the final diameter of which is governed by the milling time. The spheres were then removed via abrasion and sonically bathing the samples in organic solvents. Further details on the patterning process can be found in the following by Weekes *et al*[34, 33]. The dimensions of two substrates for samples A and B were respectively  $25 \text{ mm} \times 25 \text{ mm}$  so as to provide a large area to maximize the scattered neutron flux, and  $5 \text{ mm} \times 10 \text{ mm}$  to allow the sample to fit in the U4B sample chamber holder.

To ensure that there was no form of coupling, other than magnetostatic, between the Co/Pt pillars and the following  $[\text{Co}(40\text{\AA})/\text{Ru}(18\text{\AA})] \times 20$  and  $[\text{Co}(31\text{\AA})/\text{Ru}(32\text{\AA})] \times 20$  multilayers, 400Å of Ru was then deposited to form a large non-magnetic spacer layer.

The total bilayer thickness for the Co/Ru multilayer stacks was tailored to be  $\approx 60\text{\AA}$  thick. This was to provide a structural Bragg peak around  $\approx 0.1\text{ \AA}^{-1}$  in reciprocal space which can be reached using both ADAM and U4B beamlines.

### 6.3.2 Characterisation

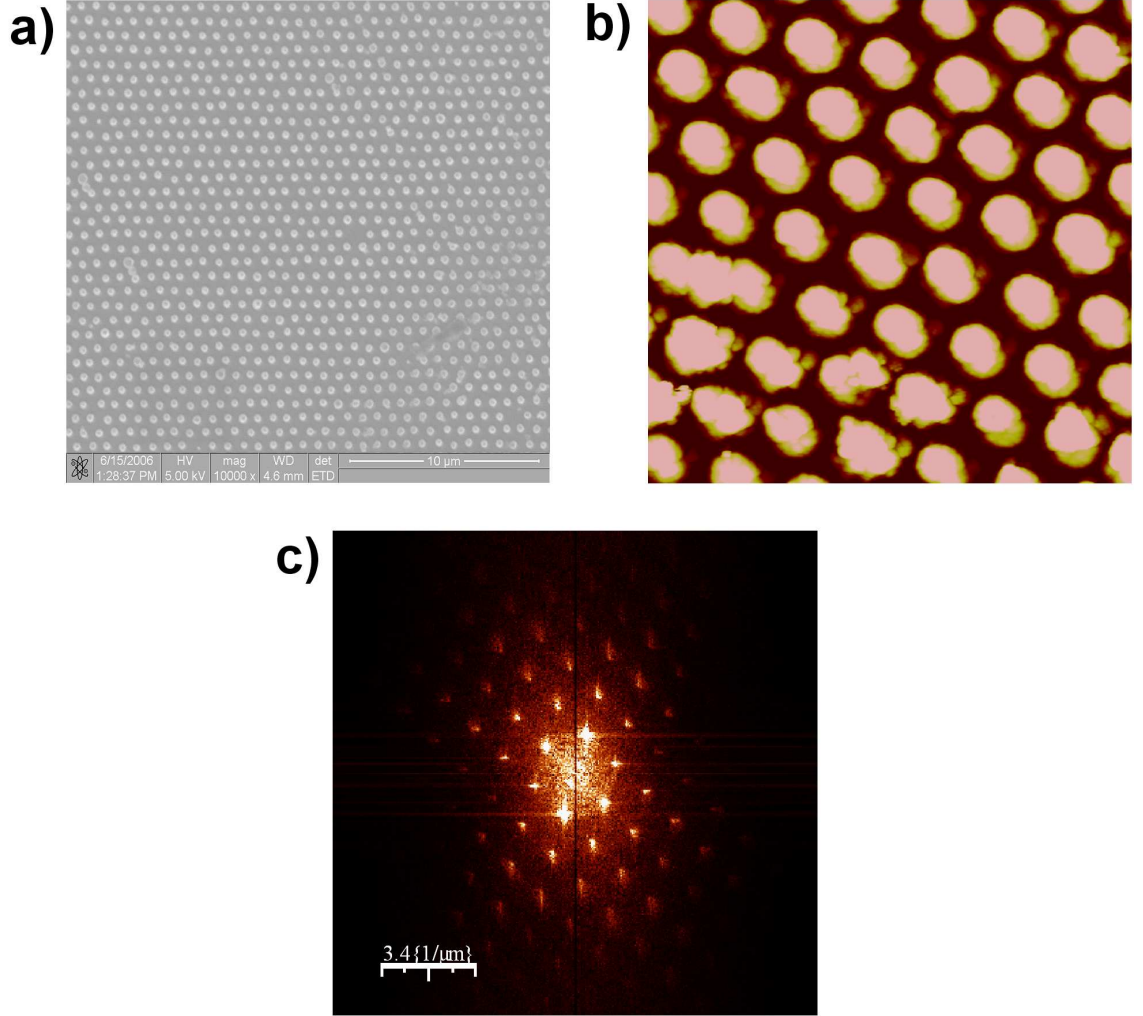


Figure 6.2: Microscopy for sample A: a)  $25\text{ }\mu\text{m} \times 25\text{ }\mu\text{m}$  SEM image of Co/Pt Dots after milling. b)  $5\text{ }\mu\text{m} \times 5\text{ }\mu\text{m}$  AFM image. c) FFT of  $50\text{ }\mu\text{m} \times 50\text{ }\mu\text{m}$  AFM image showing a hexagonal pattern. The AFM images were taken after Co/Ru deposition on top of the nanodots. (SEM image courtesy of L. S. E. Alvarez[157].)

Scanning electron microscope (SEM) and atomic force (AFM) and magnetic force microscopy (MFM) images of both samples are shown in figures 6.2 and 6.3 for samples A and B respectively. Panel (a) of figure 6.2 shows a  $25\text{ }\mu\text{m} \times 25\text{ }\mu\text{m}$  SEM image

of the Co/Pt substrate before the Co/Ru and Ru spacer was deposited. The final average diameter was found to be roughly  $\approx 420$  nm. It was found that a small stud of hardened polymer residue remained on top of the dot and resisted all attempts at removal. Panel (b) shows an  $5\ \mu\text{m} \times 5\ \mu\text{m}$  AFM image, giving the height of the dots as approximately  $\approx 230$  nm to 250 nm. The AFM/MFM images were taken after the Co/Ru and Ru spacer was deposited due to time constraints. This height is consistent with the overall thickness of the multilayer ( $\approx 190$  nm), with the 40 nm discrepancy being put down to nanosphere residue and over milling etching into the substrate. The long range order of the substrate is confirmed by the several orders of peaks visible in the FFT shown in panel (c). The FFT was computed from a  $50\ \mu\text{m} \times 50\ \mu\text{m}$  AFM image (not shown).

The microscopy for sample B is shown in figure 6.3. The main differences between samples A and B being that this is from a new batch of patterned Co/Pt substrates and that the Co/Ru is tailored to be on the 3<sup>rd</sup> AF coupling peak. Panel (a) of figure 6.3 shows a  $16\ \mu\text{m} \times 16\ \mu\text{m}$  SEM image again taken before the Co/Ru multilayer and Ru spacer was deposited. In this case the Ar ion milling was not performed for long enough, resulting in the formation of hexagonal islands. These are much more closely packed than those for sample A shown in panel (a) of figure 6.2. The pitch of the nanodots is still the same at approximately  $\approx 780$  nm with an average dot size of around the same. Again, it was found from high magnification images that a small stud of hardened polymer residue remained on top of the dot. Panel (b) shows an  $10\ \mu\text{m} \times 10\ \mu\text{m}$  AFM image giving the height of the dots as approximately  $\approx 45$  nm to 65 nm. This is much smaller than the total height of the multilayer stack, again indicating how the sample was under milled. However the long range order of the substrate is confirmed by the several orders of peaks visible in the FFT of a  $20\ \mu\text{m} \times 20\ \mu\text{m}$  AFM image (not shown) in panel (c).

The magnetics of the Co/Pt pillars underwent further investigation using polar MOKE, the results of which are shown in panels (a) and (b) of figure 6.4. The polar MOKE loops are affected by the patterning process, effectively reducing the wasp waisted loops making them slightly squarer and introducing inflections in the magnetization during reversal. However, they are still perpendicularly magnetised.

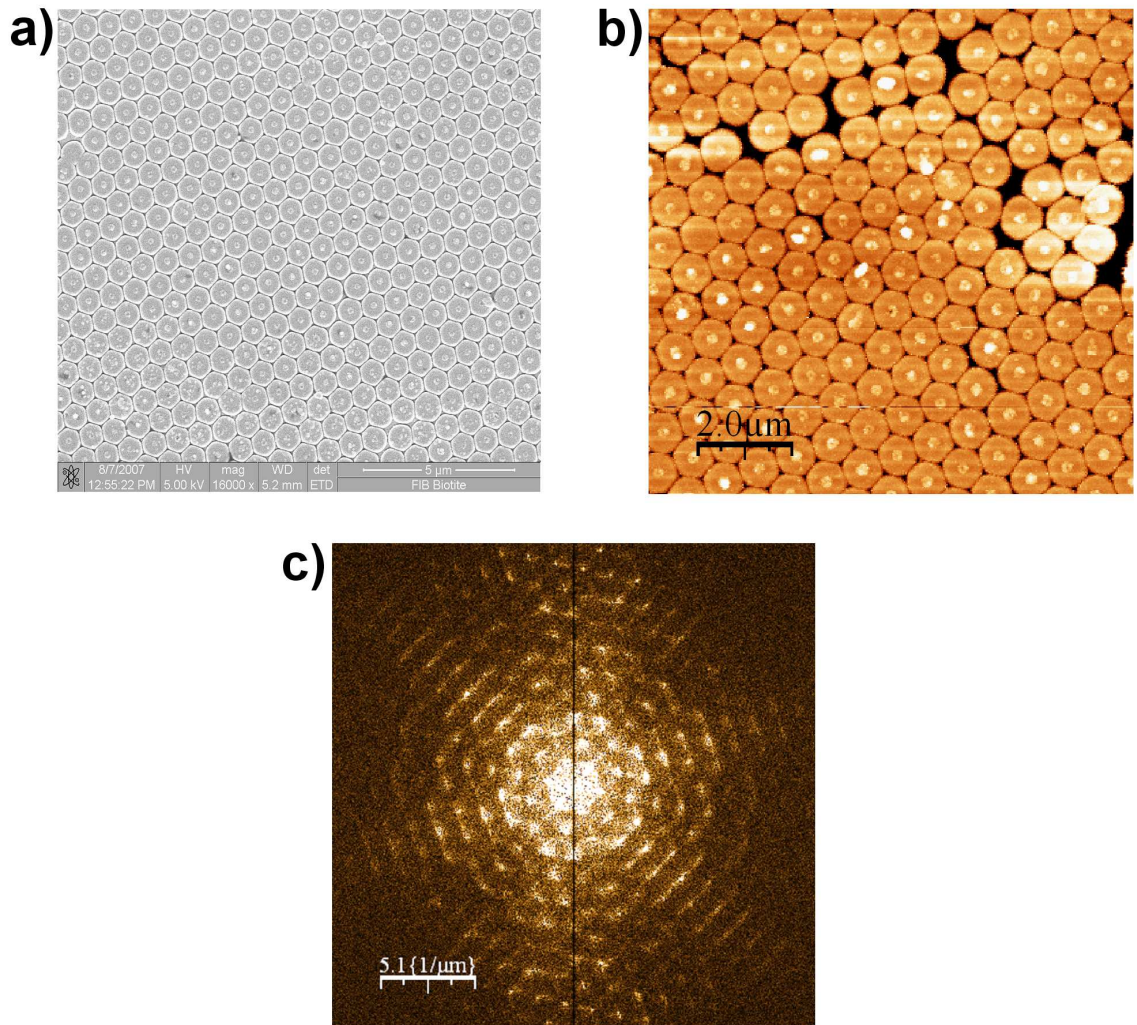


Figure 6.3: Microscopy for sample B: a)  $16\ \mu\text{m} \times 16\ \mu\text{m}$  SEM image of Co/Pt Dots after milling. b)  $10\ \mu\text{m} \times 10\ \mu\text{m}$  AFM image. c) FFT of  $20\ \mu\text{m} \times 20\ \mu\text{m}$  AFM image showing a hexagonal pattern. The AFM image was taken after Co/Ru deposition on top of the nanodots. (SEM courtesy of L. S. E. Alvarez[157] with the AFM and MFM courtesy of Kari Dempsey[158].)

Structural characterisation was performed on the patterned Co/Pt substrates using the lab based Cu  $K_\alpha$  x-ray kit at Leeds as described in section 1.4. Both specular and rocking scans, taken on the  $1^{st}$  Bragg peak, are shown. In the case of sample A in panels (c) and (e) and for sample B in panels (d) and (f). The first thing that is clear is that the position of the  $1^{st}$  order Bragg peaks are not the same, giving bilayer repeat thickness for the Co/Pt of  $27\ \text{\AA}$  and  $19\ \text{\AA}$  for samples A and B respectively. This is not critical for two reasons. Firstly, both sets of polar MOKE loops show the samples to be perpendicularly magnetised, and secondly, both Co/Pt Bragg peaks are

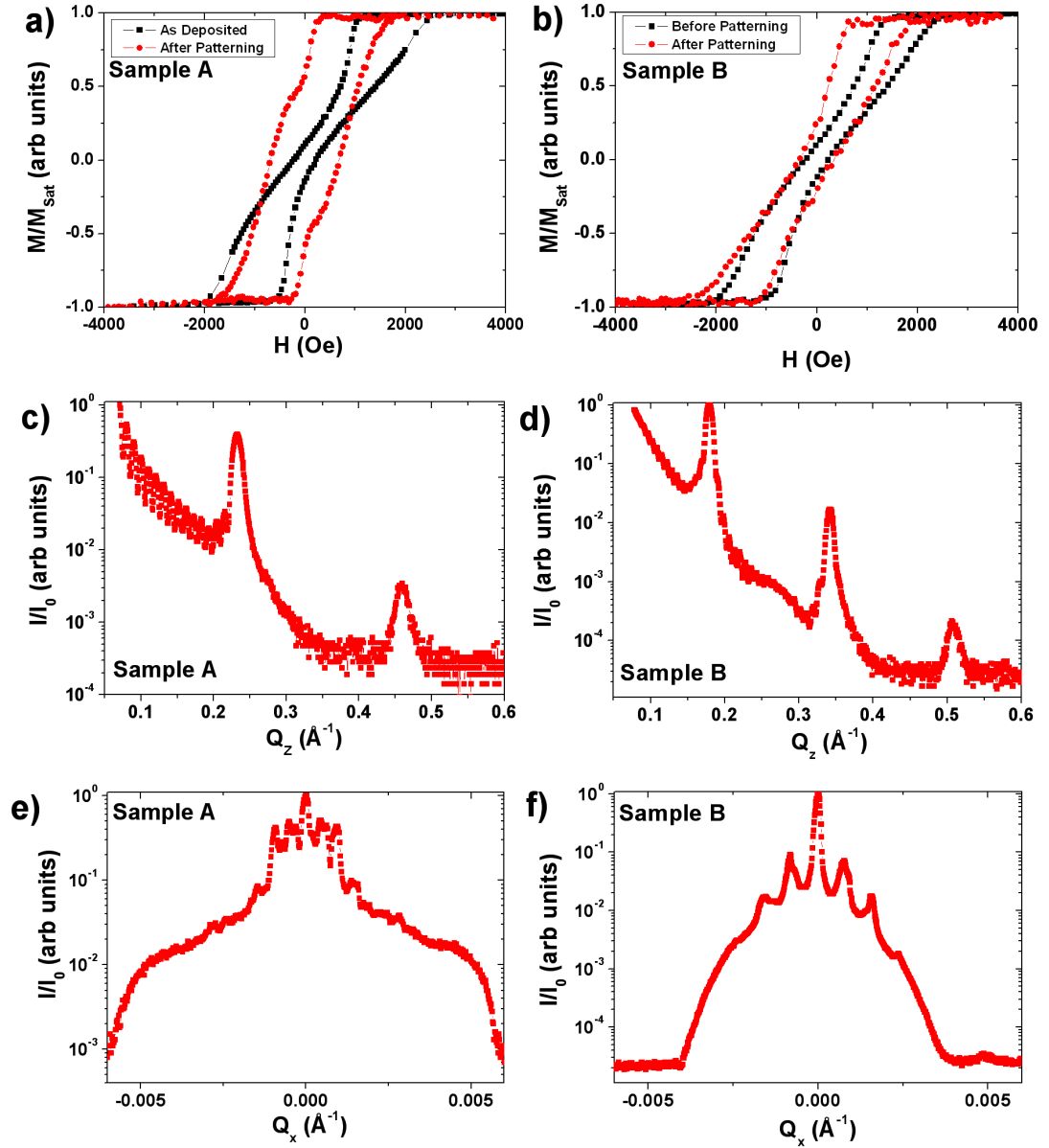


Figure 6.4: Polar MOKE and Cu K $\alpha$  x-rays of patterned Co/Pt substrates. Panels (a) and (b) show polar MOKE loops before and after patterning. Panels (c) and (d) show Specular Cu K $\alpha$  x-rays scans taken after patterning. Panels (e) and (f) show rocking scans taken on the 1<sup>st</sup> order Bragg peaks.

well away from  $0.1 \text{ \AA}^{-1}$  where the Co/Ru Bragg peak is situated for the scattering experiments. It should be noted that the intensity does not die off particularly fast even though the substrate had been patterned in both cases.

The rocking scans in panels (e) and (f) are markedly different. In the case of sample A panel (e) the intensity is bunched up in a plateau about the specular ridge. With the peaks at the edge of the plateau ( $Q_x = 0.94 \times 10^{-3} \text{ \AA}^{-1}$ ) corresponding to a dot spacing of  $\approx 670 \text{ nm}$ , just over  $100 \text{ nm}$  off the intended  $780 \text{ nm}$  pitch. It should also be noted that in the spaces between the specular position and these outer peaks there is some asymmetric structure. It is unclear as to how this asymmetric structure comes about. However it seems to be at least in part due to fabrication issues connected with the length of the etching process and how the residue of the nanospheres is removed after etching. Figure 6.5 shows an SEM image panel (c) of a clean substrate with just the small residue of the nanospheres stuck to the surface and the corresponding Cu  $K_\alpha$  x-ray rocking scan panel (a) with clean in-plane Bragg features. Panels (b) and (d) show the same information but for a sample where the spheres were deliberately left on the surface. The in-plane Bragg features in the rocking curve have doubled peaks, implying a variation in periodicities within the lateral structure. This is a possible method for the extra structure mentioned earlier but does not give any explanation for the asymmetry.

The rocking curve for sample B is shown in panel (f) and has a much cleaner diffuse scattering, being separated out into several in-plane Bragg peaks either side of the specular at the  $1^{st}$  and  $2^{nd}$  order positions of  $Q_x = \pm 0.86 \times 10^{-3} \text{ \AA}^{-1}$  and  $Q_x = \pm 0.16 \times 10^{-2} \text{ \AA}^{-1}$ , giving dot spacing of  $\approx 790 \text{ nm}$  ( $2\pi/Q_x=d$ ) in good agreement with that from the SEM image shown in figure 6.3 panel (a). In this case a different method of removing the nanodots after etching was employed, where adhesive tape of various makes was applied to the surface of several test substrates, and pulled off rapidly. Eventually one was found to remove only the nanodots leaving the slight stub of material roughly centered in the middle of the dots. Due to lack of availability of patterned substrates and time constraints, no AFM was undertaken to determine the height of this residue. However the general quality of the dot arrays was greatly improved via this method of nanodot removal, though it should also be noted that



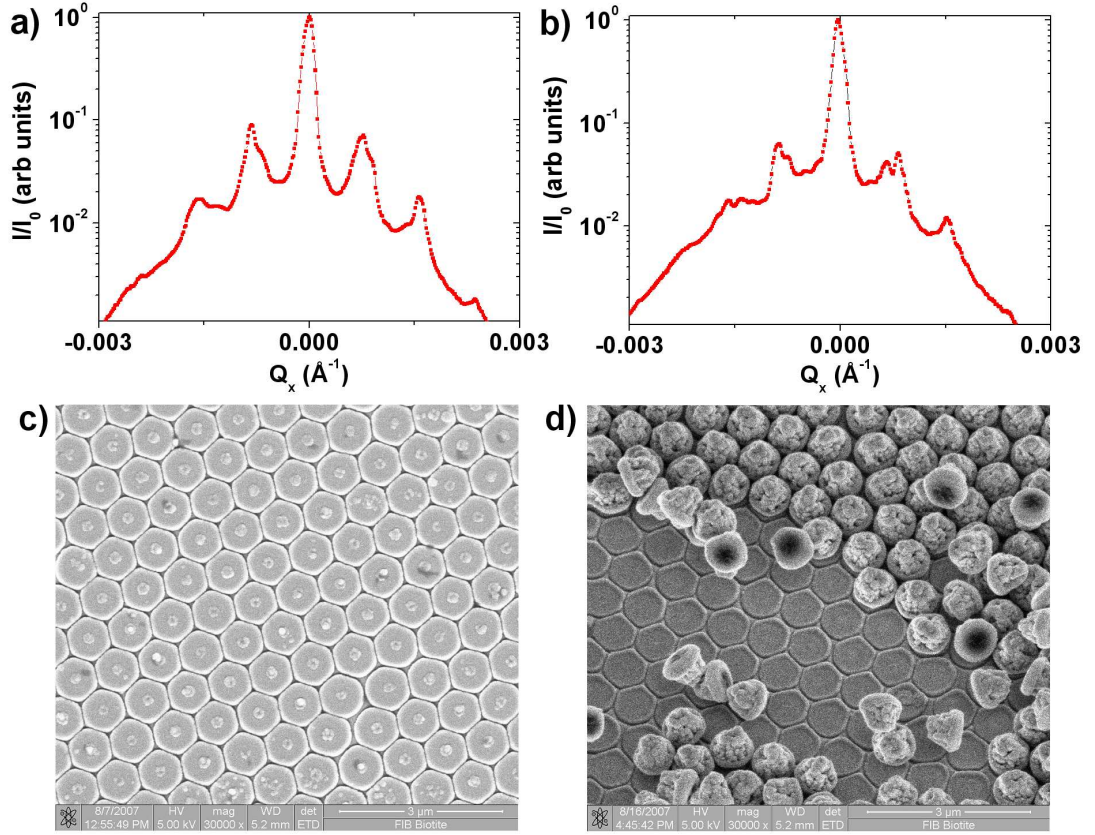


Figure 6.5: a) Rocking curve about the 1<sup>st</sup> order Bragg peak for a sample with the nanospheres removed. b) Rocking curve about the 1<sup>st</sup> order Bragg peak for a sample with the nanospheres still on the surface, note the side peaks on the in-plane Bragg features. c) Residue after sphere removal and d) Remainder of spheres after milling.(SEM courtesy of L. S. E. Alvarez[157].)

the etch was not as successful in sample B's case giving a dot height and order of magnitude smaller than in the case of sample A.

Once the nanospheres had been removed from the top of the Co/Pt pillars, a 400  $\text{\AA}$  Ru layer was deposited to separate them from the Co/Ru multilayer and ensure the only coupling between them was magnetostatic. Figure 6.6 shows longitudinal MOKE on the completed sample A in panel (a) with a MOKE loop on a sample which has not had the patterning stage performed on it but the Co/Ru multilayer and Ru spacer grown on top. There is a marked increase in the canting of the loop for the patterned sample. Panel (b) of figure 6.6 shows Cu  $K_\alpha$  x-ray reflectometry. It appears that the 400  $\text{\AA}$  Ru spacer layer and Co/Ru multilayer have vastly increased the roughness

of the sample increasing the rate at which of the intensity dies off. However it is clear that the patterned samples still have a basic, though very structurally rough, Co/Ru stack, as the 1<sup>st</sup> and 2<sup>nd</sup> order Co/Ru Bragg peaks are clearly visible and well separated from the Co/Pt Bragg peaks. In addition the MOKE loop, which is sensitive to the first  $\approx 200$  Å still has an canted AF nature, greater than for the un-patterned sample.

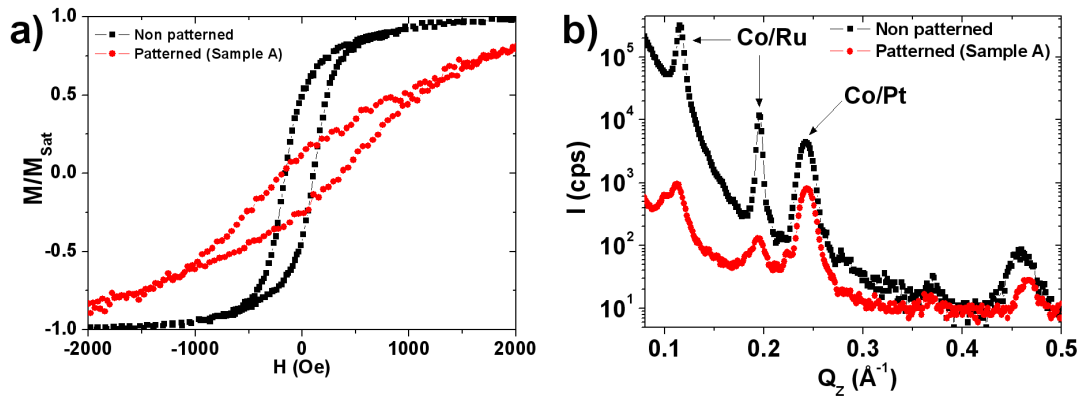


Figure 6.6: (a) Longitudinal MOKE on the completed sample A and on the same structure without patterning after Co/Ru deposition (b) Cu  $K_{\alpha}$  x-rays of the same two samples, showing a large decrease in specular scatter due to the patterning.

### 6.3.3 Polarised Neutron Measurements

PNR was carried out on the ADAM beamline at the Institute Laue Langevin research reactor as described earlier in chapter 2. All measurements were performed with the sample at room temperature with a wavelength of  $\lambda = 4.4$  Å. The principle aim was to take reciprocal space maps and standard rocking curves as well as hysteresis loops, as the sample geometry is such that the sample and detector angles allow the components of the elastic wavevector transfer  $\mathbf{Q}$  to be selected in  $x$  and  $z$ . The beamline electromagnet was employed to apply a magnetic field in the  $y$  direction of the sample up to 4 kOe.



### 6.3.4 Soft X-ray Measurements

In order to perform the SXRMS measurements the samples were taken to the U4B beamline at the national Synchrotron Light Source as described in section 2. The sample geometry is similar to that at ADAM but with the magnetic field applied in the plane of the sample, in the  $x$  direction. X-rays with a circular polarization of 90 % were used, with the reflected intensity being normalized via an Au grid monitor upstream of the entrance slits to the scattering chamber. An electromagnet allowed a field to be applied in the plane of the sample with a maximum field of 300 Oe.

## 6.4 Results and Discussion

### 6.4.1 Polarised Neutron Study

Reciprocal space maps of the sample for different incident neutron spins and applied fields are shown in figures 6.7 and 6.8. Panels (a) and (b) of figure 6.7 show reciprocal space maps for the **dd** and **ud** neutron spin states (see chapter 4 for an explanation of the notation) respectively at the coercive field ( $H_c = +255$  Oe). The neutron spin notation is covered in chapter 4. The high sample roughness leads to a poorly defined specular ridge in both cases. Panel (a) has a strong Bragg sheet at  $Q_z = 0.048 \text{ \AA}^{-1}$  (1/2-order antiferromagnetic position) and a weaker Bragg sheet at  $Q_z = 0.092 \text{ \AA}^{-1}$  (1<sup>st</sup> order ferromagnetic position) and strong Yoneda features are visible at the 1/2 order position near the sample horizons. The Bragg sheets are from one sample horizon to the other, indicative of a short in-plane correlation length for the Co/Ru multilayer stack as well as a very high roughness as evidenced by the weak specular ridge. The **dd** neutron spin state (NSF) gives both magnetic and structural information, with only the components of the magnetisation parallel to the applied field giving rise to magnetic scattering (chapter 4). This is clearly the case at the 1/2 order AF peak with strong scattering being visible, as would be expected for a randomly orientated antiferromagnetic system at coercivity.

Panel (b) shows the **ud** neutron spin state (SF) and as such is only sensitive to magnetic scatter that is perpendicular to the applied field direction. In this case the scatter at the 1<sup>st</sup> order position almost completely disappears but the intensity

remains strong at the  $1/2$  order position. This implies that the scatter at the  $1^{st}$  order position for the **dd** NSF state is partly due to some ferromagnetic order in line with the applied magnetic field, with the roughness spreading the structural scattering out so much that it is barely visible above the background.

Panels (a) and (b) of figure 6.8 show the reciprocal space maps for the **dd** and **ud** neutron spin states respectively at saturation ( $H_{sat} = +4120$  Oe). Both spin states again have very weak specular ridges. The NSF **dd** neutron spin state in panel (a) has strong scattering at the  $1^{st}$  order position forming a Bragg sheet from one sample horizon to the other due to the ferromagnetic alignment of the moments in the Co/Ru multilayer with the applied field. The  $1/2$  order AF peak has disappeared as expected for a magnetically saturated sample. The SF **ud** neutron spin state shown in panel (b) displays no scattering at all, as expected for a magnetically saturated system with all components of the magnetisation lying parallel to the applied field.

It should be noted that there are no scattering peaks visible due to the Co/Pt pillars, as the first Co/Pt Bragg peak is to be found at  $Q_z = 0.25 \text{ \AA}^{-1}$ , which is well outside the  $Q_z$  range of the reciprocal space maps. The Ru spacer layer is  $400 \text{ \AA}$  thick and would give rise to high frequency Kiessig fringes. However, due to the very high roughness these are most likely damped out and not visible.

In order to gain more quantitative information on the in-plane scattering features, rocking curves with a higher resolution were taken at the  $1/2$  order AF and the  $1^{st}$  order positions for the **dd** spin state. These are shown in panels (a) and (b) of figure 6.9. The Yoneda wings are clearly visible for the  $1/2$  order AF position ( $Q_x = \pm 0.6 \times 10^{-3} \text{ \AA}^{-1}$ ). However the first in-plane features would be found at  $Q_x = \pm 0.86 \times 10^{-3} \text{ \AA}^{-1}$  which is outside the accessible range in  $Q$  space at this  $Q_z$ , although the intensity between the Yoneda wings and the specular is highly similar to the plateau of intensity shown by the Cu  $K_\alpha$  x-rays on figure 6.4.

Panel (b) shows the rocking curve for the **dd** neutron state at the  $1^{st}$  order position. There are no in-plane features at the expected positions with a gentle decrease in intensity to the sample horizons. There is a slight increase in intensity at either side of the rocking curve where reduced Yoneda features push up the intensity slightly.

Neutron hysteresis loops are shown in panels (a) and (b) of figure 6.10. It is not

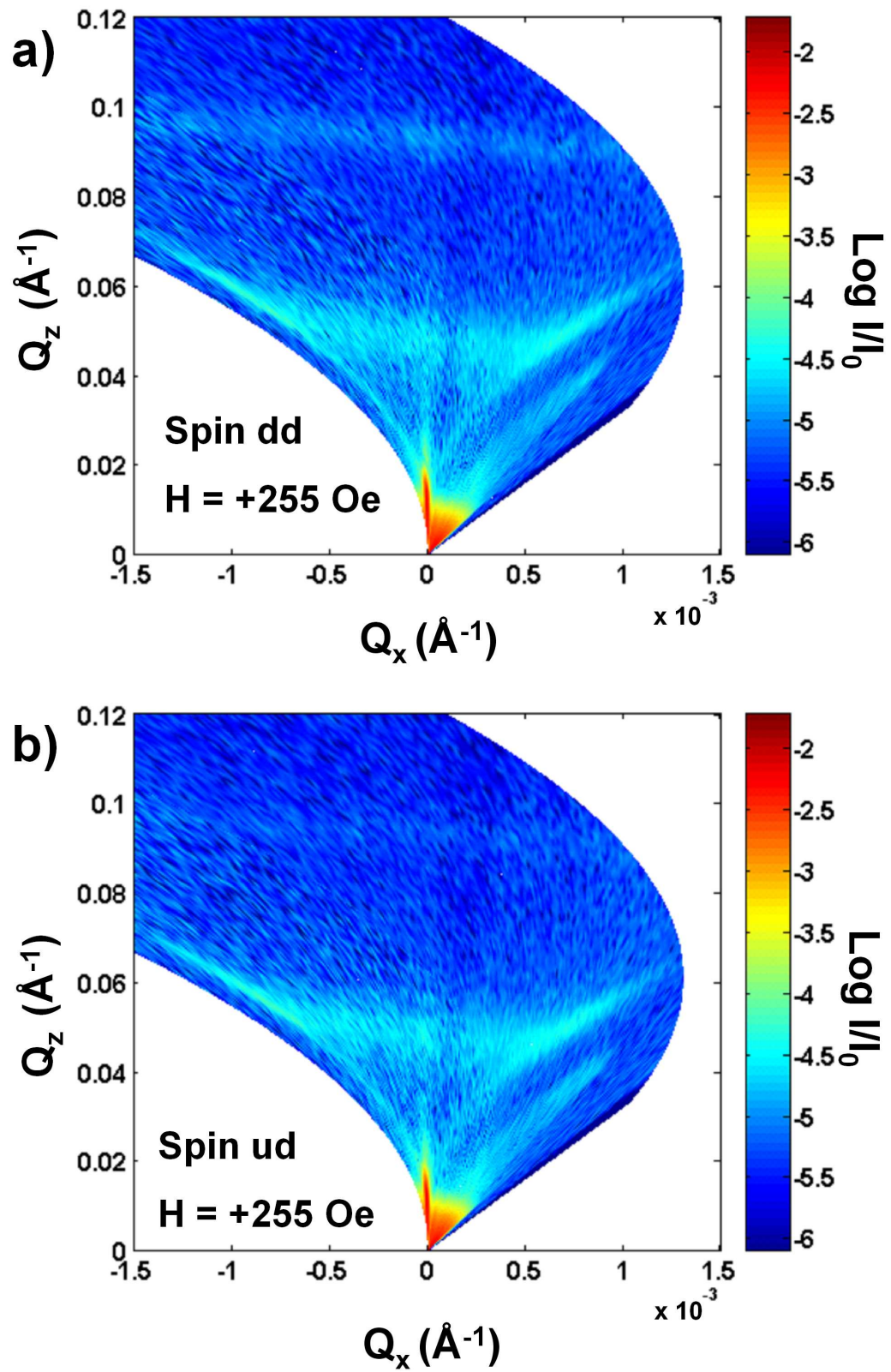


Figure 6.7: Sample A: The colour bar shows the logarithm of the reflected intensity as a fraction of that measured at the beam monitor. a) Spin **dd** neutrons at  $H = +255$  Oe. b) Spin **ud** neutrons at  $H = +255$  Oe.

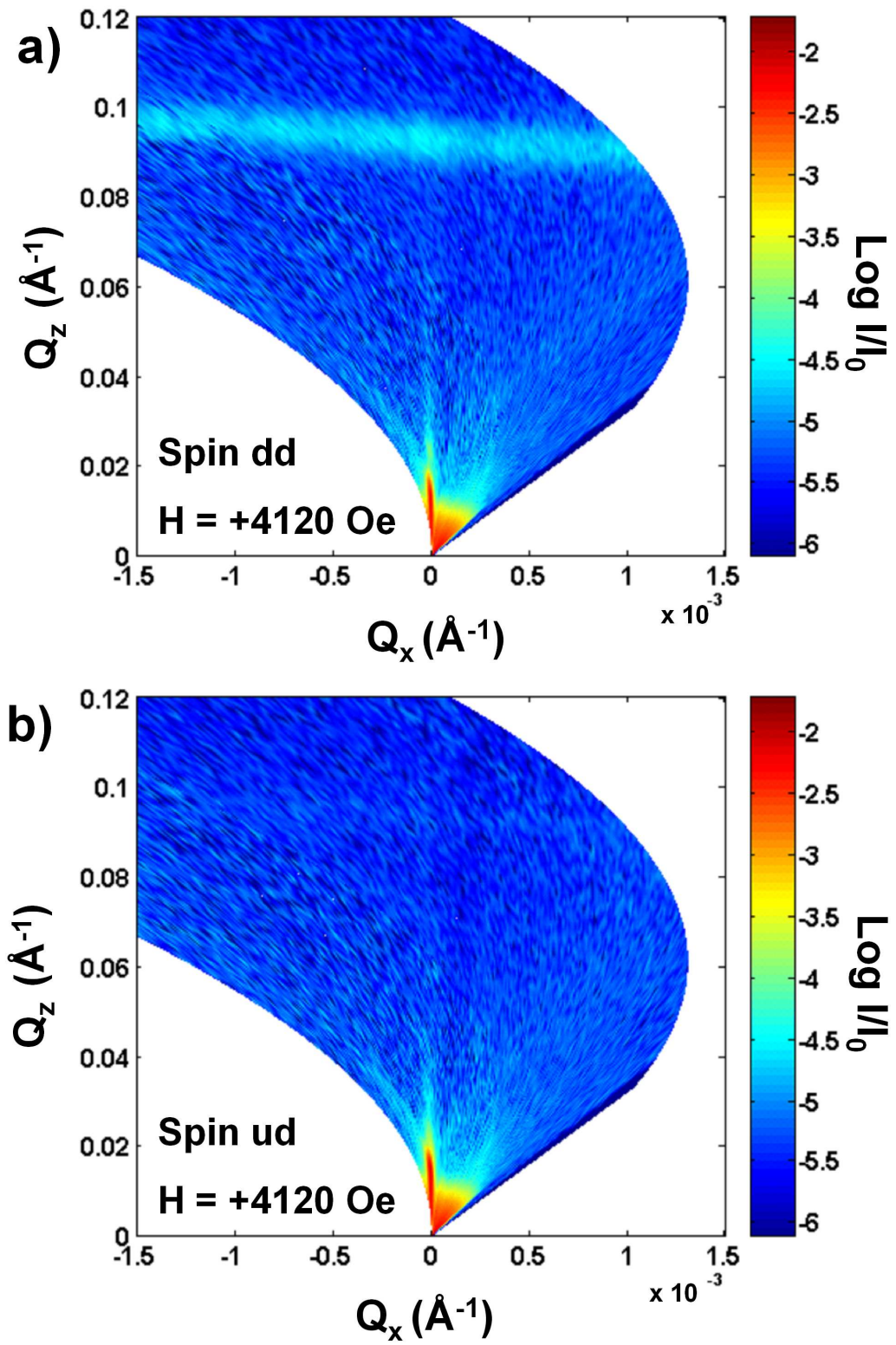


Figure 6.8: Sample A: The colour bar shows the logarithm of the reflected intensity as a fraction of that measured at the beam monitor. a) Spin **dd** neutrons at  $H_{sat} = +4120$  Oe. b) Spin **ud** neutrons at  $H_{sat} = +4120$  Oe.

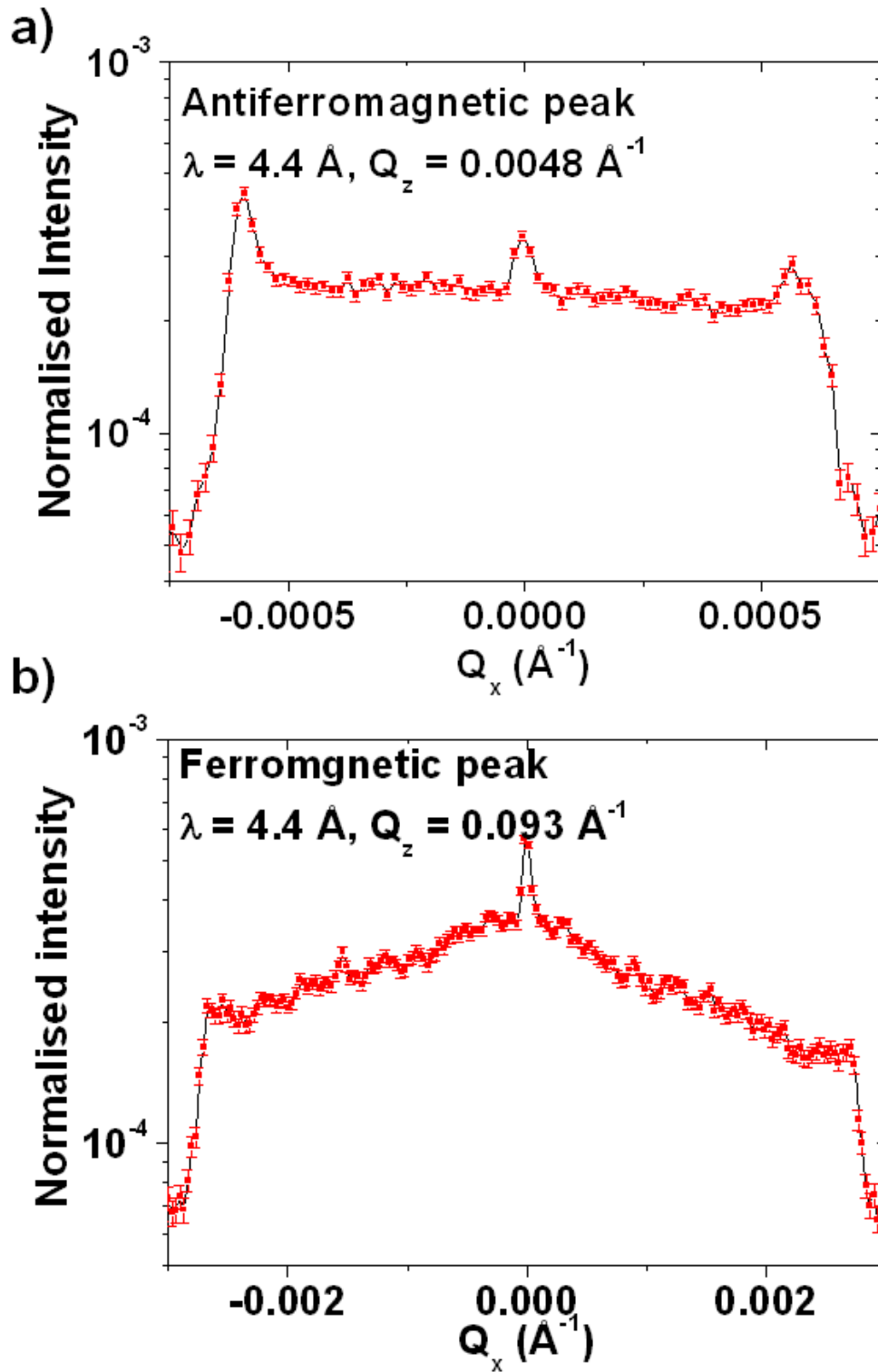


Figure 6.9: Sample A: a) Rocking curve antiferromagnetic peak for **dd** neutrons  $Q_z = 0.048 \text{ \AA}^{-1}$  at  $H = +255 \text{ Oe}$ . b) Rocking curve at the ferromagnetic peak for **dd** neutrons  $Q_z = 0.093 \text{ \AA}^{-1}$  at  $H_{sat} = +4120 \text{ Oe}$ .

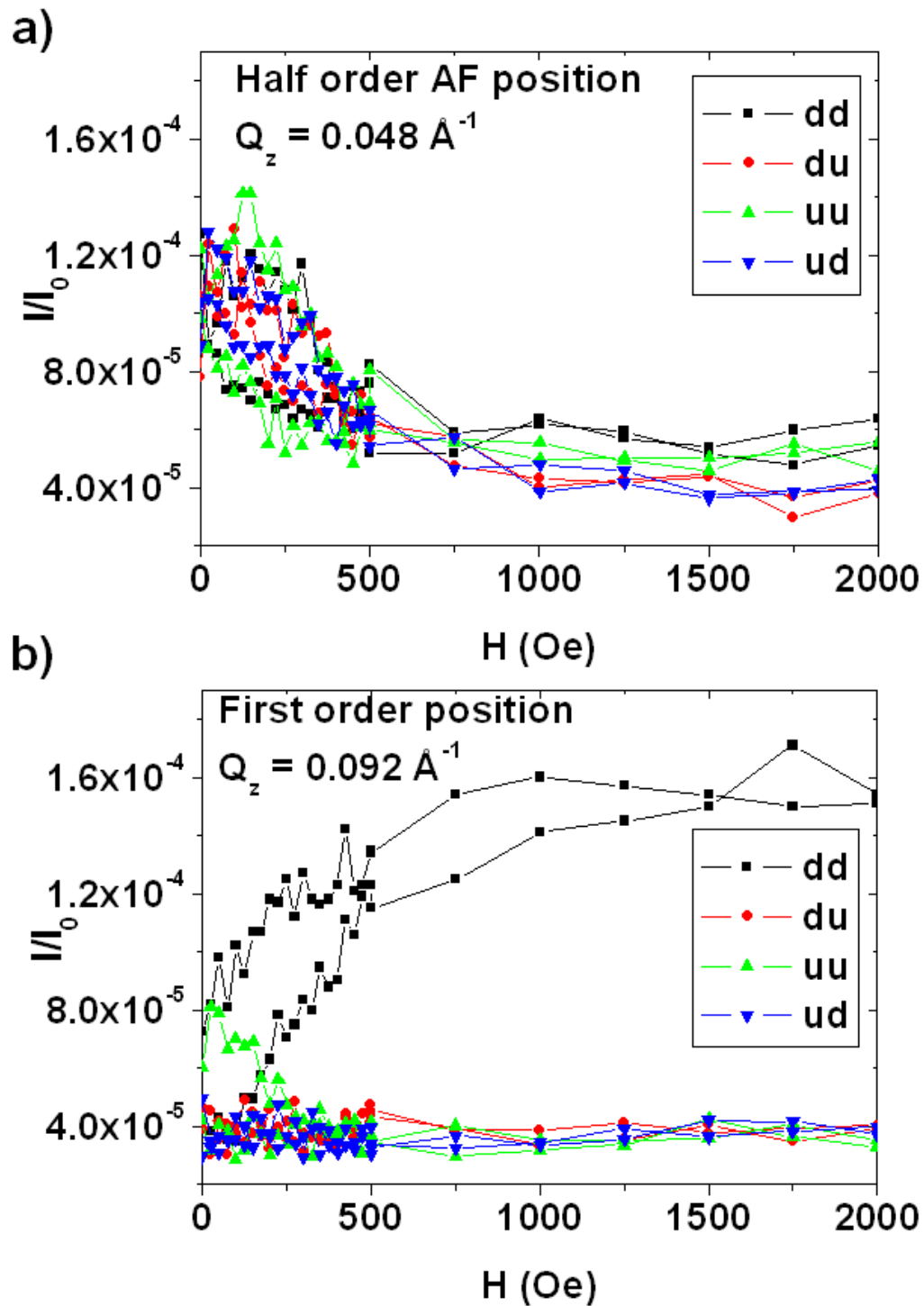


Figure 6.10: Sample A: Hysteresis loops for the **uu**, **dd**, **ud** and **du** spin channels. a) The  $1/2$  order position  $Q_z = 0.048 \text{ \AA}^{-1}$ . b) Hysteresis loops at the  $1^{st}$  order position  $Q_z = 0.093 \text{ \AA}^{-1}$ .

possible to perform PNR with the sample in a negative field as this causes depolarisation of the neutron beam at the zero crossing. For this reason only the positive field values of the hysteresis loop are measured. However reversing the neutron spin states is the same as reversing the field. The samples are saturated in both positive and negative field directions beforehand to negate measuring the virgin hysteresis curve.

Panel (a) shows the hysteresis loop taken at the 1/2 order AF specular position for all four neutron spin states. All four spin states show intensity at low field, indicating that there are components of the magnetisation both (anti)parallel and perpendicular to the incident neutron polarisation in line with a random AF domain structure. This intensity is reduced to background after  $\approx 700$  Oe when the sample starts to be magnetically saturated and the AF unit cell is swept out of the Co/Ru stack. The fact that there is scattering for the NSF neutron states indicates that the return to an antiferromagnetic state for the antiferromagnetic coupled moments is not perfect, possibly due to pinning by the magnetic modulation introduced to the Co/Ru from the Co/Pt pillars. There is a slight peaking in intensity for the NSF neutron states around 200 Oe, this being just below the coercivity of the Co/Ru multilayer, while the SF neutrons show normal increase in intensity as the field is decreased towards remanence. This increase in intensity near 200 Oe could be due to the reformation of AF domains, hence the increase in scattered intensity. Panel (b) shows the neutron hysteresis at the first order specular position. The SF neutron states show low intensity at all fields indicating that there are negligible magnetisation components perpendicular to the neutron spin. The NSF neutron states however both show intensity. For small fields  $I_{uu} > I_{dd}$  indicating that there are some components of the Co/Ru magnetisation that are parallel to the incident neutron spin near remanence.  $I_{dd}$  increases in intensity building to a maximum around  $\approx 700$  Oe. This implies that the magnetic reversal occurs via domain nucleation rather than coherent rotation, as a coherent rotation of the magnetisation would at some point increase the intensity in the SF scattering channels[148].

### 6.4.2 Soft X-ray Magnetic Scattering Study

An initial survey was undertaken on Sample B. Energy scans were performed to find the Co absorption edges. The results for the scan with  $\theta$  set to  $10^\circ$  are shown in figure 6.11. The Co  $L_{II}$  edge was found at an energy of 715.5 eV and the Fe  $L_{III}$  edge at 702.9 eV. These are shifted from literature values of 706.8 eV ( $\lambda \sim 17.6 \text{ \AA}$ ) and 719.9 eV ( $\lambda \sim 17.2 \text{ \AA}$ ) respectively[159], the slight shift from the tabulated values being due to our reflection geometry. The maximum in the SA was found to be close to the  $L_{III}$  edge at 772.5 eV. For the purposes of the experiment all measurements were made with energy set to give the biggest spin asymmetry on the Co  $L_{III}$  resonance at this energy of 772.5 eV.

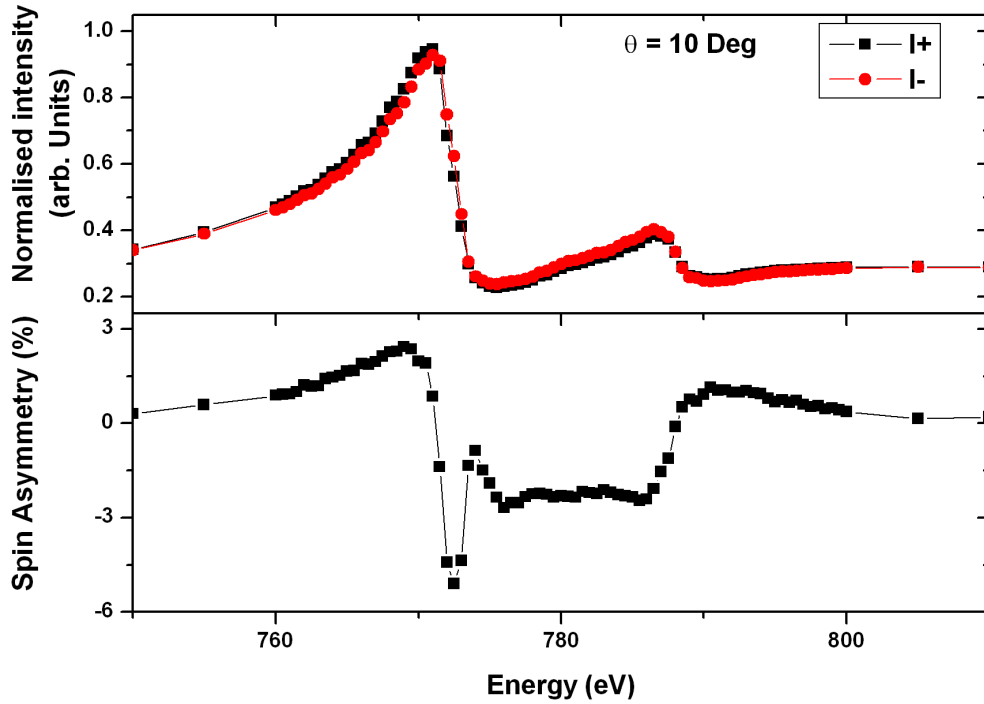


Figure 6.11: Energy scan with  $\theta = 10^\circ$  over the Co  $L_{II}$  and Co  $L_{III}$  edges for sample B.

Initial specular  $\theta/2\theta$  scans were taken on and off the Co  $L_{III}$  resonance and are shown in figure 6.12 panels (a) and (b), with the corresponding spin asymmetry plots in panels (c) and (d). Both on and off resonance there is a clear feature at  $Q_z =$



$0.108 \text{ \AA}^{-1}$ . This is in agreement with the Cu  $K_\alpha$  x-rays shown in figure 6.6 for the first order Co/Ru Bragg peak. No  $1/2$  or  $3/2$  order AF peaks were observed in the specular scatter which is in keeping with other studies using SXRMS [102] on Co/Ru multilayers. In the on resonance case the Bragg peak is slightly suppressed, probably due to absorption of the beam in the sample, while off resonance (750 eV) it is more clearly resolved, which is most likely due to more of the sample being penetrated by the non-resonant x-rays. The effects of tuning to the Co  $L_{III}$  resonance can be more easily seen in the spin asymmetry panels (c) and (d) of figure 6.12. There is clear magnetic structure visible in panel (c) at  $Q_z = 0.108 \text{ \AA}^{-1}$ , which must be from the Co in the Co/Ru multilayer. Off resonance this feature disappears, confirming the Bragg peaks' magnetic character. Again it should be noted that any scattering from the Co/Pt pillars would be found beyond  $Q_z = 0.3 \text{ \AA}^{-1}$ . Moreover there is the further point that the  $400 \text{ \AA}$  Ru spacer helps to prevent any photons from reaching the Co/Pt, allowing separation of the Co/Ru stack.

In order to probe the lateral magnetic structure, transverse  $Q_x$  scans were taken at the  $1^{st}$  order ( $Q_z = 0.108 \text{ \AA}^{-1}$ ) Bragg position on and off the Co  $L_{III}$  resonance. Figure 6.13 (b) shows the  $Q_x$  scan at the  $1^{st}$  order Bragg peak for applied fields corresponding to saturation and coercivity. The positions of the in-plane Bragg peaks are in excellent agreement with the Cu  $K_\alpha$  x-ray data shown in figure 6.13 (a). The satellite peak positions are also in agreement with what would be expected for their positions via  $Q_x \approx 2\pi/d$ , which for a centre to centre nanosphere separation of  $780 \text{ nm}$  gives a spacing in  $Q_x$  of  $\approx 8 \times 10^{-4} \text{ \AA}^{-1}$ . It is also clear that the  $Q_x$  scans at coercivity are slightly more intense than the  $Q_x$  scans at saturation due to there being more lateral ferromagnetic (F) disorder at coercivity. There is good agreement between both the  $I^+$  and  $I^-$  curves at both saturation and coercivity indicating that the in-plane F domain disorder is strongly correlated to the structural modulation. This becomes more evident when looking at the SA shown in figure 6.13 (c). The SA shows that at saturation there is definitely magnetism locked on the structural modulation. At coercivity any correlation of the ferromagnetic domains and the structure are very weak as there is no net magnetization, but peaks are still just about visible, probably due to the fact that the sample was not quite at coercivity

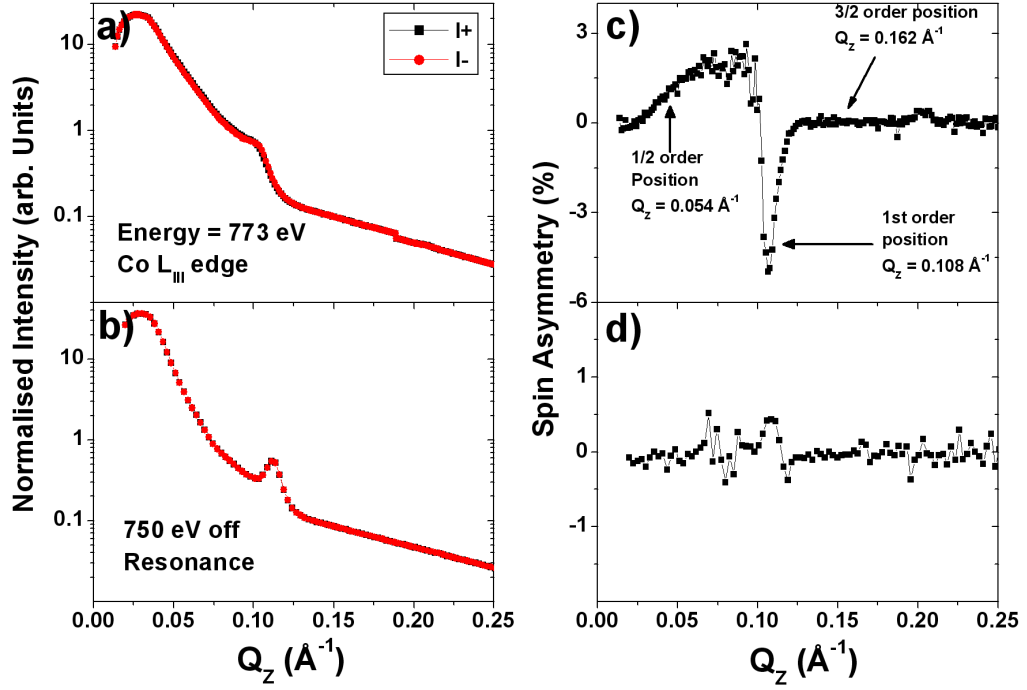


Figure 6.12: Specular scans on and off the Co  $L_3$  resonance and corresponding spin asymmetry plots.

during the measurements.  $Q_x$  scans were also taken at the 1/2 order position (not shown) in order to be sensitive to the nominal lateral AF disorder between the Co layers in the Co/Ru multilayer. The curves displayed the same general features and behavior as the 1<sup>st</sup> order  $Q_x$  scan, indicating some crossover between the AF and F order parameters in both cases. A Gaussian fit to the first  $-Q_x$  in-plane Bragg peak gives a coherence length of  $\approx 5000$  nm for the dots, comparing well with the SEM data, while a fit to the diffuse background (with in-plane features removed) gives an in-plane random roughness correlation length  $\approx 420$  nm, which is of the same order as the size of the Co/Pt dots upon which the Co/Ru was deposited.

An advantage to the SXRMS technique is that by measuring the intensity variation as a function of applied field, it is possible to measure hysteresis loops[104][160]. Loops were taken at both the 1st order and 3/2 order specular positions in  $Q_z$  and are shown in figure 6.15 along with a VSM measurement over the same field range. The first

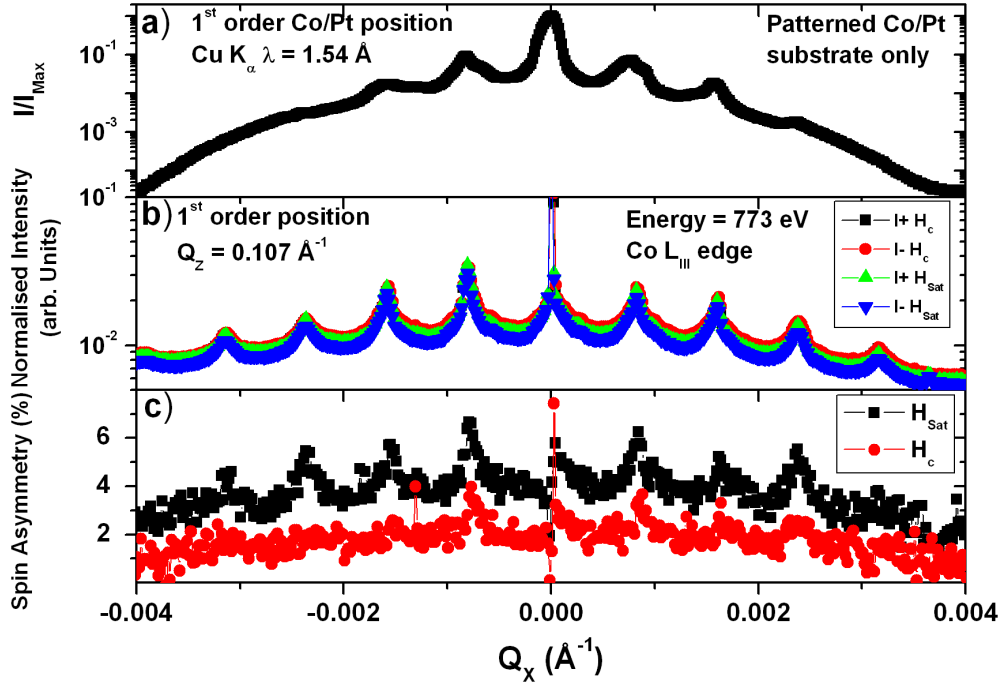


Figure 6.13: a) Cu  $K_\alpha$  x-rays on the Co/Pt patterned substrate. b) Co  $L_{\text{III}}$  resonance  $Q_x$  scans at the 1<sup>st</sup> order Co/Ru Bragg Position ( $Q_z = 0.107 \text{ \AA}^{-1}$ ) at saturation and coercivity. c) Spin asymmetry at saturation and coercivity.

Co/Pt feature is to be found at  $Q_z = 0.42 \text{ \AA}^{-1}$  hence the hysteresis measurements are sensitive to the Co/Ru multilayer stack only.

The 1<sup>st</sup> order specular loop compares well to the corresponding minor VSM loop, implying that it is largely the macroscopic magnetisation of the structure that is being probed. Hysteresis loops were also taken at the positions of the first trough and in-plane Bragg peaks in  $Q_x$  (not shown) as these off specular loops are sensitive to in-plane structure such as domains[104]. These were found to be of the same shape indicating that the magnetic disorder is similar over a range of length scales up to  $15 \text{ }\mu\text{m}$ . The loop taken at the  $3/2$  position in  $Q_z$  is sensitive to the AF magnetic structure between the Co layers in the Co/Ru multilayer. The unconventional loop shape is due to the intensity peaking at the coercive fields of the Co/Ru, where the greatest amount of AF order is present, and this then dies off as the AF order is swept out of

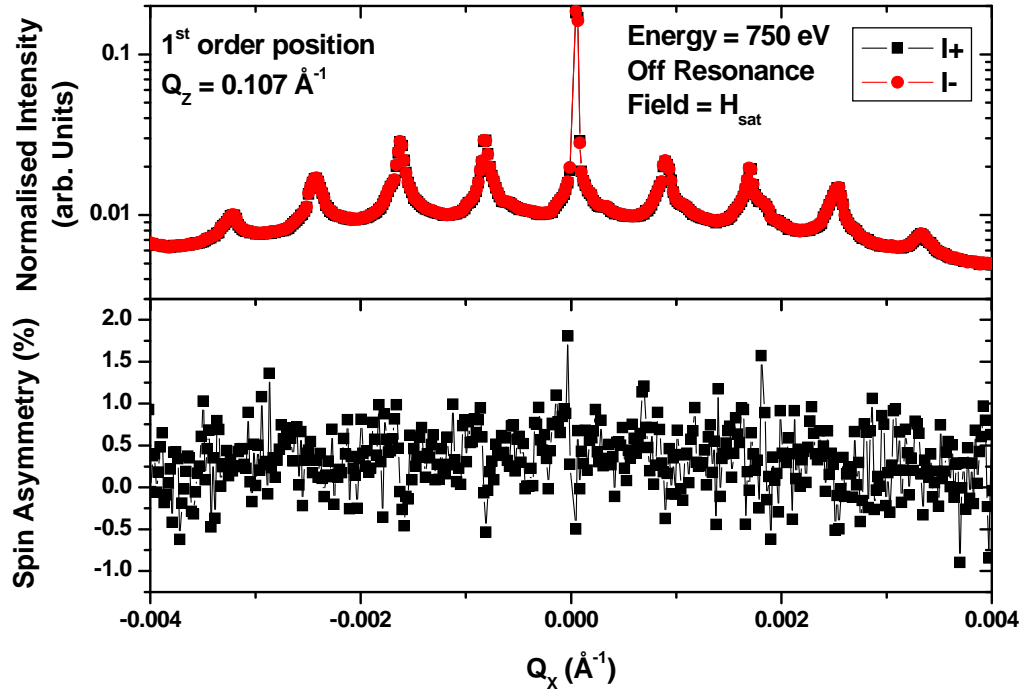


Figure 6.14: Rocking scan off resonance ( $E=750\text{eV}$ ) at saturation.

the sample. These loops are similar to the loops observed in giant magnetoresistance measurements (GMR), which are known to be sensitive to AF order[104] and show a peak in the magnetoresistance when the AF disorder is at a maximum as a function of applied field. There is also a marked similarity to the **uu** and **dd** NSF neutron spin channels in figure ?? (c) at the  $1/2$  order AF position, which also peak about 200 Oe. However care must be taken when comparing the two samples due to the differences in fabrication and the fact that sample B is on the  $3^{\text{rd}}$  AF coupling peak and sample A is on the  $2^{\text{nd}}$  AF coupling peak. So one would expect qualitative but not quantitatively similar behavior.

Magnetic roughness can have multiple forms such as lateral domain patterns, a non uniform height distribution of the moments, or vectorial differences in the directions the moments point. It has been shown in chapter 5 that it is possible to measure the domain disorder only, with minimal contributions from the chemical disorder, and that the structure and magnetism are discernable from each other using SXRMS.

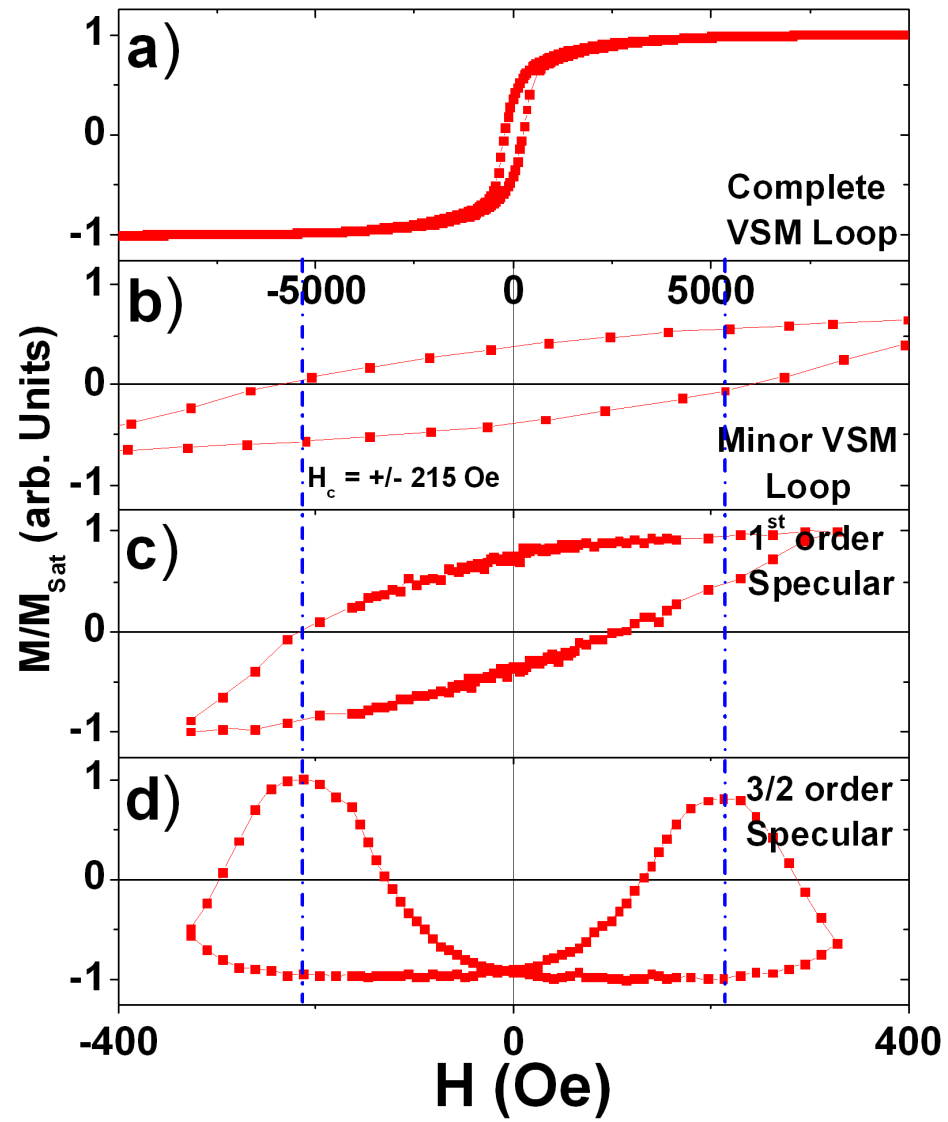


Figure 6.15: a) Full in-plane VSM Loop. b) Minor in-plane VSM loop. c) SXRMS hysteresis loops at the 1<sup>st</sup> order specular position. d) SXRMS hysteresis loops at the 3/2 order specular position.

Langridge *et al.* [154] have shown that the domain disorder does not necessarily correlate with the structural disorder in the active multilayer, while the magnetic roughness is driven by the structural feature size. In this case we pattern both the structural modulation and the domain modulation. It is clear that the magnetic roughness in samples A and B locks in on the structure at saturation, for both the PNR and the SXRMS data. However, the lack of any structural features in the PNR Rocking curve data hinders comparison. Any magnetic domain disorder has little influence since it is locked to the domain structure of the dots below the active Co/Ru multilayer. This is backed up by the SXRMS hysteresis loops which do not vary in shape as a function of  $Q_x$ , which probe the different length scales. It seems reasonable that different forms of magnetic roughness interact with the structure to different extents.

## 6.5 Summary

In conclusion, the SXRMS data show that the magnetic roughness follows the structural modulation at saturation, with little sensitivity to the magnetism at coercivity due to the low net magnetization. This is to some extent backed up by the PNR data, as the reciprocal space map in figure 6.8 (a) shows a strong structural/ferromagnetic Bragg sheet. However the rocking curve taken at that position reveals no in-plane structure due to sample quality after Co/Ru deposition.

It is possible to obtain a variety of hysteresis loops as a function of position in reciprocal space, using both PNR and SXRMS. By selecting the correct position in reciprocal space it is possible to select which part of the sample is measured (in this case the Co/Ru multilayer rather than the Co/Pt dots), while moving into the diffuse scatter allows different lateral length scales to be probed. We saw that the magnetic disorder was similar over a range of length scales out as far as  $15\ \mu\text{m}$  from the SXRMS data. In addition the PNR data gave some insight into the magnetic reversal processes in the multilayer system, indicating that it is facilitated by domain nucleation. However, there were issues with sample fabrication for sample A, which were resolved by the time sample B was fabricated, the result being that the scattering data did not provide much insight into how the structural and magnetic modulation

affected the magnetic roughness of the AF coupled Co/Ru. The SXRMS results have since been published by Kinane *et al.* [161] and presented at the Baltimore Magnetism and Magnetic Materials conference (MMM) 2007.

## Chapter 7

# CoRu Alloying at the interfaces of Co/Ru multilayers

### 7.1 Introduction

So far the effects of magnetic domains and structural modulation have been probed in flat Py and an antiferromagnetically (AF) coupled Co/Ru multilayer respectively. The next step was to investigate the effects of grading/magnetic dead layers[130] at the interfaces of a multilayer, in this case Co/Ru, and find out how it affects the magnetic structure and magnetic behavior of the multilayer system. It has been noted that alloying can quench moments at the interfaces of multilayers[127]. To do this antiferromagnetically coupled Co/Ru multilayers[2] were fabricated with a deliberate CoRu alloy layer deposited at the interfaces to simulate grading. This alloying of the interfaces should have some effect on the interlayer exchange coupling. The period of interlayer exchange coupling can be controlled by altering the thickness of the spacer layer, or by influencing the Fermi wavevector  $k_F$ . The former method has been extensively studied [2] due to its technological importance. Studying the variation of  $k_F$  is not as easy to achieve experimentally. Methods employed to vary  $k_F$  have involved alloying the spacer layer[162, 163] or incorporating hydrogen into the spacer layer [164]. We have altered  $k_F$  by introducing a solid solution of Co and Ru at the interfaces of a Co/Ru AF coupled multilayer.

Polarised neutron reflectivity measurements were taken at the CRISP beamline at ISIS to investigate the antiferromagnetic order as a function of temperature on a Co/Ru sample with no alloying at the interface and one with 6Å of CoRu alloy



deposited at the interface. A quick review of work done in a similar vein on Co/Ru systems using a variety of techniques follows, in order to provide some insight into the presented work.

## 7.2 Co/Ru Multilayer Review

Oscillatory exchange coupling was discovered by Parkin *et al.* in Co/Ru[2] in 1990. They fabricated a series of multilayers with different Ru layer thicknesses, and found that the magnitude of the saturation field and subsequent GMR oscillated as a function of the Ru spacer layer thickness, with a period of  $\approx 12 - 14 \text{ \AA}$ . This oscillation was also seen in Co/Cr and Fe/Cr systems, however with larger oscillation periods. This effect was linked to the Ruderman-Kittel-Kasuya-Yosida (RKKY) interaction with the longer oscillation period later being explained by lattice aliasing[165]. This is where the RKKY waveform is sampled at a rate below the Nyquist frequency producing a longer wavelength oscillation.

The behaviour of the exchange coupled Co/Ru as a function of temperature has been studied by several groups. Co/Ru hcp superlattices have been reported to display perpendicular magnetic anisotropy for Co thicknesses  $< 15 \text{ \AA}$  by Dinia *et al.* [166] and Sakurai *et al.* [167]. Dinia *et al.* also noted that the magnetoresistance oscillations had a different shape and phase of oscillation between RT and 4.2 K, which they attributed to CoRu alloying at the interfaces.

Zhang *et al.* [168][169] studied the temperature dependence of interlayer exchange coupling field  $H_{\text{ex}}$  and the effective anisotropy field  $H_{\text{eff}}$  in Co/Ru/Co trilayer structures prepared in UHV by evaporation on mica substrates. They performed Nuclear Magnetic Resonance measurements (NMR) and determined that for their structures there was intermixing at the Co/Ru interfaces across 2 atomic layers. The temperature dependence was studied by Ferromagnetic resonance (FMR) and Brillouin light scattering (BLS) to observe how  $H_{\text{ex}}$  and  $H_{\text{eff}}$  varied with temperature, noting how both decreased upon warming from 50 K to 300 K. They only observed an increase in oscillation amplitude at low temperature, and that the phase and oscillation period were independent of temperature.

The effects of alloying at the interface have been studied by Rahmouni *et al.* [170],

who have performed simulations of the magnetic properties of Co/Ru interfaces as well as looking at the magnetic and transport properties of Co/Ru/Co sandwiches. They showed that the moment of the Co atoms at the interfaces decreased with increasing Ru concentration. They give results for MR simulations with perfectly flat and intermixed interfaces based on NMR measurements, which indicated intermixing of about 3 monolayers ( $6\text{\AA}$ ) through the interface. The results gave a magnetic profile which is composed of two parts: (i) a non magnetic region corresponding to a CoRu alloy with a high Ru concentration, (ii) a magnetic region with CoRu alloy with average Ru concentration but with a reduced magnetic moment from pure Co.

Furthering this Bakonyi *et al.* [171] tested the idea that CoRu alloy at the interfaces had a large effect on the interfacial magnetic and GMR properties of Co/Ru multilayers. They grew Co(Ru)/Ru multilayers, where  $\text{Co(Ru)} = \text{Co}_{98.5}\text{Ru}_{1.5}$  alloy, via electro deposition. They found that alloying Co with small amounts of Ru reduces the anisotropic magnetoresistance (AMR) ratio and points towards changes in the electronic band structure of the Co by Ru addition and hence an alteration of the Fermi surface.

Bloemen *et al.* [172] studied sputtered Co/Ru multilayers using VSM, MOKE and FMR techniques. They demonstrate that the preparation procedure, whether via sputtering or evaporation, is very important for the magnetic behaviour. They studied the effects of: (i) the number of bilayer repetitions on MOKE loops, (ii) the determination of the interlayer coupling on samples with perpendicular to plane anisotropy and samples with in-plane anisotropy. The sputtered bilayer samples displayed clear perpendicular magnetic anisotropy compared to evaporation grown samples where it was less well defined. They also noted an oscillating exchange coupling strength as a function of Ru thickness with a period of  $\approx 12\text{\AA}$  in agreement with other published work [2].

Interesting behaviour of exchange coupling has also been observed in systems other than Co/Ru, as a function of temperature. For instance Döbrich *et al.* [173] have observed a temperature induced sign reversal of magnetic interlayer exchange coupling in epitaxial trilayers of the magnetic rare-earth metals Gd and Tb.

Dinia *et al.* [174] studied the structural, magnetic and transport properties of

Co/Rh sandwiches grown by ultra high vacuum evaporation and sputtering. The samples had a very strong antiferromagnetic exchange coupling in the case of fcc (111) epitaxial grown Co/Rh while polycrystalline Co/Rh sandwiches had a value which was 10 times smaller. Both of these values are larger than that observed in Co/Ru in the reports mentioned above. They put the difference down to interfacial magnetism: the sharper the magnetic nature of the interface is, the higher is the electronic confinement in the spacer layer and, consequently, the larger is the interlayer exchange coupling. So clearly the quality of the interface can have dramatic effects on the magnetic properties of simple multilayer thin films.

### 7.3 Experimental

The samples were grown by d.c. magnetron sputtering as described in the sputtering section of chapter 1. The working gas was Ar at a pressure of 2.8 mTorr. The samples were deposited onto a (001)Si substrates. It should be noted that the samples were not grown in a magnetic field other than the stray field from the magnetron sputtering guns. The main sample in question has the following nominal structure which is also shown in figure 7.1:

$$[\text{CoRu}(6\text{\AA})/\text{Co}(34\text{\AA})/\text{CoRu}(6\text{\AA})/\text{Ru}(14\text{\AA})] \times 20.$$

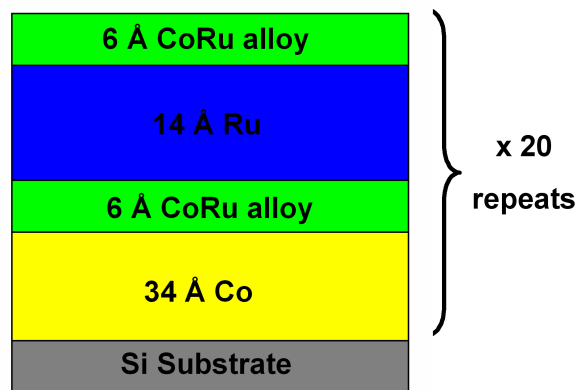


Figure 7.1: Sample Structure. Ru layer thickness corresponds to 2<sup>nd</sup> AF coupling peak.

The thickness of the Ru corresponds to the 2<sup>nd</sup> antiferromagnetic (AF) coupling peak [2]. The overall structural repeat unit thickness was selected to be  $\approx 60$  Å so as

to give a structural Bragg peak position of around  $0.1 \text{ \AA}^{-1}$  in reciprocal space. This is approximately the ideal position for the Q space range that the CRISP reflectometer is capable of reaching using a multidetector. The 2<sup>nd</sup> AF coupling peak gives strong AF coupling yet has a saturation field low enough to allow saturation by the 5 kOe magnet on the CRISP beamline.

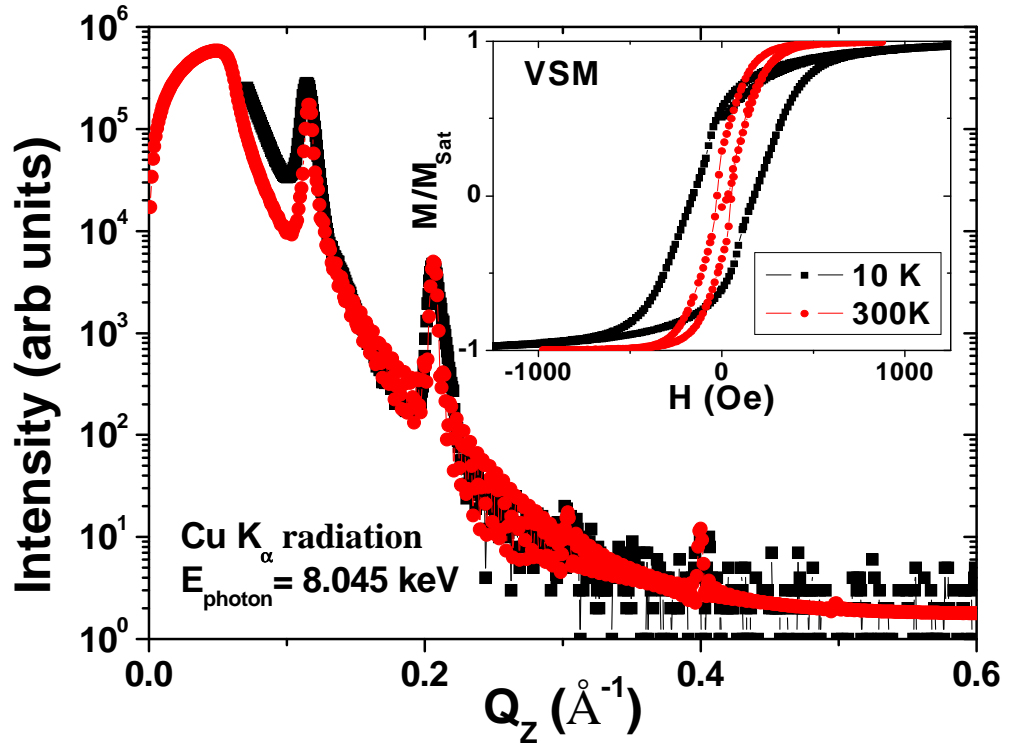


Figure 7.2: Specular x-ray reflectivity spectrum of the Co/Ru multilayer with  $6 \text{ \AA}$  of CoRu alloy at the interfaces, measured with Cu  $K_\alpha$  radiation. The black data points are experimental data whilst the red are the best fit using the Bede Refs Software package[95]. The insert shows the room temperature (300 K) and 10 K VSM hysteresis loops.

The overall repeat unit thickness was confirmed by specular reflectivity data taken using Cu  $K_\alpha$  x-rays, and is displayed in figure 7.2. The first two multilayer Bragg peaks are clearly visible, giving the multilayer repeat unit as  $\approx 58 \pm 3 \text{ \AA}$ . The lack of any visible Kiessig fringes indicates that the top and bottom surfaces of the stack are not correlated. The full width half maximum of the 1<sup>st</sup> order Bragg peaks shows

this to be the case giving a vertical structural correlation length of  $\approx 113$  Å, about two multilayer repeat units, where the total multilayer stack height is  $\approx 1200$  Å. The data were fitted using the Born approximation which gives the individual thicknesses as  $t_{Co} = 36 \pm 3$  Å,  $t_{Ru} = 14 \pm 3$  Å and  $t_{CoRu} = 5.5 \pm 3$  Å. Roughness of individual layers was found to be  $R_{Co} = 7 \pm 4$  Å,  $R_{Ru} = 12 \pm 5$  Å and  $R_{CoRu} = 5.6 \pm 6$  Å. These roughness values are actually the interface width which is defined as the sum by quadrature of the rms structural roughness and the grading, as explained in section 3.3.3 of chapter 3.

The inset of figure 7.2 shows VSM hysteresis loops taken at room temperature (300K) and at 10 K. There is a clear increase in coercivity at low temperature, as well as a slight increase in the canting of the loop indicating a more strongly antiferromagnetic alignment of the system. The saturation field is just under 1000 Oe thus allowing the sample to be fully saturated during the scattering experiment by the application of a field of 4.7 kOe which we will now refer to as  $H_{sat}$  from now on. The coercive field  $H_c$  was found to be 43 Oe.

Co and Ru are known to form a continuous series of solid solutions[175]. The  $Co_xRu_{1-x}$  alloy was obtained by co-deposition using the angled d.c. magnetron arrangement in the sputter system described in section 1.2 of chapter 1. The alloy was grown to be a nominal 50:50 ratio of Ru to Co, and the composition has been determined to be  $x \approx 0.53$  corresponding to respective deposition rates for Ru and Co of  $0.9\text{Å/s}$  and  $1\text{Å/s}$ . By tuning the amount of Co to Ru in the alloy it is possible to change the Curie temperature of the alloy, as shown in panels (a) and (b) of figure 7.3. These show data on the saturation and remnant magnetisations for a range of samples, where the growth rates were altered to grow different CoRu alloy compositions for a standard alloy thickness of  $280$  Å. Both panels show a rapid drop in the magnetisation as a function of Ru concentration. Below 40% ( $x \approx 0.4$ ) Ru the  $Co_xRu_{1-x}$  alloy is ferromagnetic at 300 K becoming paramagnetic above this concentration. Panels (c) and (d) show data on the saturation and remnant magnetisations as a function of temperature for the 50:50 CoRu alloy  $280$  Å sample from the initial concentration set. It is clear that the sample is paramagnetic at room temperature and has a Curie temperature  $\approx 50$  K.

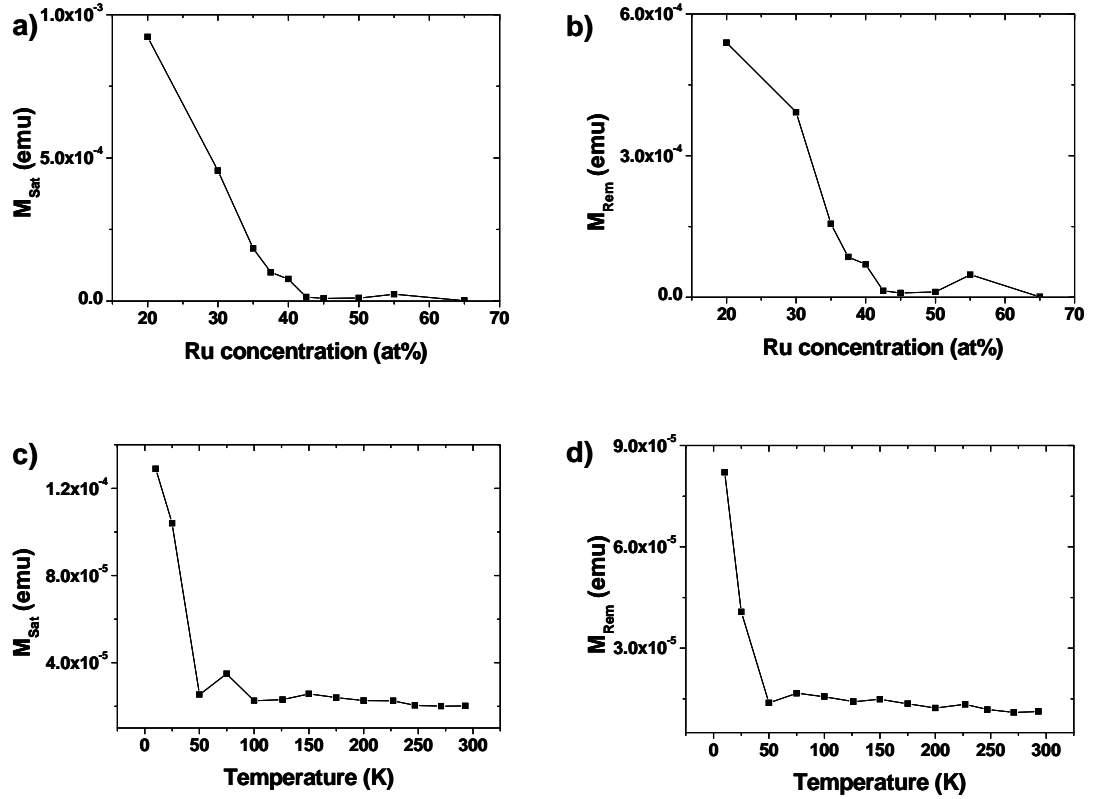


Figure 7.3: a) and b) Concentration dependence for 280 Å of CoRu alloy at 300K for  $M_{sat}$  and  $M_{rem}$  respectively. c) and d) Temperature dependence for 280 Å of CoRu alloy with a 50:50 (at%) ratio of Co to Ru for  $M_{sat}$  and  $M_{rem}$  respectively. All four data sets were measured by VSM.

Neutron reflectometry was carried out on the CRISP polarized neutron reflectometer at ISIS as discussed in chapter 2. The reflected neutrons were detected with a 1-dimensional  $^3\text{He}$  detector. The combination of the time-of-flight technique and the multidetector ensure that both the parallel  $Q_z$  and perpendicular  $Q_x$  (to the surface normal) components of the neutron wave-vector are obtained in a single measurement. Typical acquisition times are in the order of 2 hours for an entire reciprocal space map. In-plane reversible magnetic fields of up to 5 kOe were applied to the sample with an electro-magnet.

## 7.4 Results and Discussion

Two samples were measured at the CRISP beamline. The first was a control sample consisting of a simple Co/Ru multilayer with no deliberate alloying at the interface. It was deliberately fabricated to be on the 2<sup>nd</sup> AF coupling peak but with the same bilayer repeat spacing of 60Å. It has the following nominal structure:

$$[\text{Co}(42\text{\AA})/\text{Ru}(18\text{\AA})]\times 20,$$

and is referred to from now on as the clean sample. Neutron reflectivity multi-detector maps are shown for the **u** neutron spin state, in figures 7.4 and 7.5. Panel (a) of figure 7.4 shows the scattering at room temperature and in a field equal to the coercive field  $H_c \approx 43$  Oe of the sample. There is a large diffuse peak visible at  $Q_z = 0.053 \text{ \AA}^{-1}$  which is due to the AF order creating a magnetic unit cell at twice the structural unit cell space as shown by the schematic inset. A sharp structural peak is found as expected at  $Q_z = 0.106 \text{ \AA}^{-1}$  and the specular ridge is visible. A second inset shows a MOKE hysteresis loop of the structure which gives the sample coercivity as  $H_c \approx 43$  Oe and the saturation field as  $H_{sat} \approx 1000$  Oe. The AF order was seen to disappear upon magnetically saturating the sample using a field of  $H_{sat} = 4.7$  kOe, and then to return once the field had been cycled round the hysteresis loop back to  $H_c = 43$  Oe, confirming its magnetic origin. This was confirmed using single detector specular scans which are not shown. The sample was then cooled to 10K in an applied field of  $H_c = 43$  Oe. This reciprocal space map is shown in panel (b) of figure 7.4. All the main features present at 300 K are still present at 10 K.

Figure 7.5 panel (a) shows the neutron reciprocal space maps at 10 K for saturation, while figure 7.5 panel (b) shows the map with the field back at coercivity having cycled around the hysteresis loop. Panel (a) shows clearly how the AF disorder is swept out of the sample at saturation as the AF peak disappears. The main structural peak at  $Q_z = 0.106 \text{ \AA}^{-1}$  is seen to increase in intensity, as would be expected from the magnetic part of the neutron scattering factor coming into play. It is clear that the AF domain state returns upon cycling the sample back to the coercive field panel (b) however the width of the AF peak has increased. This is due to the field cycling destroying the virgin magnetic state and reducing the AF correlation length

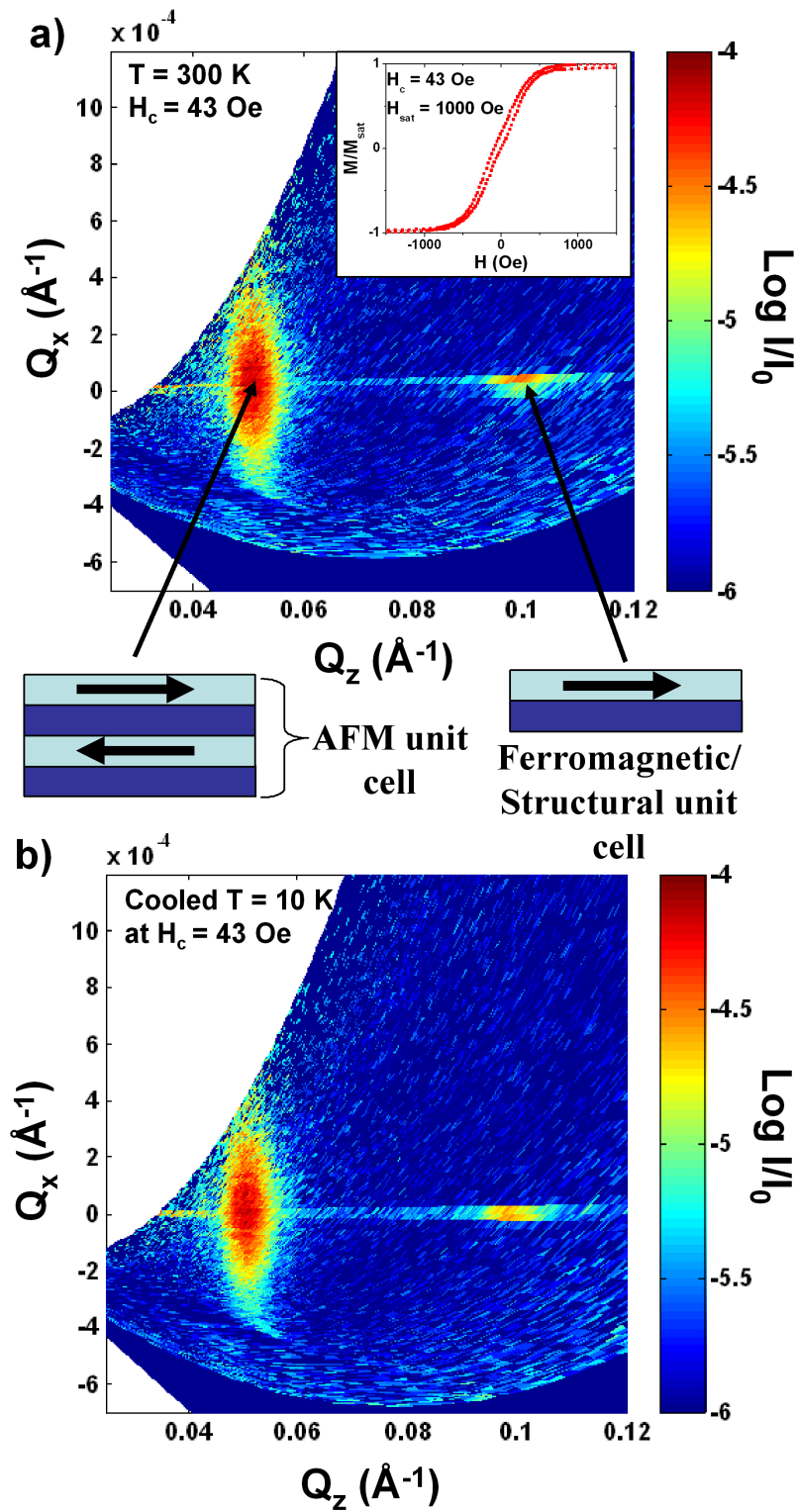


Figure 7.4: Reciprocal space map for spin  $\mathbf{u}$  neutrons. a) 300 K and  $H_c = 43 \text{ Oe}$  b) Sample cooled in a field of  $H_c = 43 \text{ Oe}$  to 10 K.



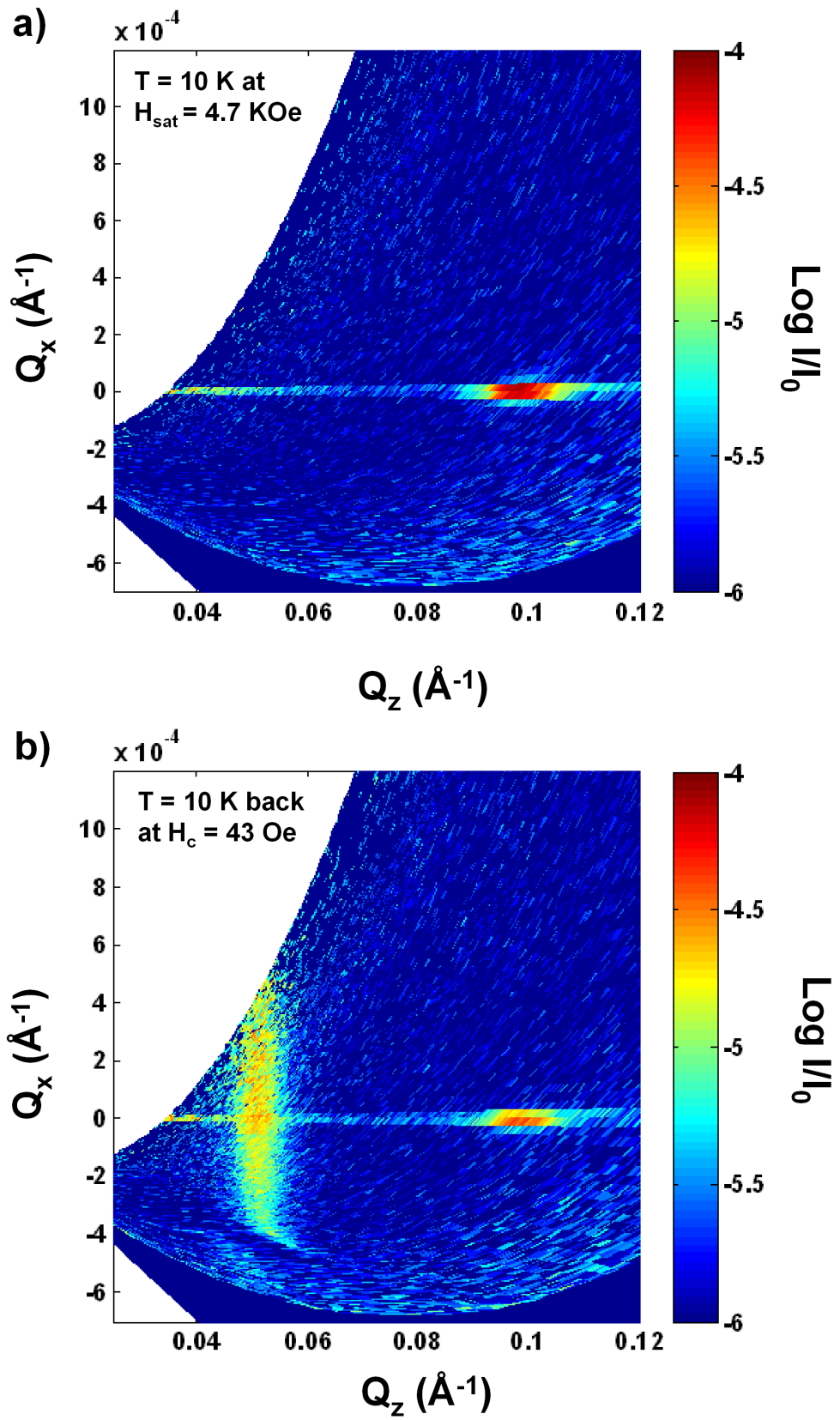


Figure 7.5: Reciprocal space map for spin  $\mathbf{u}$  neutrons. a) 10 K in a saturating field of 4.7 kOe. b) 10 K with the field brought back to  $H_c = 43$  Oe.

when the AF order reforms. This is all as expected for an AF coupled multilayer structure.

The interesting feature of this system comes from examination of the neutron data from the samples with alloying at the interfaces. Neutron reflectivity multi-detector maps are shown for the  $\mathbf{u}$  neutron spin state, in figures 7.6, 7.7, 7.8 and 7.9. Panel (a) of figure 7.6 displays the main scattering features of the system. There is a large diffuse peak visible at  $Q_z = 0.054 \text{ \AA}^{-1}$  which is due to the AF order creating a magnetic unit cell at twice the structural unit cell space, as shown in panel (a). A sharp structural peak is found as expected at  $Q_z = 0.108 \text{ \AA}^{-1}$ , although both are not as intense as those displayed by the clean sample. The specular ridge is less visible as well, as would be expected for a sample with grading present at the interfaces. The structural peak is seen to be spin split in the specular line cut along  $Q_x = 0 \text{ \AA}^{-1}$  shown in panel (b) as expected for a structural/ferromagnetic scattering peak, while the AF Bragg peak is not spin split as expected. Panels (c) and (d) show transverse  $Q_x$  line cuts along  $Q_z = 0.054 \text{ \AA}^{-1}$  and  $Q_z = 0.108 \text{ \AA}^{-1}$  positions respectively. There is a large area of diffuse scatter about the specular ridge in the AF  $Q_x$  scan indicative of a domain distribution[135] while the F  $Q_x$  scan is clean and sharp, which would be expected for a well correlated sample stack. Simple fitting of a lorentzian to the AF peak and extraction of the FWHM allows in and out-of-plane correlation lengths to be calculated ( $\xi_m = 2/\text{FWHM}$ )[102]. The AF correlations have a vertical correlation length of  $\approx 20 \text{ nm}$ , while fitting the off-specular diffuse scattering reveals the in-plane AF correlation length to be  $\approx 1 \text{ }\mu\text{m}$ .

Panels (a) and (b) of figure 7.7 show the behavior of the graded sample at room temperature upon application of a saturation field and when it is returned to coercivity. To get back to coercivity the sample was field cycling around the hysteresis loop. The only difference is a slight decrease in the intensity of the AF scattering peak. The sample was then cooled to 10K while at the coercive field  $H_c = 43 \text{ Oe}$ . Panel (a) of figure 7.8 shows the scatter from the sample at 10 K after cooling is the same as it was at 300K. Panel (b) shows the scatter upon applying a saturating field to the sample and again the system is the same as at 300K at this field. However, upon magnetically cycling the system and returning to coercivity both at  $H_c = 43$

Oe (shown), which is the 300 K value, and at  $H_c = 165$  Oe, which is the 10 K value, the AF scattering peak remains gone. This is shown in panel (a) of figure 7.9. No amount of AC demagnetising the sample at 10 K could get the AF disorder to return. The scattering was seen to reappear upon warming at around  $\approx 150 - 200$  K. Panel (b) of figure 7.9 shows the sample after it has been warmed back up in a field of 43 Oe, and the AF scatter has returned. This is unusual as the AF order should be more stable at the lower temperature and should reassert itself once the field is removed, and is at odds with the results for the clean sample and where the AFM coupling is stronger at low temperature and recoverable on field cycling.

In order to verify this counter intuitive behaviour, a section of the sample was placed in a VSM and a moment vs temperature sweep was performed, repeating the magnetic field history that the sample underwent during the neutron measurements. The results are displayed in figure 7.10. A hysteresis loop was recorded at 300K, saturating the sample and cycling around the hysteresis loop. This loop is shown in the top RHS inset of figure 7.10. Then a moment vs temperature curve was recorded while a constant field of 43 Oe was applied, shown by the black curve. The VSM automatically re-centers the sample every 10K to reduce any effect of expansion/contraction of the sample stick. The moment is seen to decrease as the temperature is reduced. The decrease in the signal is due to the change in the shape of the hysteresis loop between 300 K and 10 K. At 10 K another hysteresis loop was performed to again simulate magnetically saturating and cycling the sample. This is shown in the LHS inset. Both these loops agree well with the originals shown in the inset of figure 7.2. It is after the hysteresis loop has been taken and the system cycled around to 43 Oe for the moment vs temperature curve upon warming that the jump in the measured magnetisation appears. There is an increase of  $1 \times 10^{-4}$  emu which is the most important feature in this data. Upon warming, the new curve joins the old at approximately  $\approx 150$  K, the temperature that the AF coupling was found to reappear. A clean sample was also measured with both warming and cooling curves matching well.

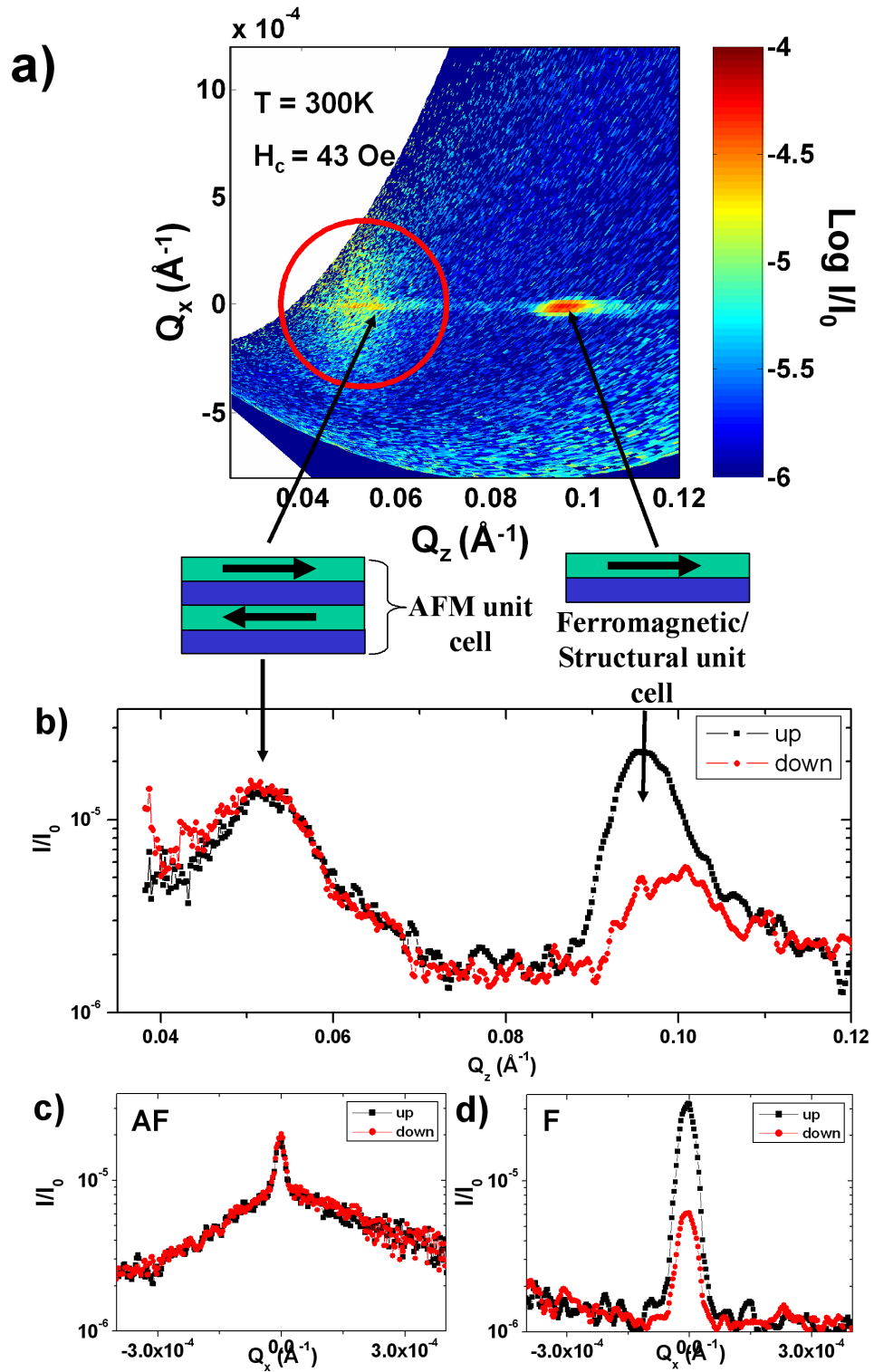


Figure 7.6: Neutron data at a temperature = 300K and at coercivity (43 Oe): a) Reciprocal space map for spin **u** neutrons. b) Specular line cut along  $Q_z = 0 \text{ \AA}^{-1}$  c) Transverse  $Q_x$  line cut along  $Q_z = 0.054 \text{ \AA}^{-1}$  d) Transverse  $Q_x$  line cut along  $Q_z = 0.108 \text{ \AA}^{-1}$

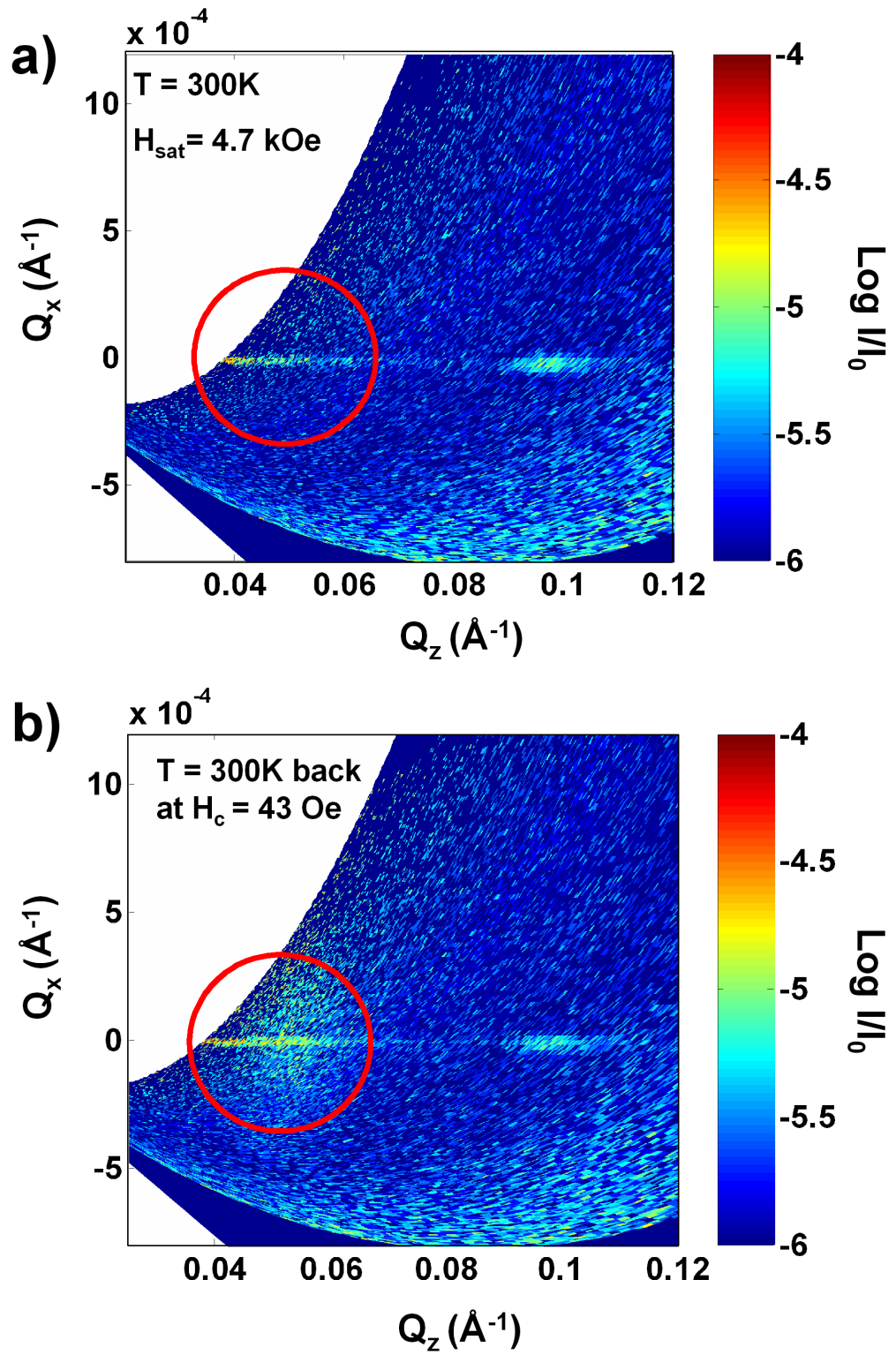


Figure 7.7: Reciprocal space maps: a) 300K at saturation, b) 300K back at coercivity after field cycling.

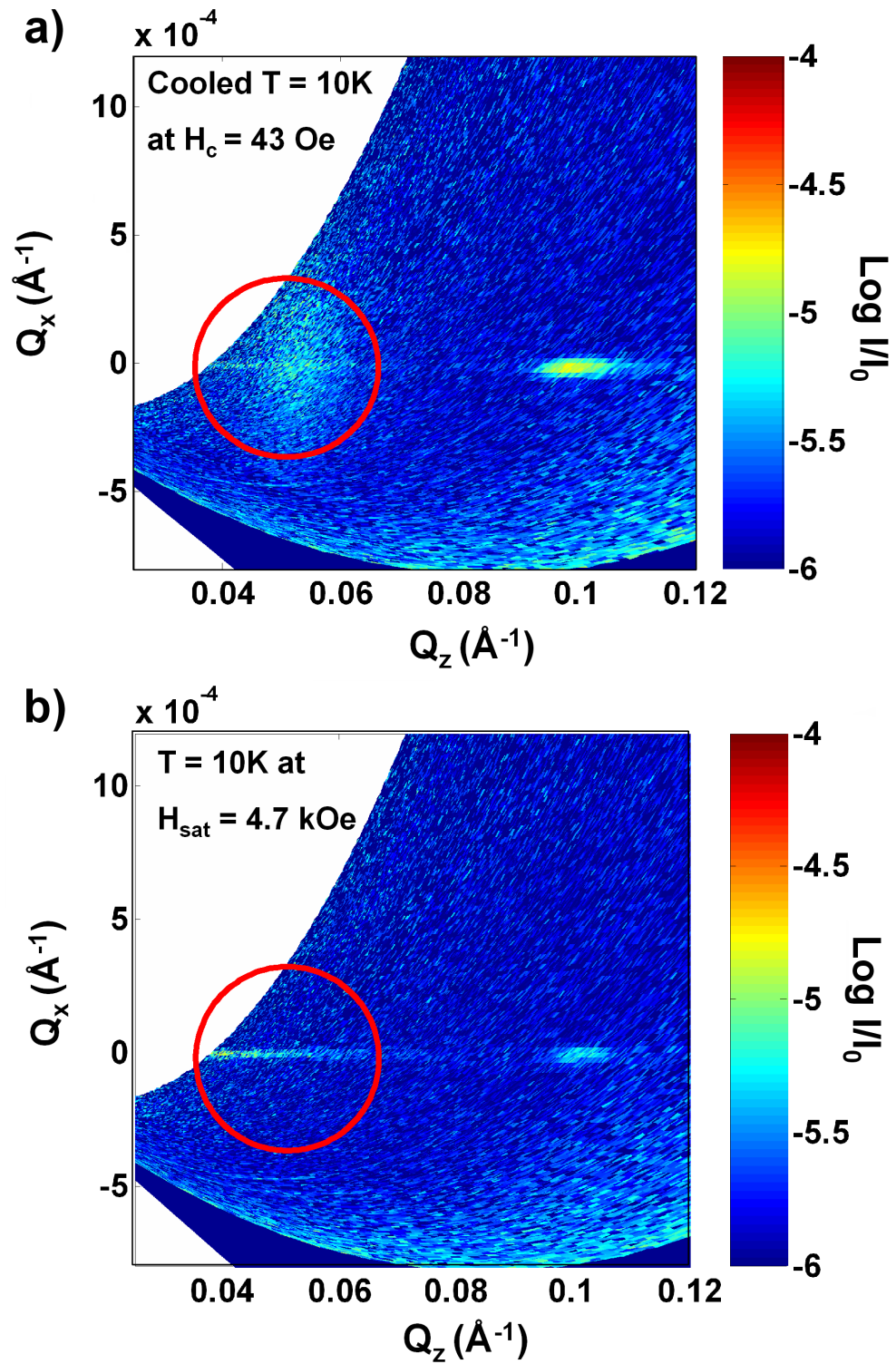


Figure 7.8: Reciprocal space maps: a) After cooling to 10K in the coercive field, b) 10 K in a saturating field of 4.7 kOe. The AF disorder is swept out of the system and the AF scattering disappears.



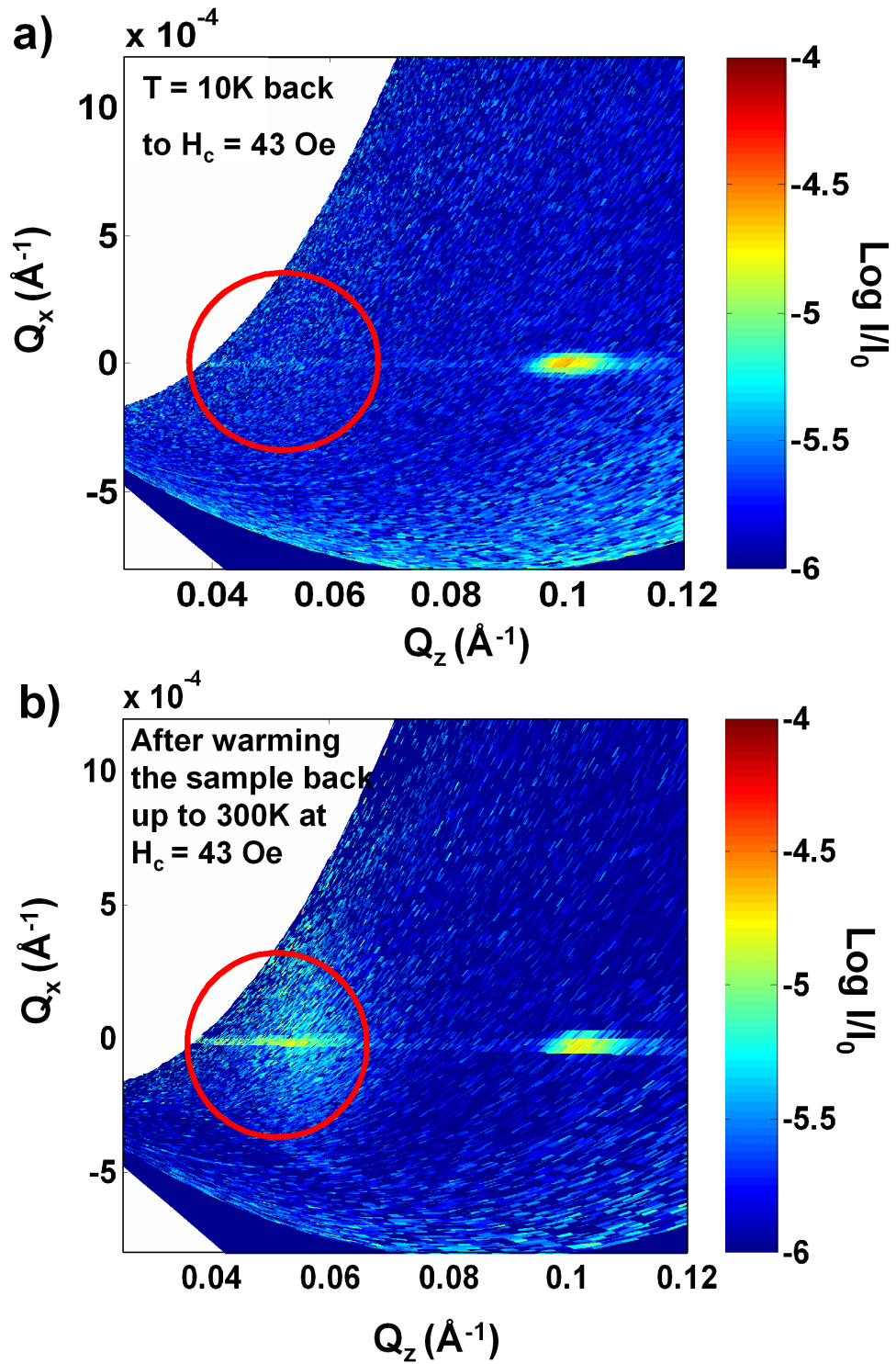


Figure 7.9: Reciprocal space maps: a) 10 K with the field brought back to  $H_c = 43$  Oe after field cycling. Note that the AF scattering is still absent. b) Warmed back up to 300 K at coercivity (43 Oe). Note that the AF scatter has returned.

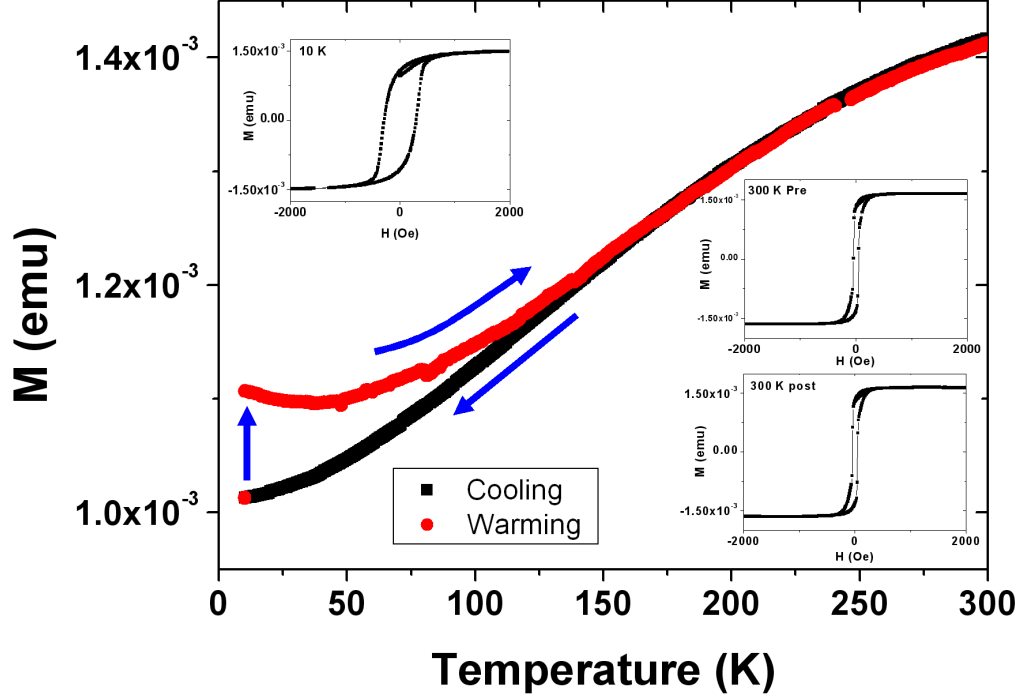


Figure 7.10: VSM moment vs temperature sweep following the field history of the PNR neutron experiment. The sample is warmed and cooled in a field of 43 Oe with full field cycling at room temperature and 10K.

At present the reason for this counter intuitive behaviour seen with both the neutrons and the VSM is not known. One possible explanation was that the effective thickness of the spacer changes with temperature. The Curie temperature for 50:50 CoRu alloy is approximately 50 K. Hence, when cooled below this temperature, the alloy moves from being part of the spacer layer to being part of the ferromagnet, effectively changing the spacer layer thickness and shifting the sample into a ferromagnetic state. This would in theory give the same coupling period but different phases at RT and 10K. To this end a series of samples was grown with the same structure as the neutron sample,  $[\text{CoRu}(6\text{\AA})/\text{Co}(34\text{\AA})/\text{CoRu}(6\text{\AA})/\text{Ru}(x)] \times 20$ , but the thickness of the spacer was varied from  $1\text{\AA} \leq x \leq 30\text{\AA}$  in a similar way to the original oscillatory exchange coupling experiments by Parkin *et al.* [2]. These samples were measured by VSM at both 300K and at 10K and the saturation field  $H_{\text{sat}}$  determined for each



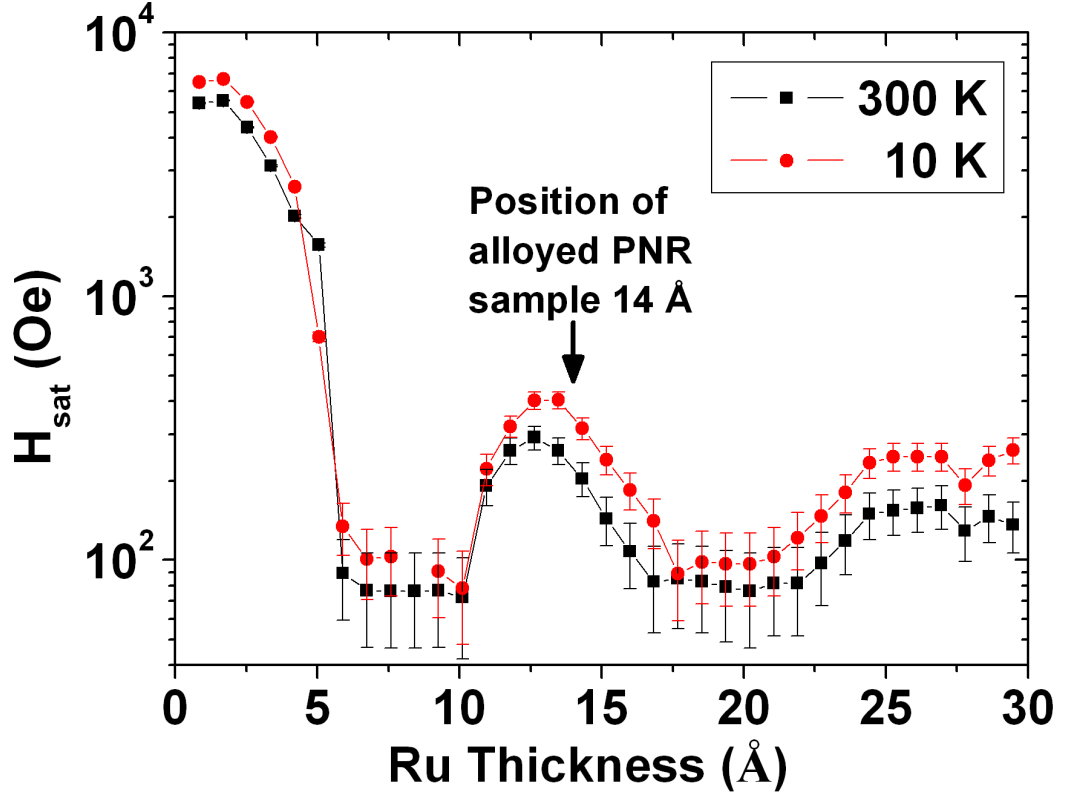


Figure 7.11: Coupling curves of  $[\text{Co}/\text{Ru}]\times 10$  with  $6\text{\AA}$  of 50:50 CoRu alloy at the interfaces at 10 K and 300 K

loop. In this case  $H_{\text{sat}}$  was taken to be the field value at 95% of the  $M_{\text{sat}}$ .

These data are displayed in figure 7.11. There is no obvious phase shift between room temperature and 10K. The main effect of alloying is to reduce the over coupling strength and shift both room temperature and 10K curves back by the same amount of one alloy layer thickness. However  $6\text{\AA}$  of CoRu alloy is probably only enough material to form a monolayer or two of material. This fact in addition to the error on the thickness calibration, for the coupling curve samples gives an estimated accuracy of  $\pm 4\text{\AA}$ , making it seem unlikely that any shift between 300K and 10K would be easy to see. However, this does not explain why the AF order is only destroyed on saturation of the sample at low temperature.

## 7.5 Summary

In conclusion, it is clear that the introduction of a thin CoRu alloy layer to deliberately simulate a graded interface has an effect on the AF coupling as a function of temperature.

- AF correlations observed at room temperature.
- AF correlations exist at low temperature but are destroyed by a saturating field.
- AF correlations restored upon warming.

An odd effect is also seen in the VSM data taken to repeat the field history of the neutron experiment. When there was magnetic saturation of the sample below the curie temperature of the alloy (50K), there was an increase in the magnetisation. None of these effects were seen on clean samples with either the neutrons or the VSM measurements. The simplest explanation of a temperature dependent change in the spacer layer thickness was inconclusive, with no shift in the coupling oscillation being observed between 300K and 10K in the measured coupling curve.

The most promising route to an explanation is the determination of the anisotropies of the system at both room temperature and 10K[176, 177]. The CoRu alloy interfaces seem to undergo some magnetic change as a function of temperature, and as a result the interface anisotropy may also change. This is a possible explanation for the odd effects seen with the neutrons, as the saturating field could pull all the moments into an easy axis direction. Due to the anisotropy strengthening on cooling, this would then prevent the system getting back to an AF state after saturation and would also explain the return of the AF order when the sample is warmed.

## Chapter 8

# Conclusion

The main aims of this thesis were to investigate how physical structural disorder affects the magnetic structure and disorder in several artificial magnetic multilayer systems, by making use of the complementary techniques of SXRMS and PNR. This was done after first testing, again by careful sample design, the ability of the SXRMS technique to measure magnetic disorder. Effects of a second form of structural disorder, in the form of grading at the interfaces of a coupled Co/Ru multilayer, were also studied using PNR to find out how it altered the temperature dependence of the system.

### 8.1 Conclusion

We have investigated a domain pattern imprinted on a structurally smooth permalloy layer and detected off-specular satellite peaks in the soft x-ray resonant magnetic scattering, corresponding to a periodic magnetic modulation. These appeared in the sum signal ( $I^+ + I^-$ ) but were extremely weak in the difference ( $I^+ - I^-$ ), indicating that the magnetism self-correlation function contains a strong periodic part which is almost absent from the structure-magnetism cross-correlation function. Thus we have exploited the element specific features of SXRMS to discern the purely magnetic correlations with little or no overlap from the charge and charge-magnetic cross correlations. This is in good agreement with Osgood *et al.* [137].

Following on from magnetically patterning a flat magnetic layer, we have patterned a Co/Ru multilayer grown on the 2<sup>nd</sup> (sample A) and 3<sup>rd</sup> (sample B) antiferromagnetic coupling peaks. Sample A was investigated by PNR and sample B with SXRMS. Only

a qualitative comparison was possible due to fabrication issues with the removal of the latex nanospheres. The SXRMS data shows that the magnetic roughness follows the structural modulation at saturation, while there is little sensitivity to the magnetism at coercivity due to the low net magnetization. This is to some extent backed up by the PNR data, which shows strong Bragg sheet scattering at the ferromagnetic position upon saturation. However, the rocking curve taken at that position reveals no in-plane structure due to sample quality after Co/Ru deposition. It was possible to obtain a variety of hysteresis loops as a function of position in reciprocal space, using both PNR and SXRMS. By selecting the correct position in reciprocal space it is possible to select which part of the sample is measured (in this case the Co/Ru multilayer rather than the Co/Pt dots), while moving into the diffuse scatter allows different lateral length scales to be probed. From the SXRMS data, we saw that the magnetic disorder was similar over a range of length scales, out as far as  $15\text{ }\mu\text{m}$ . In addition the PNR data gave some insight into the magnetic reversal processes in the multilayer system, indicating that it is facilitated by domain nucleation.

We investigated the effect of deliberate grading at the interface of an antiferromagnetically coupled Co/Ru multilayer as a function of temperature. It is clear that the introduction of a thin CoRu alloy layer has an effect on the AF coupling. In summary the AF scattering is observed at room temperature and is maintained as the system is cooled down to 10K. However, the the AF correlations are destroyed upon magnetically saturating the system and are not recovered upon field cycling the system. The AF correlations reappear at about 150 K upon warming. An effect is also seen when repeating the magnetic field and measuring the moment of the sample as a function of temperature in a VSM. When there was magnetic saturation of the sample below the Curie temperature of the alloy (50K), there was an increase in the magnetisation. None of these effects were seen on clean samples with either the neutrons or the VSM measurements. The simplest explanation of a temperature dependent change in the spacer layer thickness was inconclusive, with no shift in the coupling oscillation being observed between 300K and 10K in the measured coupling curve sample series.

This work has shown the complementary techniques of PNR and SXRMS in studying the effects of magnetic and chemical roughness at the interfaces, as well as demonstrating that small defects like the presence of  $6\text{\AA}$  of alloy at the interface can have a large effect on the behaviour of the whole system.

## 8.2 Future Work

The work on the domain patterning with SXRMS on a flat magnetic layer has reached a suitable point of conclusion. The next logical progression in this work would be to introduce a known structural modulation and to examine the effects on a single permalloy layer. Some preliminary work has been done with this in mind. In this case a sample with the following nominal structure was fabricated on a Co/Pt multilayer substrate that had been patterned into a nano-dot array via the method described in section 1.4 of chapter 1. A drawing of the desired structure is shown in figure 8.1.

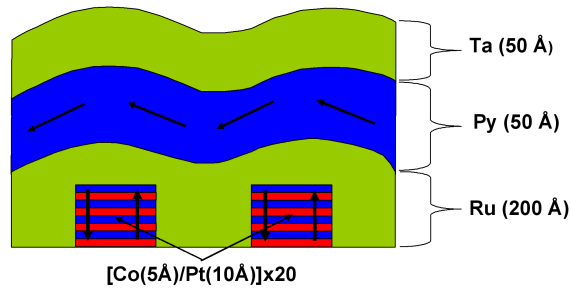


Figure 8.1: Depiction of a possible new sample structure.

An attempt to fabricate a sample like this was made. However due to issues with patterning the Co/Pt substrate into dots similar to that involved with the fabrication of the nano dot samples, the resultant preliminary scattering data was uninterpretable. However this would be a logical stepping stone to the nanosphere patterned samples studied in chapter 6.

As for the nanosphere samples the ongoing work on improving the sample fabrication during this research hindered the neutron experiments, in that the substrates were not adequately clean enough to provide good in-plane features once the second multilayer structure was deposited. The result of this was that the substrate

roughness was not periodic enough to give any periodic structure in the off specular scattering. This would be an ideal system to use on the new PolREF beamline currently under construction at ISIS Target station 2. The higher resolution and intensity as well as the greater range in  $Q$ , coupled with the planned implementation of an XYZ magnet stage, would allow the roughness in a system such as this to be more completely probed.

There is plenty of scope for future work within the subject matter of deliberately adding grading to the interfaces of the multilayers and the subsequent effect on the magnetic properties. In the case of the Co/Ru multilayers discussed there are several questions unanswered, as there is no obvious mechanism for the behaviour of the AF correlations at low temperature. It is clear that several avenues of investigation are still open.

For instance, the determination of the anisotropies of the system at both room temperature and 10K[176, 177] would be of interest. The CoRu alloy interfaces seem to undergo some magnetic change as a function of temperature, and as a result the interface anisotropy may also change. This is a possible explanation for the odd effects seen with the neutrons, as the saturating field could pull all the moments into an easy axis direction resulting in a stable ferromagnetic structure due to the weakened exchange coupling caused by the alloying. A study of the texture of the interfaces and the Co/Ru alloy would also be useful in this regard[174].

Another point worth investigating would be to further study the CoRu alloy material on its own, to see if it has any spin glass or super paramagnetic properties that might have some effect on the properties of the multilayer system.

## Chapter 9

## Appendix A : Publications:

## Soft x-ray resonant magnetic scattering from an imprinted magnetic domain pattern

C. J. Kinane,<sup>a)</sup> A. K. Suszka, C. H. Marrows,<sup>b)</sup> and B. J. Hickey

*School of Physics and Astronomy, E. C. Stoner Laboratory, University of Leeds, Leeds LS2 9JT, United Kingdom*

D. A. Arena

*National Synchrotron Light Source, Brookhaven National Laboratory, Upton, New York 11973-5000*

J. Dvorak

*Department of Physics, Montana State University, Bozeman, Montana 59717*

T. R. Charlton and Sean Langridge

*ISIS, Rutherford Appleton Laboratory, Chilton, Didcot OX11 0QX, United Kingdom*

(Received 27 March 2006; accepted 20 July 2006; published online 1 September 2006)

The authors report on the use of a Co/Pt multilayer, which exhibits strong perpendicular magnetic anisotropy, to magnetostatically imprint a domain pattern onto a 50 Å thick Permalloy layer. Element specific soft x-ray magnetic scattering experiments were then performed so as to be sensitive to the magnetic structure of the Permalloy only. Off-specular magnetic satellite peaks, corresponding to a periodic domain stripe width of 270 nm, were observed, confirmed by magnetic force microscopy and micromagnetic modeling. Thus the authors have exploited the element specificity of soft x-ray scattering to discern the purely magnetic correlations in a structurally flat Permalloy film. © 2006 American Institute of Physics. [DOI: 10.1063/1.2344935]

Proper knowledge and control of structural and magnetic disorder at the interfaces of thin film and multilayer heterostructures is important both technologically and scientifically. The applications of these systems include hard disk media,<sup>1</sup> magnetic random access memory,<sup>2</sup> and other spintronic devices.<sup>3</sup> Soft x-ray resonant magnetic scatterings<sup>4</sup> (SXRMS) makes use of the large source intensities and tunable nature of the incident photon energy available at synchrotron facilities. By tuning to an absorption edge for a specific element, a large enhancement to the magnetic scattering is obtained with the advantage of being element specific. Diffuse magnetic scatter is generated by lateral magnetic inhomogeneities<sup>5</sup> and can be easily observed with SXRMS.<sup>6</sup> Although a powerful technique for these reasons, difficulties in the interpretation of data can arise due to the indirect nature of the spin-photon interaction, as compared to neutrons.<sup>7</sup> This makes it hard to separate the structural and magnetic contributions: for circularly polarized photons, the difference in scattering for the two opposite helicities of photons has been shown to be related to cross correlations between structure and magnetism,<sup>8,9</sup> while intensity related to purely magnetic autocorrelations is found in the sum signal, where it is usually dwarfed by scattered intensity from the structural autocorrelations. Recent x-ray studies have taken advantage of controlled structural disorder to study the cross correlations.<sup>10,11</sup>

In this letter we report on the SXRMS investigation of the magnetic domain pattern imprinted on a structurally smooth Permalloy (Py=Ni<sub>80</sub>Fe<sub>20</sub>) layer by a Co/Pt multilayer, which exhibits strong perpendicular magnetic anisotropy and, hence, forms a stripe domain state that gener-

ates a strong stray field just above its surface. The Py is separated from the Co/Pt multilayer by an 80 Å thick Ta layer, ensuring that the only coupling between the layers is magnetostatic. As shall be seen, the structural roughness in this sample is very low and, thus, we have exploited the element specific features of the SXRMS to discern the purely magnetic autocorrelations in the sum signal. (There has been work undertaken using magneto-optic diffraction on periodic domain structures<sup>12</sup> produced by magnetostatic coupling.)

The samples were prepared using dc magnetron sputtering at a partial pressure of 2.8 mTorr of Ar, in a chamber with a base pressure of  $\sim 5 \times 10^{-9}$  Torr. The nominal structure of the samples is shown in Fig. 1(d). In-plane and out-

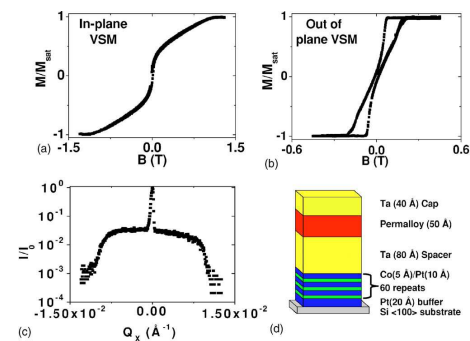


FIG. 1. (Color online) In-plane (a) and out-of-plane (b) VSM hysteresis loops for the completed sample, the structure of which is shown in panel (d). The important parts are a structurally smooth Py film separated from a perpendicularly magnetized Co/Pt multilayer by a thin Ta spacer. (c) Diffuse rocking scan using Cu K $\alpha$  radiation measured at the detector angle corresponding to the Co/Pt multilayer Bragg peak.

<sup>a)</sup>Also at: ISIS, Rutherford Appleton Laboratory, Chilton, Didcot OX11 0QX, United Kingdom.

<sup>b)</sup>Electronic mail: c.h.marrows@leeds.ac.uk



of-plane vibrating sample magnetometer (VSM) hysteresis loops are shown in Figs. 1(a) and 1(b). The data in Fig. 1(b) clearly show the features for out-of-plane magnetization.<sup>13</sup> The structure was initially characterized by x-ray reflectometry using Cu  $K\alpha$  radiation. The first order Bragg peak for the Co/Pt multilayer is the strongest feature in the specular scan, giving a bilayer repeat thickness of  $\sim 18$  Å. A rocking scan on the Co/Pt Bragg peak is shown in Fig. 1(c). The interfacial roughness was determined by the method employed by Savage *et al.*,<sup>14</sup> giving an interfacial roughness of  $\sim 2.5$  Å. The specular scan also contained Kiessig fringes, the separation of which give a thickness of  $\sim 170$  Å corresponding to the total thickness of the Ta(80 Å)/Py(50 Å)/Ta(40 Å) layers atop the Co/Pt multilayer. Rocking curves were also taken at these positions giving a roughness of  $\sim 5.4$  Å. Atomic force microscopy images showed the sample surface roughness to be  $\sim 7.5$  Å. Hence, although roughness is accumulated through the stack, the Py layer is structurally smooth, with subnanometer roughness. This value is consistent with the result of a distorted wave born approximation fit<sup>15</sup> to the specular Cu  $K\alpha$  data (not shown).

The samples were then taken to the U4B beamline at the National Synchrotron Light Source, Brookhaven.<sup>16</sup> The x rays used were 90% circularly polarized and the reflected intensity was normalized using a Au grid monitor upstream of the entrance slits to the scattering chamber. A field of up to  $\pm 300$  Oe could be applied in both the plane of the sample and the scattering plane; this defines the  $x$  axis of our coordinate system. The  $z$  axis is the sample normal, with the x rays incident from the top of the sample. In accordance with earlier studies,<sup>6,17</sup> at each point in reciprocal space the scattered intensity was measured separately for both field directions and the sum ( $I_+ + I_-$ ) and difference ( $I_+ - I_-$ ) calculated. The sum is representative of self-correlations in the structure and magnetism, while cross correlations between the two give rise to the difference signal. We refer to the ratio  $(I_+ - I_-)/(I_+ + I_-)$  as the spin asymmetry of the signal. A negligible linear background was recorded with the main beam shutter closed, but was not subtracted in the interests of manipulating the data as little as possible.

Energy scans were recorded across the Fe edges, with maxima in the spin asymmetry being found close to the Fe  $L_3$  edge at 702.9 eV and the Fe  $L_2$  at 715.5 eV: the slight shifts from the tabulated values for absorption measurements are due to our reflection geometry. Transverse ( $Q_x$ ) scans, shown in Fig. 2, were then carried out with the photon energy set to be on (702.9 eV) and off (670 eV) the Fe  $L_3$  resonance, at  $Q_z = 0.059$  Å<sup>-1</sup>. This position in  $Q_z$  corresponded to the largest spin asymmetry on the  $Q_z$  scan (specular  $\theta/2\theta$ , not shown) taken on the Fe  $L_3$  resonance. Off resonance [panel (b)], the diffuse background is extremely weak. A Gaussian fit to the diffuse scatter gives an in-plane correlation length of  $\approx 900$  Å for any disordered structural roughness, confirming the smoothness of the Py layer, and the spin asymmetry [panel (d)] is zero.

On resonance, magnetic satellite peaks are observed [panel (a)], offset at  $Q_x \approx \pm 0.001$  Å<sup>-1</sup>. This corresponds to a real space period of  $2\pi/Q_x \approx 565$  nm. A Gaussian fit to the magnetic satellites gives an in-plane magnetic correlation length of  $\approx 8000$  Å. A fit to the low intensity broad diffuse scattering below the well defined magnetic structural peak scatter gives a disordered correlation length of  $\approx 1000$  Å.

Downloaded 23 Jul 2007 to 129.11.68.127. Redistribution subject to AIP license or copyright, see <http://apl.aip.org/apl/copyright.jsp>

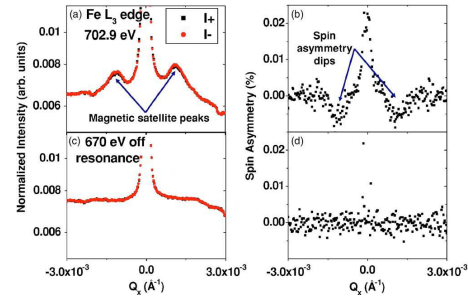


FIG. 2. (Color online)  $Q_x$  scans at  $Q_z$  equal to  $0.059$  Å<sup>-1</sup> at (a) the Fe  $L_3$  resonance at 702.9 eV, and (b) off resonance at 670 eV. Spin asymmetry at (c) the Fe  $L_3$  resonance at 702.9 eV and (d) off resonance at 670 eV.

The magnetic origin of the satellite peaks is confirmed, as a small spin asymmetry [panel (c)], of opposite sign to that on the specular ridge, is also observed at these off-specular values of  $Q_x$ . For truly pure magnetic correlations this asymmetry would be expected to be absent. The fact that it is so weak shows that the experiment has largely succeeded in minimizing the structure-magnetism cross correlations. They are clearly due to a periodic magnetic structure in the Py, the only layer in the structure containing Fe. These peaks (and their absence off resonance) is our main result.

Real space images of the micromagnetic structure have been obtained by magnetic force microscopy (MFM). The image shown in Fig. 3(a) is a rendering of the domain images obtained over a  $5 \times 5$   $\mu\text{m}^2$  scan, which shows stripes with a period of 540 nm. The slight discrepancy with our SXRMS results is perhaps due to the fact that the MFM samples only a very small area of the overall film. Panel (e) of Fig. 3 shows a fast Fourier transform (FFT) of a  $50 \times 50$   $\mu\text{m}^2$  MFM image. The FFT appears as an annulus of intensity with the two bright spots reflecting the preferential alignment of the periodic stripes in this particular part of the sample. There is no way to relate the in-plane orientation of the  $Q$  vectors to that of the  $Q$  vectors from the SXRMS exactly so they are set arbitrarily to have the stripe domains roughly along the  $y$  direction. A cut through the two-dimensional (2D) FFT, convoluted with the instrument function of the SXRMS apparatus, including a  $\delta$  function at  $Q_x = 0$  to simulate the specular ridge, is shown in Fig. 3(f). The resemblance to the SXRMS data of Fig. 2(a) is self-evident.

The satellite peaks are in the correct positions and of a comparable width. However, as expected for a FFT, there is no intensity asymmetry in the satellite peaks, which is seen in the SXRMS scan. Asymmetry in scattering data can arise from beam footprint corrections, but this would lead to the satellite peak at negative  $Q_x$  being the more intense. Spin asymmetry calculations have been carried out on the background scan confirming the asymmetry is not a background effect. Dürr *et al.* observed magnetic satellite peaks from a stripe domain state in an epitaxial FePd film,<sup>18</sup> with an asymmetry related to the coupling between the helicity of the photon and the chirality of the domain structure. Since on the beamline used in this experiment our helicity is fixed, we cannot perform the exact experiment that this group carried out. However, this is a plausible explanation for the observed asymmetry in our data.

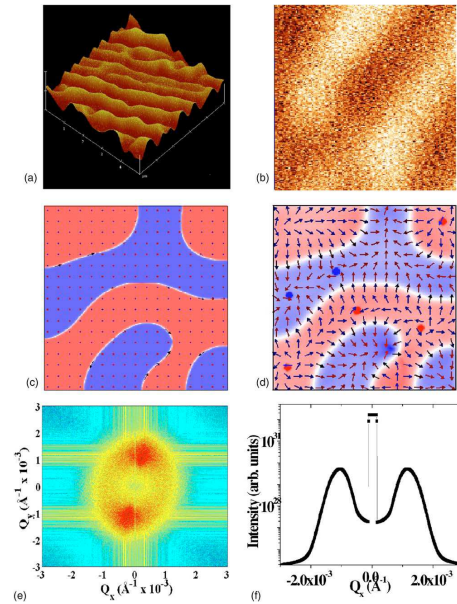


FIG. 3. (Color online) (a) Three-dimensional rendering of a  $5 \times 5 \mu\text{m}^2$  MFM image of the completed sample. (b) 2D  $1 \mu\text{m}^2$  zoom of the MFM image. (c)  $1 \mu\text{m}^2$  OOMMF simulation of the Co/Pt in zero field. (d)  $1 \mu\text{m}^2$  OOMMF simulation of the Py separated from the Co/Pt stack by a Ta layer in zero field. Several vortices are visible. (e) FFT of a  $50 \times 50 \mu\text{m}^2$  MFM image. (f) Cut through the FFT convoluted with the experimental SXRMS resolution.

To simulate the domain pattern obtained in the Py layer from the Co/Pt stack, micromagnetic simulations were performed using the OOMMF code.<sup>19</sup> A cell size of  $5 \times 5 \times 5 \text{ nm}^3$  in a  $1 \times 1 \mu\text{m}^2$  sample area was used. The Co/Pt multilayer was modeled as a continuous slab with the perpendicular anisotropy constant  $K_u = 0.21 \text{ MJ/m}^3$  and magnetization  $M_{\text{sat}} = 0.26 \text{ MA/m}$ . These values were derived from our VSM data and are in good agreement with those found in the literature.<sup>13</sup> The use of the Kaplan-Gehring<sup>20</sup> formula for the stripe domain width allowed us to calculate a value for the domain wall energy, which leads to an exchange stiffness constant  $A = 4.6 \text{ pJ/m}$ . A magnetically dead spacer layer was used to separate the Co/Pt layer and the Py layer, with the Py layer taking the standard OOMMF values of  $K_u = 0 \text{ MJ/m}^3$ ,  $M_{\text{sat}} = 0.86 \text{ MA/m}$ , and  $A = 13 \text{ pJ/m}$ . Calculated domain patterns, for zero applied field, in the Co/Pt stack and Py layer are shown in Figs. 3(c) and 3(d), respectively, and can be compared with the  $1 \mu\text{m}^2$  zoom of the MFM data in panel (b). A magnetic texture in the Py that closely matches the underlying domain pattern in the Co/Pt is immediately evident.

A closer inspection shows that the magnetization in the Py always lies across the top of the Co/Pt domain walls, where the stray field will be horizontal. The magnetization lies in alternating directions on subsequent walls, giving the same spatial period as the underlying domain pattern, and it is this periodic structure that the SXRMS has detected in the

Py layer. Where the stray field is vertical, above the Co/Pt domains, the Py moments are canted out of the plane by a few degrees, but otherwise only follow the Co/Pt inasmuch as the moments try to form flux-closed structures between those that are locked to the top of the walls. We have also performed calculations seeded with this structure for in-plane applied fields of  $\pm 300 \text{ Oe}$ , as in the experiment. We found that the Py moments locked to the walls are rigid and barely change direction in these fields. Large regions of the Permalloy above the domains are easily reversed in these fields, but as their lateral structure is aperiodic, they will only give rise to an incoherent off-specular background in the SXRMS.

In conclusion, we have investigated a domain pattern imprinted on a structurally smooth Permalloy layer and detected off-specular satellite peaks in the SXRMS corresponding to a periodic magnetic modulation. These appeared in the sum signal ( $I_+ + I_-$ ) but were extremely weak in the difference ( $I_+ - I_-$ ), indicating that the magnetism self-correlation function contains a strong periodic part which is almost absent from the structure-magnetism cross-correlation function. Thus we have exploited the element specific features of SXRMS to discern the purely magnetic correlations with little or no overlap from the charge and charge-magnetic cross correlations.

The authors would like to thank the NSLS for provision of beam time, and the EPSRC, the EU (through the ULTRASMOOTH contract), and the Centre for Materials Physics and Chemistry at CCLRC for funding.

- <sup>1</sup>D. Weller and M. F. Doerner, *Annu. Rev. Mater. Sci.* **30**, 611 (2000).
- <sup>2</sup>S. Tehrani, J. M. Slaughter, M. Deherrera, B. N. Engel, N. D. Rizzo, J. Salter, M. Durlam, R. W. Dave, J. Janesky, B. Butcher, K. Smith, and G. Grynkeiwich, *Proc. IEEE* **91**, 703 (2003).
- <sup>3</sup>*Spin Electronics*, Lecture Notes in Physics, edited by M. Ziese and M. J. Thornton (Springer, Berlin, 2001), Vol. 569/2001, pp. 3–31.
- <sup>4</sup>S. K. Sinha, E. B. Sirota, S. Garoff, and H. B. Stanley, *Phys. Rev. B* **38**, 2297 (1988).
- <sup>5</sup>G. H. Lander, *J. Magn. Magn. Mater.* **242**, 3 (2002).
- <sup>6</sup>J. F. MacKay, C. Teichert, D. E. Savage, and M. G. Lagally, *Phys. Rev. Lett.* **77**, 3925 (1996).
- <sup>7</sup>S. Langridge, J. Schmalin, C. H. Marrows, D. T. Dekadjevi, and B. J. Hickey, *Phys. Rev. Lett.* **85**, 4964 (2000).
- <sup>8</sup>R. M. Osgood III, S. K. Sinha, J. W. Freeland, Y. U. Idzerda, and S. D. Bader, *J. Appl. Phys.* **85**, 4619 (1999).
- <sup>9</sup>C. S. Nelson, G. Srajer, J. C. Lang, C. T. Venkataraman, S. Sinha, H. Hashizume, N. Ishimatsu, and N. Hosoi, *Phys. Rev. B* **60**, 12234 (1999).
- <sup>10</sup>J. W. Freeland, K. Bussmann, and Y. U. Idzerda, *Appl. Phys. Lett.* **76**, 2603 (2000).
- <sup>11</sup>L.-A. Michez, C. H. Marrows, P. Steadman, B. J. Hickey, D. A. Arena, H.-L. Zhang, D. G. Bucknall, and S. Langridge, *Appl. Phys. Lett.* **86**, 112502 (2005).
- <sup>12</sup>J. L. Costa-Krämer, C. Guerrero, S. Melle, P. García-Mochales, and F. Briones, *Nanotechnology* **14**, 239 (2003).
- <sup>13</sup>S. Landis, B. Rodmacq, and B. Dieny, *Phys. Rev. B* **62**, 12271 (2000).
- <sup>14</sup>D. E. Savage, J. Kleiner, N. Schimke, Y. H. Phang, T. Jankowski, J. Jacobs, R. Kariotis, and M. G. Lagally, *J. Appl. Phys.* **69**, 1411 (1991).
- <sup>15</sup>M. Wormington, C. Panaccione, K. M. Matney, and D. K. Bowen, *Philos. Trans. R. Soc. London, Ser. A* **357**, 2827 (1999).
- <sup>16</sup><http://www.nsls.bnl.gov/beamlines/beamline.asp?bld=u4b>
- <sup>17</sup>J. W. Freeland, K. Bussmann, P. Lubitz, Y. U. Idzerda, and C.-C. Kao, *Appl. Phys. Lett.* **73**, 2206 (1998).
- <sup>18</sup>H. A. Dürr, E. Dudzik, S. S. Dhesi, J. B. Goedkoop, G. van der Laan, M. Belakhovsky, C. Mocuta, A. Marty, and Y. Samson, *Science* **284**, 2166 (1999).
- <sup>19</sup>M. Donahue and D. Porter, *OOMMF Users Guide*, Version 1.2a3, NIST, 2002 (<http://math.nist.gov/oommf>).
- <sup>20</sup>B. Kaplan and G. A. Gehring, *J. Magn. Magn. Mater.* **128**, 111 (1993).

## Structural and magnetic roughness in a Co/Ru multilayer patterned into a large scale hexagonal array

C. J. Kinane

*School of Physics and Astronomy, E. C. Stoner Laboratory, University of Leeds, Leeds, LS2 9JT, UK and ISIS, Rutherford Appleton Laboratory, Chilton, Didcot, OX11 0QX, UK*

N. A. Porter, C. H. Marrows,<sup>a)</sup> and B. J. Hickey

*School of Physics and Astronomy, E. C. Stoner Laboratory, University of Leeds, Leeds, LS2 9JT, UK*

D. A. Arena

*National Synchrotron Light Source, Brookhaven National Laboratory, Upton, New York 11973-5000, USA*

J. Dvorak

*Department of Physics, Montana State University, Bozeman, Montana 59717, USA*

E. Sirotkin and F. Y. Ogryn

*School of Physics, University of Exeter, Stocker Road, Exeter EX4 4QL, UK*

T. Charlton and S. Langridge

*ISIS, Rutherford Appleton Laboratory, Chilton, Didcot, OX11 0QX, UK*

(Presented on 7 November 2007; received 11 September 2007; accepted 3 October 2007; published online 11 February 2008)

Self-assembled arrays of nanospheres have been used to pattern a Co/Pt multilayer into nanopillars. On top of this has been deposited a Co/Ru multilayer, which is antiferromagnetically coupled. The nanopillars introduce a known structural and magnetic lateral modulation into the multilayer. Soft x-ray magnetic scattering was used to observe the interference patterned from the patterned substrate. This has allowed us to show how the magnetic roughness correlates with the structural roughness and obtain selective magnetometry of the various magnetic elements. © 2008 American Institute of Physics. [DOI: 10.1063/1.2829394]

There are great difficulties in obtaining information on buried interfaces in multilayer nanostructures. This is a crucial problem in magnetic information storage and spintronics research, where the magnetic properties are strongly coupled to the structure. Internal characterization of nanostructures is possible using neutron and x-ray scattering, particularly off-specular scattering techniques to investigate lateral disorder.<sup>1,2</sup> There has been great interest in lateral structures recently partly because the behavior of such systems, when patterned into large scale arrays, provides model systems that can be utilized to study scientifically interesting areas such as digital computation<sup>3</sup> and artificial frustrated magnetism,<sup>4</sup> as well as applications where surface magnetism is important like giant magnetoresistance (GMR) and tunneling magnetoresistance (TMR) devices and patterned media.<sup>5</sup> In this case, large scale arrays are an ideal system to study the effects of small local deviations in the magnetic structure. These are of interest since these magnetic deviations can affect properties such as polarized electron transport. Scattering techniques allow averaged statistical quantities to be measured from arrays of devices more easily than from local probes on single devices. Past studies have concentrated on patterned samples with nonmagnetic structural modulations using both polarized neutron reflectivity and soft x-ray resonant magnetic scattering (SXRMS).<sup>6,7</sup> We have made use of

off-specular SXRMS in a previous study on structurally flat Permalloy, which has a domain pattern imprinted upon it by a perpendicularly magnetized Co/Pt multilayer.<sup>8</sup> In this report, self-assembled arrays of nanospheres were used to pattern perpendicularly a magnetized Co/Pt multilayer into nanopillars. On top of this has been deposited a Co/Ru multilayer, which is antiferromagnetically coupled,<sup>9</sup> introducing a known structural and magnetic modulation.

The samples were prepared using a dc magnetron sputtering system with a base pressure of  $\sim 5 \times 10^{-8}$  Torr. A partial pressure of 2.8 mTorr of Ar was used during deposition. The nominal structure of the samples was [Co(5 Å)/Pt(10 Å)]  $\times$  20(patterned)/Ru(400 Å)/[Co(31 Å)/Ru(31 Å)]  $\times$  20, shown in the inset of Fig. 1. Co/Pt was deposited to obtain a perpendicularly magnetized film.<sup>10,11</sup> This Co/Pt multilayer was then patterned into a hexagonal dot array using commercially available suspensions of monodisperse polystyrene nanospheres with diameters of approximately 780 nm. These formed a hexagonal template via self-assembly, allowing arrays with ordering over the range of  $\sim 1$  cm<sup>2</sup>. A combination of reactive ion etching and Ar ion milling was used to produce nanosphere capped Co/Pt pillars. The spheres were then removed via abrasion. Further details on this process can be found in the following by Weekes *et al.*<sup>12,13</sup> A scanning electron microscope (SEM) image of the patterned Co/Pt multilayer is shown in Fig. 1. To ensure that there was

<sup>a)</sup>Electronic mail: c.h.marrows@leeds.ac.uk.

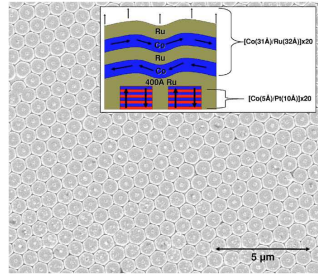


FIG. 1. (Color online)  $16 \times 16 \mu\text{m}^2$  SEM image of Co/Pt dots after milling. Inset: schematic of the complete sample structure.

no form of coupling other than magnetostatic between the Co/Pt pillars and the following  $[\text{Co}(31 \text{ \AA})/\text{Ru}(32 \text{ \AA})] \times 20$  multilayer,  $400 \text{ \AA}$  of Ru was then deposited to form a large nonmagnetic spacer layer. The Co/Ru multilayer had thicknesses tailored to be on the third antiferromagnetically (AF) coupling peak.<sup>9</sup>

Figure 2(a) shows a  $\text{Cu } K\alpha$  rocking curve taken through the first order Co/Pt Bragg peak for just the patterned Co/Pt multilayer. The in-plane structure is clearly evident from the satellite peaks about  $Q_x=0$ . Vibrating sample magnetometry (VSM) loops are shown in Figs. 3(a) and 3(b) for the completed sample structure. Panel (a) shows the full VSM loop, while panel (b) shows a minor loop in the range of  $\pm 400$  Oe. VSM is sensitive to the bulk magnetization of the sample. However, the Co/Ru moment is four times the size of the Co/Pt moment, so it is evident that the majority of the minor loops in panel (b) comes from the Co/Ru.

In order to perform the SXRMS measurements, the samples were taken to the U4B beamline at the National Synchrotron Light Source.<sup>14</sup> U4B is equipped with an electromagnet able to apply a field of up to  $\pm 300$  Oe in both the plane of the sample and the scattering plane. We define the coordinate system for scattering such that the  $z$  direction lies normal to the sample, while the  $x$  direction lies in both the sample and scattering planes. The sample geometry is such

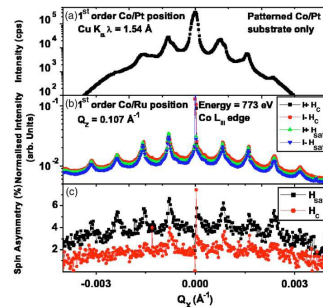


FIG. 2. (Color online) (a)  $\text{Cu } K\alpha$  x rays on the Co/Pt patterned substrate. (b)  $Q_x$  scans at the first order Co/Ru Bragg position ( $Q_z=0.108 \text{ \AA}^{-1}$ ) at saturation and coercivity. (c) Spin asymmetry at saturation and coercivity.

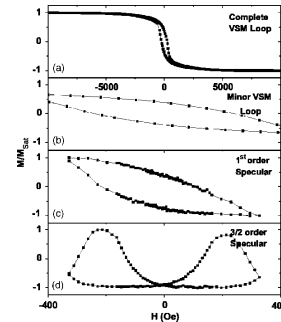


FIG. 3. (a) Full in-plane VSM loop. (b) Minor in-plane VSM loop. (c) SXRMS hysteresis loops at the first order specular position. (d) SXRMS hysteresis loops at the  $3/2$  order specular position.

that the sample and detector angles allow the components of the elastic wavevector transfer  $\mathbf{Q}$  to be selected in  $x$  and  $z$ . X rays with a polarization of 90% were used, with the reflected intensity being normalized via a Au grid monitor upstream of the entrance slits to the scattering chamber.

In accordance with earlier studies<sup>15,16</sup> at each point in reciprocal space, the scattered intensity was measured for both field directions ( $I^+$  and  $I^-$ ). The sum ( $I^+ + I^-$ ) and difference ( $I^+ - I^-$ ) are calculated, with the sum representative of the structure and magnetism self-correlations, and the difference the cross-correlations between the two.<sup>17</sup> We refer to the ratio  $(I^+ - I^-)/(I^+ + I^-)$  as the spin asymmetry (SA).

Energy scans (not shown) were recorded across the Co absorption edges, with the maximum in the SA being found close to the  $L_{III}$  edge at  $772.5 \text{ eV}$  and the slight shift from the tabulated value of  $778.1 \text{ eV}$  (Ref. 18) being due to our reflection geometry. A specular scan (not shown) was taken to determine the position of the Co/Ru Bragg peak at  $Q_z = 0.107 \text{ \AA}^{-1}$ . No  $1/2$  order AF peak was observed in the specular scatter, which is in keeping with other studies using SXRMS.<sup>19</sup> In order to probe the lateral magnetic structure, transverse  $Q_x$  scans were taken at the  $1/2$  order ( $Q_z = 0.054 \text{ \AA}^{-1}$ ) and first order ( $Q_z = 0.107 \text{ \AA}^{-1}$ ) Bragg positions.

Figure 2(b) shows the  $Q_x$  scan at the first order Bragg peak for applied fields corresponding to saturation and coercivity. The positions of the in-plane Bragg peaks are in excellent agreement with the  $\text{Cu } K\alpha$  x-ray data shown in Fig. 2(a). The satellite peak positions are also in agreement with what would be expected for their positions via  $Q_x \approx 2\pi/d$ , which for a center to center nanosphere separation gives a spacing in  $Q_x$  of  $\approx 8 \times 10^{-4} \text{ \AA}^{-1}$ . It is also clear that the  $Q_x$  scans at coercivity are slightly more intense than the  $Q_x$  scans at saturation due to there being more lateral ferromagnetic (F) disorder at coercivity. There is a good agreement between both the  $I^+$  and  $I^-$  curves at both saturation and coercivity, indicating that the in-plane F domain disorder is strongly correlated to the structural modulation. This becomes more evident when looking at the SA shown in Fig. 2(c). The SA shows that at saturation, there is a definite magnetic correlation with the structural modulation. At coer-



civity, any correlations of the ferromagnetic domains and the structure are very weak as there is no net magnetization, but peaks are still just about visible, probably due to the fact that the sample was not quite at coercivity during the measurements.  $Q_x$  scans were also taken at the 1/2 order position (not shown) in order to be sensitive to the nominal lateral AF disorder between the Co layers in the Co/Ru multilayer. The curves displayed the same general features and behavior as the first order  $Q_x$  scan, indicating some crossover between the AF and F order parameters in both cases. A Gaussian fit to the left hand side in-plane Bragg peak gives a coherence length of  $\approx 5000$  nm for the dots, comparing well the SEM data, while a fit to the diffuse background (with in-plane features removed) gives an in-plane random roughness of  $\approx 420$  nm, which is of the same order as the size of the Co/Pt dots upon which the Co/Ru was deposited.

An advantage of the SXRMS technique is that by measuring the intensity variation as a function of applied field, it is possible to measure hysteresis loops.<sup>2,20</sup> Loops were taken at both the first order and 3/2 order specular positions in  $Q_z$  and are shown in Fig. 3 along with a VSM measurement over the same field range for comparison. The first Co/Pt feature is to be found at  $Q_z = 0.42 \text{ \AA}^{-1}$ ; hence, the hysteresis measurements are sensitive to the Co/Ru multilayer stack only.

The first order specular loop compares well to the corresponding minor VSM loop, implying that it is largely the macroscopic magnetization of the structure that is being probed. Hysteresis loops were also taken at the positions of the first trough- and in-plane Bragg peaks in  $Q_x$  (not shown) as these off specular loops are sensitive to in-plane structures such as domains.<sup>2</sup> These were found to be of the same shape, indicating that the magnetic disorder is similar over a range of length scales as far out as  $15 \mu\text{m}$ . The loop taken at the 3/2 position in  $Q_z$  is sensitive to the AF magnetic structure between the Co layers in the Co/Ru multilayer. The unconventional loop shape is due to the intensity peaking at the coercive fields of the Co/Ru, where the greatest amount of AF order is present. This then dies off as the AF order is swept out of the sample. These loops are similar to the loops observed in GMR measurements, which are known to be sensitive to the AF order.

Magnetic roughness can have multiple forms such as lateral domain patterns, a nonuniform height distribution of the moments, and vectorial differences in the directions to which the moments point. It has been shown by Kinane *et al.*<sup>8</sup> that it is possible to measure the domain disorder only, with minimal contributions from the chemical disorder, and that the structure and magnetism are discernible from each other using SXRMS. Langridge *et al.*<sup>6</sup> have shown that the domain disorder does not necessarily correlate with the structural disorder in the active multilayer, while the magnetic roughness is driven by the structural feature size. In this case, we pattern both the structural modulation and the domain modulation. It is clear that the magnetic roughness locks in on the structure at saturation, while the domain disorder has little influence since it is locked to the domain structure of the dots below the active Co/Ru multilayer. This is backed up by the SXRMS hysteresis loops, which do not vary in

shape as a function of  $Q_x$ , which probe the different length scales. It seems a reasonable that different forms of magnetic roughness interact with the structure to different extents.

In conclusion, the magnetic roughness has been shown to follow the structural modulation at saturation, with little sensitivity to the magnetism at coercivity due to the low net magnetization. It is possible to obtain a variety of hysteresis loops as a function of position in reciprocal space. By selecting the correct position in reciprocal space, it is possible to select which part of the sample is measured. In this case, the Co/Ru multilayer rather than the Co/Pt dots, while moving into the diffuse scatter, allows different lateral length scales to be probed. We saw that the magnetic disorder was similar over a range of length scales as far out as  $15 \mu\text{m}$ .

The authors thank Brookhaven National Laboratory for NSLS beamtime. We are grateful to EPSRC, and the STFC Centre for Materials Physics and Chemistry for funding. We acknowledge Lara San Emeterio Alvarez for the SEM image.

- <sup>1</sup>S. Langridge, J. Schmalian, C. H. Marrows, D. T. Dekadjevi, and B. J. Hickey, *Phys. Rev. Lett.* **85**, 4964 (2000).
- <sup>2</sup>C. H. Marrows, P. Steadman, A. C. Hampson, L.-A. Michez, B. J. Hickey, N. D. Telling, D. A. Dvorak, and S. Langridge, *Phys. Rev. B* **72**, 024421 (2004).
- <sup>3</sup>J. I. Martin, J. Nogués, K. Liu, J. L. Vicentand, and I. K. Schuller, *J. Magn. Magn. Mater.* **256**, 449 (2003).
- <sup>4</sup>A. Imre, G. Csaba, L. Ji, A. Orlov, G. Bernstein, and W. Porod, *Science* **311**, 205 (2006).
- <sup>5</sup>R. F. Wang, C. Nisoli, R. S. Freitas, J. Li, W. McConville, B. J. Cooley, M. S. Lund, N. Samarth, C. Leighton, V. H. Crespi, and P. Schiffer, *Nature (London)* **439**, 303 (2006).
- <sup>6</sup>S. Langridge, L. A. Michez, M. Ali, C. H. Marrows, B. J. Hickey, T. R. Charlton, R. M. Dalgliesh, M. Toohey, E. W. Hill, S. McFadzean, and J. N. Chapman, *Phys. Rev. B* **74**, 014417 (2006).
- <sup>7</sup>L.-A. Michez, C. H. Marrows, P. Steadman, B. J. Hickey, D. A. Arena, H.-L. Zhang, D. G. Bucknall, and S. Langridge, *Appl. Phys. Lett.* **86**, 112502 (2005).
- <sup>8</sup>C. J. Kinane, A. K. Suszka, C. H. Marrows, B. J. Hickey, D. A. Arena, J. Dvorak, T. R. Charlton, and S. Langridge, *Appl. Phys. Lett.* **89**, 092507 (2006).
- <sup>9</sup>S. S. P. Parkin, N. More, and K. P. Roche, *Phys. Rev. Lett.* **64**, 2304 (1990).
- <sup>10</sup>L. S. E. Alvarez, G. Burnell, C. H. Marrows, K.-Y. Wang, A. M. Blackburn, and D. A. Williams, *J. Appl. Phys.* **101**, 09F508 (2007).
- <sup>11</sup>S. Landis, B. Rodmacq, and B. Dieny, *Phys. Rev. B* **62**, 12271 (2000).
- <sup>12</sup>S. M. Weekes, F. Y. Ogrin, and W. A. Murray, *Langmuir* **20**, 11208 (2004).
- <sup>13</sup>S. M. Weekes, F. Y. Ogrin, W. A. Murray, and P. S. Keatley, *Langmuir* **23**, 1057 (2007).
- <sup>14</sup>See <http://www.nsls.bnl.gov/beamlines/beamline.asp?bliduu4b> for more information.
- <sup>15</sup>J. F. MacKay, C. Teichert, D. E. Savage, and M. G. Lagally, *Phys. Rev. Lett.* **77**, 3925 (1996).
- <sup>16</sup>J. W. Freeland, K. Bussmann, P. Lubitz, Y. U. Idzerda, and C.-C. Kao, *Appl. Phys. Lett.* **73**, 2206 (1998).
- <sup>17</sup>R. M. Osgood III, S. K. Sinha, J. W. Freeland, Y. U. Idzerda, and S. D. Bader, *J. Appl. Phys.* **85**, 4619 (1999).
- <sup>18</sup>A. Thompson, D. Attwood, E. Gullikson, M. Howells, K. Kim, J. Kirz, J. Kortright, I. Lindau, P. Pianetta, A. Robinson, J. Scofield, J. Underwood, D. Vaughan, G. Williams, and H. Winick, *X-Ray Data Booklet* (University of California, Berkeley, CA, 2001).
- <sup>19</sup>T. P. A. Hase, J. D. R. Buchanan, B. K. Tanner, S. Langridge, R. M. Dalgliesh, S. Foster, C. H. Marrows, and B. J. Hickey, *J. Appl. Phys.* **93**, 6510 (2003).
- <sup>20</sup>C. Spezzani, P. Torelli, M. Sacchi, R. Delaunay, C. F. Hague, V. Cros, and F. Petroff, *Appl. Phys. Lett.* **81**, 3425 (2002).

# References

- [1] F. J. Himpsel, J. E. Ortega, G. J. Mankey, and R. F. Willis, *Advances in Physics* **47**(4), 511 (1998).
- [2] S. S. P. Parkin, N. More, and K. P. Roche, *Phys. Rev. Lett.* **64**(19), 2304 (1990).
- [3] R. E. Camley and J. Barnaś, *Phys. Rev. Lett.* **63**, 664 (1989).
- [4] E. E. Fullerton, J. Pearson, C. H. Sowers, S. D. Bader, X. Z. Wu, and S. K. Sinha, *Phys. Rev. B* **48**, 17432 (1993).
- [5] P. Beliën, R. Schad, C. D. Potter, G. Verbanck, V. V. Moshchalkov, and Y. Bruynseraede, *Phys. Rev. B* **50**, 9957 (1994).
- [6] M. Ziese and M. J. Thornton, eds., *Spin Electronics* (Springer, Berlin, 2001).
- [7] S. Wolf, D. Awschalom, R. Buhrman, J. Daughton, S. von Molnar, M. Roukes, Y. Chtchelkanova, and D. Treger, *Science* **294**, 1488 (2001).
- [8] W. H. Meiklejohn and C. P. Bean, *Phys. Rev.* **105**, 904 (1957).
- [9] K. Takano, R. Kodama, A. Berkowitz, W. Cao, and G. Thomas, *Phys. Rev. Lett.* **79**, 1130 (1997).
- [10] D. Weller and M. F. Doerner, *Annu. Rev. Mater. Sci.* **30**, 611 (2000).
- [11] S. Tehrani, J. M. Slaughter, M. Deherrara, B. N. Engel, N. D. Rizzo, J. Salter, M. Durlam, R. W. Dave, J. Janesky, B. Butcher, K. Smith, and G. Grynkewich, *Proc. IEEE* **91**, 703 (2003).
- [12] J. Slonczewski, *J. Magn. Magn. Mater.* **247**, 324 (2002).

- [13] R. F. Wang, C. Nisoli, R. S. Freitas, J. L. W. McConville, B. J. Cooley, M. S. Lund, N. Samarth, C. Leighton, V. H. Crespi, and P. Schiffer, *Nature* **439**, 303 (2006).
- [14] A. Imre, G. Csaba, L. Ji, A. Orlov, G. Bernstein, and W. Porod, *Science* **311**, 205 (2006).
- [15] C. J. Chen, *Introduction to scanning Tunneling Microscopy* (Oxford Science Publications, 2008), second edition ed.
- [16] S. K. Sinha, S. Roy, M. Fitzsimmons, S. Park, M. Dorn, O. Petravic, I. Roshchin, Z. pan. Li, X. Batlle, R. Morales, A. Misra, X. Zhang, *et al.*, *PRAMANA - Journal of physics* **67**(1), 47 (2006).
- [17] S. K. Sinha, *Acta Physica Polonica A* **89**(2), 219 (1996).
- [18] V. Holý and T. Baumbach, *Phys. Rev. B* **49**, 10668 (1994).
- [19] S. K. Sinha, E. B. Sirota, S. Garoff, and H. B. Stanley, *Phys. Rev. B* **38**, 2297 (1988).
- [20] S.J.Blundell and J. Bland, *Phys. Rev. B.* **46**(6), 3391 (1992).
- [21] G. H. Lander, *J. Magn. Magn. Mater.* **242245**, 3 (2002).
- [22] D. R. Lee, S. K. Sinha, D. Haskel, Y. Choi, J. C. Lang, S. A. Stepanov, and G. Srajer, *Phys. Rev. B* **68**(224409), 224409 (2003).
- [23] D. R. Lee, S. K. Sinha, C. S. Nelson, J. C. Lang, C. T. Venkataraman, G. Srajer, and R. M. O. III, *Phys. Rev. B.* **68**(224410), 224410 (2003).
- [24] D. Gibbs, D. R. Harshman, E. D. Isaacs, D. B. McWhan, D. Mills, and C. Vettier, *Physical Review Letters* **61**, 1241 (1988).
- [25] *U4b beamline webpage*  
, URL <http://www.nsls.bnl.gov/beamlines/beamline.asp?blid=u4b>.
- [26] *Crisp beamline webpage*  
, URL <http://www.isis.rl.ac.uk/LargeScale/crisp/crisp.htm>.

- [27] *Adam beamline webpage old address*  
, URL <http://www.ill.fr/YellowBook/ADAM/>.
- [28] W. R. Grove, Philos Trans Faraday Soc **87**, 142 (1852).
- [29] K. Ellmer *et al.*, J. Phys. D: Appl. Phys. **33**(R17) (2000).
- [30] R. V. Stuart, *Vacuum Technology, thin films and sputtering: an introduction* (Academic press, 1983).
- [31] A. T. Hindmarch, *Spin Transport in Rare-Earth Magnetic Heterostructures*, Ph.D. thesis, Univeristy of Leeds (2003).
- [32] A. Potenza, *Structural, Electroni and Magnetic Properties of Superconductor/Ferromagnet Multilayers*, Ph.D. thesis, SCHOOL OF PHYSICS AND ASTRONOMY (2006).
- [33] S. M. Weekes, F. Y. Ogrin, W. A. Murray, and P. S. Keatley, Langmuir **23**, 1057 (2007).
- [34] S. M. Weekes, F. Y. Ogrin, and W. A. Murray, Langmuir **20**, 11208 (2004).
- [35] Wernerwerk für Meßtechnik karlsruhe, *Siemens Diffractometer with omega Drive Instructions Eg 4401 1e*, Siemens (1968).
- [36] B. D. Cullity, *Elements of X-ray Diffraction* (Addison-Wesley Publishin Company, inc. Second edition, 1978).
- [37] Wernerwerk für Meßtechnik karlsruhe, *Siemens Types SZ and SA Scintillation Counters for Longwave X-rays Operating instructions Eg 4A 201/2e*, Siemens (1970).
- [38] Oxford Instruments, *MagLab<sup>VSM</sup> Vibrating Sample Magnetometer Superconducting system with integral VTI* (2000).
- [39] S. Foner, Review of Scientific Instruments **30**(7), 548 (1959).
- [40] *What is a Lock-in Amplifier? TECHNICAL NOTE TN 1000*, Tech. Rep., PerkinElmer instruments (2000).



- [41] L. Michez, *CPP Transport in Multilayers: Simulations and Experiments*, Ph.D. thesis, Physics and Astronomy (2002).
- [42] M. Faraday, Philosophical Transactions of the Royal Society of London **136**, 1 (1846).
- [43] J. Kerr, Philosophical Transactions of the Royal Society **3**, 321 (1877).
- [44] S. D. Bader, JMMM **100**, 440 (1991).
- [45] M. Ali, *Growth and Study of Magnetostrictive FeSiBC Thinfilms for Device Applications*, Phd thesis, Department of Physics and Astronomy, Univeristy of sheffield (1999).
- [46] E. Hecht, *Optics* (Addison Wesley, 2002), 4th ed.
- [47] J. Zak, E. R. Moog, C. Liu, and S. D. Bader, Journal of Applied Physics **68**(8), 4203 (1990).
- [48] G. Daalderop, F. Mueller, R. Albers, and A. Boring, Journal of Magnetism and Magnetic Materials **74**, 211 (1988).
- [49] J. Zak, E. Moog, C. Liu, and S. Bader, Journal of Magnetism and Magnetic Materials **89**, 107 (1990).
- [50] C.-Y. You and S.-C. Shin, Applied Physics Letters **69**, 1315 (1996).
- [51] H. Laidler, *X-ray and Magnetisation Measurements of MBE-Grown Magnetic Multilayers*, Phd thesis, School of Physics and Astronomy, Unieristy of Leeds (1997).
- [52] W. Kleemann, Review of Scientific Instruments **78**, 120901 (2007).
- [53] A. Westphalen, M.-S. Lee, A. Remhof, and H. Zabel, Review of Scientific Instruments **78**, 121301 (2007), good review of make stuff and theory.
- [54] F. J. Giessibl, S. Hembacher, H. bielefeldt, and J. Mannhart, Science **267**, 68 (1995).

- [55] G. Binnig, C. F. Quate, and C. Gerber, *Physical Review Letters* **56**, 930 (1986).
- [56] S. Alexander, L. Hellemans, O. Marti, J. Schneir, V. Elings, P. K. Hansma, M. Longmire, and J. Gurley, *J. Appl. Phys.* **65**, 164 (1988).
- [57] G. Meyer and N. M. Amer, *Appl. Phys. Lett* **53**(12), 1045 (1988).
- [58] *Dimension 3100 Manual Rev D*.
- [59] Y. Martin and H. K. Wickramasinghe, *Appl. Phys. Lett.* **50**, 1455 (1987).
- [60] U. Hartmann, *Annu. Rev. Mater. Sci.* **29**, 53 (1999).
- [61] *Nist website*, URL <http://www.nist.gov/>.
- [62] T. L. Gilbert, *Physical Review* **100**, 1243 (1955).
- [63] R. Schäfer, *Handbook of Magnetism and Advanced Magnetic Materials, Volume 2: Micromagnetism*, vol. 2 (Wiley, 2007).
- [64] M. Donahue and D. Porter, *OOMMF Users guide Version 1.2a3*, NIST (2002), URL <http://math.nist.gov/oommf>.
- [65] A. Michette and C. Buckley, eds., *X-ray Science and Technology* (Institute of Physics Publishing Bristol and Philadelphia, 1993).
- [66] J. Als-Nielsen and D. McMorrow, *Elements of Modern X-Ray Physics* (Wiley, 2001).
- [67] R. Talman, *Accelerator X-ray Sources* (WILEY-VCH, 2006).
- [68] T. Hase, *Condensed matter physics course x-rays and neutrons*.
- [69] J. W. M. DuMond, *Physical Review* **52**(8), 872 (1937).
- [70] V. Holý, U. Pietsch, and T. Baumbach, *High-Resolution X-ray Scattering from Thin Films and Multilayers* (Springer, 1999), *springer Tracts in Modern Physics*.

- [71] R. Schäfer, *Handbook of Magnetism and Advanced Magnetic Materials, Volume 3: Novel Techniques for Characterising and Preparing Samples*, vol. 3 (Wiley, 2007).
- [72] H. C. N. Tolentino, J. L. C. Cezar, N. M. Souza-Neto, and A. Y. Ramos, *Journal of Synchrotron Radiation* **12**, 168 (2004).
- [73] *NSLS vuv ring webpage*, URL <http://www.nsls.bnl.gov/facility/accelerator/vuv/>.
- [74] C. T. Chen and F. Sette, *Rev. Sci. Instrum* **60**(7), 1616 (1989).
- [75] C. T. Chen, *Rev. Sci. Instrum.* **63**(1), 1229 (1992), synchrotron radiation VUV/Soft X-ray: Beamlines and Monochromators.
- [76] Y. U. Idzerda, V. Chakarian, and J. W. Freeland, *Synchrotron Radiation News* **10**(3), 6 (1997).
- [77] R. Weinstein, *Nuclear Engineering Fundamentals: Interaction of Radiation with Matter*, vol. 3 (McGraw-Hill, 1964).
- [78] A.-J. Dianoux and G. Lander, eds., *Neutron Data Booklet* (Institut Laue-Langevin, 2002), 1st ed.
- [79] J. Penfold, R. C. Ward, and W. G. Williams, *Journal of Physics E: Scientific Instruments* **20**(11), 1411 (1987).
- [80] R. Ballou, N. Berk, P. Brown, T. Chatterji, G. Ehlers, C. F. Majkrzak, F. Mezei, K. V. O'Donovan, B. Ouladdiaf, C. Pappas, L. P. Regnault, J. Schweizer, *et al.*, *Neutron Scattering from Magnetic Materials* (Elsevier, 2006), 1st ed.
- [81] A. Schreyer, R. Siebrecht, U. Englisch, U. Pietsch, and H. Zabel, *Physica B* **248**, 349 (1998).
- [82] *Adam beamline webpage*, URL <http://www.ill.eu/adam/home-adam/>.
- [83] *Crisp beamline online manual*, URL <http://epubs.cclrc.ac.uk/bitstream/1305/RAL-TR-97-022.pdf>.

- [84] R. Felici *et al.*, Applied Physics A: Solids and Surfaces **45**, 169 (1988), cRISP beamline overview.
- [85] W. C. Röntgen, Science **3**(59), 227 (1896).
- [86] L. G. Parratt, Physical Review **95**(2), 359 (1954).
- [87] M. Manciu, L. Dudas, C. Sürgers, and R. Manaila, Journal of Applied Crystallography **28**(2), 160 (1995).
- [88] T. P. A. Hase, *X-ray Scattering from Magnetic Metallic Multilayers*, Ph.D. thesis, The University of Durham (1998).
- [89] A. A. Cole, *Transport properties of Magnetic Hetrostructures Grown by Molecular Beam Epitaxy*, Ph.D. thesis, Univeristy of Leeds Department of Physics and Astronomy (2004).
- [90] R. Eisberg and R. Resnick, *Quantum Physics of Atoms, Molecules, Solids, Nuclei, and Particles* (Wiley, 1985), 2nd ed., Appendix L.
- [91] W. L. Bragg, Proc. Cam. Phil. Soc. **17**, 43 (1912), w. L. Bragg went on to jointly win the Nobel Prize with his father, the then Cavendish Proffessor at Leeds Univeristy, for there work on x-ray crystallography.
- [92] C. Kittel, *Introduction to Solid State Physics* (Wiley, 2005), 8th ed.
- [93] B. E. Warren, *X-ray Diffraction* (Dover Publications, 1990).
- [94] D. E. Savage, J. Kleiner, N. Schimke, Y. H. Phang, T. Jankowski, J. Jacobs, R. Kariotis, and M. G. Lagally, J. Appl. Phys. **69**(3), 1411 (1991).
- [95] M. Wormington, C. Panaccione, K. M. Matney, and D. K. Bowen, Phil. Trans. R. Soc. Lond **A 357**(1761), 2827 (1999).
- [96] H. Kiessig, Ann Phys **10**(5), 769 (1931).
- [97] M. Wormington, I. Pape, T. P. A. Hase, B. K. Tanner, and D. K. Bowen, Phil. Mag. Lett. **74**(3), 211 (1996).

- [98] L. Nénot and P. Croce, *Revue de Physique Appliquée* **15**, 761 (1980).
- [99] W. M. Plotz and K. Lischka, *J. Phys. III France*. **4**, 1503 (1994).
- [100] I. Pape, T. Hase, B. Tanner, and M. Wormington, *Physica B* **253**, 278 (1998).
- [101] Mandelbrot, *The Fractal Geometry of Nature* (Freeman, New York, 1982).
- [102] T. Hase, J. D. Buchanan, B. K. Tanner, S. Langridge, R. M. Dalgliesh, S. Foster, C. H. Marrows, and B. J. Hickey, *J. Appl. Phys.* **93**(10), 6510 (2003).
- [103] V. Holý, J. Kubêna, I. Ohlídal, K. Lischka, and W. Plotz, *Phys. Rev. B* **47**, 15896 (1993).
- [104] C. H. Marrows, P. Steadman, A. C. Hampson, L.-A. Michez, B. J. Hickey, N. D. Telling, D. A. Arena, J. Dvorak, and S. Langridge, *Phys Rev B* **72**, 024421 (2004).
- [105] M. Blume, *J. Appl. Phys.* **57**, 3615 (1985).
- [106] F. Bergevin and M. Brunel, *Physics Letters* **39A**(2), 141 (1972).
- [107] K. Namikawa, M. Ando, T. Nakajima, and H. Kawata, *Journal of the Physical Society of Japan* **54**(11), 4099 (1985).
- [108] J. P. Hannon, G. T. Tramell, M. Blume, and D. Gibbs, *Phys. Rev. Lett.* **61**(10), 1245 (1988).
- [109] C. Vettier, *Journal of Magnetism and Magnetic Materials* **129**, 59 (1994).
- [110] J. P. Hill and D. F. McMorrow, *Acta Crystallographica Section A* **A52**, 236 (1996).
- [111] J. F. MacKay, C. Teichert, D. E. Savage, and M. G. Lagally, *Phys. Rev. Lett.* **77**, 3925 (1996).
- [112] C. Kao, J. B. Hastings, E. D. Johnson, D. P. Siddons, G. C. Smith, and G. A. Prinz, *Phys. Rev. Lett.* **65**, 373 (1990).

- [113] J. M. Tonnerre, L. Sève, D. Raoux, G. Soullié, B. Rodmacq, and P. Wolfers, Phys. Rev. Lett. **75**, 740 (1995).
- [114] S. W. Lovesey and S. P. Collins, *X-ray scattering and absorption by magnetic materials*, Oxford series on synchrotron radiation: 1 (Oxford : Clarendon Press, 1996).
- [115] G. Y. Guo, Phys. Rev. B **55**, 11619 (1997).
- [116] J. L. Erskine and E. A. Stern, Phys. Rev. B **12**(11), 5016 (1975).
- [117] G. Schütz, W. Wagner, W. Wilhelm, P. Kienle, R. Zeller, R. Frahm, and G. Materlik, Phys. Rev. Lett. **58**(7), 737 (1987).
- [118] C. T. Chen, Y. U. Idzerda, H.-J. Lin, N. V. Smith, G. Meigs, E. Chaban, G. H. Ho, E. Pellegrin, and F. Sette, Physical Review Letters **75**(1), 152 (1995).
- [119] J. Chadwick, *Nobel prize webpage*, 1935 Nobel prize on the discovery of the neutron and its properties., URL <http://nobelprize.org>.
- [120] B. N. Brockhouse and C. G. Shull, *Nobel prize webpage*, 1994 Nobel Prize in Physics for the development of neutron spectroscopy and neutron diffraction., URL <http://nobelprize.org>.
- [121] G. L. Squires, *Introduction to the Theory of Thermal Neutron Scattering* (Dover Publications, INC. Mineola, New York, 1996).
- [122] T. Chatterji, ed., *Neutron Scattering from Magnetic Materials* (Elsevier, 2006).
- [123] R. M. Moon, T. Riste, and W. C. Koehler, Phys. Rev. **181**(2), 920 (1969).
- [124] C. F. Majkrzak, Physica B **221**(1-4), 342 (1996).
- [125] M. Fitzsimmons, S.D.Bader, J.A.Borchers, G.P.Felcher, J. Furdyna, A. Hoffmann, J. Kortright, I. K. Schuller, T.C.Schulthess, S. Sinha, M. Toney, D. Weller, *et al.*, Journal of Magnetism and Magnetic materials **271**, 103 (2004).
- [126] H. Zabel, Materials Today **9**(1-2), 42 (2006).

- [127] H. Zabel, R. Siebrechtb, and A. Schreyer, *Physica B: Condensed Matter* **276 - 278**, 17 (2000).
- [128] J. F. Ankner and G. P. Felcher, *Journal of Magnetism and Magnetic Materials* **200**(1-3), 741 (1999).
- [129] F. Ott, *Comptes Rendus Physique* **8**(7-8), 763 (2007).
- [130] R. M. Osgood III, S. K. Sinha, J. W. Freeland, Y. U. Idzerda, and S. D. Bader, *J. Appl. Phys.* **85**(4619), 4619 (1999).
- [131] C. S. Nelson, G. Srajer, J. C. Lang, C. T. Venkataraman, S. Sinha, H. Hashizume, N. Ishimatsu, and N. Hosoiito, *Phys. Rev. B* **60**, 12234 (1999).
- [132] S. Landis, B. Rodmacq, and B. Dieny, *Phys. Rev. B.* **62**(18), 12 271 (2000).
- [133] Y. U. Idzerda, V. Chakarian, and J. W. Freeland, *Phys. Rev. Lett.* **82**, 1562 (1999).
- [134] J. A. Borchers, J. A. Dura, J. Unguris, D. Tulinsky, M. H. Kelley, C. F. Majkrzak, S. Y. Hsu, R. Loloee, J. W. P. Pratt, and J. Bass, *Phys. Rev. Lett.* **82**, 2796 (1999).
- [135] S. Langridge, J. Schmalian, C. H. Marrows, D. T. Dekadjevi, and B. J. Hickey, *Phys. Rev. Lett.* **85**, 4964 (2000).
- [136] J. J. Kelly, B. M. Barnes, F. Flack, D. P. Lagally, D. E. Savage, M. Friesen, and M. G. Lagally, *J. Appl. Phys.* **91**(12), 9978 (2002).
- [137] R. M. Osgood III, S. K. Sinha, J. W. Freeland, Y. U. Idzerda, and S. D. Bader, *J. Magn. Magn. Mater.* **199**(698), 698 (1999).
- [138] J. W. Cable, M. R. Khan, G. P. Felcher, and I. K. Schuller, *Phys. Rev. B.* **34**, 1643 (1986).
- [139] M. J. Pechan, J. F. Ankner, C. F. Majkrzak, D. M. Kelly, and I. K. Schuller, *J. Appl. Phys* **75**, 6178 (1994).

- [140] J. W. Freeland, V. Chakarian, K. Bussmann, Y. U. Idzerda, H. Wende, and C.-C. Kao, *J. Appl. Phys.* **83**, 6290 (1998).
- [141] H. A. Dürr, E. Dudzik, S. S. Dhesi, J. B. Goedkoop, G. van der Laan, M. Belakhovsky, C. Mocuta, A. Marty, and Y. Samson, *Science* **284**, 2166 (1999).
- [142] E. Dudzik, S. S. Dhesi, H. A. Dürr, S. P. Collins, M. D. Roper, G. van der Laan, K. Chesnel, M. Belakhovsky, A. Marty, and Y. Samson, *Phys. Rev. B.* **62**(9), 5779 (2000).
- [143] H. A. Dürr, E. Dudzik, S. S. Dhesi, J. B. Goedkoop, G. van der Laan, M. Belakhovsky, C. Mocuta, A. Marty, and Y. Samson, *J. Synchrotron Rad.* **7**, 178 (2000).
- [144] B. Kaplan and G. A. Gehring, *J. Magn. Magn. Mater.* **128**(111), 111 (1993).
- [145] C. J. Kinane, A. K. Suszka, C. H. Marrows, B. J. Hickey, D. A. Arena, J. Dvorak, T. R. Charlton, and S. Langridge, *Appl. Phys. Lett.* **89**, 092507 (2006).
- [146] J. I. Martin, J. Nogués, K. Liu, J. L. Vicentand, and I. K. Schuller, *Journal of Magnetism and Magnetic materials* **256**, 449 (2003).
- [147] T. P. A. Hase, I. Pape, B. K. Tanner, H. Dürr, E. Dudzik, G. van der Laan, C. H. Marrows, and B. J. Hickey, *Phys. Rev. B* **61**, R3792 (2000).
- [148] K. Temst, M. J. V. Bael, and H. Fritzsche, *Appl. Phys. Lett.* **79**, 991 (2001).
- [149] K. Temst, M. J. V. Baela, and H. Fritzsche, *Journal of Magnetism and Magnetic Materials* **226-230**(2), 1840 (2001).
- [150] K. Temst, M. J. V. Bael, V. V. Moshchalkov, and Y. Bruynseraede, *J. Appl. Phys.* **87**, 4216 (2000).
- [151] K. Theis-Bröhl, T. Schmitte, V. Leiner, H. Zabel, K. Rott, H. Brückl, and J. McCord, *Phys. Rev. B* **67**, 184415 (2003).
- [152] K. Theis-Bröhl, *Physica B: Condensed Matter* **345**, 161 (2004).



- [153] L.-A. Michez, C. H. Marrows, P. Steadman, B. J. Hickey, D. A. Arena, H.-L. Zhang, D. G. Bucknall, and S. Langridge, Appl. Phys. Lett **86**(112502), 112502 (2005).
- [154] S. Langridge, L. A. Michez, M. Ali, C. H. Marrows, B. J. Hickey, T. R. Charlton, R. M. Dalgliesh, M. Toohey, E. W. Hill, S. McFadzean, and J. N. Chapman, Phys. Rev. B. **74**(014417), 014417 (2006).
- [155] L.-A. Michez, C. H. Marrows, P. Steadman, B. J. Hickey, D. A. Arena, J. Dvorak, and S. Langridge, Submitted to: J. Phys.: Condens. Matter (2008).
- [156] L. S. E. Alvarez, G. Burnell, C. H. Marrows, K.-Y. Wang, A. M. Blackburn, and D. Williams, Journal of applied Physics **101**, 09F508 (2007).
- [157] L. S. E. Alvarez, *Univeristy of leeds school of physics condensed matter group*, email: phylsea@leeds.ac.uk, URL <http://www.stoner.leeds.ac.uk/>.
- [158] K. Dempsey, *Univeristy of leeds school of physics condensed matter group*, email: phy9kjd@leeds.ac.uk, URL <http://www.stoner.leeds.ac.uk/>.
- [159] A. Thompson, D. Attwood, E. Gullikson, M. Howells, K. Kim, J. Kirz, J. Kortright, I. Lindau, P. Pianetta, A. Robinson, J. Scofield, J. Underwood, *et al.*, *X-ray data booklet* (Centre for X-ray Optics and Advance Light Source, Lawrence Berkely National Laboratory, Univeristy of California, Berkley, CA 94720, 2001).
- [160] C. Spezzani, P. Torelli, M. Sacchi, R. Delaunay, C. F. Hague, V. Cros, and F. Petroff, Appl. Phys. Lett **81**, 3425 (2002).
- [161] C. J. Kinane, N. A. Porter, C. H. Marrows, B. J. Hickey, D. A. Arena, J. Dvorak, E. Sirotkin, F. Y. Ogrin, T. Charlton, and S. Langridge, Journal of Applied Physics **103**(07B513), 07B513 (2008).
- [162] S. S. P. Parkin, C. Chappert, and F. Herman, Europhys. Lett. **24**(71) (1993).
- [163] S. N. Okuno and K. Inomata, Phys. Rev. Lett. **70**(11), 1711 (1993).

- [164] V. Leiner, K. Westerholt, A. M. Blixt, H. Zabel, and B. Hjörvarsson, Phys. Rev. Lett. **91**(037202), 037202 (2003).
- [165] J. Kubler, *The Theory of Itinerant Electron Magnetism* (Oxford Science Publications, 2000).
- [166] A. Dinia, K. Ounadjela, A. Arbaoui, G. Suran, D. Muller, and P. Panissod, Journal of Magnetism and Magnetic Materials **104-107**, 1871 (1992).
- [167] T. T. M. Sakurai and I. Moritani, J. Magn. Soc. Japan **15**, 411 (1991).
- [168] Z. Zhang, L. Zhou, P. E. Wigen, and K. Ounadjela, Journal of applied physics **75**(10), 6434 (1994).
- [169] Z. Zhang, L. Zhou, P. E. Wigen, and K. Ounadjela, Physical Review Letters **73**(2), 336 (1994).
- [170] K. Rahmouni, S. Zoll, N. Persat, D. Stoeffler, and A. Dinia, Computational Materials Science **10**, 269 (1998).
- [171] I. Bakonyi *et al.*, Journal of the Electrochemical Society **149**(10), C469 (2002).
- [172] P. J. H. Bloemen, H. W. van Kesteren, H. J. M. Swagten, and W. J. M. de Jonge, Physical Review B **50**(18), 13505 (1994-II).
- [173] K. Döbrich, M. Wietstruk, J. E. Prieto, F. Heigl, O. Krupin, K. Starke, and G. Kaindl, Physical Review Letters **100**, 227203 (2008).
- [174] A. Dinia *et al.*, Eur. Phys. J. **5**, 203 (1998).
- [175] T. B. Massalski, *Handbook of phase Diagrams of binary alloys*. (ASM Intl, 1996).
- [176] C. A. F. Vaz, J. A. C. Bland, and G. Lauhoff, Reports on Progress in Physics **71**(5), 056501 (2008).
- [177] C. H. Marrows, S. Langridge, and B. J. Hickey, Physical Review B **62**(17), 11340 (2000).